



**HAL**  
open science

# Multifunctional nanoparticles for MR and fluorescence imaging

Sonia Luzia Claro Pinho

► **To cite this version:**

Sonia Luzia Claro Pinho. Multifunctional nanoparticles for MR and fluorescence imaging. Material chemistry. Université Sciences et Technologies - Bordeaux I, 2011. English. NNT : 2011BOR14399 . tel-00661206

**HAL Id: tel-00661206**

**<https://theses.hal.science/tel-00661206>**

Submitted on 18 Jan 2012

**HAL** is a multi-disciplinary open access archive for the deposit and dissemination of scientific research documents, whether they are published or not. The documents may come from teaching and research institutions in France or abroad, or from public or private research centers.

L'archive ouverte pluridisciplinaire **HAL**, est destinée au dépôt et à la diffusion de documents scientifiques de niveau recherche, publiés ou non, émanant des établissements d'enseignement et de recherche français ou étrangers, des laboratoires publics ou privés.



Distributed under a Creative Commons Attribution - NonCommercial - NoDerivatives 4.0 International License

N° d'ordre :4399



# THÈSE

EN CO-TUTELLE PRÉSENTÉE A

## L'UNIVERSITÉ BORDEAUX 1 ET L'UNIVERSITÉ d' AVEIRO

ÉCOLE DOCTORALE DES SCIENCES CHIMIQUES

Par Sonia Luzia Claro de PINHO

POUR OBTENIR LE GRADE DE  
DOCTEUR

SPÉCIALITÉ : *Physico-chimie de la matière condensée.*

### MULTIFUNCTIONAL NANOPARTICLES FOR MR AND FLUORESCENCE IMAGING

Soutenue le 14 décembre 2011

Après avis de :

**S. Begin-Colin**, University of Strasbourg

**H. D. Burrows**, University of Coimbra

*Rapporteur*

*Rapporteur*

Devant la commission d'examen formée de :

MME BEGIN-COLIN Sylvie,  
M. BURROWS HUGH D.,  
M. CARLOS Luis,  
MME DELVILLE Marie-Hélène,  
M. ETOURNEAU Jean,  
M. GERALDES Carlos F.G.C.,  
M. ROCHA Joao,  
M. VIEIRA Joaquim Manuel,

Professeur des Universités  
Professeur en établissement étranger  
Professeur en établissement étranger  
Directeur de recherche CNRS  
Professeur des Universités  
Professeur en établissement étranger  
Professeur en établissement étranger  
Professeur en établissement étranger

*Rapporteur*  
*Rapporteur*  
*Rapporteur*  
*Directeur de thèse*  
*Rapporteur*  
*Rapporteur*  
*Directeur de thèse*  
*Président*





**Sonia Luzia Claro de  
Pinho**

**Nanopartículas Multifuncionais para Imagens de RM  
e Fluorescência**

**Multifunctional Nanoparticles for MR and  
Fluorescence Imaging**





**Sonia Luzia Claro de  
Pinho**

**Nanop rticulas Multifuncionais para Imagens de RM  
Fluoresc ncia**

### **Multifunctional Nanoparticles for MR and Fluorescence Imaging**

Disserta o apresentada   Universidade de Aveiro para cumprimento dos requisitos necess rios   obten o do grau duplo de Doutor em Qu mica pela Universidade de Aveiro e de Physico-chimie de la mati re condens e pela Universidade de Bord us 1, realizada sob o regime de co-tutela com a orienta o cient fica do Doutor Jo o Carlos Matias Celestino Gomes da Rocha, Professor Catedr tico do Departamento de Qu mica da Universidade Aveiro, do Doutor Lu s Ant nio Ferreira Martins Dias Carlos Professor Catedr tico do Departamento de F sica da Universidade Aveiro e da Doutora Marie-H l ne Delville, Directeur de Recherche do Institut de Chimie de la Mati re Condens e de Bordeaux.

Apoio financeiro da FCT e do FSE no  mbito do III Quadro Comunit rio de Apoio.



UNI O EUROPEIA  
Fundo Social Europeu



**À memória da minha avó  
Aos meus pais e irmãos,  
Ao Pedro**



## **o júri / the jury**

presidente / president

**Prof. Doutor Joaquim Manuel Vieira**

Professor Catedrático do Departamento de Engenharia Cerâmica e do Vidro da Universidade de Aveiro

vogais / members

**Prof. Doutor Syvie Begin-Colin**

Professor catedrático do Institut de Physique et de chimie des Matériaux de Strasbourg da Universidade de Strasbourg

**Prof. Doutor Hugh Douglas Burrows**

Professor Catedrático da Faculdade de Ciências e Tecnologia da Universidade de Coimbra

**Prof. Doutor Jean Etourneau**

Professor catedrático do Institut de Chimie de la Matière Condensée de Bordeaux da Universidade de Bordeaux 1

**Prof. Doutor Carlos Frederico de Gusmão Campos de Galdes**

Professor Catedrático da Faculdade de Ciências e Tecnologia da Universidade de Coimbra

**Prof. Doutor João Carlos Matias Celestino Gomes da Rocha**

Professor Catedrático do Departamento de Química da Universidade de Aveiro

**Prof. Doutor Luís António Ferreira Martins Dias Carlos**

Professor Catedrático do Departamento de Física da Universidade de Aveiro

**Doutora Marie-Hélène Delville**

Directeur de Recherche CNRS do Institut de Chimie de la Matière Condensée de Bordeaux da Universidade de Bordeaux 1 .



## **agradecimentos / acknowledgements**

After almost four years of working on this project it was time to wrap it up in a thesis. Through good and less good times, this story came to a 'happy ending' and I should now thank people for their help, support, friendship or for just being around making my life colorful.

I have to say that this thesis was crafted by several remarkable people. First of all, I would like to thank my supervisors/co-supervisors Dr. Marie-Hélène Delville, Dr. João Rocha, Dr Luis Carlos and finally Dr. Carlos Geraldés, whose importance for this thesis as well as for my personal development is inexpressible. They have all shared with me their passion for Science, the most important jewel that I will take home. Marie-Hélène, you've been an amazing teacher and an example for me. You have let me into your world and your philosophy of life and sense of humour. Dr. João Rocha and Dr. Luís Carlos you have given me this PhD opportunity, you have always respected my choices in the research line I have traced and most importantly you've supported me in these choices. Dr. Carlos Geraldés, you have introduced me into the addictive and sophisticated world of NMR. Thank you all for everything! Next in my list are all my labmates from ICMCB in Bordeaux and at the University of Aveiro, a huge "thank you" for the patience, help, brainstorming and enjoyable moments spent together. I will miss those afternoon coffee breaks. A special thanks to my good friend Laetitia Etienne, all your dropping by 'just to say hi' and our great discussions about life. You were always there when I needed you, it always felt good to share either my successes or troubles, being sure of your sincere support in everything. Of course I cannot forget my good friend Dr Patricia Lima for all her support, availability and friendship.

Next in my list are all my labmates from ICMCB in Bordeaux and at the University of Aveiro, a huge "thank you" for the patience, help, brainstorming and enjoyable moments spent together. I will miss those afternoon coffee breaks. A special thanks to my good friend Laetitia Etienne, all your dropping by 'just to say hi' and our great discussions about life. You were always there when I needed you, it always felt good to share either my successes or troubles, being sure of your sincere support in everything. Of course I cannot forget my good friend Dr Patricia Lima for all her support, availability and friendship.

I cannot forget to thank Dr. Stéphane Mornet for his help in chemistry at the early stage of this work and his availability in the lab, as well as, Dr. Pierre Voisin and Dr. Emeline Ribot from RMSB for opening up their lab to me. Many thanks should also be given to François, Patrick, Laetitia and Virginia from the ICMCB, for all their support, friendship and wonderful moments.

I am also very grateful to Dr. Giovannia Pereira for all her help at the NMR lab. She has taught me well.

I cannot forget to thank Dr. Henrique Faneca, Dr. Sophie Laurent and Inês Violante for the precious scientific inputs. Without you I would not be able to have obtain such good biological results

My thanks go also to the friends that were always there, in a parallel world, to keep my sanity by giving me pleasant non-scientific moments. They proven over and over again that true friends are able to grow old without growing apart. Finally, but not less important, I would like to thank my family, specially my parents, and my husband Pedro for all their unconditional support, understanding and affection.



## palavras-chave

Nanopartículas multifuncionais, core-shell/corona, sílica, Fe<sub>2</sub>O<sub>3</sub>, lantanídeos, agentes de contraste para IRM, agentes de contraste ópticos, relaxometria, RMND, fotoluminescência

## resumo

Nos últimos anos, surgiu uma nova geração de nanopartículas (NPs) multifuncionais destinada a aplicações biomédicas, mais concretamente para uso em técnicas de diagnóstico, reconstrução celular e em diversas aplicações terapêuticas. Em relação às suas antecessoras, estas novas nanopartículas apresentam uma estrutura mais elaborada, integrando vários componentes ativos com diferentes funcionalidades que, em princípio, permitem realizar diversas tarefas em simultâneo (como o direccionamento ativo para determinadas células ou compartimentos celulares, imagem e libertação de fármacos). Estas nanopartículas são designadas, por isso, de nanopartículas multifuncionais.

A presente dissertação relata o desenvolvimento de dois tipos de sondas bimodais e as propriedades físico-químicas destas, nomeadamente a sua textura, estrutura e relaxometria e dinâmica de <sup>1</sup>H, com o objectivo de avaliar o seu potencial como agentes de contraste para Imagem por Ressonância Magnética Nuclear (IRM). São, também, apresentados estudos de fotoluminescência que permitem avaliar o potencial daquelas sondas para serem usadas como agentes de contraste óptico. Estes materiais combinam as propriedades dos complexos de lantanídeos trivalentes (Ln<sup>3+</sup>) e das NPs funcionando, assim, como agentes bimodais.

Foram desenvolvidos os seguintes sistemas fotoluminescentes e com contraste  $T_1$  em IRM em que os iões Ln<sup>3+</sup> magnética (Gd<sup>3+</sup>) e opticamente (Eu<sup>3+</sup>, Tb<sup>3+</sup>) activos se encontram à superfície das NPs de sílica: SiO<sub>2</sub>@APS/DTPA:Gd:Ln e SiO<sub>2</sub>@APS/Pyd-DTPA:Gd:Ln (Ln = Eu ou Tb). No que respeita às propriedades de relaxometria, na presença destas NPs observa-se um aumento moderado de  $r_1$  e considerável de  $r_2$ , especialmente a campos magnéticos altos (devido aos efeitos de susceptibilidade para  $r_2$ ). Os iões Eu<sup>3+</sup> apresentam um único ambiente local de baixa simetria, sendo que a emissão de fotoluminescência não é influenciada pela presença simultânea de Gd<sup>3+</sup> e Eu<sup>3+</sup>. Verificou-se que a presença de Tb<sup>3+</sup> (em lugar do ião Eu<sup>3+</sup>) aumenta ainda mais o valor  $r_1$ , diminuindo  $r_2$ . A internalização das NPs em células vivas é rápida e resulta num aumento de intensidade nas imagens ponderadas em  $T_1$ . Foram estudadas as características ópticas de pastilhas de células ("cellular pellets") contendo NPs, tendo-se confirmado o interesse das novas sondas propostas enquanto agentes para imagem bimodal.

Esta dissertação relata, ainda, agentes com contraste em  $T_2$  para IRM, que consistem em um sistema núcleo-coroa ("core-shell") em que é ajustável a espessura da coroa de sílica envolvendo o núcleo de óxido de ferro. A espessura do revestimento de sílica tem um efeito significativo sobre a relaxividade  $r_2$  e  $r_2^*$ , sendo aqui proposto um modelo para explicar este comportamento. A viabilidade celular e a expressão da desidrogenase mitocondrial das células da microglia foram também avaliadas.



## keywords

Multifunctional nanoparticles, core-shell/corona, silica, Fe<sub>2</sub>O<sub>3</sub>, lanthanides, MRI contrast agents, optical contrast agents, relaxometric, RMRD, photoluminescence

## abstract

In the past few years a new generation of multifunctional nanoparticles (NPs) has been proposed for biomedical applications, whose structure is more complex than the structure of their predecessor monofunctional counterparts. The development of these novel NPs aims at enabling or improving the performance in imaging, diagnosis and therapeutic applications. The structure of such NPs comprises several components exhibiting various functionalities that enable the nanoparticles to perform multiple tasks simultaneously, such as active targeting of certain cells or compartmentalization, imaging and delivery of active drugs.

This thesis presents two types of bimodal bio-imaging probes and describes their physical and chemical properties, namely their texture, structure, and <sup>1</sup>H dynamics and relaxometry, in order to evaluate their potential as MRI contrast agents. The photoluminescence properties of these probes are studied, aiming at assessing their interest as optical contrast agents. These materials combine the properties of the trivalent lanthanide (Ln<sup>3+</sup>) complexes and nanoparticles, offering an excellent solution for bimodal imaging.

The designed *T*<sub>1</sub>-type contrast agent are SiO<sub>2</sub>@APS/DTPA:Gd:Ln or SiO<sub>2</sub>@APS/PMN:Gd:Ln (Ln= Eu or Tb) systems, bearing the active magnetic center (Gd<sup>3+</sup>) and the optically-active ions (Eu<sup>3+</sup> and Tb<sup>3+</sup>) on the surface of silica NPs. Concerning the relaxometry properties, moderate *r*<sub>1</sub> increases and significant *r*<sub>2</sub> increases are observed in the NPs presence, especially at high magnetic fields, due to susceptibility effects on *r*<sub>2</sub>. The Eu<sup>3+</sup> ions reside in a single low-symmetry site, and the photoluminescence emission is not influenced by the simultaneous presence of Gd<sup>3+</sup> and Eu<sup>3+</sup>. The presence of Tb<sup>3+</sup>, rather than Eu<sup>3+</sup> ion, further increases *r*<sub>1</sub> but decreases *r*<sub>2</sub>. The uptake of these NPs by living cells is fast and results in an intensity increase in the *T*<sub>1</sub>-weighted MRI images. The optical features of the NPs in cellular pellets are also studied and confirm the potential of these new nanoproboscopes as bimodal imaging agents.

This thesis further reports on a *T*<sub>2</sub> contrast agent consisting of core-shell NPs with a silica shell surrounding an iron oxide core. The thickness of this silica shell has a significant impact on the *r*<sub>2</sub> and *r*<sub>2</sub><sup>\*</sup> relaxivities, and a tentative model is proposed to explain this finding. The cell viability and the mitochondrial dehydrogenase expression given by the microglial cells are also evaluated.



**Mots clés**

Nanoparticules multifonctionnelles, coeur-écorce/couronne, silice,  $\text{Fe}_2\text{O}_3$ , lanthanides, agents de contraste IRM, agents de contraste optiques, relaxométrie, RMRD, photoluminescence

**resumée**

Cette thèse décrit une stratégie de synthèse de nouvelles générations des nanoparticules (NPs) pour applications biomédicales, visant à une amélioration de leurs performances pour l'imagerie, le diagnostic thérapeutique. Ces NPs présentent plusieurs fonctionnalités leur permettant de réaliser des tâches multiples. Deux types de sondes bimodales ont été développés et étudiés afin d'évaluer leur potentiel comme agents (1) de contraste en IRM et (2) luminescents. Ces objets combinent les propriétés des complexes de lanthanide ( $\text{Ln}^{3+}$ ) et celles des NPs de silice ou de type coeur-écorce  $\text{Fe}_2\text{O}_3@\text{SiO}_2$  pour une imagerie bimodale. Ces NPs testées sur des cellules vivantes ont permis d'illustrer la preuve du concept aussi bien en IRM avec une augmentation d'intensité des images et un impact significatif sur les relaxivités  $r_1$ ,  $r_2$  et  $r_2^*$  qu'en photoluminescence. L'étude du système coeur-écorce a montré que l'influence du contrôle fin de l'écorce autour du noyau d'oxyde de fer a pu être modélisée.

# Contents

## 1. Introduction

---

1.1	Context of the thesis	3
1.2	Scope and Objectives of the thesis	8
1.3	Outline of the thesis	9
1.4	References	11

## 2. Magnetic Resonance Imaging Background Concepts

---

2.1	Magnetic Resonance Imaging	17
2.2	MRI Contrast Agents	22
2.2.1	Relaxation	24
2.2.1.1	Spin-Lattice Relaxation	24
2.2.1.2	Spin-Spin Relaxation	26
2.2.2	Relaxivity	28
2.2.2.1	Inner Sphere Relaxivity	30
2.2.2.2	Second and Outer Relaxivity	35
2.2.2.3	Paramagnetic Relaxation Parameters	37
2.2.3	Nuclear Magnetic Resonance Dispersion	39
2.3	Classification of CAs	44
2.3.1	Chemical Composition, Magnetic Properties and Effect on the MRI Image	45
2.3.2	Biodistribution and Applications	48
2.3.2.1	Non-specific Agents	48
2.3.2.2	Specific or Targeted Agents	52
2.3.2.3	Nono-injectable Organ Specific Agents	56
2.3.2.4	Responsive, Smart or Bioactivated Agents	58
2.3.2.5	Contrast Agents Based on Other Properties	63
2.4	References	67

### **3. Fluorescence Imaging Background Concepts**

---

3.1	Optical Imaging	80
3.2	Luminescence	82
3.3	Tissue Optical Properties	91
3.4	Optical Imaging Technology	93
3.5	Optical Contrast Agents	95
3.6	References	102

### **4. Lanthanide-Chelate Grafted Silica Nanoparticles as Bimodal-Imaging Contrast Agents**

---

4.1	Introduction	113
4.2	Experimental Procedures	116
4.3	Results and Discussion	121
4.3.1.	Characterization of Nanoparticles	121
4.3.2.	Photoluminescence Properties	131
4.3.3.	Relaxivity Properties	151
4.3.4.	Cell Imaging	159
4.4	Conclusions	161
4.5	References	163

### **5. Core-Shell Nanoparticles for Bimodal-Imaging Contrast Agents**

---

5.1	Introduction	172
5.2	Experimental Procedures	174
5.3	Results and Discussion	178
5.3.1.	Characterization of Nanoparticles	178
5.3.2.	Relaxivity Properties	185
5.3.3.	Cytotoxicity	199
5.4	Conclusions	201
5.5	References	204

### **6. Final Conclusions and Future Work**

---

Final Conclusions and Future Work	211
-----------------------------------	-----

Nomenclature, symbols and acronyms

$B_0$ : The static, homogeneous magnetic field used to polarize spins, creating magnetization. This can refer to both the direction and the magnitude of the field. The direction of  $B_0$  defines the longitudinal axis.

$B_1$ : Magnetic component of a radio-frequency field applied perpendicular to the longitudinal axis ( $B_0$ ) to perturb the magnetization in some manner (e.g., excitation pulses, inversion pulses, etc).

BOLD, or blood oxygenation level dependent: The BOLD effect is the source of contrast in fMRI. The presence of deoxygenated blood leads to signal loss due to a reduction in  $T_2^*$ .

BPA: Blood pool agents.

Contrast Agent (CA): A substance that enhances contrast, i.e., shortens the relaxation time of water molecules, making them appear 'brighter' in  $T_1$  or  $T_2$  weighted MR images.

Dephasing: In an ensemble of spins, each has a phase angle in the transverse plane. The ensemble can either be coherent (have the same angle) or incoherent (varying angle). Loss of coherence is referred to as "dephasing", which leads to net signal loss. BOLD and diffusion contrast are both based on dephasing.

DNP: Dynamic nuclear polarization.

Echo time (TE): The time between the excitation of magnetization and the acquisition of signal. For long acquisition windows, the TE is usually defined as the point at which the acquisition is closest to the center of  $k$ -space.

ED: Electric-dipole.

Emission quantum efficiency ( $\eta$ ): the fraction of emission processes in which emission of light is involved: 
$$\eta = \frac{\tau_{EXP}}{\tau_{RAD}} = \frac{A_{RAD}}{A_{RAD} + A_{NRAD}}.$$

Emission quantum yield ( $\phi$ ): the ratio of the number of photons emitted and the absorbed: 
$$\phi = \frac{\text{number of emitted photons}}{\text{number of absorbed photons}}.$$

Nomenclature, symbols and acronyms (cont.)

Extracellular fluid agents (ECF): are the contrast agents that have been in clinical use for the longest period of time in contrast-enhanced MR imaging of the liver.

Frequency encode (FE) direction: The direction along which individual lines are acquired in  $k$ -space. Note that one may also refer to the frequency encode direction in the image (i.e., if the FE direction is along  $k_x$ , one may also refer to the x direction in image space as the FE direction). See also phase encode (PE) direction.

Gradient: Spatially varying magnetic field used to manipulate the resonance frequency across an object. MRI scanners incorporate three linearly-varying gradient fields across x, y and z. The strength of the gradient is controlled by the pulse sequence and can be rapidly manipulated (or "switched").

Gradient echo, or GRE/GE: Any MRI sequence that detects an un-refocused signal (i.e., a non-spin-echo sequence).

Inner Coordination Sphere. Used to describe any water molecules that are directly coordinated to the metal ion of a contrast agent.

Inversion: Rotation of magnetization from alignment with  $B_0$  (along +z) to anti-alignment (along -z), caused by a RF pulse with  $180^\circ$  flip angle.

Inversion time (IT): The time between inversion of magnetization and its excitation (often to acquire signal that has been "prepared" with an inversion pulse).

$k$ -space: The conceptual space in which MRI images are acquired. Data in  $k$ -space provides a map of the amount of structure in the image that can be attributed to each spatial frequency. The image and  $k$ -space are related by the mathematical operation called the Fourier transform (FT).

Nomenclature, symbols and  
acronyms (cont.)

Larmor frequency: See resonance frequency.

LLBs: Lanthanide luminescent bioprobes.

LMCT: ligand to-metal charge-transfer.

Longitudinal axis (z): The direction parallel to the main magnetic field ( $B_0$ ), which represents the direction along which magnetization is in equilibrium. After an RF pulse, the magnetization recovers to this equilibrium according to the rate  $T_1$ . The component of magnetization along z cannot be detected.

MD: Magnetic dipole.

Magnetization: The net nuclear magnetic moment induced in an object or tissue when exposed to an external magnetic field. The magnetization is at equilibrium when it is aligned parallel to the external field (along the longitudinal axis) and at its maximum magnitude. MRI experiments manipulate the magnetization away from this equilibrium, into the transverse plane to detect its signal.

MRI: Magnetic Resonance Imaging, a non-invasive technique using strong magnetic fields and radiofrequency pulses to create images of internal anatomy.

NIR: Near-infrared.

NPs: Nanoparticles.

NMR: Nuclear Magnetic Resonance, an analytical technique commonly employed in chemistry.

NMRD. Nuclear Magnetic Resonance Dispersion profile.

OCT: Optical coherence tomography.

Outer Coordination Sphere: Used to describe any water molecules that are not in the inner- or second-coordination spheres.

Nomenclature, symbols and acronyms (cont.)

PARACEST: Paramagnetic chemical exchange saturation transfer.

PHIP: Parahydrogen-induced polarization.

PET: Positron-emission tomography.

Phase: In MRI, phase most commonly refers to the angle of the magnetization in the transverse plane.

Phase encode (PE) direction: The direction perpendicular to individual lines in k-space. Note that one may also refer to the phase encode direction in the image (i.e., if the PE direction is along  $k_y$ , one may also refer to the y direction in image space as the PE direction). Image artefacts are often most severe along the PE direction. See also frequency encode (FE) direction.

Polarization: The tendency for spins to align in the presence of an external magnetic field, creating a net magnetic moment (or, magnetization).

Precession: Gyration of a spinning body, which traces out a cone about the axis of precession. In MRI, the magnetization that is out of alignment with the longitudinal axis precesses about this axis.

Relaxation Time: The time it takes nuclear spins to return to their equilibrium state after excitation by an RF pulse.

Relaxivity: The ability of a contrast agent to shorten the relaxation time of nearby water protons. The higher the relaxivity, the shorter the relaxation time.

Pulse sequence: The series of RF pulses, gradient field amplitudes and acquisition periods applied to acquire a spectrum or an image. Also used to refer to sets of sequences with common properties (e.g., the family of spin echo pulse sequences include structural and diffusion variants).

QDs: Quantum dots.

Nomenclature, symbols and acronyms (cont.)

$R_1$ : The expression of time constant  $T_1$  as a rate:  $R_1=1/T_1$ .

$R_2$ : The expression of time constant  $T_2$  as a rate:  $R_2=1/T_2$ .

Relaxation: The process by which the magnetization slowly returns to equilibrium following the rotation of the magnetization away from the longitudinal axis with an RF pulse. Relaxation (decay) in the transverse plane has the characteristic time  $T_2$ ; relaxation (recovery) along the longitudinal axis has characteristic time  $T_1$ .

Refocusing: The rotation of magnetization in the transverse plane by  $180^\circ$ , usually with the intention of removing the effect of field inhomogeneities on signal.

Repetition time (TR): The time between repeated excitations of a given component of the magnetization. For multi-slice sequences that sequentially excite different imaging slices, the TR is the time between repeated excitations of the same slice. For volume-excite (3D) sequences that repeated excite the entire imaging volume, the TR is the time between repeated excitations of the volume.

Resonance frequency ( $\omega_0$ ): The frequency at which the magnetization can be excited and detected. The frequency varies directly with magnetic field strength, and is normally in the radio frequency (RF) range. Also called Larmor frequency.

RF pulse: A brief transmission of energy in the RF range. In MRI, RF pulses are used to manipulate the direction of the magnetization (e.g., to excite or invert).

Nomenclature, symbols and acronyms (cont.)

Saturation: Removal or reduction of a component of the magnetization using excitation into the transverse plane. Most commonly used to in the context of " $T_1$  saturation", where repeated excitations of magnetization result in incomplete  $T_1$  recovery, and therefore signal reduction. Can also refer to an excitation followed by a "spoiling" mechanism, which deliberately removes signal.

Second Coordination Sphere. Used to describe any water molecules that are coordinated to only the contrast agent ligand, not to the metal ion inside a contrast agent. For example, a water molecule that is hydrogen bound to a polar group on the ligand.

Shimming: The process of improving field homogeneity by compensating for imbalances in the main magnetic field of an MRI system. Accomplished by a combination of constant ("passive") shims and controllable ("active") shim coils.

Spin: The property exhibited by atomic nuclei that contain an odd number of protons and/or neutrons. The property spin causes nuclei to behave as though they are spinning charges. These nuclei are often referred to colloquially as "spins".

Spin echo, or SE: Any MRI pulse sequence characterized by the use of a refocusing pulse to reverse the effect of off-resonance precession. The signal is said to form a spin echo when the off-resonance precession of all spins is reversed, such that the spins re-align to form a signal peak (or "echo").

$T_1$ : The time constant defining the rate of recovery of magnetization along the longitudinal (z) axis following an RF pulse. Also called the spin-lattice relaxation time.

$T_2$ : The time constant defining the irreversible loss of magnetization (and therefore signal) in the transverse (xy) plane following excitation. Also called the spin-spin relaxation time. In tissue,  $T_2$  is shorter than  $T_1$  (often by an order of magnitude). This signal loss cannot be recovered by a spin echo.

Nomenclature, symbols and acronyms (cont.)

$T_2^*$ : The time constant defining the loss of signal following excitation. Two components contribute to  $T_2^*$ . First, some signal loss occurs due to  $T_2$  relaxation (i.e., loss of magnetization). Second, some signal loss is caused by variation in precession angles for different spins within a voxel. This does not represent loss of magnetization, and this component can be recovered with a spin echo.

$T_{1M}$  and  $T_{2M}$ : The longitudinal and transverse proton relaxation enhancement experienced by the inner-sphere water molecules, respectively.

TRL: Time-resolved luminescent.

Transverse plane: The plane orthogonal to the longitudinal axis, denoted as the xy plane. It is defined by the direction of the main ( $B_0$ ) field, and the plane in which the magnetization is observable (i.e., where signal can be detected).

Voxel: A resolution element in a 3D imaging experiment (coming from the term "volume element"); the 3D extension of a pixel (a "picture element").

$C$ : the molar concentration of the paramagnetic complex.

$q$ : the number of water molecules in the inner-coordination sphere directly coordinated to the paramagnetic centre.

$\Delta\omega_M$ : the chemical shift difference between the free and the bound water molecules.

$\gamma$ : the proton gyromagnetic ratio.

$\tau_M$ : the mean residence lifetime of the coordinated water protons within the inner-sphere coordination sphere.

$\tau_R$ : The rotational correlation time of a contrast agent. This is related to how fast the contrast is physically tumbling in solution.

$\tau_{RAD}$ : Radiative lifetime.



**1.**

# *Introduction*

---

1.1. Context of the thesis	3
1.2. Scope and objectives of the thesis	8
1.3. Outline of the thesis	9
1.4. References	11

## 1.1. CONTEXT OF THE THESIS

Nanomedicine is defined as the medical application technology in the nanometer range (ranging from biomedical imaging to drug delivery and therapeutics).<sup>1</sup> This is a new, fast expanding and growing medical field. The overall goals of traditional medicine and nanomedicine are the same: early and accurate diagnosis, effective treatments, free from side effects and non-invasive evaluation of the efficacy of the treatment. Nanotechnology used in nanomedicine brings not only improvements to the existing techniques but also provides completely new tools and capabilities.<sup>2,3</sup>

Nanotechnology is the study, understanding and control of matter at dimensions in the range of 1 to ~100 nanometres, where unique phenomena enable novel applications.<sup>4</sup> It is a very broad interdisciplinary research field that involves various areas of science, such as chemistry, physics, engineering, biology and medicine, while eroding the traditional boundaries between them.<sup>5</sup>

Indeed, there is a radical change in the physical and chemical properties of materials as their size is scaled down to small clusters of atoms. When the size decreases the surface-area-to-volume ratio increases, since there is a larger percentage of surface atoms compared with bulk materials.<sup>6</sup> As nanodevices in the same range of dimension as antibodies, membrane receptors, nucleic acids and proteins, among other biomolecules the can possess biomimetic features.<sup>7</sup>

Given all these outstanding features nanoparticles are powerful tools for imaging, diagnosis and therapy. Over the last few years, a new generation of nanoparticles has arisen with improved performances for the same type of applications and with a more complex structure compared to the simpler monofunctional nanoparticles. These complex nanoparticles comprise different components that can carry out various functions, which enable these nanoparticles to perform multiple tasks simultaneously (active targeting a given type of cells or compartment, imaging them and delivering an active compound). For example, a core particle may be linked to a specific targeting functional group that recognises the unique surface signatures of the target cells. The same particle can be modified with an imaging functional group to monitor the drug transport process, a molecular entity to evaluate the therapeutic efficacy of a drug, a specific cellular

penetration moiety and a therapeutic agent.<sup>7</sup> Therefore, these complex nanoparticles are termed multifunctional nanoparticles.<sup>8</sup> A schematic representation of these systems is given in Figure 1.1.

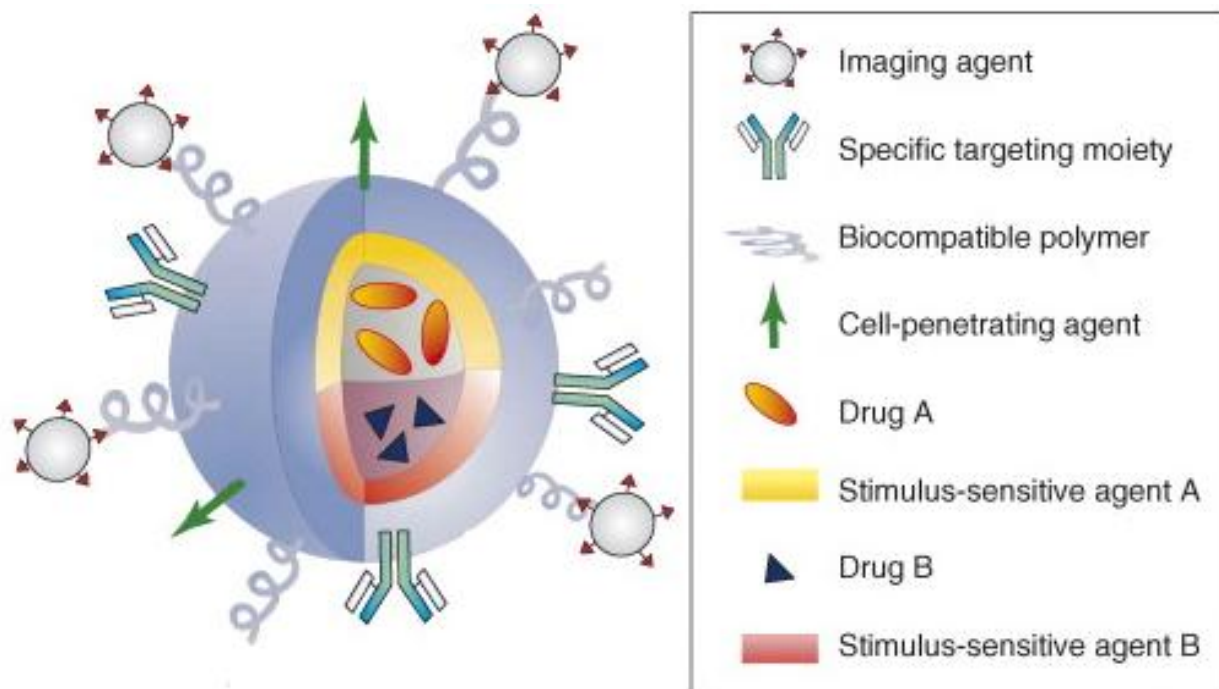


**Figure 1.1.** Schematic representation of a multifunctional nanoparticle<sup>7</sup>

A large variety of therapeutic entities can be incorporated or attached on the surface of the multifunctional nanoparticles while other components can be used for targeting and/or imaging. Nanoparticles are prepared with organic polymers (organic nanoparticles) and/or inorganic elements (inorganic nanoparticles).<sup>7</sup> Figure 1.2 depicts examples of nanomaterials and nanocarrier systems. There are three major categories in which the multifunctional nanoparticles may be classified: liposomes and micelles, polymeric carriers, and core-shell/corona structures.

**Table 1.1.** Strategies for constructing multifunctional nanoparticles.<sup>6</sup>

Properties	Benefits	Functional group	Refs
Stability, biocompatibility	Maintain drug levels in the blood, thereby improving specificity	Polyethylene glycol	[9]
		Modified acrylic acid polymers	[10]
		Phospholipid micelles	[11]
Specific targeting	Increase efficiency, reduce toxicity	Polypeptides	[12]
		Antibodies	[13]
		Peptides	[14]
		Aptamers	[15]
		Carbohydrate	[16]
Intracellular penetration	Modify nanoparticle pharmacokinetics and biodistribution, increasing drug efficacy	Folic acid	[17]
		Peptides	
		Trans-activating transcriptional activator (TAT)	[18]
		Ligands	
		Transferrin	[19]
		Positively charged moieties	
		Cationic lipids	[20]
Cationic polymers	[21]		
Imaging	Report real-time nanoparticle biodistribution	Quantum dots	[22]
		Magnetic nanoparticles	[23]
Stimulus-sensitive drug release	Control bioavailability, reduces toxicity	pH-labile	[18]
		Photosensitive	[24]
		Thermosensitive	[25]
		Magnetic sensitive	[26]
		Photothermal sensitive	[27]
Redox sensitive	[28]		

## Liposomes and micelles

One of the earliest forms of nanomedicine was the development of liposomes as drug delivery vesicles. As their sizes vary from 100 nm up to a few micrometers they can

carry within their phospholipid bilayered membrane different types of vesicles (e.g. small molecules to proteins, peptides, DNA, magnetic nanoparticles).<sup>29,30,31</sup>

Liposomes are generally considered non-toxic, biodegradable and non-immunogenic, although recently some adverse effects have been described.<sup>32</sup> Although the underlying mechanism has not yet been fully elucidated, it appears that the choice of liposome characteristics plays an important role and that choosing the appropriate lipids and their size helps to overcome these unexpected effects.<sup>33,34</sup>

PEGylation is the process of covalent attachment of polyethylene glycol polymer chains to another molecule, normally a drug or therapeutic protein. By employing PEGylation the circulation time is increased and by combining the liposomes with a therapeutic agent the multifunctionality of the vesicles is increased.<sup>35</sup>

Micelles (lipid vesicles of 20 to 100 nm) present similar features as liposomes (long circulating behaviour, high biocompatibility and the possibility of increasing the functionality number). They also offer a better method of delivering hydrophobic drugs. In this system, the hydrophobic parts form the core to minimize their exposure to aqueous surroundings, whereas the hydrophilic blocks form the corona-like shell that stabilizes the core through direct contact with water.<sup>36</sup> The hydrophobic core is capable of carrying pharmaceuticals (poorly water soluble drugs), with high loading capacity (5–25% weight), while its hydrophilic shell provides not only a steric protection for the micelle (with increased stability in blood) but also functional groups suitable for further micelle modification.<sup>37</sup>

### **Polymeric carriers (polymeric or dendrimers)**

The polymeric carriers are formed by a hydrophobic core that is capable of carrying pharmaceuticals (poorly water soluble drugs) with high loading capacity (5–25% weight) and a hydrophilic shell that provides not only a steric protection for the micelle (with increased stability in blood) but also functional groups suitable for further micelle modification (repeated relative to previous phrase, reword)<sup>38,39</sup>, such as starch,<sup>40</sup> poly(ethylene glycol) –PEG,<sup>41,42</sup> poly(lactic-co-glycolic acid) -PLGA<sup>43,44</sup>).

Dendrimers are a relatively novel class of synthetic polymers with highly ordered structure. They are highly branched (<15 nm) and have layered architectures consisting of a central core, an internal region and numerous terminal groups that determine dendrimer characteristics.<sup>7</sup> They present a highly interbranched cavity density, therefore a high

density of functional groups on the surface. Their functionalisation possibilities, symmetry perfection, diameters in the range of 10 to 100 nm and internal cavities provide many potential applications in biochemistry, gene therapy and nanomedicine. Nanoparticles coated with dendrimers can alter the charge, functionality, reactivity and enhance their both stability and dispersibility.<sup>45,46,47</sup>

### **Core – shell/corona structures (Inorganic or magnetic nanoparticles, quantum dots or carbon nanotubes)**

The core – shell/corona architecture is another attractive alternative approach for developing multifunctional nanoparticles. These structures normally comprise optical, targeting and delivery functions. Nanoparticles visualisation is normally achieved through the core's functionality. The shell/corona protects the core and acts as the scaffold for adding further functions, such as drug delivery (drugs are incorporated and released in a controlled manner, either via diffusion or active delivery via pH), temperature modulation, active targeting (through surface modification with specific ligands), or even a tool for an alternative way of visualisation through the incorporation of a different imaging agent. A large variety of combinations of materials that are assembled in core-shell/corona architecture can be found in the literature as the core quantum dots<sup>48,49,50</sup>, fluorophores<sup>51</sup> or magnetic nanoparticles<sup>52,53</sup> are the most researched moieties. The most commonly used coating layers are either organic layers (polymethyl methacrylate) (PMMA),<sup>54</sup> polylactic acid (PLA),<sup>55,56</sup> poly(lactic-co-glycolic acid) (PLGA),<sup>26,43</sup> polyvinyl alcohol (PVA)<sup>25,57</sup> or inorganic materials as silica (amorphous,<sup>58</sup> mesoporous<sup>59</sup>), apatite,<sup>60</sup> or have a metallic layer of gold<sup>61</sup> or silver.<sup>62</sup>

Extensive *in vivo* application of nanoparticles will require a more exhaustive exploration of the physicochemical and physiological processes occurring in the biological environments. The smallest capillaries in the human body are 4-6  $\mu\text{m}$  in diameter. When considering possible medical applications (both *in-vivo* or *in-vitro*) the nanoparticles have to possess some basic properties. Specifically they must have a size of less than 20 nm (especially for intravenous (i.v.) administration), high surface area with a larger platform for surface functionalisation, high colloidal stability (with minimum agglomeration and aggregation) and the ability to overcome biological barriers.<sup>63</sup> For the particular case of *in-*

*in vivo* applications the particles should adhere to more strict requirements: non-toxicity, non-immunogenicity, long term retention during blood circulation and the ability to reach, and pass through, the endothelial capillary membranes without causing an embolism of the bigger vessels.<sup>64,65</sup>

The three major applications of nanoparticles in medicine are imaging (diagnosis), drug delivery (therapeutics) and cell reconstruction. In this thesis I report the design and synthesis of nanoparticles for bi-modal imaging with potential to be further developed in the future with the addition of cell-targeting agents and drug delivery molecules.

### 1.2. SCOPE AND OBJECTIVES OF THIS THESIS

Nanoparticles have to meet several specifications in order to be applied *in-vivo* and *in-vitro*. Important features these particles should have are a small overall size, high surface area for surface functionalisation, high colloidal stability and the ability to pass the biological barriers.

To achieve the proposed objective two sets of contrast agents were designed, synthesized and characterized:

- **$T_1$  contrast agent with an optical  $\text{Ln}^{3+}$  probe**

The nanoparticles we will consider are hybrid inorganic-organic  $\text{SiO}_2$ @APS core-corona. Lanthanide chelates are linked onto these particles, for their relaxometry ( $\text{Gd}^{3+}$ ) and luminescence ( $\text{Eu}^{3+}$  or  $\text{Tb}^{3+}$ ) properties. Subsequently, these nanoparticles are internalised in living cells in the form of cellular pellets in order to confirm their potential as new probes for bimodal imaging.

- **$T_2$  contrast agent**

These are core-shell nanoparticles,  $\text{Fe}_2\text{O}_3$ @ $\text{SiO}_2$ . The influence of the silica shell on the relaxometry and cytotoxicity properties was studied.

### 1.3. OUTLINE OF THIS THESIS

This thesis is organised in six chapters, as follows.

**Chapter 1** provides an overview of different multifunctional nanoparticles for applications in medicine.

**Chapter 2** presents a general introduction of magnetic resonance imaging and MRI contrast agents, as well as the parameters governing the relaxivity of the latter, presenting a summary of the various classes of contrast agents, classified according to their applications.

**Chapter 3** gives a brief introduction to optical imaging and its main applications are presented. A short overview is provided of the photoluminescence phenomenon, in particular of trivalent lanthanides. The optical properties of tissues are succinctly described as well as the different techniques available for optical imaging. A summary of the various types of optical contrast agents is also presented.

**Chapter 4** describes the synthesis of  $T_1$  contrast agents, with an optical  $\text{Ln}^{3+}$  probe attached. In order to optimise the nanoparticles emission, two types of chelating agents, with and without an aromatic ring, were used. The physical and chemical properties were studied by several different techniques. The uptake of these nanoparticles by living RAW cells was evaluated using cellular pellets. The optical and magnetic features of these probes in the cellular pellet were assessed in order to confirm their potential as bimodal imaging agents.

**Chapter 5** reports the synthesis both, the core of the magnetic iron oxide nanoparticles, with a well-defined size, and the silica shell. I shall show that the silica-shell thickness determines the relaxometry properties, and I shall propose a tentative theoretical to explain this fact. The effect of these nanoparticles on the viability and the mitochondrial dehydrogenase expression of microglial cells were also evaluated. The magnetic properties of these nanoparticles and their  $T_1$  relaxivities as a function of the external magnetic field (Nuclear Magnetic Relaxation Dispersion (NMRD) plots) were also studied in detail and rationalized on the basis of current theory.

Finally, **chapter 6** presents the concluding remarks of this thesis and an outlook for the future.

#### 1.4. REFERENCES

- 1 Bawarski, W. E.; Chidlow, E.; Bharali, D. J.; Mousa, S. A., Emerging nanopharmaceuticals. *Nanomedicine-Nanotechnology Biology and Medicine* **2008**, 4 (4), 273-282.
- 2 Freitas, R. A., Jr., What is nanomedicine? *Nanomedicine : nanotechnology, biology, and medicine* **2005**, 1 (1), 2-9.
- 3 Caruthers, S. D.; Wickline, S. A.; Lanza, G. M., Nanotechnological applications in medicine. *Current Opinion in Biotechnology* **2007**, 18 (1), 26-30.
- 4 National Nanotechnology Initiative. What is nanotechnology? <http://www.nano.gov/html/facts/whatIsNano.html> Accessed 10 January 2010.
- 5 Thompson, M., Nanomedicine - A tremendous research opportunity for analytical chemists. *Analyst* **2004**, 129 (8), 671-671.
- 6 Moghimi, S. M.; Hunter, A. C.; Murray, J. C., Nanomedicine: current status and future prospects. *Faseb Journal* **2005**, 19 (3), 311-330.
- 7 Sanvicens, N.; Marco, M. P., Multifunctional nanoparticles - properties and prospects for their use in human medicine. *Trends in Biotechnology* **2008**, 26 (8), 425-433.
- 8 Liu, Z.; Kiessling, F.; Gaetjens, J., Advanced Nanomaterials in Multimodal Imaging: Design, Functionalization, and Biomedical Applications. *Journal of Nanomaterials* **2010**.
- 9 Gref, R.; Minamitake, Y.; Peracchia, M. T.; Trubetskoy, V.; Torchilin, V.; Langer, R., Biodegradable long-circulating polymeric nanospheres. *Science* **1994**, 263 (5153), 1600-1603.
- 10 Sathe, T. R.; Agrawal, A.; Nie, S., Mesoporous silica beads embedded with semiconductor quantum dots and iron oxide nanocrystals: Dual-function microcarriers for optical encoding and magnetic separation. *Analytical Chemistry* **2006**, 78 (16), 5627-5632.
- 11 Dubertret, B.; Skourides, P.; Norris, D. J.; Noireaux, V.; Brivanlou, A. H.; Libchaber, A., In vivo imaging of quantum dots encapsulated in phospholipid micelles. *Science* **2002**, 298 (5599), 1759-1762.
- 12 Pinaud, F.; King, D.; Moore, H. P.; Weiss, S., Bioactivation and cell targeting of semiconductor CdSe/ZnS nanocrystals with phytochelatin-related peptides. *Journal of the American Chemical Society* **2004**, 126 (19), 6115-6123.
- 13 Lukyanov, A. N.; Elbayoumi, T. A.; Chakilam, A. R.; Torchilin, V. P., Tumor-targeted liposomes: doxorubicin-loaded long-circulating liposomes modified with anti-cancer antibody. *Journal of Controlled Release* **2004**, 100 (1), 135-144.
- 14 Akerman, M. E.; Chan, W. C. W.; Laakkonen, P.; Bhatia, S. N.; Ruoslahti, E., Nanocrystal targeting in vivo. *Proceedings of the National Academy of Sciences of the United States of America* **2002**, 99 (20), 12617-12621.

- 
- 15 Farokhzad, O. C.; Cheng, J. J.; Teply, B. A.; Sherifi, I.; Jon, S.; Kantoff, P. W.; Richie, J. P.; Langer, R., Targeted nanoparticle-aptamer bioconjugates for cancer chemotherapy in vivo. *Proceedings of the National Academy of Sciences of the United States of America* **2006**, *103* (16), 6315-6320.
- 16 Zhu, J.; Xue, J.; Guo, Z.; Zhang, L.; Marchant, R. E., Biomimetic glycoliposomes as nanocarriers for targeting P-selectin on activated platelets. *Bioconjugate Chemistry* **2007**, *18* (5), 1366-1369.
- 17 Kukowska-Latallo, J. F.; Candido, K. A.; Cao, Z. Y.; Nigavekar, S. S.; Majoros, I. J.; Thomas, T. P.; Balogh, L. P.; Khan, M. K.; Baker, J. R., Nanoparticle targeting of anticancer drug improves therapeutic response in animal model of human epithelial cancer. *Cancer Res* **2005**, *65* (12), 5317-5324.
- 18 Sawant, R. M.; Hurley, J. P.; Salmaso, S.; Kale, A.; Tolcheva, E.; Levchenko, T. S.; Torchilin, V. P., "SMART" drug delivery systems: Double-targeted pH-responsive pharmaceutical nanocarriers. *Bioconjugate Chemistry* **2006**, *17* (4), 943-949.
- 19 Bartlett, D. W.; Su, H.; Hildebrandt, I. J.; Weber, W. A.; Davis, M. E., Impact of tumor-specific targeting on the biodistribution and efficacy of siRNA nanoparticles measured by multimodality in vivo imaging. *Proceedings of the National Academy of Sciences of the United States of America* **2007**, *104* (39), 15549-15554.
- 20 Li, W.; Szoka, F. C., Jr., Lipid-based nanoparticles for nucleic acid delivery. *Pharmaceutical Research* **2007**, *24* (3), 438-449.
- 21 Luten, J.; van Nostruin, C. F.; De Smedt, S. C.; Hennink, W. E., Biodegradable polymers as non-viral carriers for plasmid DNA delivery. *Journal of Controlled Release* **2008**, *126* (2), 97-110.
- 22 Derfus, A. M.; Chen, A. A.; Min, D.-H.; Ruoslahti, E.; Bhatia, S. N., Targeted quantum dot conjugates for siRNA delivery. *Bioconjugate Chemistry* **2007**, *18* (5), 1391-1396.
- 23 Medarova, Z.; Pham, W.; Farrar, C.; Petkova, V.; Moore, A., In vivo imaging of siRNA delivery and silencing in tumors. *Nature Medicine* **2007**, *13* (3), 372-377.
- 24 Skirtach, A. G.; Javier, A. M.; Kreft, O.; Koehler, K.; Alberola, A. P.; Moehwald, H.; Parak, W. J.; Sukhorukov, G. B., Laser-induced release of encapsulated materials inside living cells. *Angewandte Chemie-International Edition* **2006**, *45* (28), 4612-4617.
- 25 Stover, T. C.; Kim, Y. S.; Lowe, T. L.; Kester, M., Thermoresponsive and biodegradable linear-dendritic nanoparticles for targeted and sustained release of a pro-apoptotic drug. *Biomaterials* **2008**, *29* (3), 359-369.
- 26 Hu, S.-H.; Liu, T.-Y.; Huang, H.-Y.; Liu, D.-M.; Chen, S.-Y., Magnetic-sensitive silica nanospheres for controlled drug release. *Langmuir* **2008**, *24* (1), 239-244.
- 27 Park, H.; Yang, J.; Seo, S.; Kim, K.; Suh, J.; Kim, D.; Haam, S.; Yoo, K.-H., Multifunctional nanoparticles for photothermally controlled drug delivery and magnetic resonance imaging enhancement. *Small* **2008**, *4* (2), 192-196.

- 28 Trewyn, B. G.; Giri, S.; Slowing, I. I.; Lin, V. S. Y., Mesoporous silica nanoparticle based controlled release, drug delivery, and biosensor systems. *Chemical Communications* **2007**, (31), 3236-3245.
- 29 Torchilin, V. P., Recent advances with liposomes as pharmaceutical carriers. *Nature Reviews Drug Discovery* **2005**, *4* (2), 145-160.
- 30 Koning, G. A.; Krijger, G. C., Targeted multifunctional lipid-based nanocarriers for image-guided drug delivery. *Anti-Cancer Agents in Medicinal Chemistry* **2007**, *7* (4), 425-440.
- 31 Mezei, M.; Gulasekharan, V., Liposomes - a selective drug delivery system for the topical route of administration I. Lotion dosage form *Life Sciences* **1980**, *26* (18), 1473-1477.
- 32 Chanan-Khan, A.; Szebeni, J.; Savay, S.; Liebes, L.; Rafique, N. M.; Alving, C. R.; Muggia, F. M., Complement activation following first exposure to pegylated liposomal doxorubicin (Doxil): possible role in hypersensitivity reactions. *Annals of Oncology* **2003**, *14* (9), 1430-1437.
- 33 Ishida, T.; Harada, M.; Wang, X. Y.; Ichihara, M.; Irimura, K.; Kiwada, H., Accelerated blood clearance of PEGylated liposomes following preceding liposome injection: Effects of lipid dose and PEG surface-density and chain length of the first-dose liposomes. *Journal of Controlled Release* **2005**, *105* (3), 305-317.
- 34 Ishida, T.; Ichikawa, T.; Ichihara, M.; Sadzuka, Y.; Kiwada, H., Effect of the physicochemical properties of initially injected liposomes on the clearance of subsequently injected PEGylated liposomes in mice. *Journal of Controlled Release* **2004**, *95* (3), 403-412.
- 35 Sun, C.; Lee, J. S. H.; Zhang, M., Magnetic nanoparticles in MR imaging and drug delivery. *Advanced Drug Delivery Reviews* **2008**, *60* (11), 1252-1265.
- 36 Torchilin, V. P., Recent advances with liposomes as pharmaceutical carriers. *Nature Reviews Drug Discovery* **2005**, *4* (2), 145-160.
- 37 Zhang, L.; Gu, F. X.; Chan, J. M.; Wang, A. Z.; Langer, R. S.; Farokhzad, O. C., Nanoparticles in medicine: Therapeutic applications and developments. *Clinical Pharmacology & Therapeutics* **2008**, *83* (5), 761-769.
- 38 Mikhaylova, M.; Kim, D. K.; Berry, C. C.; Zagorodni, A.; Toprak, M.; Curtis, A. S. G.; Muhammed, M., BSA immobilization on amine-functionalized superparamagnetic iron oxide nanoparticles. *Chemistry of Materials* **2004**, *16* (12), 2344-2354.
- 39 Raynal, I.; Prigent, P.; Peyramaure, S.; Najid, A.; Rebuzzi, C.; Corot, C., Macrophage endocytosis of superparamagnetic iron oxide nanoparticles - Mechanisms and comparison of Ferumoxides and Ferumoxtran-10. *Investigative Radiology* **2004**, *39* (1), 56-63.
- 40 Kim, D. K.; Mikhaylova, M.; Wang, F. H.; Kehr, J.; Bjelke, B.; Zhang, Y.; Tsakalagos, T.; Muhammed, M., Starch-coated superparamagnetic nanoparticles as MR contrast agents. *Chemistry of Materials* **2003**, *15* (23), 4343-4351.

- 
- 41 Kim, D. K.; Mikhaylova, M.; Zhang, Y.; Muhammed, M., Protective coating of superparamagnetic iron oxide nanoparticles. *Chemistry of Materials* **2003**, *15* (8), 1617-1627.
- 42 Mikhaylova, M.; Kim, D. K.; Bobrysheva, N.; Osmolowsky, M.; Semenov, V.; Tsakalakos, T.; Muhammed, M., Superparamagnetism of magnetite nanoparticles: Dependence on surface modification. *Langmuir* **2004**, *20* (6), 2472-2477.
- 43 Naik, S.; Carpenter, E. E., Poly(D,L-lactide-co-glycolide) microcomposite containing magnetic iron core nanoparticles as a drug carrier. *Journal of Applied Physics* **2008**, *103* (7).
- 44 Cheng, J.; Teply, B. A.; Sherifi, I.; Sung, J.; Luther, G.; Gu, F. X.; Levy-Nissenbaum, E.; Radovic-Moreno, A. F.; Langer, R.; Farokhzad, O. C., Formulation of functionalized PLGA-PEG nanoparticles for in vivo targeted drug delivery. *Biomaterials* **2007**, *28* (5), 869-876.
- 45 Bawarski, W. E.; Chidlow, E.; Bharali, D. J.; Mousa, S. A., Emerging nanopharmaceuticals. *Nanomedicine-Nanotechnology Biology and Medicine* **2008**, *4* (4), 273-282.
- 46 Lee, C. C.; MacKay, J. A.; Frechet, J. M. J.; Szoka, F. C., Designing dendrimers for biological applications. *Nature Biotechnology* **2005**, *23* (12), 1517-1526.
- 47 Koo, O. M.; Rubinstein, I.; Onyuk, H., Role of nanotechnology in targeted drug delivery and imaging: a concise review. *Nanomedicine : nanotechnology, biology, and medicine* **2005**, *1* (3), 193-212.
- 48 Darbandi, M.; Thomann, R.; Nann, T., Single quantum dots in silica spheres by microemulsion synthesis. *Chemistry of Materials* **2005**, *17* (23), 5720-5725.
- 49 Koole, R.; van Schooneveld, M. M.; Hilhorst, J.; Donega, C. d. M.; Hart, D. C.; van Blaaderen, A.; Vanmaekelbergh, D.; Meijerink, A., On the incorporation mechanism of hydrophobic quantum dots in silica spheres by a reverse microemulsion method. *Chemistry of Materials* **2008**, *20* (7), 2503-2512.
- 50 Hu, S.-H.; Liu, D.-M.; Tung, W.-L.; Liao, C.-F.; Chen, S.-Y., Surfactant-Free, Self-Assembled PVA-Iron Oxide/Silica Core-Shell Nanocarriers for Highly Sensitive, Magnetically Controlled Drug Release and Ultrahigh Cancer Cell Uptake Efficiency. *Advanced Functional Materials* **2008**, *18* (19), 2946-2955.
- 51 Burns, A.; Ow, H.; Wiesner, U., Fluorescent core-shell silica nanoparticles: towards "Lab on a Particle" architectures for nanobiotechnology. *Chemical Society Reviews* **2006**, *35* (11), 1028-1042.
- 52 Heitsch, A. T.; Smith, D. K.; Patel, R. N.; Ress, D.; Korgel, B. A., Multifunctional particles: Magnetic nanocrystals and gold nanorods coated with fluorescent dye-doped silica shells. *J Solid State Chem* **2008**, *181* (7), 1590-1599.

- 53 Modak, S.; Karan, S.; Roy, S. K.; Mukherjee, S.; Das, D.; Chakrabarti, P. K., Preparation and characterizations of SiO(2)-coated nanoparticles of Mn(0.4)Zn(0.6)Fe(2)O(4). *Journal of Magnetism and Magnetic Materials* **2009**, *321* (3), 169-174.
- 54 Ninjbadgar, T.; Yamamoto, S.; Fukuda, T., Synthesis and magnetic properties of the gamma-Fe<sub>2</sub>O<sub>3</sub>/poly-(methyl methacrylate)-core/shell nanoparticles. *Solid State Sciences* **2004**, *6* (8), 879-885.
- 55 Gomez-Lopera, S. A.; Arias, J. L.; Gallardo, V.; Delgado, A. V., Colloidal stability of magnetite/poly(lactic acid) core/shell nanoparticles. *Langmuir* **2006**, *22* (6), 2816-2821.
- 56 Chen, F.; Gao, Q.; Hong, G.; Ni, J., Synthesis of magnetite core-shell nanoparticles by surface-initiated ring-opening polymerization of L-lactide. *Journal of Magnetism and Magnetic Materials* **2008**, *320* (13), 1921-1927.
- 57 Liu, T.-Y.; Huang, L.-Y.; Hu, S.-H.; Yang, M.-C.; Chen, S.-Y., Core-shell magnetic nanoparticles of heparin conjugate as recycling anticoagulants. *Journal of Biomedical Nanotechnology* **2007**, *3* (4), 353-359.
- 58 Pinho, S. L. C.; Pereira, G. A.; Voisin, P.; Kassem, J.; Bouchaud, V.; Etienne, L.; Peters, J. A.; Carlos, L. D.; Mornet, S.; Geraldès, C. F. G. C.; Rocha, J.; Delville, M.-H., Fine Tuning of the Relaxometry of gamma-Fe(2)O(3)@SiO(2) Nanoparticles by Tweaking the Silica Coating Thickness. *Acs Nano* **2010**, *4* (9), 5339-5349.
- 59 Liu, H.-M.; Wu, S.-H.; Lu, C.-W.; Yao, M.; Hsiao, J.-K.; Hung, Y.; Lin, Y.-S.; Mou, C.-Y.; Yang, C.-S.; Huang, D.-M.; Chen, Y.-C., Mesoporous silica nanoparticles improve magnetic labeling efficiency in human stem cells. *Small* **2008**, *4* (5), 619-626.
- 60 Pon-On, W.; Meejoo, S.; Tang, I. M., Substitution of manganese and iron into hydroxyapatite: Core/shell nanoparticles. *Materials Research Bulletin* **2008**, *43* (8-9), 2137-2144.
- 61 Wang, L. Y.; Luo, J.; Fan, Q.; Suzuki, M.; Suzuki, I. S.; Engelhard, M. H.; Lin, Y. H.; Kim, N.; Wang, J. Q.; Zhong, C. J., Monodispersed core-shell Fe<sub>3</sub>O<sub>4</sub>@Au nanoparticles. *Journal of Physical Chemistry B* **2005**, *109* (46), 21593-21601.
- 62 Lai, C. H.; Wu, T. F.; Lan, M. D., Synthesis and property of core-shell Ag@Fe<sub>3</sub>O<sub>4</sub> nanoparticles. *IEEE T Magn* **2005**, *41* (10), 3397-3399.
- 63 Kreyling, W. G.; Semmler-Behnke, M.; Moeller, W., Health implications of nanoparticles. *Journal of Nanoparticle Research* **2006**, *8* (5), 543-562.
- 64 Pathak, P.; Katiyar, V. K., Multifunctional nanoparticles and their role in cancer drug delivery – a review. *Journal of Nanotechnology Online* 2007, *3*, 1 - 17.
- 65 Tartaj, P.; Morales, M. D.; Veintemillas-Verdaguer, S.; Gonzalez-Carreño, T.; Serna, C. J., The preparation of magnetic nanoparticles for applications in biomedicine. *Journal of Physics D-Applied Physics* **2003**, *36* (13), R182-R197.

## **2.**

# *Magnetic Resonance Imaging Background Concepts*

---

2.1. Magnetic Resonance Imaging	17
2.2. MRI Contrast Agents	22
2.2.1. Relaxation	24
2.2.1.1. Spin-Lattice Relaxation	24
2.2.1.2. Spin-Spin Relaxation	26
2.2.2. Relaxivity	28
2.2.2.1. Inner Sphere Relaxivity	30
2.2.2.2. Second and Outer Relaxivity	35
2.2.2.3. Paramagnetic Relaxation Parameters	37
2.2.3. Nuclear Magnetic Resonance Dispersion	39
2.3. Classification of CAs	44
2.3.1. Chemical Composition, Magnetic Properties and Effect on the MRI Image	45
2.3.2. Biodistribution and Applications	48
2.3.2.1. Non-specific Agents	48
2.3.2.2. Specific or Targeted Agents	52
2.3.2.3. Nono-injectable Organ Specific Agents	56
2.3.2.4. Responsive, Smart or Bioactivated Agents	58
2.3.2.5. Contrast Agents Based on Other Properties	63
2.4. References	67

## 2.1. MAGNETIC RESONANCE IMAGING

Magnetic Resonance Imaging (MRI) is a non-invasive diagnostic tool providing high-resolution ( $\mu m$  scale) anatomical images of soft tissue and allowing the quantitative assessment of disease pathogenesis by measuring up-regulated biomarkers. MRI is based on the principles of Nuclear Magnetic Resonance (NMR), a spectroscopic technique applied by scientists to obtain microscopic chemical and physical information about molecules.

Felix Bloch and Edward Purcell independently discovered the phenomenon of magnetic resonance in 1946 and for this they were awarded the Nobel Prize in 1952. Until the 1970s the NMR technique was used only for chemical and physical analysis. The first step towards the discovery of the magnetic resonance was taken in 1971 by Raymond Damadian who showed that the nuclear magnetic relaxation times of healthy and pathogenic tissues are different.<sup>1</sup> It was only in 1973, however, that imaging moved from the single dimension of NMR spectroscopy to the second dimension of spatial orientation with the discovery of NMR-zero field gradients by Paul Lauterbur. He published this new imaging technique in a short and concise paper in *Nature* entitled "Image formation by induced local interaction; examples employing magnetic resonance".<sup>2</sup>

MRI is an extension of nuclear magnetic resonance spectroscopy used in chemistry. The nuclei of certain atoms have an inherent magnetic dipole moment resulting from their electrical charge and spin. If these nuclei are placed in a strong, static magnetic field,  $B_0$ , they precess around it at the Larmor frequency,  $\omega_l$ . The energy levels of the spins are determined by their orientation along the axis parallel to  $B_0$  (either with or against  $B_0$ ). There are more spins aligned with the field (parallel - low energy state) than spins aligned against the field (anti-parallel- high energy state). Due to this slight excess of parallel spins, the net equilibrium magnetization (macroscopic magnetization) is parallel to  $B_0$  (figure 2.1a). The difference in energy between the two spin states increases as the magnetic field strength increases.

Besides the static  $B_0$  field applied along  $z$ , we apply a time varying field  $B_1$ , perpendicularly to  $B_0$  and oscillating at  $\omega_0$ , which perturbs the populations of the spin-up

and spin-down states and gives phase coherence to the spins. A  $90^\circ$  pulse ( $B_1$  along the x axis) brings the magnetisation vector to the xy plane (figure 2.2b). In this case, the magnetisation precesses about  $B_0$  at  $\omega_0$  and  $B_1$  at  $\omega_1$ . At this point, it is appropriate to introduce a new frame of reference for viewing the evolution of the magnetisation vector, the rotating frame ( $x',y',z$ ) rotating about the z-axis at frequency  $\omega_0$ . In the rotating frame the magnetisation precesses about the  $x'$  axis with frequency  $\omega_1 = \gamma B_1$  (figure 2.3c).

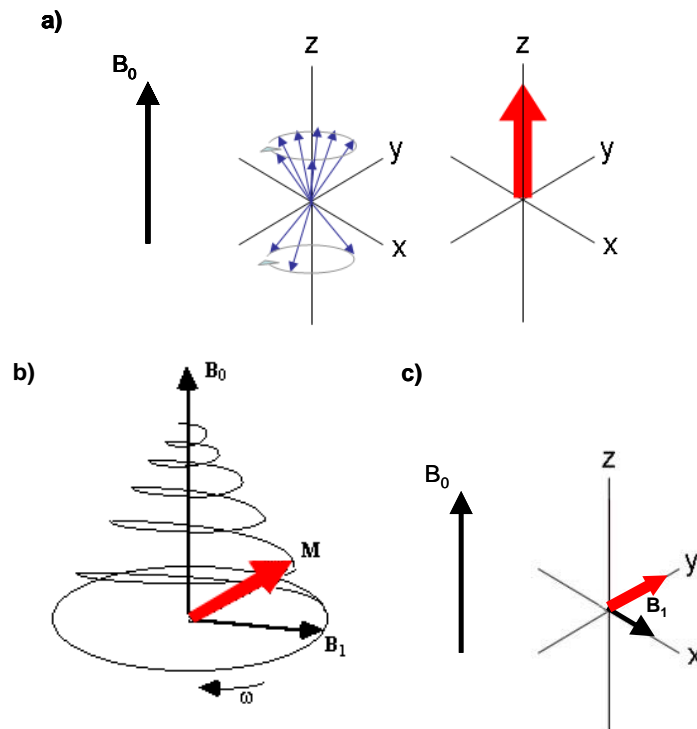


**Figure 2.1.** a) Precession of the spins in a static the external magnetic field and equilibrium magnetisation b) Precession of the net magnetisation in the laboratory frame under the influence of the static  $B_0$  field and the RF field  $B_1$ , c) Net magnetisation viewed in the rotating frame after a on-resonance  $90^\circ$  ( $x$ ) pulse.<sup>3,4</sup>

In MRI the unpaired nuclear spins (mainly from hydrogen atoms in water - 70% to 90% of most tissues - and organic compounds) align themselves when exposed to a magnetic field. A temporary radiofrequency pulse at the Larmor frequency changes the alignment of the spins, and their return to thermal equilibrium (relaxation) is detected in a coil. Protons from different tissues react differently giving a picture of anatomical structures.<sup>5</sup>

In order to create a MRI image of a patient it is necessary to create different voxels (volume picture elements) of its volume. This is accomplished by applying perpendicular magnetic gradients. MRI allows a complete and flexible image orientation; although normally in clinical use the reference employed for the magnetic gradient is the principal axis of the patient (patient's images are obtained in the x and y axis while the z axis is the head to toe direction). These gradients are small perturbations superimposed on the main magnetic field  $B_0$ , with a typical imaging gradient producing a total field variation of less than 1%. Therefore, in the presence of a field gradient, each proton will resonate at a unique frequency that depends on its exact position within the gradient field. The spatial encoding is obtained by applying magnetic field gradients which encode the position within the phase of the signal.

In the case of one dimension, a linear relationship of phase with respect to position can be obtained via collection of data in the presence of a magnetic field gradient. In the case of three dimensions (3D), a plane can be defined by "slice selection" where a RF pulse of defined bandwidth is applied in the presence of a magnetic field gradient (Figure 2.2). This procedure is applied in order to reduce spatial encoding to two dimensions (2D). Figure 2.2 is an illustration of slice selection during the RF excitation phase using a longitudinal magnetic field gradient. The typical medical resolution is about  $1 \text{ mm}^3$ , while research models can exceed  $1 \text{ }\mu\text{m}^3$ .<sup>6</sup>

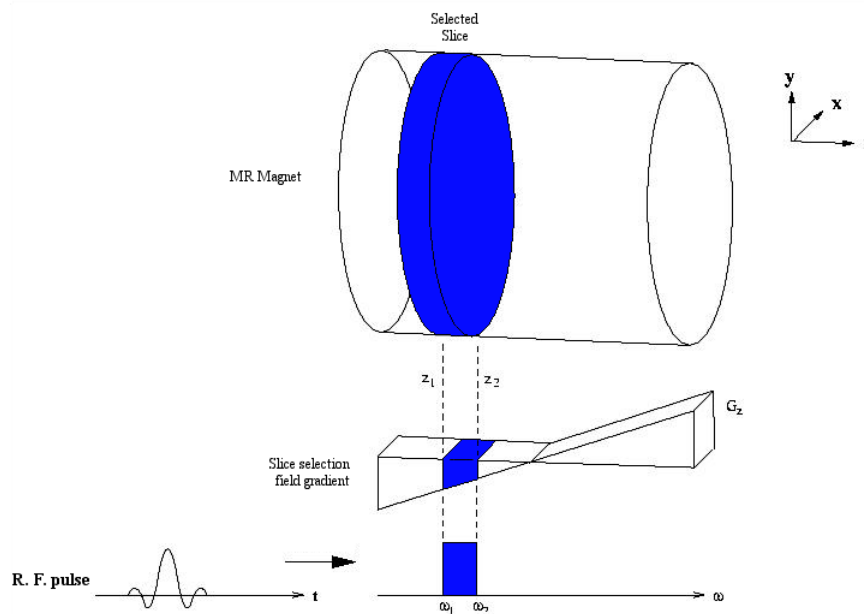


**Figure 2.2.** Illustration of slice selection during the RF excitation phase using a longitudinal magnetic field gradient<sup>5</sup>

Although the most common sequence is a spin-echo sequence, there are numerous pulse sequence types. The spin-echo sequence (Figure 2.3) consists on the application of a  $90^\circ$  pulse to the spin system. This  $90^\circ$  pulse rotates the magnetization to the  $x'y'$  plane, where the transverse magnetization begins to dephase. Following the  $90^\circ$  pulse a  $180^\circ$  rephasing pulse at  $TE/2$  is applied. This pulse rotates the magnetization by  $180^\circ$  about the  $x'$  axis, forcing the magnetization to at least partially rephase and generating a signal called a spin echo. In terms of time this is an echo time (TE).

This pulse sequence is repeated at each time interval TR (Repetition Time). With each repetition a  $k$ -space line acquisition (often refers to the temporary image space, usually a matrix, in which data from digitized MR signals are stored during data acquisition) is filled due to a different phase encoding. Three types of gradients are applied: slice selection (GS), phase encoding (GP) and frequency encoding (GF).

One of the advantages of using a spin-echo sequence is that it introduces  $T_2$  (see 2.2.1 for definition) dependence to the signal intensity, since some tissues and pathologies have similar  $T_1$  values but different  $T_2$  values. It is, thus, of interest to have an imaging sequence that can produce images with  $T_2$  dependence (since the  $180^\circ$  rephasing pulse compensates for the constant field heterogeneities to obtain an echo that is weighted in  $T_2$  and not in  $T_2^*$ ). The pulse sequence timing can be adjusted to give  $T_1$ -weighted proton or spin density and  $T_2$ -weighted images. This sequence also provides a high signal-to-noise ratio.

A spin-echo sequence has two essential parameters: repetition time (TR) and echo time (TE), in which TR is defined as the time between repetitions of the sequence and TE is the time between the  $90^\circ$  pulse and the maximum amplitude in the echo, respectively. This sequence has a clear contrast mechanism for a  $T_1$ -weighted image, where a short TR (450 – 850 ms) and TE (10 – 30 ms) are used. In the case of a  $T_2$ -weighted image a long TR (>2000 ms) and TE (>60 ms) are used. In the case of  $^1\text{H}$  images a long TR with a short TE are used.

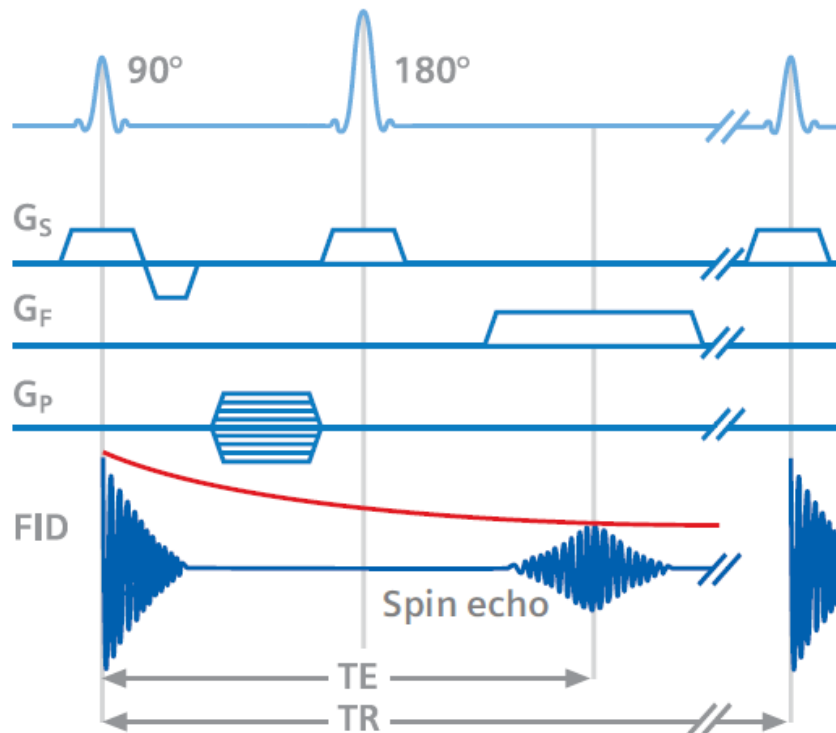


**Figure 2.3.** Spin-echo pulse sequence used in MRI.<sup>7</sup>

The signal intensity (SI) is given by Eq. 2.1, where  $k$  is a proportionality constant dependent on flow, perfusion and diffusion, and  $\rho$  is the density of spins in the sample.

$$SI = k\rho(1 - e^{-TR/T_1}) e^{-TE/T_2} \quad (2.1)$$

Three types of spin echo sequences are commonly used: standard single echo, standard multi-echo, and echo-train spin echo. Standard single-echo sequences are generally used to produce  $T_1$ -weighted images when acquired with relatively short TR and TE (less than 700 ms and 30 ms, respectively). A multi-slice loop structure is used with a single pair of excitation and refocusing pulses applied per slice loop. The pixel intensity is proportional to the number of protons contained within the voxel weighted by the  $T_1$  and  $T_2$  relaxation times for the tissues within the voxel. The echo-train spin echo sequence is

similar to the multi-echo sequences, except that each spin echo is acquired with a different phase encoding as well as its own TE. The echo-train length (or turbo factor) is the number of echoes acquired in each TR period. Here, k-space is filled segmentally with one echo from each echo-train filling each segment of  $k$ -space and, as such, is an efficient sequence. These sequences are typically used to create  $T_2$ -weighted images.

Nevertheless, at times insufficient contrast is observed and the administration of Contrast Agents (CAs) or Contrast Media is necessary. MRI CAs are able to change the  $^1\text{H}$  relaxation properties of the tissues, leading to MR images with improved contrast. In MRI the object or patient is exposed to a powerful magnetic field. The hydrogen protons of the water molecules in the object or body are excited by radio-frequency pulses. During the time they are “recovering” (or relaxing back) they transmit signals that are recorded and compiled into an image. The faster the atomic nuclei return from an excited to an unexcited state, the stronger the signal and thus also the contrast. Most approved MRI contrast agents are based on the rare earth element gadolinium, adding paramagnetic properties to the compound. This element causes the atomic nuclei to relax more quickly and thus to transmit stronger signals.

## 2.2. MRI CONTRAST AGENTS

One of the strengths of MRI is the significant amount of intrinsic contrast between tissues. This contrast is due to differences in the longitudinal ( $T_1$ ) and/or transverse ( $T_2$ ) proton relaxation times of the tissues under observation accentuated by the chosen TR and TE. Pathologic tissue may or may not exhibit significant differences in  $T_1$  or  $T_2$  relatively to the surrounding normal tissue. For this reason, there may be little signal difference between normal and pathologic tissue in spite of the inherent high contrast in the images. An example of difference between a  $T_1$  and  $T_2$ -weighted image is given in Figure 2.4a and b.

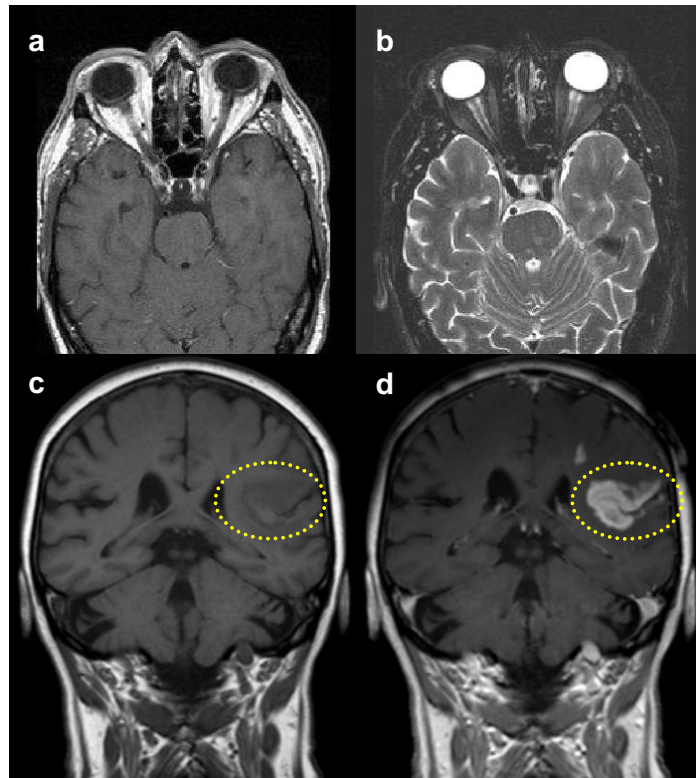


**Figure 2.4.** Brain MRI images with **a)**  $T_{1w}$ , **b)**  $T_{2w}$ , **c)**  $T_{1w}$  without the administration of a commercial CA and **d)**  $T_{1w}$  with the administration of a commercial CA<sup>8</sup>

A MRI Contrast Agent (CA) is a chemical substance introduced to the anatomical or functional region being imaged in order to increase the differences between different tissues, or between normal and abnormal tissue, by altering the relaxation times. Therefore, the aim of using CAs in MRI is to accelerate the relaxation of water proton spins with their surrounding. This can be achieved by using paramagnetic substances. Examples of these achievements are the experiments of Bloch et al.<sup>9</sup> and Lauterbur et al.<sup>10</sup>

The MRI contrast mechanism can be affected by many intrinsic and extrinsic factors such as proton density and MRI pulse sequences. Based on their relaxation processes the contrast agents can be classified as  $T_1$  or  $T_2$  contrast agents. The commercially approved  $T_1$  contrast agents are usually paramagnetic complexes, while the  $T_2$  contrast agents are based on iron oxide nanoparticles, which are the most representative nanoparticulate agents.

The most common paramagnetic complexes are the paramagnetic chelates containing a lanthanide ion. Currently, gadolinium (III) complexes are by far the most widely used CAs in clinical practice because it has seven unpaired electrons making it the most paramagnetic (highest spin density) stable metal ion. Gadolinium (III) also has another significant feature due to the symmetrical  $^8S$  ground state: its electron spin relaxation is relatively slow, which is relevant to its efficiency as an MRI CA. There are a number of excellent reviews<sup>11-18</sup> covering the development and properties of first and second-generation contrast agents, particularly focusing on gadolinium complexes.

### 2.2.1. RELAXATION

Relaxation is a fundamental process in MR and presents the main mechanism for the image contrast. The RF pulse turns the macroscopic magnetization away from the z-axis. Once the  $B_1$ -field has been turned off the magnetization rotate around the main magnetic field ( $B_0$ ) at the Larmor frequency. Due to relaxation processes, the magnetization will eventually return to its equilibrium position along the z-axis and the NMR signal will as a result fade away. There are two different relaxation pathways possible: the spin-lattice relaxation and the spin-spin relaxation.

#### 2.2.1.1. SPIN-LATTICE RELAXATION

The spin-lattice relaxation, or longitudinal relaxation, or  $T_1$  relaxation, is responsible for the return of the z-magnetization component,  $M_z$ , to its equilibrium value. It provides the mechanism by which the protons give up their energy and return to the thermal equilibrium. Therefore, if a  $90^\circ$  pulse at the resonant frequency,  $\omega_0$ , is applied to a sample its magnetization,  $M_0$ , will rotate to the x'y' plane as shown in Figure 2.4-a, and  $M_z$  will be zero. With time,  $M_z$  will increase, as the protons release their energy (Figure 2.4-b). This return of magnetization to equilibrium follows an exponential growth process, with a time constant  $T_1$  describing the rate of growth (equation 2.2):

$$M(\tau) = M_0(1 - e^{(-\tau/T_1)}) \quad (2.2)$$

where  $\tau$  is the time following the RF pulse. After three  $T_1$  time periods,  $M$  will have returned to 95% of its value prior to the excitation pulse,  $M_0$ . The term *spin-lattice* refers to the fact that the excited proton (“spin”) transfers its energy to its surroundings (“lattice”) rather than to another spin, where the energy will no longer contribute to spin excitation. This energy transfer to the surroundings has some very important consequences. The key to this energy transfer is the presence of some type of molecular motion (e.g., vibration, rotation) in the vicinity of the excited proton with an intrinsic frequency,  $\omega_L$ , that matches the resonant frequency,  $\omega_0$ . The closer  $\omega_0$  is to  $\omega_L$ , the more willingly the motion absorbs the energy and the more frequently this energy transfer occurs, allowing the protons to return to equilibrium.

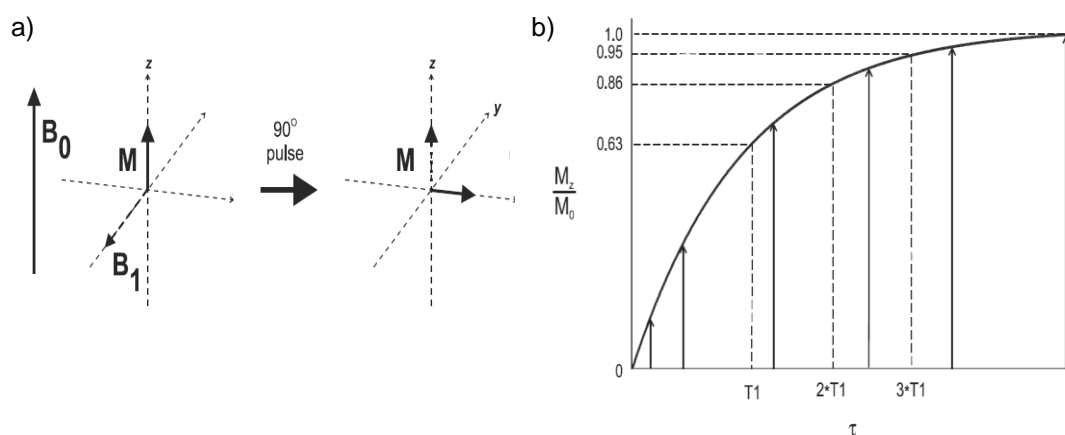


**Figure 2.4. a)** Effect of a  $90^\circ$  RF pulse on the net magnetization, viewed in the rotating frame. **b)** Plot of the relative  $M_z$  component as a function of time after the RF pulse, known as the  $T_1$  relaxation curve.

In general any mechanism which gives rise to fluctuating magnetic fields is a possible relaxation mechanism. Therefore all mechanisms contribute to the observable relaxation time according to equation 2.3.

$$\frac{1}{T_1} = \sum_m \frac{1}{T_{1m}} \quad (2.3)$$

where  $T_{1m}$  is the time constant of mechanism  $m$ . The magnitude of the contribution to the overall relaxation rate from a single mechanism may differ greatly among different chemical groups, the chemical environment and has a dependence regarding parameters such as temperature and field strength.

### 2.2.1.2. SPIN-SPIN RELAXATION

Spin–spin relaxation time or transverse relaxation time or the relaxation time  $T_2$  is the time required for the transverse component of  $M$  to decay to 37% of its initial value via irreversible processes. The net magnetization  $M_0$  is initially along the z-axis ( $B_0$ ). If a  $90^\circ$  pulse is applied to a sample,  $M_0$  will rotate as shown in Figure 2.5a-1. This causes  $M_0$  to rotate entirely into the x'y' plane, so that the individual spin magnetic moments have phase coherence in the transverse plane at the end of the pulse. With time this phase coherence disappears and the value of  $M$  in the x'y' plane decreases toward 0.  $T_2$  or  $T_2^*$  relaxation is the process by which this transverse magnetization is lost. At the end of the  $90^\circ$  RF pulse, when the proton spins have absorbed energy and are oriented in the transverse plane, all spins precess at the same frequency  $\omega_0$  and are synchronized at the same point or phase of its precessional cycle. Given that a nearby proton of the same type will have the same molecular environment, and the same  $\omega_0$ , it can easily absorb the energy that is being released by its neighbour. Therefore the spin–spin relaxation refers to this energy transfer from an excited proton to another nearby proton and the absorbed energy remains as spin excitation rather than being transferred to the surroundings as in  $T_1$  relaxation. Figure 2.5a illustrates a rotating frame slower than  $\omega_0$  and the various steps of the net magnetization after a  $90^\circ$  RF pulse, where:

- 1- Net magnetization  $M$  is oriented parallel to  $B_0$ ,
- 2- following a  $90^\circ$  RF pulse the protons initially precess in phase in the transverse plane,
- 3- due to inter- and intramolecular interactions the protons begin to precess at different frequencies and become asynchronous with each other
- 4 and 5- as more time elapses the transverse coherence becomes smaller until,
- 6- there is complete randomness of the transverse components and no coherence.

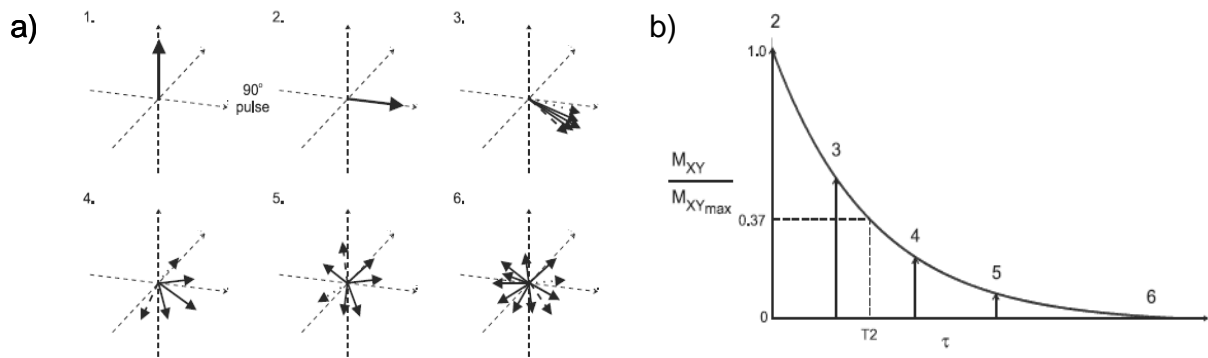


**Figure 2.5.** a) Illustration of the net magnetization  $\mathbf{M}$  with regards to the  $x'y'$  plane within a rotating frame slower than  $\omega_0$ . b) Plot of the relative  $M_{XY}$  component as a function of time, known as the  $T_2$  relaxation curve.

If the protons continue in close proximity and remain at the same  $\omega_0$  the proton–proton energy transfer will occur many times. The local magnetic field of the protons can fluctuate due to intermolecular and intramolecular interactions such as vibrations or rotations. This fluctuation produces a gradual, irreversible loss of phase coherence of the spins as they exchange energy and reduce the magnitude of the transverse magnetization as well as reduce the generated signal (Figure 2.5b). With the increase in time this transverse coherence completely disappears, only to reform in the longitudinal direction as  $T_1$  relaxation occurs.

There are two main causes for a loss of transverse coherence to  $M$ . The first cause is the movement of the adjacent spins due to molecular vibrations or rotations (responsible for spin–spin relaxation or the true  $T_2$ ). The second cause is due to the inhomogeneity of the magnetic field. As the proton spin precesses it experiences a fluctuating local magnetic field, causing a change in  $\omega_0$  and a loss in transverse phase coherence.

The proper design of the pulse sequence can eliminate the imaging gradients as a source of dephasing. While, the other sources contribute to the total transverse relaxation time,  $T_2^*$  equation 2.4:

$$\frac{1}{T_2^*} = \frac{1}{T_2} + \frac{1}{T_{2M}} + \frac{1}{T_{2MS}} \quad (2.4)$$

where  $T_{2M}$  is the dephasing time due to the main field inhomogeneity and  $T_{2MS}$  is the dephasing time due to the magnetic susceptibility differences.

The decay of the transverse magnetization following a  $90^\circ$  rf pulse follows an exponential process with the time constant of  $T_2^*$  rather than just  $T_2$  equation 2.5:

$$M_{XY}(t) = M_{XY_{\max}} e^{(-t/T_2^*)} \quad (2.5)$$

where  $M_{XY_{\max}}$  is the transverse magnetization  $M_{XY}$  immediately following the excitation pulse. For most tissues or liquids,  $T_{2M}$  is the major factor in determining  $T_2^*$ , whereas for tissue with significant iron deposits or air filled cavities,  $T_{2MS}$  dominates  $T_2^*$  ( $T_2$  determined using the spin-echo experiment).

### 2.2.2. RELAXIVITY

Relaxivity is the ability of magnetic compounds in enhancing the relaxation rate of the surrounding water proton spins. Therefore, the longitudinal and transverse relaxivity values,  $r_1$  and  $r_2$ , refer to the amount of increase in  $1/T_1$  and  $1/T_2$ , respectively, per millimolar concentration of agent (often given as per mM of Gd).  $T_1$  agents usually have  $r_2/r_1$  ratios of 1-2, whereas  $T_2$  agents normally have  $r_2/r_1$  ratios  $\sim 10$  or higher. <sup>19-23</sup>

Solomon, Bloembergen and Morgan developed the general theory of solvent nuclear relaxation in the presence of paramagnetic substances.<sup>19-23</sup> The Gd (III) complexes induce an increase of both the longitudinal and transverse relaxation rates,  $1/T_1$  and  $1/T_2$ , respectively, of the solvent nuclei (normally water). Diamagnetic and paramagnetic relaxation rates are additive and given by equation 2.6:

$$\frac{1}{T_{i,obs}} = \frac{1}{T_{i,d}} + \frac{1}{T_{i,p}}, \quad (i=1,2) \quad (2.6)$$

$$\frac{1}{T_{i,obs}} = \frac{1}{T_{i,d}} + r_i[Gd], \quad (i=1,2) \quad (2.7)$$

where  $\frac{1}{T_{i,obs}}$  is the observed solvent relaxation rate,  $\frac{1}{T_{i,d}}$  the diamagnetic relaxation rate, and  $1/T_{i,p}$  the paramagnetic relaxation rate that depends on the concentration of paramagnetic species expressed in millimolar for diluted samples. Relaxivity,  $r_i$ , is defined as the slope of the concentration dependence, equation 2.7., and is normally expressed in  $\text{mM}^{-1} \text{ s}^{-1}$ ; molal (mol/kg) concentrations should be used when dealing with nondilute systems.

Within the Solomon, Bloembergen and Morgan's (SBM) theory the paramagnetic relaxation process is described on the basis of a model that considers 'inner sphere' and 'outer-sphere' contributions (equation 2.8).

$$\frac{1}{T_{i,p}} = \frac{1}{T_{i,p}^{is}} + \frac{1}{T_{i,p}^{os}}, \quad (i=1,2) \quad (2.8)$$

$$\frac{1}{T_{i,obs}} = \frac{1}{T_{i,p}^{is}} + \frac{1}{T_{i,p}^{os}} + \frac{1}{T_{i,d}} = r_i[Gd^{3+}] + \frac{1}{T_{i,d}} \quad (i=1,2) \quad (2.9)$$

where  $T_{i,p}$ ,  $T_{i,p}^{is}$  and  $T_{i,p}^{os}$  are, respectively, the total paramagnetic, the inner- and outer-sphere paramagnetic contributions to the longitudinal ( $i=1$ ) or transverse ( $i=2$ ) NMR relaxation times. The inner-sphere contribution is related to the exchange between the bound water molecules and bulk water, and the outer sphere-contribution is caused by water molecules diffusing near the paramagnetic centre during their translational diffusion.<sup>13,24</sup> Often, a third contribution is also taken into account, the 'second-sphere', that is caused by the presence of mobile protons or water molecules in the second coordination sphere of the paramagnetic species (Figure 2.6).<sup>25</sup> The relaxivity ( $r_i$ ) is defined in equation 2.9 (combination of eqs. 2.14, 2.15 and 2.16), if the second sphere contribution is not considered.

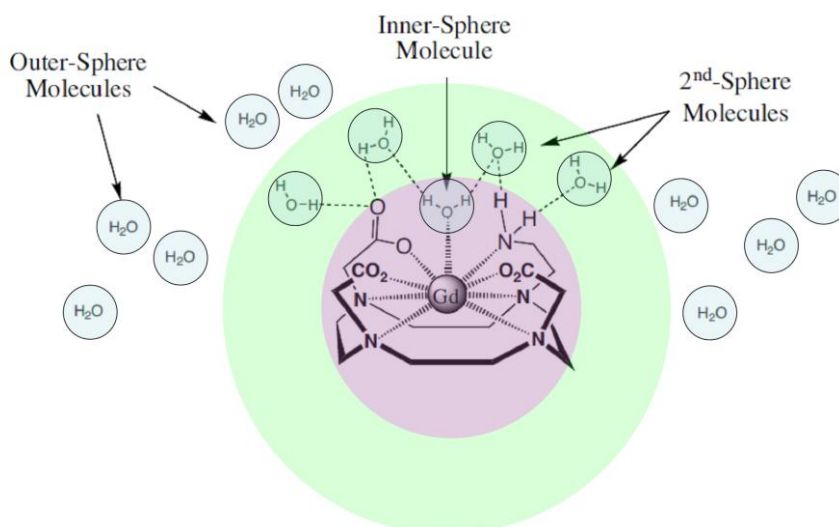


**Figure 2.6.** Schematic representation of the three types of water molecules surrounding the metal complex.

### 2.2.2.1. INNER SPHERE RELAXIVITY

The inner-sphere contribution to the overall relaxation rates is described in equations 2.10 and 2.11. The parameters involved in this inner-sphere mechanism are *i*)  $q$ , the number of water molecules in the inner-coordination sphere directly coordinated to the paramagnetic centre, *ii*)  $C$ , the molar concentration of the paramagnetic complex, *iii*)  $\tau_M$ , the mean residence lifetime of the coordinated water protons within the inner-sphere coordination sphere, *iv*)  $T_{1M}$  and  $T_{2M}$ , the longitudinal and transverse proton times enhancement experienced by the proton of the inner-sphere water molecules, respectively, and *v*)  $\Delta\omega_M$ , the chemical shift difference between the free and the bound water molecules.

$$\frac{1}{T_1^{is}} = R_1^{is} = \frac{q[C]}{55.5(T_{1M} + \tau_M)} \quad (2.10)$$

$$\frac{1}{T_{2,p}^{is}} = R_2^{is} = \frac{q[C]}{55.5\tau_M} \left[ \frac{T_{2M}^{-1}(\tau_M^{-1} + T_{2M}^{-1}) + \Delta\omega_M^2}{(\tau_M^{-1} + T_{2M}^{-1})^2 + \Delta\omega_M^2} \right] \quad (2.11)$$

In the case where the system is in the ‘fast exchange’ regime ( $T_{1M} \gg \tau_M$ ) the inner-sphere contribution becomes important and is transferred to the bulk water. When the coordinated water molecule is in the ‘slow exchange’ regime ( $T_{1M} \ll \tau_M$ ), the water exchange rate becomes the limiting factor of the relaxivity.

The Solomon-Bloembergen-Morgan theory<sup>18,20</sup> provides a foundation to understand the basis of  $T_{iM}$  (Equations 2.12-18). The two components of the  $T_{iM}$  term (Equation 2.12) are dipole-dipole (arising from random fluctuations of the through-space interaction of the nuclear dipole with the unpaired electron dipole) and scalar interactions (resulting from a through-bond delocalization of the unpaired spin density on the nucleus) that are noted by the “DD” and “SC” superscripts respectively.

$$\frac{1}{T_{iM}} = \frac{1}{T_i^{DD}} + \frac{1}{T_i^{SC}} \quad (i = 1,2) \quad (2.12)$$

$$\frac{1}{T_1^{DD}} = R_1^{DD} = \frac{2}{15} \cdot \frac{\gamma_I^2 g^2 \mu_B^2 S(S+1)}{r_{GdH}^6} \left( \frac{\mu_o}{4\pi} \right)^2 \left[ \frac{3\tau_{c1}}{1 + \omega_I^2 \tau_{c1}^2} + \frac{7\tau_{c2}}{1 + \omega_S^2 \tau_{c2}^2} \right] \quad (2.13)$$

$$\frac{1}{T_1^{SC}} = R_1^{SC} = \frac{2}{3} S(S+1) \cdot \left( \frac{A}{\hbar} \right)^2 \left[ \frac{\tau_{e2}}{1 + \omega_S^2 \tau_{e2}^2} \right] \quad (2.14)$$

$$\frac{1}{T_2^{DD}} = R_2^{dip} = \frac{1}{15} \cdot \frac{\gamma_I^2 g^2 \mu_B^2 S(S+1)}{r_{GdH}^6} \left( \frac{\mu_o}{4\pi} \right)^2 \left[ \frac{3\tau_{1C}}{1 + \omega_I^2 \tau_{c1}^2} + \frac{13\tau_{2C}}{1 + \omega_S^2 \tau_{c2}^2} + 4\tau_{c1} \right] \quad (2.15)$$

$$\frac{1}{T_2^{SC}} = R_2^{SC} = \frac{1}{3} S(S+1) \cdot \left( \frac{A}{\hbar} \right)^2 \left[ \frac{\tau_{e2}}{1 + \omega_S^2 \tau_{e2}^2} + \tau_{e1} \right] \quad (2.16)$$

$$\frac{1}{\tau_{ci}} = \frac{1}{\tau_M} + \frac{1}{\tau_R} + \frac{1}{T_{ie}} \quad (i=1,2) \quad (2.17)$$

$$\frac{1}{\tau_{ei}} = \frac{1}{\tau_M} + \frac{1}{T_{ie}} \quad (i=1,2) \quad (2.18)$$

where  $\gamma_I$  is the proton gyromagnetic ratio,  $g$  is the electronic g-factor,  $\mu_B$  is the Bohr magneton,  $S$  is the number of unpaired electrons in the paramagnetic metal ion,  $r_{GdH}$  is the distance between the water protons and the unpaired electrons of the paramagnetic metal ion,  $\mu_0$  is the magnetic permeability of a vacuum,  $\left(\frac{A}{\hbar}\right)$  is the hyperfine coupling constant between the metal electrons and the water protons,  $\omega_I$  and  $\omega_S$  are the nuclear and electron Larmor frequencies, respectively ( $\omega_{I,S} = \gamma_{I,S}B$ , where  $B$  is the magnetic field). For field strengths used in MRI the electronic contributions (the “7” term inside the square brackets in equation 2.13) may be conveniently ignored since,  $\omega_s^2 \tau_{c2}^2 \gg 1$ , reducing the electronic contributions to an insignificant amount. The nuclear contribution (the “3” term also inside the square brackets in equation 2.13) is determined by  $\omega_I^2$ , the proton Larmor frequency, and  $\tau_{c1}$ , the local correlation time. The relaxation enhancement efficiency of the CA depends on how closely matched the proton frequency (i.e., the Larmor frequency,  $\omega_I$ ) is to the correlation frequency of the contrast agent  $\left(\frac{1}{T_{1,c}}\right)$ . The nuclear contributions to relaxation are maximized when  $\left(\frac{1}{T_{1,c}}\right)$  approaches the Larmor frequency of the protons.

The local correlation time ( $\tau_{ci}$ ), defined by equations 2.17 and 2.18, has three components,  $T_{1,e}$  (the electronic relaxation time of the unpaired electrons,  $\tau_M$ ) the water residency lifetime, and  $T_R$  – the rotational correlation lifetime. The high-field strengths used in MRI again simplify matters,  $T_{1,e}$  is long enough to reasonably ignore the

contributions from the  $\left(\frac{1}{T_{1,c}}\right)$  term.  $\tau_M$  is the same term from equation 2.10.  $\tau_R$  is the rotational correlation time and is related to the physical tumbling time of the CA in solution.

Considering equations 2.13 and 2.15,  $R_1^{dip}$  and  $R_2^{dip}$  are roughly equal at the fast motion limit (in the case of small  $\tau_c$ ), while far from this limit (in the case of long  $\tau_c$ ) the dipole-dipole mechanism behaviour differs. In this case  $R_1^{dip}$  decreases with  $\tau_c$  and  $R_2^{dip}$  is constantly increasing due to the presence of the frequency independent term  $4\tau_c$ . Regarding the contact contribution, SC, due to its nature the correlation time modulating this contribution is not affected by  $\tau_R$  (equations 2.14 and 2.16) and since  $\omega_S^2\tau_e^2$  is extremely large, for  $Gd^{3+}$  complexes,  $R_1^{SC}$  is usually negligible. In the case of  $R_2$ , however, the contact contribution ( $R_2^{SC}$ ) is often the dominant mechanism, mainly from nuclei near the metal ion<sup>26</sup>.

At high magnetic fields, especially if  $\tau_R$  is much larger than  $T_{i,e}$ , the Curie or susceptibility mechanism is another dipolar effect that must be considered (equations 2.19 and 2.20).<sup>27</sup>

$$\frac{1}{T_{1,\chi}} = \frac{6}{5} \left( \frac{\mu_o}{4\pi} \right)^2 \cdot \frac{\gamma_I^2 B_o^2 \mu_{eff}^4 \beta^4}{(3kT)^2 r^6} \cdot \left( \frac{\tau_R}{1 + \omega_I^2 \tau_R^2} \right) \quad (2.19)$$

$$\frac{1}{T_{2,\chi}} = \frac{1}{5} \left( \frac{\mu_o}{4\pi} \right)^2 \cdot \frac{\gamma_I^2 B_o^2 \mu_{eff}^4 \beta^4}{(3kT)^2 r^6} \cdot \left( 4\tau_R + \frac{3\tau_R}{1 + \omega_I^2 \tau_R^2} \right) \quad (2.20)$$

where  $B_0$  is the magnetic field strength,  $T$  is the absolute temperature,  $\mu_{eff}$  is the effective magnetic moment of the metal ion,  $k$  is the Boltzmann constant,  $r$  is the distance between the nuclear spin and the metal ion.

The Curie mechanism describes the dipolar interaction between the nuclear spins and the magnetic moment generated by the thermally averaged excess of electron

population in the electronic spins levels. The contribution of the Curie mechanism to the total longitudinal relaxation is only relevant for slowly rotating macromolecules (long  $\tau_R$ ).

The electronic relaxation rates ( $1/T_{1e}$ ) described by Bloembergen and Morgan<sup>20</sup> and McLachlan<sup>28</sup> depend on the magnetic field. For  $Gd^{3+}$  complexes, these are normally interpreted in terms of a modulation of the zero field splitting (ZFS)<sup>29</sup>(only once) These relaxation rates are described by Equations. 2.21 and 2.22, referred to as the Bloembergen-Morgan theory of paramagnetic electron spin relaxation:

$$\left(\frac{1}{T_{1e}}\right)^{ZFS} = \frac{\Delta^2}{25} \tau_V [4S(S+1) - 3] \left( \frac{1}{1 + \omega_S^2 \tau_V^2} + \frac{4}{1 + 4\omega_S^2 \tau_V^2} \right) \quad (2.21)$$

$$\left(\frac{1}{T_{2e}}\right)^{ZFS} = \frac{\Delta^2}{50} \tau_V [4S(S+1) - 3] \left( \frac{5}{1 + \omega_S^2 \tau_V^2} + \frac{2}{1 + \omega_S^2 \tau_V^2} + 3 \right) \quad (2.22)$$

where  $\Delta^2$  is the mean squared ZFS energy and  $\tau_V$  is the correlation time for the modulation of the ZFS interaction. This modulation results from the transient distortions of the complex “metal coordination cage”. A transient ZFS of the spin levels can be induced by vibration, intramolecular rearrangement and collisions between solvent molecules and the metal complexes, allowing the coupling of rotation with spin transitions. The validation of equations 2.21 and 2.22 is restricted to certain conditions where  $\omega_0 \tau_V \ll 1$  is fulfilled.

At low magnetic field ( $B_0 < 0.1$  T) the relaxivity of the  $Gd^{3+}$  complexes depends mainly on the electronic relaxation (Equation. 2.23). At high magnetic field ( $B_0 > 1.5$  T) the electronic relaxation rate decreases and becomes slower than the rotational rate of the complex (Equation. 2.24).

$$\left(\frac{1}{T_{1e}}\right), \left(\frac{1}{T_{2e}}\right) \gg \left(\frac{1}{\tau_R}\right); T_{1e} \approx \tau_{c1}; T_{2e} \approx \tau_{c2} \quad (2.23)$$

$$\left(\frac{1}{T_{1e}}\right), \left(\frac{1}{T_{2e}}\right) \ll \left(\frac{1}{\tau_R}\right); \tau_R \approx \tau_{c1} \approx \tau_{c2} \quad (2.24)$$

A reported temperature and magnetic field dependence EPR study<sup>30</sup> demonstrated that  $\left(\frac{1}{T_{1e}}\right)$  of various aqueous solutions of a series of  $Gd^{3+}$  complexes is described to a good approximation by the previously developed equations. The major contribution to the observed EPR line widths is due to electronic relaxation.

A more recent description of electron spin relaxation requires EPR measurements over a very wide range of temperatures and magnetic fields.<sup>31</sup> This theoretical model shows that the electronic relaxation mechanisms at the origin of the EPR line shape arise from the combined effects of the modulation of the static crystal field by the random Brownian rotation of the complex and of the transient zero-field splitting.

#### 2.2.2.2. SECOND AND OUTER SPHERE RELAXIVITY

Water molecules not directly coordinated to the metal ion also experience relaxation enhancement in the presence of the CA. These water molecules may be organized into a second- and outer-coordination sphere as shown in Figure 2.6. The Solomon-Bloembergen-Morgan theory may also be applied to second-sphere water molecules, thus  $T_1^{SS}$  may be modelled from equations 2.10, 2.14 and 2.15.

The outer-sphere relaxation enhancement may be modelled using theories developed by Hwang and Freed<sup>32,33,34</sup> that take into account the electronic relaxation and diffusion. Essentially,  $T_1^{OS}$  is determined by  $T_{je}$ , the electronic relaxation time,  $J(\omega_i; T_{je})$  is a non-Lorentzian spectral density function,  $N_A$  is the Avogadro's number,  $\gamma_S$  is electron gyromagnetic ratio,  $a_{GdH}$  is the distance of closest approach of the solvent protons to the paramagnetic centre,  $D_{GdH}$  is the sum of the diffusion coefficients of the water proton and of the  $Gd^{3+}$  complex and  $\tau_{GdH}$  is the diffusion correlation time. The symbols not mentioned here maintain the meaning given before.

$$\frac{1}{T_1^{OS}} = R_1^{OS} = \left(\frac{32\pi}{405}\right) \left(\frac{\mu_o}{4\pi}\right)^2 \cdot \gamma_I^2 \gamma_S^2 \hbar^2 S(S+1) \cdot \frac{N_A}{a_{GdH} \cdot D_{GdH}} \cdot [3J(\omega_I; T_{1e}) + 7J(\omega_S; T_{2e})] \quad (2.23)$$

$$J(\omega_i; T_{je}) = \text{Re} \left[ \frac{1 + \frac{1}{4} \left( i\omega_i \tau_{GdH} + \frac{\tau_{GdH}}{T_{je}} \right)^2}{1 + \left( i\omega_i \tau_{GdH} + \frac{\tau_{GdH}}{T_{je}} \right)^2 + \frac{4}{9} \left( i\omega_i \tau_{GdH} + \frac{\tau_{GdH}}{T_{je}} \right) + \frac{1}{9} \left( i\omega_i \tau_{GdH} + \frac{\tau_{GdH}}{T_{je}} \right)^3} \right]$$

$j = 1, 2 ; i = I, S$  (2.24)

$$\tau_{GdH} = \frac{a_{GdH}^2}{D_{GdH}} \quad (2.25)$$

In the case of small-sized  $Gd^{3+}$  complexes the outer sphere contribution is responsible for about 50% of the total relaxivity. For macromolecular systems, the outer sphere contribution may be considered less important. Complexes of similar shape and size have similar diffusion coefficients and outer sphere contribution to the relaxivity.

The second sphere water molecules should be considered as bound via hydrogen bonds to the functional group in the ligand molecule. The second-sphere contribution is difficult to evaluate due to the number of second-sphere water molecules and their exchange rates, which are unknown. Usually, the second sphere effect is included in the outer-sphere contribution. The explanation of unexpected high relaxivity of some  $Gd^{3+}$  complexes, such as  $[Gd(DOTP)]^7$  where no water molecules can be found in the inner-sphere, is given by a very strong second-sphere contribution.<sup>35</sup>

It is problematic to separate the inner-, second- and outer-sphere components of  $T_1^{CA}$ . An approach often used to approximate  $T_1^{IS}$  of a CA is to simply remove  $T_1^{CA}$  of a second sphere component, related CA that has  $q = 0$ . In the case of the second CA,  $T_1^{IS}$  is zero (since  $q = 0$ ) and the observed relaxation enhancement is attributed solely to  $T_1^{SS}$  and  $T_1^{OS}$ , therefore providing a reasonable estimate of  $T_1^{SS}$  and  $T_1^{OS}$  for the first CA because these parameters are not expected to differ significantly among structurally related CAs. Nevertheless, there are noteworthy exceptions to this assumption and this approach must be carefully applied. Presently there is no satisfactory experimental method to partition the second- and outer sphere components of  $T_1^{CA}$ .

### 2.2.2.3. PARAMAGNETIC RELAXATION PARAMETERS

In order to better understand the potential of the different parameters to affect  $T_1^{CA}$ , equations 2.6-2.25 are condensed and presented into equation 2.26. Two reasonable assumptions are made in simplifying the equations,  $\frac{1}{T_1^{SC}}$  is omitted because  $\frac{A}{\hbar} \approx 0$  for water proton metal interactions in CA's and  $\frac{7\tau_{c2}}{(1 + \omega_s^2 \tau_{c2}^2)}$  because  $B_0$  is sufficiently strong.

$$\frac{1}{T_1^{CA}} = k_{IS} \frac{\overbrace{q[C]}^{\text{InnerSphereContribution}}}{\underbrace{S(S+1) \left( \frac{\tau_{c1}}{1 + \omega_I^2 \tau_{c1}^2} \right)}_{\text{OuterSphereContribution}} + \tau_M} + k_{SS} \frac{\overbrace{q'[C]}^{\text{SecondSphereContribution}}}{\underbrace{r'^6 S(S+1) \left( \frac{\tau'_{c1}}{1 + \omega_I^2 \tau'^2_{c1}} \right)}_{\text{OuterSphereContribution}} + \tau'_M} \quad (2.26)$$

$$+ k_{OS} \frac{1}{S(S+1)[C](3j(\omega_H) + 7j(\omega_S))}$$

The development of more effective contrast agents involves the optimization of various parameters governing the relaxivity. The relation between the molecular structure and electronic relaxation is still not well established. This task is focused on the optimization of three parameters, which are the number of water molecules coordinated to the metal ion ( $q$ ), the exchange lifetime ( $\tau_M$ ) and the reorientation correlation time ( $\tau_R$ ). An example of the variation of  $T_1^{CA}$  with respect to these three parameters is given in Figure 2.7. Figure 2.7, which represents the inner-sphere proton relaxivity ( $r_1$ ) calculated at two magnetic fields as a function of  $\tau_M$  and  $\tau_R$  for two electronic relaxation time values,  $q = 1$  and  $r = 3.1 \text{ \AA}$ . Several important conclusions may be drawn from these simulated curves: *i*) the optimal relaxivities are obtained by slowing down the rotation of the complex and optimizing the exchange lifetime (for the later, an extreme exchange lifetime has a negative influence on the relaxivity); *ii*) the optimal relaxivity decreases with increasing magnetic field strength; *iii*) when one parameter begins to be optimized the other

parameters become more critical and, therefore a compromise has to be reached; and *iv*)  $T_{1e}$  increases as the magnetic field strength increases and at 0.5 T,  $T_{1e}$  may be a limiting factor, while at 1.5 T it may reach a point where it does not influence  $r_1$ .

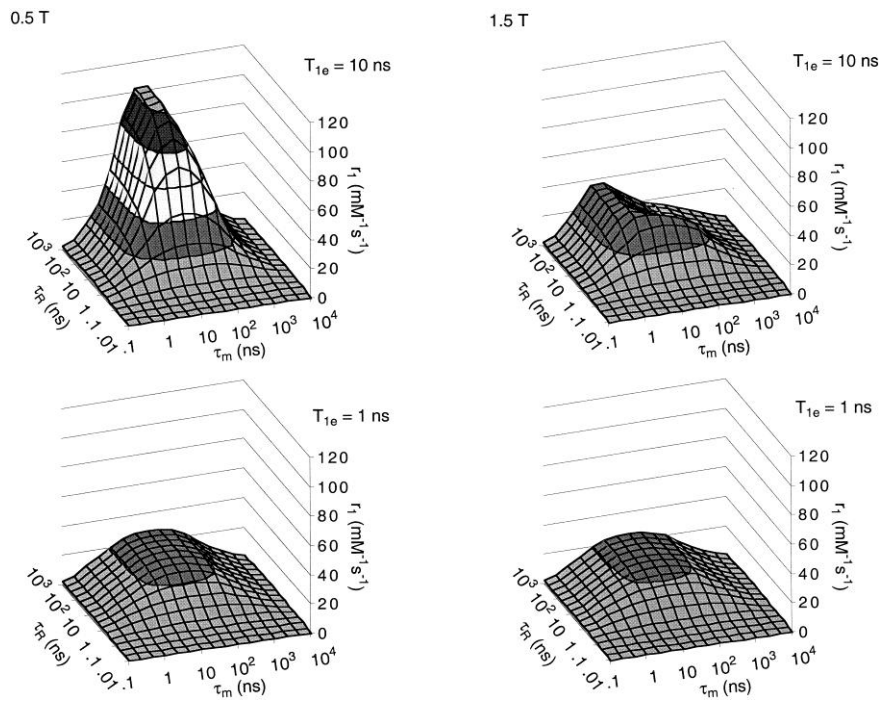


**Figure 2.7.** Inner-sphere relaxivities calculated as a function of  $\tau_M$  and  $\tau_R$  for values of  $T_{1e}$  at 0.5T (~21MHz) and 1.5T (~64MHz).<sup>11</sup>

The relaxation induced by superparamagnetic particles<sup>36</sup>, briefly outlined in the next section, is explained by the classical outer-sphere relaxation theory, reformulated by the Curie relaxation theory,<sup>24</sup> since the former considers the relaxation rates of water protons diffusing near the unpaired electrons responsible for the particle's magnetization.<sup>37</sup> These agents exhibit strong  $T_1$  relaxation properties and due to susceptibility differences to their surroundings, also produce a strongly varying local magnetic field, which enhances  $T_2$  relaxation. An important result from the outer-sphere theory is that the  $r_2/r_1$  ratio increases with increasing particle size and, thus, smaller particles are much better  $T_1$ -shortening agents than larger ones.<sup>32,38,39</sup>

### 2.2.3. NUCLEAR MAGNETIC RESONANCE DISPERSION

The nuclear magnetic relaxation properties of a compound are ideally acquired by a magnetic field dependence study. This is performed by measuring the proton longitudinal and transverse relaxation over a range of magnetic fields with a Fast-Field-Cycling (FFC) spectrometer that switches the magnetic field strength over a range of proton Larmor frequencies. The data acquired represents the Nuclear Magnetic Resonance Dispersion (NMRD) profile, which can be fitted by eqs 2.10-2.18, eqs 2.21-2.22 and eqs 2.23-2.24, in order to obtain the values of the relaxation parameters. The underlying complexity is a major drawback to this technique, since there are too many influencing parameters inducing possible errors in the fitting of the NMRD profile. For this reason,<sup>40</sup> an accurate interpretation of NMRD profiles may only be made by reference to independent information from other techniques, such as <sup>17</sup>O NMR, <sup>2</sup>H or <sup>13</sup>C NMR and Electron Paramagnetic Resonance (EPR). The <sup>17</sup>O NMR relaxation rates and chemical shifts, over a range of magnetic fields and as function of temperature and pressure, allow estimates of the number of inner-sphere water molecules ( $q$ ), the rotational correlation time ( $\tau_R$ ), the water exchange rate ( $\tau_M$ ), and the longitudinal electronic relaxation rate. With <sup>2</sup>H or <sup>13</sup>C NMR it is also possible to determine the rotational correlation time ( $\tau_R$ ), while the EPR line widths give direct access to transverse electronic relaxation rates.<sup>30</sup>

With these techniques a more reliable determination of the set of parameters governing proton relaxivity provide a more stringent test of the relaxation theories applied to the techniques and allow a validation of current models for the dynamics in paramagnetic solutions.

Within a NMRD profile, despite possible inaccuracies, it is viable to draw some valuable conclusions concerning the relaxation processes: *i*) at the high magnetic field region (10-100 MHz) the inner-sphere relaxation is governed by the reorientational correlation ( $\tau_R$ ) time, which is dependent on the molecular weight of the complexes; *ii*) at the low magnetic field, this region is mainly determined by the zero-field electronic relaxation time ( $\tau_{s0}$ ), where  $\tau_{s0} = \frac{1}{12\Delta^2\tau_v}$  and is dependent on the symmetry of the complex and on the chemical nature of the coordinating groups.

An example of a typical NMRD profile of low-molecular-weight Gd(III) complexes with one inner-sphere water molecule such as [Gd(DTPA-BMA)(H<sub>2</sub>O)], [Gd(DTPA)(H<sub>2</sub>O)]<sup>2-</sup>

, or  $[\text{Gd}(\text{DOTA})(\text{H}_2\text{O})]^-$  (three clinically approved CAs) have the general forms shown in Figure 2.8.

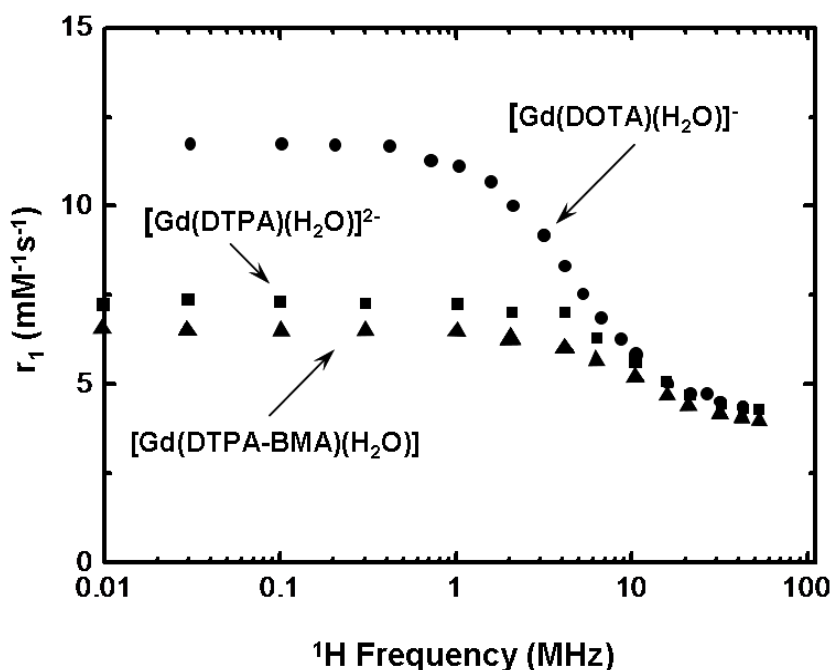


**Figure 2.8.** NMRD profile of three commercially-available CAs  $[\text{Gd}(\text{DTPA-BMA})(\text{H}_2\text{O})]$ ,  $[\text{Gd}(\text{DTPA})(\text{H}_2\text{O})]^{2-}$ , or  $[\text{Gd}(\text{DOTA})(\text{H}_2\text{O})]^-$ .<sup>14</sup>

The main feature of these profiles is that the relaxivity is limited by fast rotation, especially at high frequencies ( $>10$  MHz). As a consequence, the high-field relaxivities of these three agents are practically the same, since their sizes and therefore their rotational correlation times ( $\tau_R$ ) are very similar. The lower value for the water exchange rate (one-order of magnitude) determined for  $[\text{Gd}(\text{DTPA-BMA})(\text{H}_2\text{O})]$  has no influence on the high-field relaxivities, since at these fields the relaxivity is exclusively limited by the rotation of the CA. In the low-field region the different relaxivities reflect the extremely slower electronic relaxation of the symmetric  $[\text{Gd}(\text{DOTA})(\text{H}_2\text{O})]^-$  species, as compared to the linear chelates. The higher relaxivity is a consequence of its much longer zero-field electronic relaxation time ( $\tau_{s0}$ ). The determined  $\tau_{s0}$  values are 650ps for  $[\text{Gd}(\text{DOTA})(\text{H}_2\text{O})]^-$ <sup>41</sup> and 72 and 81ps for  $[\text{Gd}(\text{DTPA})(\text{H}_2\text{O})]^{2-}$  and  $[\text{Gd}(\text{DTPA-BMA})(\text{H}_2\text{O})]$ , respectively.<sup>41</sup>

In the case of superparamagnetic NPs the relaxation induced by these crystals is complicated by another feature. The ferromagnetic crystals are dispersed in a liquid media

to form a colloid suspension. As their size is much smaller than the size of one magnetic domain, they are completely magnetized, constituting a nanomagnet made of a fully magnetized single domain. In addition to the value of its magnetization, each single monodomain is also characterized by its anisotropy energy. The magnetic energy of each nanomagnet depends upon the direction of its magnetization vector with respect to the crystallographic directions, increasing with the tilt angle between the magnetization vector and the anisotropy directions (or easy axes) which minimize this magnetic energy. The difference between the maximum and minimum energy is called the anisotropy energy,  $E_a$ , which is proportional to the crystal volume ( $V$ ),  $E_a = K_a V$ , where  $K_a$  is the anisotropy constant.

In these conditions, the return of the magnetization to equilibrium is determined by two different processes. The first one is the Néel relaxation, which is determined by the anisotropy energy, and is characterized by a relaxation time constant  $\tau_N$ , which defines the fluctuations that arise from the jumps of the magnetic moment between different easy directions causing the return of the magnetization to equilibrium after a perturbation (Figure 2.9). The second process is the Brownian relaxation, which characterizes the viscous rotation of the entire particle, is characterized by a (Figure 2.9).<sup>36</sup> Therefore, the global magnetic relaxation rate of the colloid ( $1/\tau$ , where  $\tau$  is the global magnetic relaxation time) is the sum of the Néel relaxation rate ( $1/\tau_N$ ) and the Brownian relaxation rate ( $1/\tau_B$ ). The Brownian relaxation time is proportional to the crystal volume while the Néel relaxation time is an exponential function of the volume. Then, in the case of larger particles,  $\tau_B$  is shorter than  $\tau_N$ , so the viscous rotation of the particle becomes the dominant process determining the global relaxation. In these conditions, the magnetization curve is perfectly reversible because the fast magnetic relaxation allows the system to be always at thermodynamic equilibrium. This behavior has been named “superparamagnetism” by Bean and Livingston.<sup>36</sup>

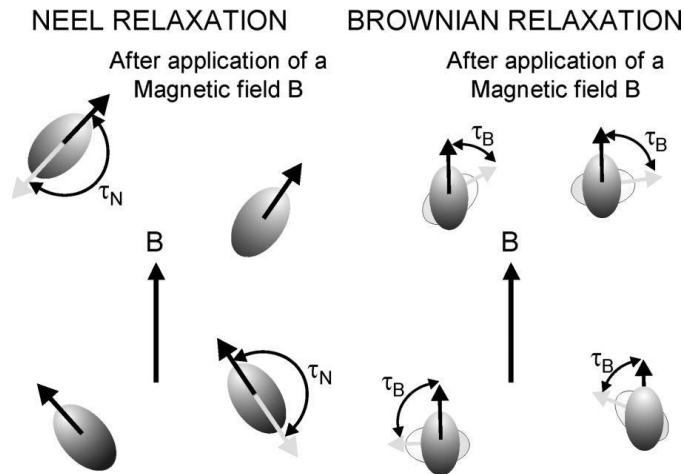


**Figure 2.9.** Illustration of the two components of the magnetic relaxation of a magnetic fluid.<sup>36</sup>

Therefore, the influence of the electron magnetic moment is modulated by the Néel relaxation, which depends upon the crystal anisotropy. In the case of large superparamagnetic crystals or crystals with a very high anisotropy constant<sup>42</sup> the anisotropy energy is larger than the thermal energy, maintaining the direction of the crystal magnetic moment very close to that of the anisotropy axes. This characteristic simplifies the models, enabling the precession of the electron magnetization. Considering small crystals, the anisotropy energy is of the same order of magnitude as the thermal energy, therefore it is possible for the magnetic moment to point in a different direction from the anisotropy axes, allowing some electron precession.

In both these cases the explanation of the longitudinal relaxation rate dependence with the magnetic field (NMRD profile) is based on the so-called Curie relaxation.<sup>27</sup> This relaxation arises from considering separately two contributions to relaxation: *i*) diffusion into the inhomogeneous non-fluctuating magnetic field created by the mean crystal moment, aligned onto  $B_0$  (the accurately termed Curie relaxation) and *ii*) the fluctuations of the electronic magnetic moment or the Néel relaxation.

The different contributions to proton relaxation, in the simplified model for crystals with large anisotropy, are given in Figure 2.10. As shown at low field, the proton longitudinal relaxation rate is obtained by introducing into the Freed equations the precession prohibition mentioned above (the electron Larmor precession frequency is set to zero).<sup>43</sup> Figure 2.10 shows the dispersion of this density spectral function, called Freed function, centred around  $\omega_l = \frac{1}{\tau_c}$ . At high field strength the magnetic vector is locked

along the  $B_0$  direction and the Curie relaxation dominates and the corresponding relaxation rates are given by Ayant's model.<sup>44</sup> In the case of intermediate field strength, the proton relaxation rates ( $R_1$  and  $R_2$ ) are combinations of the high- and low-field strength contributions, weighed by factors depending upon the Langevin function.<sup>45</sup>

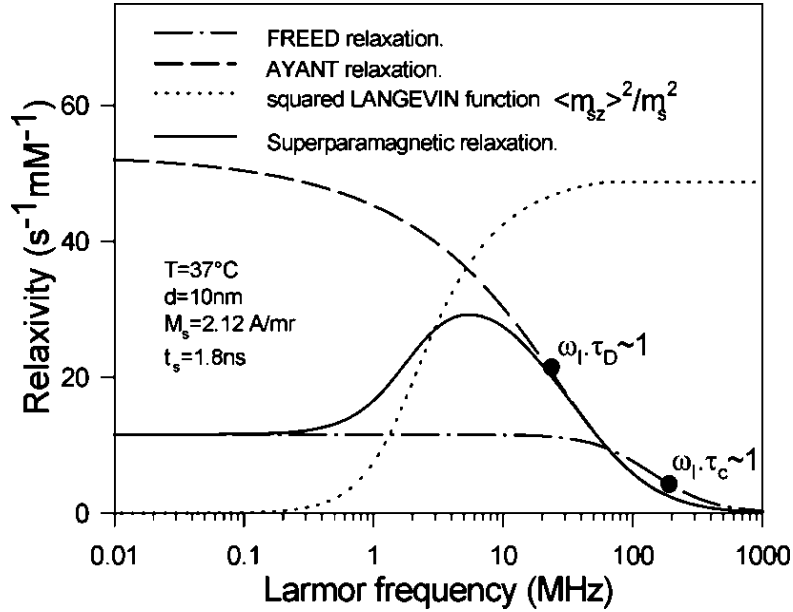


**Figure 2.10.** Different contributions to proton relaxation in the simplified model for crystals with large anisotropy.

In the case of superparamagnetic nanoparticles, the fitting of the NMRD profiles by adequate theories provides information on: their average radius ( $r$ ), their specific magnetization ( $M_s$ ), anisotropy energy ( $E_A$ ), and Néel relaxation time ( $\tau_N$ ).<sup>46</sup> Figure 2.11 illustrates a standard NMRD profile of magnetite particles in colloidal suspension. The average radius ( $r$ ) may be determined since at high magnetic fields the relaxation rate only depends upon  $\tau_D$  as the inflection point corresponds to the condition  $\omega_l \tau_D \sim 1$  (see

Figure 2.11) and given that  $\tau_D = \frac{r^2}{D}$ , the determination of  $\tau_D$  gives the crystal size  $r$ .

Regarding the specific magnetization ( $M_s$ ), also at high fields,  $M_s$  can be obtained from

the equation:  $M_s \sim \left( \frac{R_{\max}}{C \tau_D} \right)^{1/2}$ , where  $C$  is a constant and  $R_{\max}$  is the maximal relaxation

rate. The absence or presence of dispersion at low fields provides information about the magnitude of the anisotropy energy. In the case of crystals characterized by a high

anisotropy energy ( $E_A$ ) value as compared to the thermal agitation the low field dispersion disappears. These conclusions have also been confirmed in previous work with cobalt ferrites,<sup>39</sup> which are known to have high anisotropy energy. The relaxation rate at very low fields  $R_0$  is governed by a “zero magnetic field” correlation time  $\tau_{C0}$ , which is equal to  $\tau_N$  if  $\tau_N \ll \tau_D$ . Often this situation is not met; therefore,  $\tau_N$  is often reported as qualitative information in addition to the crystal size and the specific magnetization.

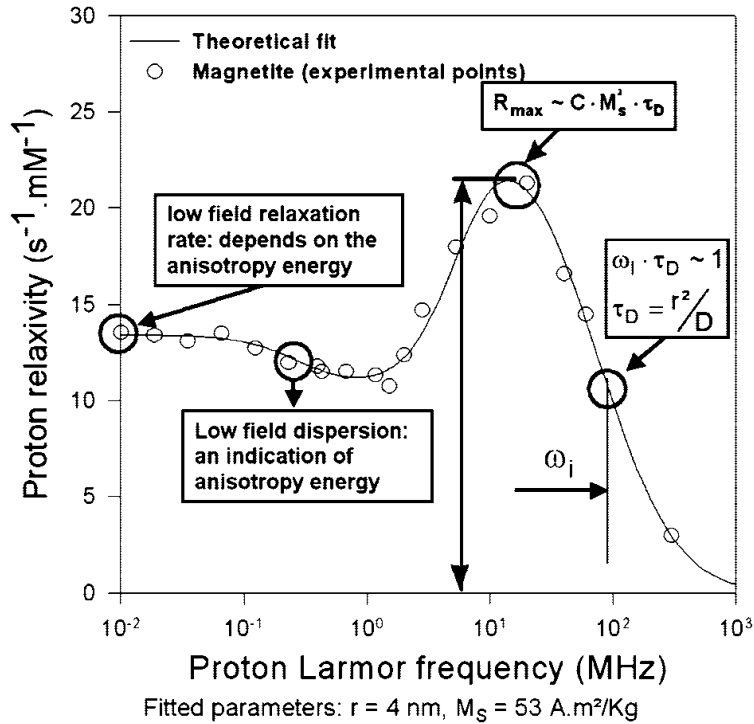


Figure 2.11. NMRD profile of magnetite particles in colloidal suspension.<sup>39</sup>

### 2.3. CLASSIFICATION OF CAs

According to their various features, the currently available MR CAs may be classified in different ways, based on the: *i)* presence and nature of the metal centre, *ii)* their magnetic properties, *iii)* effect on the magnetic resonance image (MRI), *iv)* chemical structure and ligands present, and *v)* biodistribution and applications. A simplification of the above classification may be made, since several of these characteristics are closely related: on one side the chemical composition (metal and ligands), the magnetic properties and the effects on the MRI image and, on the other side, their applications resulting from their *in vivo* bio-distribution.

### 2.3.1. CHEMICAL COMPOSITION, MAGNETIC PROPERTIES AND EFFECTS ON THE MRI IMAGE

The chemical nature of MRI CAs varies widely. They can be *i)* small mononuclear or polynuclear paramagnetic chelates, *ii)* metalloporphyrins, *iii)* polymeric or macromolecular carriers (covalently or noncovalently labelled with paramagnetic chelates, such as dendrimers or proteins), *iv)* particulate CAs, *v)* paramagnetic or superparamagnetic particles, *vi)* diamagnetic or paramagnetic chemical exchange saturation transfer (PARACEST) polymers or chelates, *vii)* diamagnetic hyperpolarization probes, such as  $^{13}\text{C}$  labelled compounds or ions.<sup>47</sup>

The most common and simplest paramagnetic chelates use  $\text{Gd}^{3+}$  or  $\text{Mn}^{2+}$  (due to their properties already described) as metal centres with linear or macrocyclic polyaminocarboxylate/phosphonate derivative ligands. In the case of particulate CAs,  $\text{Gd}^{3+}$  ions are also used in various forms, for example: bound to amphiphilic chelates in paramagnetic micelles, in the bilayer of liposomes, as small chelates in their aqueous internal compartment, or bound to porous materials like zeolites.<sup>47</sup> When considering paramagnetic or superparamagnetic particles, gadolinium oxide nanoparticles and iron oxide particles with different sizes and coatings are considered, respectively.<sup>47</sup>

Other paramagnetic chelates containing different  $\text{Ln}^{3+}$  ions, such as  $\text{Dy}^{3+}$  or  $\text{Tm}^{3+}$ , are used as MRI CAs with different variations. Examples of these variations are as susceptibility agents, when they are in a compartment, affecting  $T_2$  or  $T_2^*$  relaxation,<sup>48</sup> or as PARACEST and LIPOCEST agents, where the paramagnetic shift effect of the ion on the proton nuclei of the CA facilitates the irradiation of their shifted resonances and consequent saturation transfer by chemical exchange (CEST effect), thus decreasing the water proton signal intensity and leading to a negative image contrast.<sup>49</sup>

Less conventional MRI CAs do not contain any metal centre. Examples include the oral agents or the CEST agents.

Recently a new class of MRI CAs has been developed, dynamic nuclear polarization (DNP) agents, such as hyperpolarized noble gases ( $^3\text{He}$ ,  $^{129}\text{Xe}$ ) and  $^{13}\text{C}$ -labeled organic compounds or ions like  $^6\text{Li}^+$ . The probe's nuclei (with long  $T_1$  values) exhibit a strong signal enhancement allowing the direct imaging of the probe's molecular distribution.<sup>47</sup>

CAs may also be classified according to their magnetic properties as paramagnetic or superparamagnetic agents. Metal ions with one or more unpaired

electrons are paramagnetic and consequently possess a permanent magnetic moment. Organic free radicals are also paramagnetic due to their unpaired valence electron. Within an aqueous suspension a dipolar magnetic interaction between the electronic magnetic moment of the paramagnetic atom and the much smaller magnetic moments of the protons of the nearby water molecules is formed. Random fluctuations in this dipolar magnetic interaction can be caused by the molecular motions, therefore reducing both the longitudinal ( $T_1$ ) and the transverse ( $T_2$ ) relaxation times of the water protons. As already mentioned,  $Gd^{3+}$  and  $Mn^{2+}$  are examples of paramagnetic ions used as MR CAs, because their physical properties are suitable for efficiently reducing the  $T_1$  and  $T_2$  proton relaxation times.<sup>47</sup>

Unfortunately, paramagnetic metal ions, like  $Gd^{3+}$ , can not be used as CAs in their ionic form due to their undesirable biodistribution (accumulating in bones, liver or spleen) and relatively high toxicity. Therefore, metal ion complexes (chelates) with high thermodynamic and kinetic stabilities are required in order to use these paramagnetic metal ions *in vivo*. Small  $Gd^{3+}$  or  $Mn^{2+}$ -based paramagnetic chelates are nonspecific CAs and have similar  $r_1$  and  $r_2$  effects in water. Currently these agents are used mainly for positive contrast  $T_1$ -weighed images. As already mentioned, the relaxivity effects of these agents result mostly from both inner- and outer-sphere mechanisms.

The superparamagnetic agents consist of materials, such as iron oxides, in the form of colloids made up of particles (typically 5 – 200nm in diameter) in suspension, which are composed of very small crystallites (1 – 10 nm) containing several thousand magnetic ions. These agents exhibit a behaviour similar to paramagnetism except that, instead of each individual atom being independently influenced by an external magnetic field, the magnetic moment of the entire crystallite tends to align with that magnetic field.<sup>47</sup> Therefore the magnetic moments of the individual ions do not cancel out but are mutually aligned, inducing a much higher permanent magnetic moment within the crystallites when in the presence of a magnetic field compared to a single molecule of a Gd chelate.<sup>47</sup>

These particles are embedded in a coating such as dextrans (in ferumoxide) or siloxanes (in ferumoxsil), which prevents agglomeration. There are three kinds of particulate superparamagnetic iron oxides, according to the overall size of the particles: *i*) if they have a diameter  $d < 50 \text{ nm}$ , they are known as ultra-small superparamagnetic iron oxide (USPIO) particles; *ii*) if  $1 \mu\text{m} > d > 50 \text{ nm}$ , they are called small superparamagnetic iron oxide (SPIO) particles; and *iii*) micron-sized particles of iron oxide (MPIO) are large particles, with a diameter of several microns. Intravenous administration is only possible

for the former two, while the large particles can only be administered orally to explore the gastrointestinal tract, otherwise they would be trapped in the lung alveoli. Yet more nomenclatures exist, such as monocrystalline iron oxide particles (MION) and cross-linked iron oxides (CLIO).

As a consequence of their larger size and magnetic moment SPIOs were initially developed as  $T_2$ -agents, producing a dark area on MRI images resulting from their negative contrast effect.<sup>50</sup> A new generation of USPIOs with sizes less than 10 nm has also been reported to have excellent  $T_1$ -enhancing properties.<sup>39,51,52,53</sup> As already mentioned, the relaxation induced by superparamagnetic particles is explained by the classical outer-sphere relaxation theory, reformulated by the Curie relaxation theory.<sup>48</sup>

The susceptibility agents induce long-range interactions which can dominate the  $T_2$  or  $T_2^*$  relaxation. This relaxation mechanism, known as susceptibility-induced relaxation,<sup>47</sup> is related to the magnetization of the CA, which results from the partial alignment of the individual magnetic moments in the direction of the magnetic field.

An example of this type of agent is when a CA becomes compartmentalized, like when superparamagnetic particles are taken up by Kupffer cells, or in a vessel, the compartment containing these CA functions as a secondary CA. In this case the water protons on the outside of the compartment are affected by the overall magnetization of the magnetic bulk material inside that compartment and are, therefore, relaxed by an outer-sphere mechanism.<sup>47</sup> The blood oxygen level dependent (BOLD) effect is due to this long-range  $T_2/T_2^*$  relaxation effect, where the paramagnetic hemoglobin is compartmentalized within blood erythrocytes. This phenomenon is the basis of functional MRI<sup>54</sup> and can depend on several parameters such as the magnetic moment and local concentration of the CA, the dimensions and geometry of the compartment, the diffusion constant of water within the compartment and so on.

As already mentioned, the classification of MR CAs as ' $T_1$  agents' or ' $T_2$  agents' is not always accurate, since any CA that reduces  $T_1$  also reduces  $T_2$ . Nevertheless any agent that reduces  $T_2$  does not necessarily reduce  $T_1$ , at least at MRI field strengths. Therefore the CA functions as a ' $T_1$  agent' or ' $T_2$  agent' depending on the imaging sequence used, the magnetic field strength, the size of the CA and how the CA is compartmentalized in the tissue.<sup>47</sup>

### 2.3.2. BIODISTRIBUTION AND APPLICATIONS

The biodistribution of CAs is very important because it is vital to know what happens to the CAs and where they go when they are intravenously administered. The main distribution sites and excretion pathways for soluble metal complexes are summarized in Figure 2.12.

There are several types of possible classifications and divisions for CAs such as: *i)* non-specific agents, *ii)* specific or targeted agents, *iii)* non-injectable organ-specific agents, *iv)* responsive, smart or bio-activated agents and *v)* CEST and Hyperpolarized agents.

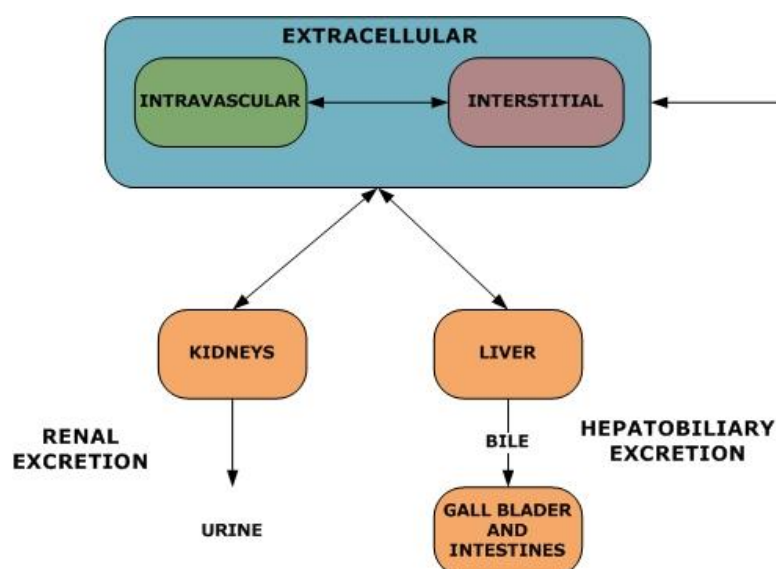


**Figure 2.12.** Main distribution sites and excretion pathways for intravenously administered soluble metal complexes.<sup>47</sup>

#### 2.3.2.1. NON-SPECIFIC AGENTS

Nonspecific CAs (those that do not interact specifically with any type of cells) encompass the extracellular fluid (ECF) agents and the blood pool agents (BPA). The

former are low molecular weight extracellular complexes that equilibrate rapidly between the intravascular and interstitial space and are mainly excreted by the kidneys.<sup>55-58</sup> BPA have high molecular weight, such as high generation dendrimers, which stay within the intravascular space and are slowly excreted via the kidneys and/or the liver.<sup>55,56,57,58</sup>

The ECF agents leak rapidly from the blood into the interstitium with a distribution half-life of about 5 minutes and are cleared by the kidney with an elimination half-life of about 80 minutes. ECF agents have been extensively used in extra-cranial applications. Since these agents rapidly clear out of the blood, the images are typically acquired in the early phase following a bolus injection, when used in conjunction with MRA. The most common ECF agents are  $Gd^{3+}$  chelates of linear or macrocyclic polyaminocarboxylate ligands and are the main commercially-available MRI CAs. These type of CAs can be divided into two groups: neutral and ionic agents (Figure 2.13, Table 2.1). In conclusion,  $Gd^{3+}$ -based ECF agents are typically safe when used in clinically recommended doses, and adverse reactions and side effects, such as allergy, are very rare.<sup>47</sup>

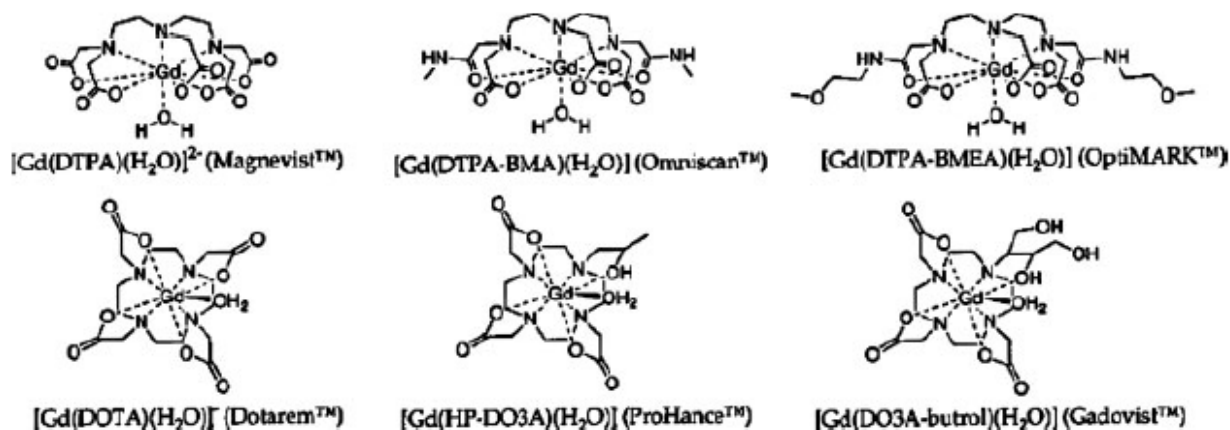


**Figure 2.13.** Structures of commercial ECF contrast agents with intravascular and extracellular distribution.<sup>36</sup>

**Table 2.1.** Properties of commercial ECF contrast agents with intravascular and extracellular distribution.

Short Name & Generic Name	Trade Name	Relaxivity ( $\text{mM}^{-1}\text{s}^{-1}$ ) $B_0 = 1.0 \text{ T}$ ( $37^\circ\text{C}$ )	MRI Enhancement & Physiochemical Properties
Gd-DTPA - Gadopentetate dimeglumine	Magnevist® Bayer Schering Pharma AG	$r_1 = 3.4, r_2 = 3.8$	positive – charged (ionic) – linear
Gd-DOTA – Gadoterate meglumine	Dotarem® Guerbet	$r_1 = 3.4, r_2 = 4.8$	positive – charged (ionic) – macrocyclic
Gd-DTPA-BMA - Gadodiamine	Omniscan® GE Healthcare	$r_1 = 3.9, r_2 = 4.3$	positive – neutral (non-ionic) – linear
Gd-HP-DO3A – Gadoteridol	Prohance® Bracco SpA	$r_1 = 3.7, r_2 = 4.8$	positive – charged (ionic) – macrocyclic
Gd-BT-DO3A - Gadobutrol	Gadovist® Bayer Schering Pharma AG	$r_1 = 3.6, r_2 = 4.1$ (at 0.47 T)	positive – charged (ionic) – macrocyclic
Gd-DTPA-BMEA – Gadoversetamide	OptiMARK® Mallinckrodt	$r_1 = 3.8, r_2 = 4.2$	positive – neutral (non-ionic) – linear
Gd-BOPTA – Gadobenate dimeglumine	MultiHance® Bracco Diagnostics	$r_1 = 4.6, r_2 = 6.2$	positive – charged (ionic) – linear

Blood-pool agents (BPA) or intravascular agents are compounds with larger ‘sizes’ than the previous ECF agents and also have higher  $r_1$  relaxivities. These two characteristics offer many advantages in MR angiography (MRA) when compared to ECF agents.<sup>14,59</sup> Because their high molecular weight (>20 kDa) prevents leakage into the interstitium, they remain in the intravascular system longer than conventional ECF agents.<sup>60</sup> These agents have been primarily developed for MRA and their main properties are to have a relatively long vascular half-life and the highest possible  $r_1$ -relaxivity. Their  $r_2$  relaxivity must be low enough to avoid excessive signal loss due to  $T_2/T_2^*$  relaxation.<sup>47</sup>

The potential advantage of using a BPA in MRA is the prolonged imaging window given that a longer image acquisition time is granted. This translates into a higher image resolution and/or signal-to-noise ratio, therefore higher-quality angiograms may potentially be attained when compared to gadolinium-based ECF agents. In this respect, vascular abnormalities, associated with certain tumours or atherosclerosis, can be more easily detected. Additionally, tissue blood volume and perfusion can be measured.<sup>61</sup> The disadvantage of this ‘steady-state’ approach is that arteries and veins are equally enhanced, thus making their differentiation more challenging.

According to their action mechanism the BPA can be divided into several classes: *i)* the noncovalent binding of low molecular weight  $Gd^{3+}$ -based complexes to human serum albumin –HSA (the most abundant plasma protein) which prevents immediate leakage into the interstitial space; *ii)* systems based on polymers or liposomes (increases the size of the CA molecule); and *iii)* systems based on particles (involves a change in the route of elimination). Figure 2.14 and Table 2.2 display several examples of these different classes of BPA.

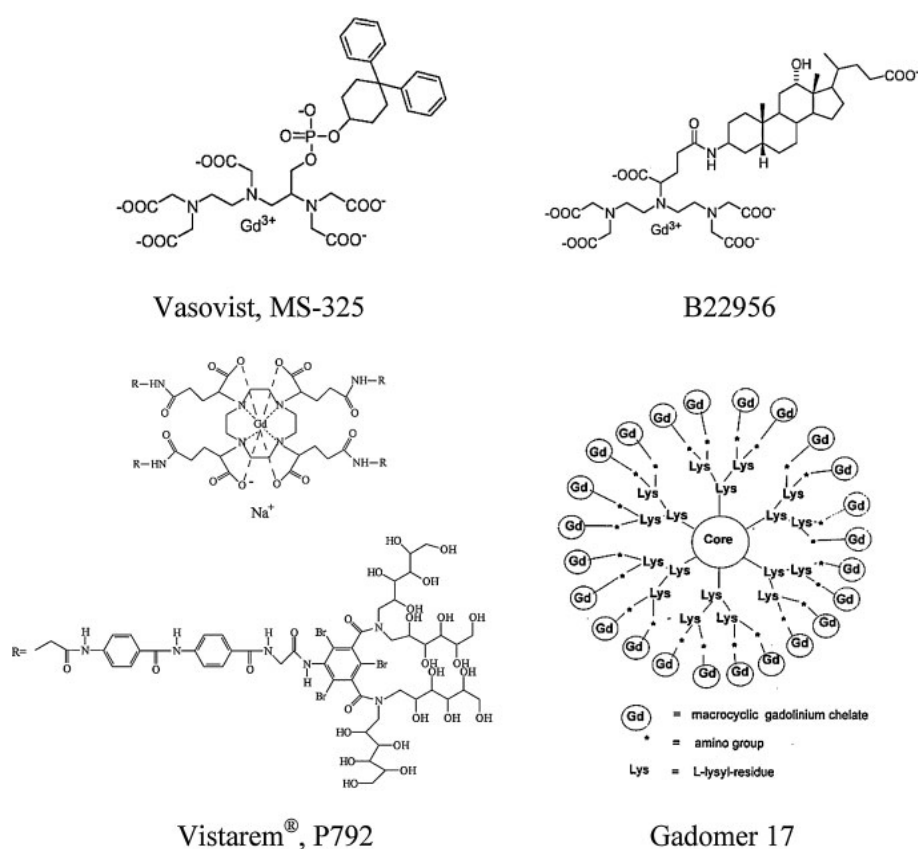


**Figure 2.14.** Structures of some HSA-binding and polymeric  $Gd^{3+}$  complexes, as potential or approved blood pool CAs for MRA (simplified structure for Gadomer 17).<sup>47</sup>

**Table 2.2.** Properties of commercial BPA contrast agents.

Short Name & Generic Name	Trade Name	Relaxivity ( $\text{mM}^{-1}\text{s}^{-1}$ ) (37 °C)	MRI Enhancement & Physiochemical Properties
MS-325 – Diphenylcyclohexyl phosphodiester-Gd-DTPA	Vasovist® Bayer Schering Pharma AG	$r_1 = 19, B_0 = 1.5 \text{ T}$	positive – Albumin binding molecules – MRA vascularisation, capillary permeability
B-22956 or B-22956/1 – Gadocoletic acid	Bracco SpA	$r_1 = 27, B_0 = 0.5 \text{ T}$	positive – Reversible albumin binding – coronary MRA
Gadomer-17 or Gd-DTPA-17	Bayer Schering Pharma AG	$r_1 = 11.9, r_2 = 16.5 B_0 = 0.5 \text{ T}$	positive – Polymeric Gd complex – MRA vascularisation and tumor differentiation
P792 – Gadomelitol	Vistarem® Guerbet	$r_1 = 42, r_2 = 50 B_0 = 0.47 \text{ T}$	positive – Polymeric Gd complex) – MRA
Gadofluorine-M	–	$r_1 = 137, B_0 = 1.5 \text{ T}$	positive – Polymeric Gd complex – MRA
AMI-227 – Ferumoxtran-10	Sinerem® Guerbet, Combindex® AMAG	$r_1 = 22.7, r_2 = 53.1 B_0 = 1.0 \text{ T}$	Positive or negative – Coated USPIO particles – MRA
SH U 555 C – Ferucarbotran	Supravist® Bayer Schering Pharma AG	$r_1 = 14, B_0 = 1.5 \text{ T}$	Positive – Coated USPIO particles – MRA

### 2.3.2.2. SPECIFIC OR TARGETED AGENTS

Specific or targeted agents can also be divided into two main groups: those that are actively targeted to a molecularly specific site with an appropriate ligand and those that are passively directed to a particular type of cell. The first group includes agents that target pathologic processes or states, such as inflammation, angiogenesis, apoptosis, atherosclerosis and tumour. The cell labelling CAs function through recognition of specific molecular markers of those processes at the cell surface (such as cell-specific receptors or transport proteins) and accumulate at those molecular sites (usually in the intracellular space).<sup>47</sup> Therefore, these cell labelling CAs are essential for MRI molecular imaging. The second main group are the organ-specific agents for the liver (hepatobiliary), spleen, lymph nodes, bone marrow or brain, based mainly on the agent size and/or chemical structure. Nevertheless, all CAs can be considered organ-specific CAs to some extent, as they are excreted either by the liver or the kidneys.

## Actively Targeted or cell labelling Contrast Agents

The actively targeted or cell labelling CAs are able to recognize specific molecular sites (e.g. cell-specific receptors or transport proteins) at the cellular membrane and accumulate at those sites. Researchers involved in the synthesis of MRI contrast agents devote special attention to these types of agents. The development of agents enables the recognition and imaging of a specific 'signature' of a given disease (molecular imaging) that simplifies the task of diagnosis and therapy.<sup>62</sup> One of the requirements for efficient molecular probes is the development of high affinity ligands and their conjugation to contrast agents Figure 2.15A. A major problem is the need to have a local concentration of CA of ca. 0.5 mM in order to have 50% enhancement of contrast. It is possible to increase the payload of reporter groups delivered at the target site by using many reporters bound to a single carrier, as illustrated in Figure 2.15B.

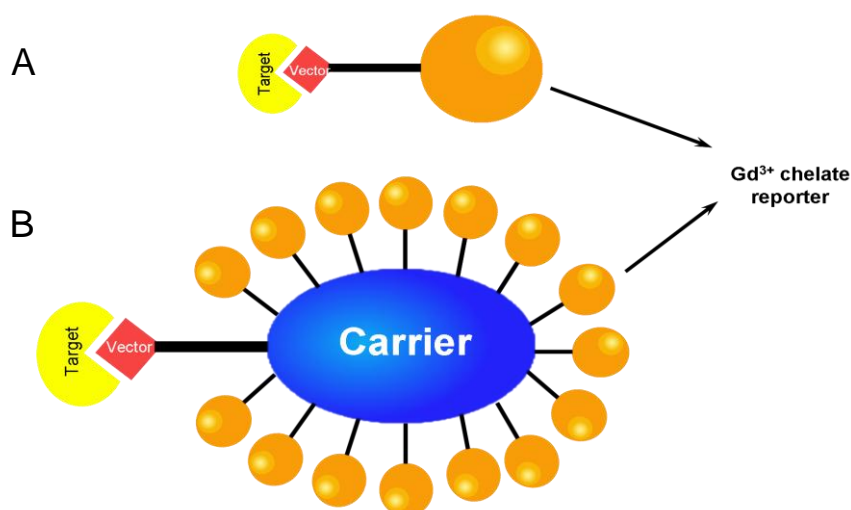


**Figure 2.15.** General structure of a targeted CA for cell labelling a) with a single reporter group, b) with a carrier of many reporter groups.<sup>47</sup>

The main applied targeting strategies are cell-surface targeting and receptor targeting. In the former, specific epitopes easily available at the cell surface are targeted to which the CA stays bound. This strategy has been used together with the pretargeting approach in order to facilitate the detection and imaging of tumour cells (as tumour cells are known to have abnormally high negative charges on their cell surface). It is clear that

the use of low-molecular-weight targeting CAs that are able to accumulate quickly at specific cell surface sites have more advantages with regards to the use of macromolecular agents.<sup>47</sup> Another example of cell-surface targeting is the well-known non-specific binding of porphyrins to the interstitial space of tumours, e.g. Dy-TPPS (TPPS=tetraphenylporphyrin sulfonate). One expanded porphyrin (texaphyrin) complex, [Gd(Tex)]<sup>2+</sup> (PCI-120), selectively accumulates in tumours, inducing a prolonged enhancement in MRI images and provides the possibility of being used as a radiation sensitizer for brain cancer.<sup>63</sup>

The targeting of cell-surface receptors approach can be pursued using labelled antibodies or low-molecular-weight targeting complexes. In the first approach, due to the slow diffusion of the antibodies, the most accessible targets are those present on the endothelial vessels.<sup>47</sup> A typical example is the targeting of the endothelial integrin receptor  $\alpha_V\beta_3$ , a specific angiogenesis marker whose concentration correlates to the tumour grade. An example of an imaging probe containing many reporter groups per carrier is a Gd<sup>3+</sup>-containing polymerized liposome. The pretargeting approach was used, where the target was bound first to a biotinylated monoclonal antibody against  $\alpha_V\beta_3$ , which is well recognized by an avidin moiety present on the liposome surface carrying the Gd<sup>3+</sup> chelate reporter groups.<sup>64</sup> The same  $\alpha_V\beta_3$  target has also been grafted with lipidic nanoparticles containing Gd<sup>3+</sup> chelates.<sup>65</sup> The large molecular size and consequently the slow delivery of these systems can be considered the major limitation of this technique.

A more efficient way to accumulate CAs at the target site is by cell internalization. For this process to be completely successful the concentration of the agent inside the cell must be higher than at the cell surface. The internalization processes may occur via phagocytosis and pinocytosis (or fluid phase endocytosis) mechanisms, which do not require a cell receptor, or receptor mediated endocytosis.<sup>47</sup> Gd-DTPA bis-stearylamine derivatives are CAs forming insoluble Gd<sup>3+</sup>-containing particles that are biodegraded after internalization and become soluble and trapped inside the cell.<sup>66</sup> Gd-HPDO3A is a CA used for labelling stem cells via pinocytosis mechanism where the stem cells are incubated in a culture medium containing Gd-HPDO3A with a concentration ranging 10–50mM.<sup>67</sup> The relaxivity of the CA entrapped in the cell endosomic compartment can be seriously limited with the exception of the internalization by electroporation, where they are delivered to the cytoplasm.<sup>68</sup> Other cell internalization mechanisms have used

membrane transporters and transmembrane carrier peptides. The latter have proven useful for the internalization of a number of substrates like proteins, oligonucleotides and plasmid DNA.

Another interesting development was the synthesis of a bimodal (optical and MR) imaging probe consisting of a  $Gd^{3+}/Eu^{3+}$ -DOTA complex, a PNA (peptide nucleic acid) sequence and a transmembrane carrier peptide.<sup>47</sup> This system can enter any type of cell, however it accumulates only in tumour cells due to the specific binding of the PNA moiety to the c-myc mRNA whose production is increased in those cells.<sup>69</sup>

### **Passively directed - organ-specific agents**

The passively directed or organ specific CAs are passively directed to a particular type of cell. Normally, there are organ-specific agents for the liver (hepatobiliary), spleen, lymph nodes, bone marrow or brain, and they are generally based mainly on the agent size and/or chemical structure.<sup>47</sup>

In general, tissue or organ-specific contrast agents consist of two components: a magnetic label capable of altering the signal intensity on MR images and a target-group molecule having a characteristic affinity for a specific type of cell or receptor. Some suitable residues have been incorporated into either the acetic side arms or the diethylenetriamine backbone of Gd-DTPA and Gd-DOTA to obtain the tissue or organ-specific contrast agents. This type of CAs provides specific advantages in terms of sensitivity of lesion detection and characterization. Examples of these types of agents are the hepatobiliary CAs,<sup>70-74</sup> the lymph nodes and bone marrow CAs,<sup>75</sup> the brain CAs<sup>76-79</sup> and the gastro-intestinal CAs<sup>80,81</sup> that can accumulate in the target sites, increasing contrast concentration and can produce stronger signal in the MR images. Table 2.3 provides a summary of the properties of these CAs.

**Table 2.3.** Properties of commercial organ-specific contrast agents.

Short Name & Generic Name	Trade Name	Relaxivity ( $\text{mM}^{-1}\text{s}^{-1}$ ) (37 °C)	MR Enhancement & Physiochemical Properties
Gd-EOB-DTPA – Gadoxetic acid	Primovist™ (formerly Eovist®) Bayer Schering Pharma AG	$r_1=5.3, r_2=6.1 B_0=0.47 \text{ T}$	positive – small charged linear complex (ionic) – Hepatobiliary liver lesions
Gd-BOPTA – Gadobenate dimeglumine	Multihance® Bracco SpA	$r_1=4.6, r_2=6.2 B_0=1.0 \text{ T}$	positive – small charged linear complex (ionic) – Intravascular/Extracellular/Hepatobiliary Neuro/whole body, liver lesions
Mn-DPDP – mangafodipir trisodium	Teslascan® GE Healthvare,	$r_1=2.3, r_2=4.0 B_0=1.0 \text{ T}$	positive – small charged – Pancreatic/Adrenal/Hepatobiliary liver lesions
AMI-25 – Ferumoxides (SPIO)	Endorem™ Guerbet, Resovist®	$r_1=40.0, r_2=160 B_0=0.47 \text{ T}$	negative – dextran-coated SPIO particles – RES-directed liver lesions
SH U 555 A – Ferucarbotran (SPIO)	/Cliavist® Bayer Schering Pharma AG	$r_1=25.4, r_2=151 B_0=0.47 \text{ T}$	negative – dextran-coated SPIO particles – RES-directed liver lesions lymph nodes
Gadofluorine-M	–	$r_1=137, B_0=1.5 \text{ T}$	positive – Polymeric Gd complex – lymph nodes
AMI-227 – Ferumoxtran-10	Sinerem® Guerbet, Combidex® AMAG	$r_1=22.7, r_2=53.1 B_0=1.0 \text{ T}$	Positive or negative – Coated USPIO particles – lymph nodes
EPI-2104 R –	Pharmaceuticals, Inc	-	Positive – gadolinium-based small peptide – lymph nodes - visualization of blood clots
Gd-DTPA mesoporphyrin (gadophrin)	Gadophrin Bayer Schering Pharma AG	-	Positive - myocardium and necrosis targeted

### 2.3.2.3. NON INJECTABLE ORGAN-SPECIFIC AGENTS

When ingested, non-injectable organ-specific agents (oral agents) change the signal intensity at the stomach and the intestine relatively to adjacent abdominal tissues. Depending on their magnetic properties they may change the contrast of the gastrointestinal (GI) tract through various mechanisms, thus allowing MR cholangiography (Table 2.4).

Diamagnetic agents, such as fatty emulsions, fill the GI tract with materials with short  $T_1$ , enhancing its signal and producing positive contrast relatively to adjacent tissues. Within the same level, diamagnetic agents can also generate negative contrast either by decreasing the  $T_2$  of GI water protons, such as in the presence of  $\text{Ba}^{2+}$ ,  $\text{Al}^{3+}$ ,  $\text{Si}^{4+}$ -containing suspensions, or by decreasing the proton density through the use of

perfluorinated compounds like perfluorooctylbromide (PFOB).<sup>47</sup> Paramagnetic agents, such as  $\text{MnCl}_2$  solutions, Magnevist® [Gd-(DTPA)] or Gadolite®  $\text{Gd}^{3+}$ -containing zeolite Y particle suspensions,<sup>80</sup> ferric ammonium citrate (FAC) solutions, are oral positive CAs that decrease the  $T_1$  of GI water protons. Large superparamagnetic particles for oral uptake,<sup>81</sup> such as Abdoscan®, composed of monodisperse polymer particles of 3  $\mu\text{m}$  diameter coated with crystals of iron oxide, or Lumirem®, a silicone-coated superparamagnetic iron oxide suspension, belong to the group of negative oral CAs that decrease proton  $T_2/T_2^*$ . Their main purpose is to distinguish the loops of the bowel from other abdominal structures. When ingested, they flow through and darken the stomach and the small intestine in 30–45 minutes with a clear identification of the intestinal loops, and improving the visualization of adjacent abdominal tissues such as the pancreas.<sup>47</sup>

**Table 2.4.** Properties of commercial non-injectable organ-specific contrast agents.

Short Name & Generic Name	Trade Name	Relaxivity	MR Enhancement & Physiochemical Properties
Gd-DTPA – gadopentetate dimeglumine	Magnevist enteral® Bayer Schering Pharma AG	$T_1$ reduction	Positive - Paramagnetic
Ferric ammonium citrate Geritol	Ferriseltz® Otsuka Pharmaceutical	-	positive – Paramagnetic
$\text{MnCl}_2$ – manganese chloride	LumenHance® ImaRx Pharmaceutical Corp. Bracco Spa	$T_1$ reduction	Positive - Paramagnetic
Gd-zeolyte Y particles – Gadolite 60 gastrointestinal	Gadolite®Pharmacyclics	$T_1$ reduction	Positive - Paramagnetic
AMI-121 - ferumoxsil (USAN)	Lumirem® / Guerbet Gastromark® AMAG Pharmaceuticals	$T_2^*$ enhanced	Negative – Superparamagnetic
OMP – Ferristene (USAN) oral magnetic particles	Abdoscan® GE Healthcare	$T_2^*$ enhanced	Negative – Superparamagnetic
PFOB - perfluorooctylbromide barium sulfate suspensions, clays mineral particles	Imagent-GI® Alliance Pharmaceutical	Proton density reduction, signal void	Negative – Diamagnetic
	Various Mixtures	Diamagnetic, $-T_1$ -short	Negative – Diamagnetic

#### 2.3.2.4. RESPONSIVE, SMART OR BIOACTIVATED AGENTS

The term 'responsive' refers to paramagnetic systems that are sensitive to a given biochemical or physiologic parameter that characterizes their microenvironment. Typical parameters to which these systems should be responsive are the pH, temperature, oxygen pressure, enzymatic activity, redox potential and concentration of a specific ion. The use of these agents induces a type of imaging, Molecular Imaging, which aims to noninvasively visualize the expression and function of bioactive molecules that often represent specific molecular signatures in disease processes.<sup>48</sup> So far, only very few of these CA have progressed to *in vivo* testing. The *in vivo* non-invasive detection of abnormalities in pH or temperature, in the oxygen pressure, in enzymatic activities or in the concentration of metal ions and radicals may serve in the future as an important diagnostic tool of the underlying diseases. Information on the redox status, an important factor governing tumour aggressiveness, can also help determine the adapted tumour treatment. Many of these abnormalities are observable in the extracellular media, which largely facilitates the chemical design of the imaging probes that have no need for intracellular CA delivery.

##### ***pH-sensitive agents***

The potential use of pH-sensitive probes is vast, though so far pH mapping of tissues has been primarily intended to facilitate cancer detection and assess the tumour status. The pH on the surface of tumours is ~0.4 units lower than that of normal tissue, but in some cases it can be as low as 6.0.<sup>82</sup> The pH-sensitive probes may also indicate neuronal activity because they induce a slight acidification of the extracellular medium (pH 7.2–7.4).<sup>83</sup> One could also imagine the use of pH-responsive probes to determine if the brain environment is suitable for a drug that functions in a pH-sensitive environment.

The main requirements for a system to be pH-sensitive are that either the dynamics or structural properties determining its relaxivity are pH-dependent. The pH dependence of the relaxivity can reflect changes in the hydration number of the metal chelates and the presence of protonatable groups on the ligands can influence these changes.<sup>36,84</sup>

Designing of pH-sensing probes has become an intensive field in MR imaging contrast agent research.<sup>49,84-89</sup> Some of the pH probes are useful for *in vivo* application. An example is the combination of the pH-sensitive amido-phosphonate derivative of Gd-DOTA and a pH-insensitive analogue, which were used in a dual injection to image renal pH in mice.<sup>90,91</sup> The assumption was made that both compounds have comparable pharmacokinetics; hence the concentration of the former can be inferred from the concentration of the latter. This mixture has been also used to obtain extracellular pH MR imaging maps in a rat glioma model, with improved spatial resolution compared with spectroscopic methods.<sup>92</sup> Differences in the order of 1 pH unit could be detected; the absolute pH values have been calculated by using a calibration method.

The key factor inducing the effectiveness of an agent is the difference between the relaxivity of the "on" state compared with that of the "off" state. Recently the amplitude of the relaxivity response to pH variation of this low-molecular-weight probe has been largely improved (doubled in some cases) by conjugating it to a macromolecular dendrimeric scaffold.<sup>93</sup> Improving the relaxivity response to pH by increasing the molecular weight may also negatively impact the effectiveness of such agents. As already mentioned, large molecules, such as dendrimers, remain in the vasculature longer than discrete agents, which are better able to diffuse into all extracellular space. Large molecules also tend to slowly clear from the body, resulting in increased liver uptake, extending their retention time in the body. Further studies into the *in vivo* behaviour of dendrimer-based MR imaging contrast media will be required to establish whether this approach, which is successful for increasing the relaxivity response, will yield agents that can actually be applied *in vivo*.

### ***Temperature-sensitive agents***

Most Ln<sup>3+</sup> chelates have temperature-dependent NMR properties, such as their <sup>1</sup>H NMR chemical shifts. These shifts can be monitored and used to determine temperature variation. For this reason some of these Ln<sup>3+</sup> chelates are considered to be good temperature probes.<sup>94,95</sup>

The encapsulation of Gd<sup>3+</sup> chelates into liposomes is also another example of a temperature-dependent probe.<sup>96</sup> The membrane transition from gel to liquid crystal occurs

at a specific temperature. At this precise temperature changes in the permeability of the membrane occurs, therefore the mobility of the water molecules through the membrane changes and consequently the relaxivity also changes.<sup>47</sup>

### ***Enzymatic activity agents***

Among all responsive agents, enzyme targeting represents a specific advantage, which is particularly valid for MR imaging detection given its low sensitivity. A small concentration of the enzyme can catalytically convert a relatively high amount of the enzyme-responsive magnetic probe, which increases the detection for the enzyme compared with other biomolecules. In addition, the remarkable specificity of enzymatic reactions, which can be observed as changes in the MR imaging properties, can be undoubtedly attributed to the targeted enzyme. The presence of certain enzymatic reactions indicates the cellular state and can provide the signature of a given pathology. Consequently the real-time non-invasive *in vivo* detection of specific enzymatic activities would have invaluable diagnostic impact.

As the enzymatic activity has been established in the processes of tumour formation, growth and metastasis, it is vital to monitor it. Molecular Biology studies have defined enzymatic steps of the apoptotic response to anticancer therapies *in vitro* and *in vivo*. Utilising this approach the detection of gene markers (such as  $\beta$ -galactosidase) could be another important field of application.<sup>47</sup>

The first enzymatically responsive potential MR imaging contrast agent was a Gd-DOTA-derivative bearing a galactopyranose residue that avoids water coordination.<sup>97,98</sup> This sugar moiety is a substrate for the enzyme  $\beta$ -galactosidase. Its enzymatic cleavage by  $\beta$ -galactosidase opens the access of water to the first coordination sphere of  $Gd^{3+}$ , resulting in an enhancement of the relaxivity, thus irreversibly activating the agent. This agent has been successfully used *in vivo* to detect by MRI  $\beta$  - galactosidase mRNA expression in living *Xenopus laevis* embryos.<sup>47</sup>

Among other examples, Nivorozhkin et al<sup>99</sup> reported the enzymatic transformation of a prodrug  $Gd^{3+}$  complex with poor affinity to HSA and low relaxivity to a

species with improved HSA affinity and enhanced relaxivity.<sup>36</sup> Mazooz et al<sup>100</sup> described a Gd-DTPA peptide acting as a transglutaminase substrate, which was used to monitor transglutaminase activity.<sup>47</sup> Anelli et al<sup>101</sup> functionalized Gd(DTPA)<sup>2-</sup> with sulfonamide, which is known as a specific carbonic anhydrase inhibitor. The agent reacts with carbonic anhydrase and thus targets enzyme-rich tissues.<sup>47</sup> Shiftan et al<sup>102</sup> reported MR imaging visualization of hyaluronidase in ovarian carcinoma, related to the aggressiveness of ovarian cancer metastasis.<sup>47</sup> Chen et al<sup>103</sup> visualized plaque rupture in atherosclerosis with a Gd-DOTA–serotonin derivative, which polymerizes in the presence of neutrophil myeloperoxidase, resulting in a remarkable relaxivity increase. Another concept for enzyme detection is based on the self-immolative mechanism.<sup>47</sup> Duimstra et al<sup>104</sup> reported a Gd<sup>3+</sup> complex with a self-immolative moiety, designed for the detection of  $\beta$ -glucuronidase.<sup>47</sup>

### ***Redox potential sensitive agents***

Hypoxia is an important factor governing tumour aggressiveness, as hypoxic tissue is more resistant to conventional therapeutics. The methodology of imaging tumour redox status would allow the noninvasive application of this potential biomarker of tumour sensitivity to existing and novel chemotherapies, as well as radiation therapy. The possibility of using such methods could also extend to other pathologies, such as cardiovascular disease, since free radical formation is associated with damaging effects on the coronary microcirculation during recovery from myocardial infarction.<sup>105</sup> Hypoxia is mostly detected by imaging techniques including positron-emission tomography (PET) and blood oxygen level-dependent (BOLD) MR imaging.

Reports on redox-sensitive MR imaging contrast agents have been rather scarce. The simplest design of these agents is based on metal complexes whose metal ion can be reduced or oxidized depending on the biologic environment and these two oxidation forms have different relaxation properties. As a result, the two redox states influence the proton relaxation of the surrounding protons to a different extent, resulting in different image intensities.

The partial oxygen pressure ( $pO_2$ ) is also an important parameter in the metabolic processes of the cells and its variation is related with certain pathologies.<sup>47</sup> The usual systems used as  $pO_2$  probes are based on the redox equilibrium of paramagnetic ions. In these systems the relaxivity depends on the oxidation state of the metal ion and

consequently on the oxygen pressure. It has been reported that the adducts formed between tpps complexes of Mn (III) and Mn (II) and poly- $\beta$ -cyclodextrin have considerably different relaxivities depending on the redox state of the metal, itself determined by the partial oxygen pressure of the solution. This technique can quantify the oxygen concentration in the surrounding environment.<sup>106</sup>

More recently, DOTA-based complexes of Gd bearing a thiol moiety were synthesized, and they form reversible covalent linkages with HSA, which contains a reactive thiol at cysteine-34. This redox-sensitive reversible binding of Gd complexes to plasma albumin was exploited for imaging the tissue-redox state.<sup>107</sup>

### ***Metal ion and radical agents***

It is known that the presence of metal ions can induce changes in the structure of the paramagnetic complexes, consequently changing their relaxivities.<sup>47</sup> Considering the  $\text{Ca}^{2+}$ -sensitive MR imaging probes two different approaches have been attempted. The first approach uses Gd-complexes with a  $T_1$  response on interaction with  $\text{Ca}^{2+}$  ions, while the second approach uses a  $T_2$  agent based on the  $\text{Ca}^{2+}$ -related aggregation of superparamagnetic iron nanoparticles and calmodulin.<sup>108</sup> Although these strategies have several limitations, the main drawback of the second approach is the relatively long time course of the  $\text{Ca}^{2+}$ -dependent aggregation (a few seconds) that prevents the sensing of fast  $\text{Ca}^{2+}$ -concentration changes.

The design of all  $\text{Gd}^{3+}$ -based  $\text{Ca}^{2+}$  ion-sensitive probes reported so far involved changes in the coordination sphere of the  $\text{Gd}^{3+}$  ion following coordination of  $\text{Ca}^{2+}$ . These probes integrate 2 coordinating units that selectively chelate  $\text{Gd}^{3+}$  and  $\text{Ca}^{2+}$  ions. In the absence of the sensed  $\text{Ca}^{2+}$  ion, one or more of the donor groups of the  $\text{Ca}^{2+}$  chelating centre, are weakly coordinated to the  $\text{Gd}^{3+}$  ion. Concerning the interaction with  $\text{Ca}^{2+}$ , this donor group switches from  $\text{Gd}^{3+}$  to  $\text{Ca}^{2+}$  coordination, consequently liberating one coordination position on the  $\text{Gd}^{3+}$  ion. This free coordination position is immediately occupied by a water molecule increasing the hydration number and the relaxivity. The work of Li et al.<sup>109</sup> is an example of this type of agents utilizing this approach.

$\text{Zn}^{2+}$  is the second most abundant transition metal ion in the body and its highest concentrations occur in the brain. Hanaoka et al.<sup>110</sup> used a ligand of DTPA with N,N,N',N'-tetrakis (2-pyridylmethyl)ethylenediamine (TREN) as a zinc specific chelator. In the absence of zinc, water is bound to the gadolinium ion. In the presence of zinc, the

carboxylic acid and pyridine moieties coordinate to zinc thus restricting the access of water to the  $Gd^{3+}$ , thereby decreasing the hydration number and respective relaxivity in the presence of zinc.<sup>47</sup>

Iron is the most abundant transition metal in the body and in the brain. Biologic iron is most commonly found in the +2 (ferrous) and +3 (ferric) oxidation states. Aime et al.<sup>111</sup> synthesized an iron-sensitive contrast agent by functionalizing DTPA with salicylate moieties. In the presence of  $Fe^{3+}$  the Gd-DTPA–salicylate complexes bind to the iron ions via the salicylate functional groups. The relaxivity increases as this binding yields an increase in  $\tau_R$ . Recently another high-molecular weight tetrametallic supramolecular complex  $[(Ln-DTPA-phen)_3Fe]^-$  (Ln=Gd, Eu, La) has been obtained upon self-assembly around one of the three iron(II) ions 1,10-phenantroline- based molecules substituted in 5'-position with the polyaminocarboxylate diethylenetriamine- N,N,N',N',N'-pentaacetate, DTPA- phen<sup>4-112</sup>.

There are reports of radical responsive CAs, consisting of  $Gd^{3+}$  chelates containing a free thiol group (Gd-HASH-DO3A) conjugated through a disulfide bond formed with SH-activated phospholipid molecules incorporated in a liposome. The long reorientational motion of the supramolecular adduct ensures a  $r_1$  relaxivity much larger than that of the free complex.<sup>47</sup> The disulfide bonds represent a radical sensitive moiety and a large decrease in the relaxivity is observed upon their cleavage.<sup>113</sup>

### 2.3.2.5. CONTRAST AGENTS BASED ON OTHER PROPERTIES

New classes of MRI CAs have recently been developed, which do not fit into the classification mentioned above. These CAs are based on their NMR properties and can be grouped into two families, chemical exchange saturation transfer agents (CEST)<sup>114</sup> and hyperpolarized agents.

#### ***Chemical exchange saturation transfer agents (CEST)***

Basically a CEST agent is a molecule possessing exchangeable protons (-NH, -OH, etc.) that resonate at a chemical shift different from that of the bulk water signal,

measurable when their exchange with the bulk water protons is slow on the NMR timescale. This occurs when the difference in frequency between those chemical environments ( $\Delta\omega$ ) is higher than the exchange rate of the process ( $k_{ex}$ ). When this condition is fulfilled the resonance of the CEST mobile protons may be selectively saturated using a specific radio frequency  $B_1$ . These protons will then transfer into the bulk water pool and lead to a reduction of its equilibrium magnetization, resulting in a decrease of its signal intensity. Consequently this water saturation process is caused by chemical exchange (see Figure 2.16). CEST agents can be used to switch the image contrast 'on' and 'off' just by changing the irradiation parameters.<sup>47</sup>

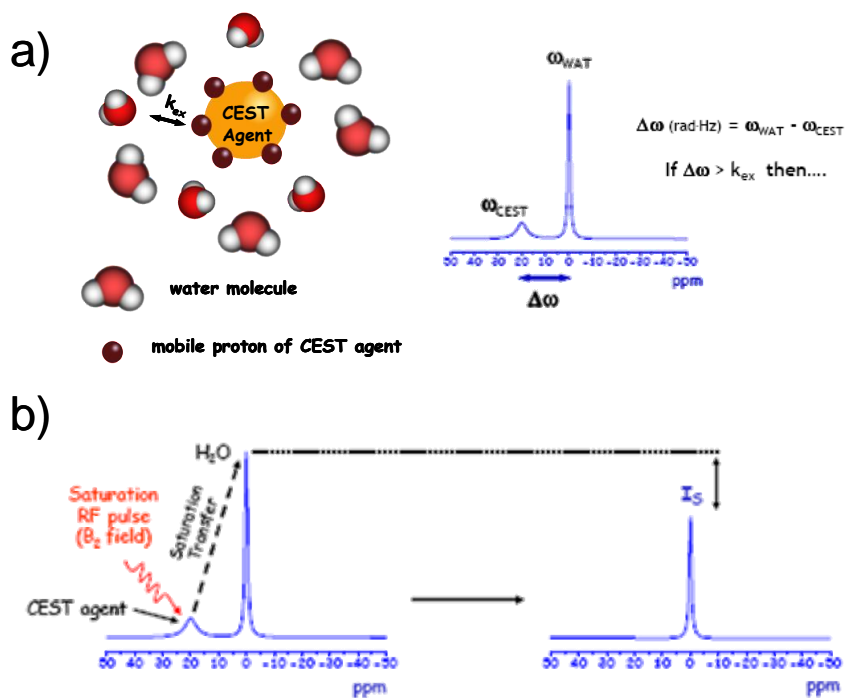


**Figure 2.16.** a) CEST agent illustration b) Schematics of the chemical exchange saturation transfer (CEST) method using molecular separation of encoding and detection for significant signal amplification. The resonance of the detection molecule at high concentration (in this case, water) is observed after off-resonance saturation (left spectrum) and after on-resonance saturation (right spectrum) of a highly diluted CEST agent.

Several agents contain exchangeable protons and consequently can generate CEST contrast.<sup>115</sup> Their signals are often very close to the bulk water signal, and broader than 2 ppm, due to the magnetic field inhomogeneity of many tissues.<sup>116</sup> Within these conditions it is difficult to distinguish contrast due to the CEST effect and the direct saturation of bulk water. Large  $\Delta\omega$  values improve the specificity of the CEST and, as  $\Delta\omega$  increases with the magnetic field strength, the overall relationship between  $\Delta\omega$  and  $k_{ex}$  will be a function of the field strength of the MR experiment.<sup>47</sup>

Since the attainable saturation transfer (ST) value is directly related to  $k_{ex}$ , it is expected that paramagnetic complexes will display large  $\Delta\omega$  values for the exchanging proton resonance and thus may improve the efficacy of the CEST agents. These agents are called *PARACEST agents* and consist of particular  $\text{Ln}^{3+}$  complexes with a coordinated water molecule undergoing extremely slow exchange with the bulk water and with very large  $\Delta\omega$  values. A good ST effect was reported by Zhang *et al.*<sup>117</sup> by irradiating the metal-bound water protons of  $\text{Eu}^{3+}$  chelates resonating at 50 ppm downfield from the bulk water. The very same effect can be obtained with slow exchanging amide protons of  $\text{Ln}^{3+}$  complexes of DOTA derivatives.<sup>118</sup> Recent reports show that paramagnetic  $\text{Ln}^{3+}$  complexes of tetraamide derivatives of DOTA have ST properties which are markedly dependent on pH and lactate concentration, making them responsive CAs.<sup>119,120,121</sup>

The main advantage of CEST agents relatively to the traditional MRI CAs is that the generation of contrast only occurs when the RF irradiation frequency is set to the same frequency as the absorption frequency of the mobile protons.<sup>49</sup> For this reason it is not necessary to register an image before the administration of the CEST agent, as the image visualization of CEST agents results from the comparison of the on and off resonance MRI scan. Co-administration of different CEST agents is also possible as the difference within the resonance frequencies of their mobile protons is large enough to avoid the overlapping of the respective CEST resonances. The detection of their biodistribution is possible and observable within the same image.<sup>122</sup>

The most critical disadvantage of CEST agents is their low sensitivity. Theoretically, the ST process is dominated by several parameters, among which  $k_{ex}$  and the number of mobile protons available are particularly relevant.<sup>47</sup> In the case of small sized CEST agents, containing less than 10 mobile protons per molecule, such as amino acids, heterocyclic compounds, sugars or paramagnetic chelates, they have a detection limit in the range of mM.<sup>114,119,123,124</sup> Several approaches to solve this problem were suggested.<sup>114,125-127</sup>

### ***Hyperpolarized agents and molecular imaging using MRI.***

Undoubtedly MRI provides incomparable soft tissue contrast, however its low sensitivity has limited the clinical use to the imaging of water protons. A radically new magnetic resonance imaging (MRI) technique, using hyperpolarized  $^3\text{He}$ ,  $^{129}\text{Xe}$ ,  $^{13}\text{C}$ ,  $^{15}\text{N}$  and  $^6\text{Li}$  is being developed to produce high-contrast images of important body tissues that have resisted conventional MRI techniques. A totally different approach for increasing the polarization of spins is to create an artificial, non-equilibrium distribution of nuclear spins called the hyperpolarized state<sup>49</sup>. A hyperpolarized state is defined as a state in which the nuclear spin populations are altered with respect to the equilibrium value described by the Boltzmann equation. Since the signal intensity is proportional to the spin population's difference, hyperpolarization leads to an increase in the NMR signal intensity by a factor as high as  $10^5$ .<sup>48</sup> Hyperpolarization can improve the detection of  $^3\text{He}$  and  $^{129}\text{Xe}$  by up to a hundred thousand times. This technology is showing dramatic results for diagnostic imaging of the lungs, brain, and other parts of the body.<sup>49</sup> A wide range of organic substances containing  $^{13}\text{C}$  has been hyperpolarized by either parahydrogen-induced polarization (PHIP)<sup>129</sup> or by dynamic nuclear polarization (DNP).<sup>130</sup> The potential applications of hyperpolarized  $^{13}\text{C}$  imaging include vascular imaging, perfusion imaging<sup>131</sup>, catheter tracking<sup>132</sup> and visualization and metabolic/molecular imaging.<sup>133</sup>

## 2.4. REFERENCES

---

- 1 Damadian, R., Tumor Detection by Nuclear Magnetic Resonance. *Science* **1971**, 171 (3976), 1151-1153.
- 2 Lauterbur, P. C., Image Formation by Induced Local Interactions: Examples Employing Nuclear Magnetic Resonance. *Nature* **1973**, 242 (5394), 190-191.
- 3 [http://users.fmrib.ox.ac.uk/~stuart/thesis/chapter\\_2/image270.gif](http://users.fmrib.ox.ac.uk/~stuart/thesis/chapter_2/image270.gif)
- 4 <http://www.cardiff.ac.uk/biosi/researchsites/emric/basics.html>
- 5 Berry, C. C.; Curtis, A. S. G., Functionalisation of magnetic nanoparticles for applications in biomedicine. *Journal of Physics D-Applied Physics* **2003**, 36 (13), R198-R206.
- 6 Mansson S, Bjørnerud A., Physical principles of medical imaging by nuclear magnetic resonance. In *The Chemistry of Contrast Agents in Medical Magnetic Resonance Imaging*, Merbach AE, Toth E (eds). *Wiley: Chichester*, **2001**; 1–44.
- 7 Alexander, H., An introduction to the basics of Magnetic Resonance. *Siemens AG Medical Solutions Magnetic Resonance* **2003**, 1-238.
- 8 [http://upload.wikimedia.org/wikipedia/commons/thumb/8/85/Bluthirnschranke\\_nach\\_Infarkt\\_nativ\\_und\\_KM.png/300px](http://upload.wikimedia.org/wikipedia/commons/thumb/8/85/Bluthirnschranke_nach_Infarkt_nativ_und_KM.png/300px) [Bluthirnschranke nach Infarkt nativ und KM.png](http://upload.wikimedia.org/wikipedia/commons/thumb/8/85/Bluthirnschranke_nach_Infarkt_nativ_und_KM.png)
- 9 Bloch, F.; Hansen, W. W.; Packard, M., The Nuclear Induction Experiment *Physical Review* **1946**, 70 (7-8), 474-485.
- 10 Lauterbur, P. C., Mendoca-Dias, M. H., and Rudin, A. M. in *Frontiers of Biological Energetics*, Dutton, P. L., Leigh, L. S., and Scarpa, A (Eds), Academic Press, New York, **1978**, p.752.
- 11 Lauffer, R. B., Paramagnetic Metal-complexes as Water Proton Relaxation Agents for NMR Imaging - Theory and Design. *Chemical Reviews* **1987**, 87 (5), 901-927.
- 12 Aime, S.; Botta, M.; Fasano, M.; Terreno, E., Lanthanide(III) chelates for NMR biomedical applications. *Chemical Society Reviews* **1998**, 27 (1), 19-29.
- 13 Aime, S.; Botta, M.; Terreno, E., Gd(III)-based contrast agents for MRI. *Advances in Inorganic Chemistry - Including Bioinorganic Studies, Vol 57* **2005**, 57, 173-237.
- 14 Caravan, P.; Ellison, J. J.; McMurry, T. J.; Lauffer, R. B., Gadolinium(III) chelates as MRI contrast agents: Structure, dynamics, and applications. *Chemical Reviews* **1999**, 99 (9), 2293-2352.
- 15 Aime, S.; Botta, M.; Fasano, M.; Terreno, E., Prototropic and water-exchange processes in aqueous solutions of Gd(III) chelates. *Accounts of Chemical Research* **1999**, 32 (11), 941-949.
- 16 Toth, E.; Burai, L.; Merbach, A. E., Similarities and differences between the isoelectronic Gd-III and Eu-II complexes with regard to MRI contrast agent applications. *Coordination Chemistry Reviews* **2001**, 216, 363-382.
- 17 Jacques, V.; Desreux, J. F., New classes of MRI contrast agents. In *Contrast Agents I: Magnetic Resonance Imaging*, Krause, W., Ed. 2002; Vol. 221, pp 123-164.

- 18 Mansson, S.; Bjørnerud, A., Physical principles of medical imaging by nuclear magnetic resonance. In *The Chemistry of Contrast Agents in Medical Magnetic Resonance Imaging*, Merbach AE, Toth E (eds). Wiley: Chichester **2001**.
- 19 Bloembergen, N.; Purcell, E. M.; Pound, R. V., Relaxation Effects in Nuclear Magnetic Resonance Absorption. *Physical Review* **1948**, 73 (7), 679-712.
- 20 Solomon, I., Relaxation Processes in a System of 2 Spins. *Physical Review* **1955**, 99 (2), 559-565.
- 21 Bloembergen, N.; Morgan, L. O., Proton Relaxation Times in Paramagnetic Solutions. Effects of Electron Spin Relaxation. *Journal of Chemical Physics* **1961**, 34 (3), 842-850.
- 22 Bloembergen, N., Proton Relaxation Times in Paramagnetic Solutions. *Journal of Chemical Physics* **1957**, 27 (2), 595-596.
- 23 Connick, R. E. and Fiat, D. Oxygen-17 Nuclear Magnetic Resonance Study of the Hydration Shell of Nickelous Ion, *J. Chem. Phys.*, **1966**, 44, 4103 – 4107.
- 24 Toth, E.; Helm, L.; Merbach, A. E. Contrast Agents I Magnetic Resonance Imaging: New Classes of MRI Contrast Agents: Relaxivity of MRI Contrast Agents, *Top.Curr.Chem.*, **2002**, 221, 61 - 101.
- 25 Botta, M., Second coordination sphere water molecules and relaxivity of gadolinium(III) complexes: Implications for MRI contrast agents. *European Journal of Inorganic Chemistry* **2000**, (3), 399-407.
- 26 Peters, J. A.; Huskens, J.; Raber, D. J., Lanthanide induced shifts and relaxation rate enhancements. *Progress in Nuclear Magnetic Resonance Spectroscopy* **1996**, 28, 283-350.
- 27 Gueron, M., Nuclear relaxation in macromolecules by paramagnetic ions: a novel mechanism. *Journal of Magnetic Resonance* **1975**, 19 (1), 58-66.
- 28 McLachlan, A. D., Line Widths of Electron Resonance Spectra in Solution. *Proceedings of the Royal Society of London Series a-Mathematical and Physical Sciences* **1964**, 280 (1380), 271-288.
- 29 Bertini, I.; Luchinat, C.; Aime, S., NMR of paramagnetic substances. *Coordination Chemistry Reviews* **1996**, 150, 1-28.
- 30 Powell, D. H.; Merbach, A. E.; Gonzalez, G.; Brücker, E.; Micskei, K.; Ottaviani, M. F.; Köhler, K.; Zelewsky, A. V.; Grinberg, O. Y.; Lebedev, Y. S., Magnetic-Field-Dependent Electronic Relaxation of Gd<sup>3+</sup> in Aqueous Solutions of the Complexes [Gd(H<sub>2</sub>O)<sub>8</sub>]<sup>3+</sup>, [Gd(propane-1,3-diamine-*N,N,N,N*-tetraacetate)(H<sub>2</sub>O)<sub>2</sub>]<sup>-</sup>, and [Gd(*N,N*-bis[(*N*-methylcarbonyl)methyl]-3-azapentane-1,5-diamine-3,*N,N*-triacetate)(H<sub>2</sub>O)] of interest in magnetic-resonance imaging, *Helv.Chim.Acta*, **1993**, 76, 2129 - 2146.
- 31 Rast, S.; Borel, A.; Helm, L.; Belorizky, E.; Fries, P. H.; Merbach, A. E., EPR spectroscopy of MRI-related Gd(III) complexes: Simultaneous analysis of multiple frequency and temperature spectra, including static and transient crystal field effects. *Journal of the American Chemical Society* **2001**, 123 (11), 2637-2644.

- 
- 32 Hwang, L. P.; Freed, J. H., Generalized Einstein relations for rotational and translational diffusion of molecules including spin. *Journal of Chemical Physics* **1975**, *63* (1), 118-130.
- 33 Freed, J. H., Dynamic effects of pair correlation functions on spin relaxation by translational diffusion in liquids. II. Finite jumps and independent T1 processes. *Journal of Chemical Physics* **1978**, *68* (9), 4034-4037.
- 34 Koenig, S. H.; Brown, R. D., Field-cycling relaxometry of protein solutions and tissue: Implications for MRI. *Progress in Nuclear Magnetic Resonance Spectroscopy* **1990**, *22*, 487-567.
- 35 Avecilla, F.; Peters, J. A.; Geraldes, C., X-ray crystal structure of a sodium salt of Gd(DOTP) (5-): Implications for its second-sphere relaxivity and the Na-23 NMR hyperfine shift effects of Tm(DOTP) (5-). *European Journal of Inorganic Chemistry* **2003**, (23), 4179-4186.
- 36 Laurent, S.; Forge, D.; Port, M.; Roch, A.; Robic, C.; Elst, L. V.; Muller, R. N., Magnetic iron oxide nanoparticles: Synthesis, stabilization, vectorization, physicochemical characterizations, and biological applications. *Chemical Reviews* **2008**, *108* (6), 2064-2110.
- 37 Gillis, P.; Koenig, S. H., Transverse relaxation of solvent protons induced by magnetized spheres: application to ferritin, erythrocytes and magnetite. *Magnetic Resonance in Medicine* **1987**, *5* (4), 323-345.
- 38 Koenig, S. H.; Kellar, K. E., Theory of 1/T1 and 1/T2 NMRD profiles of solutions of magnetic nanoparticles. *Magnetic Resonance in Medicine* **1995**, *34* (2), 227-233.
- 39 Roch, A.; Muller, R. N.; Gillis, P., Theory of proton relaxation induced by superparamagnetic particles. *Journal of Chemical Physics* **1999**, *110* (11), 5403-5411.
- 40 Koenig, S. H., Novel Derivation of Solomon-Blombergen-Morgan Equations - Application to Solvent Relaxation by Mn<sup>2+</sup> Protein Complexes. *Journal of Magnetic Resonance* **1978**, *31* (1), 1-10.
- 41 Geraldes, C.; Sherry, A. D.; Lazar, I.; Miseta, A.; Bogner, P.; Berenyi, E.; Sumegi, B.; Kiefer, G. E.; McMillan, K.; Maton, F.; Muller, R. N., Relaxometry, animal biodistribution, and magnetic resonance imaging studies of some new gadolinium (III) macrocyclic phosphinate and phosphonate monoester complexes. *Magnetic Resonance in Medicine* **1993**, *30* (6), 696-703.
- 42 Roch, A.; Muller, R. N.; Gillis, P., Water relaxation by SPM particles: Neglecting the magnetic anisotropy? A caveat. *Journal of Magnetic Resonance Imaging* **2001**, *14* (1), 94-96.
- 43 Roch, A.; Muller, R. N., Longitudinal Relaxation of Water Protons in Colloidal Suspensions of Superparamagnetic Crystals, *Proc. 11th Annu. Meet. Soc. Magn. Reson. Med.*, **1992**, *11*, 1447.

- 44 Ayant, Y.; Belorizly, E.; Alizon, J.; Gallice, Calculation of spectral density resulting from random translational movement with relaxation by magnetic dipolar interaction in liquids, *J. Phys A*, **1975**, 36, 991-1004.
- 45 Roch, A.; Gillis, P.; Ouakssim, A.; Muller, R. N., Proton magnetic relaxation in superparamagnetic aqueous colloids: a new tool for the investigation of ferrite crystal anisotropy. *Journal of Magnetism and Magnetic Materials* **1999**, 201, 77-79.
- 46 Muller, R. N.; Vander Elst, L.; Roch, A.; Peters, J. A.; Csajbok, E.; Gillis, P.; Gossuin, Y., Relaxation by metal-containing nanosystems. *Advances in Inorganic Chemistry - Including Bioinorganic Studies, Vol 57* **2005**, 57, 239-292.
- 47 Grealdes C. F. G. C., Laurent S., Classification and Basic properties of contrast agents for magnetic resonance imaging. *Contrast Media Mol. Imaging*, **2008**, 3, 1 – 23.
- 48 Yablonskiy, D. A.; Haacke, E. M., Theory of NMR signal behavior in magnetically inhomogeneous tissues. The static dephasing regime. *Magnetic Resonance in Medicine* **1994**, 32 (6), 749-763.
- 49 Aime, S.; Crich, S. G.; Gianolio, E.; Giovenzana, G. B.; Tei, L.; Terreno, E., High sensitivity lanthanide(III) based probes for MR-medical imaging. *Coordination Chemistry Reviews* **2006**, 250 (11-12), 1562-1579.
- 50 Vogl, T. J.; Hammerstingl, R.; Schwarz, W.; Mack, M. G.; Muller, P. K.; Pegios, W.; Keck, H.; EiblEibesfeldt, A.; Hoelzl, J.; Woessmer, B.; Bergman, C.; Felix, R., Superparamagnetic iron oxide-enhanced versus gadolinium-enhanced MR imaging for differential diagnosis of focal liver lesions. *Radiology* **1996**, 198 (3), 881-887.
- 51 Koenig, S. H.; Kellar, K. E., Theory of 1/T1 and 1/T2 NMRD profiles of solutions of magnetic nanoparticles. *Magnetic Resonance in Medicine* **1995**, 34 (2), 227-233.
- 52 Kellar, K. E.; Fujii, D. K.; Gunther, W. H. H.; Briley-Saebo, K.; Bjornerud, A.; Spiller, M.; Koenig, S. H., NC100150 injection, a preparation of optimized iron oxide nanoparticles for positive-contrast MR angiography. *Journal of Magnetic Resonance Imaging* **2000**, 11 (5), 488-494.
- 53 Ahlström K. H., Johansson L. O., Rodenburg J. B., Ragnarsson A. S., Akeson P, Börseth A., Pulmonary MR angiography with ultrasmall superparamagnetic iron oxide particles as a blood pool agent and a navigator echo for respiratory gating: pilot study., *Radiology*, **1999**, 211, 865 - 869.
- 54 Prasad P. V., Edelman R. R., Epstein F.H., Non-invasive evaluation of intra-renal oxygenation using BOLD MRI. *Circulation*, **1996**; 94, 3271 - 3275.
- 55 Van Wagoner M., Worah D., Gadodiamide injection. Non-invasive evaluation of intra-renal oxygenation using BOLD MRI. *Invest. Radiol.*, **1993**, 28, S44 - S48.
- 56 Oksendal, A. N.; Hals, P. A., Biodistribution and toxicity of MR imaging contrast media. *Jmri-Journal of Magnetic Resonance Imaging* **1993**, 3 (1), 157-165.

- 
- 57 Bellin, M. F.; Vasile, M.; Morel-Precetti, S., Currently used non-specific extracellular MR contrast media. *European Radiology* **2003**, *13* (12), 2688-2698.
- 58 Bellin, M.-F., MR contrast agents, the old and the new. *European Journal of Radiology* **2006**, *60* (3), 314-323.
- 59 Saeed, M.; Wendland, M. F.; Higgins, C. B., Blood pool MR contrast agents for cardiovascular imaging. *Journal of Magnetic Resonance Imaging* **2000**, *12* (6), 890-898.
- 60 Knopp, M. V.; von Tengg-Kobligk, H.; Floemer, F.; Schoenberg, S. O., Contrast agents for MRA: Future directions. *Journal of Magnetic Resonance Imaging* **1999**, *10* (3), 314-316.
- 61 Daldrup-Link, H. E.; Brasch, R. C., Macromolecular contrast agents for MR mammography: current status. *European Radiology* **2003**, *13* (2), 354-365.
- 62 Bogdanov A. A., Lewin M., Weissleder R., Approaches and agents for imaging the vascular system, *Adv. Drug Deliv. Rev.*, **1999**, *37*, 279 - 293.
- 63 Young S. W., Quing F., Harriman A., Sessler J. L., Dow W. C., Mody T. D., Hemmi G. W., Hao Y., Miller R. A., Gadolinium(III) texaphyrin: A tumor selective radiation sensitizer that is detectable by MRI. *Proc. Natl Acad. Sci. USA*. **1996**, *93*, 6610 - 6615.
- 64 Sipkins, D. A.; Cheresh, D. A.; Kazemi, M. R.; Nevin, L. M.; Bednarski, M. D.; Li, K. C. P., Detection of tumor angiogenesis in vivo by alpha(v)beta(3)-targeted magnetic resonance imaging. *Nature Medicine* **1998**, *4* (5), 623-626.
- 65 Winter, P. M.; Caruthers, S. D.; Kassner, A.; Harris, T. D.; Chinen, L. K.; Allen, J. S.; Lacy, E. K.; Zhang, H. Y.; Robertson, J. D.; Wickline, S. A.; Lanza, G. M., Molecular Imaging of angiogenesis in nascent vx-2 rabbit tumors using a novel alpha(v)beta(3)-targeted nanoparticle and 1.5 tesla magnetic resonance imaging. *Cancer Res* **2003**, *63* (18), 5838-5843.
- 66 Aime, S.; Cabella, C.; Colombatto, S.; Crich, S. G.; Gianolio, E.; Maggioni, F., Insights into the use of paramagnetic Gd(III) complexes in MR-molecular imaging investigations. *Journal of Magnetic Resonance Imaging* **2002**, *16* (4), 394-406.
- 67 Crich, S. G.; Biancone, L.; Cantaluppi, V.; Esposito, D. D. G.; Russo, S.; Camussi, G.; Aime, S., Improved route for the visualization of stem cells labeled with a Gd-/Eu-chelate as dual (MRI and fluorescence) agent. *Magnetic Resonance in Medicine* **2004**, *51* (5), 938-944.
- 68 Terreno, E.; Crich, S. G.; Belfiore, S.; Biancone, L.; Cabella, C.; Esposito, G.; Manazza, A. D.; Aime, S., Effect of the intracellular localization of a Gd-based imaging probe on the relaxation enhancement of water protons. *Magnetic Resonance in Medicine* **2006**, *55* (3), 491-497.
- 69 Heckl S., Pipkorn R., Waldeck W., Spring H., Jenne J., von der Lieth C. W., Corban-Wilhelm H., Debus J., Braun K., Intracellular visualization of prostate cancer using magnetic resonance imaging. *Cancer Res.*, **2003**, *63*, 4766 - 4772.

- 70 Schmitt-Willich H., Brehm M., Evers C. L. J., Michl G., Muller-Fahrnow A., Petrov O., Platzek J., Raduchel B., Sulzle D., Synthesis and physicochemical characterization of a new gadolinium chelate: the liver-specific magnetic resonance imaging contrast agent Gd–EOB–DTPA, *Inorg. Chem.*, **1999**, 38, 1134 - 1144.
- 71 Schuhmann-Giampieri G., Schmitt-Willich H., Press W. R., Negishi C., Weinmann H. J., Speck U., Preclinical evaluation of Gd–EOB–DTPA as a contrast agent in MR imaging of the hepatobiliary system. *Radiology*, **1992**, 183, 59 - 64.
- 72 Lim K., O., Stark D. D., Leese P. T., Pfefferbaum A., Rocklage S. M., Quay SC. Hepatobiliary MR imaging: first human experience with MnDPDP, *Radiology*, **1991**, 178, 79 - 82.
- 73 Reimer P., Rummeny E. J., Daldrup H. E., Balzer T., Tombach B., Berns T., Peters P. E., Clinical results with Resovist: a phase 2 clinical trial. *Radiology*, **1995**, 195, 489 - 496.
- 74 Hamm B., Thoeni R. F., Gould R. G., Bernardino M. E., Luning M., Saini S., Mahfouz A. E., Taupitz M., Wolf K. J., Focal liver lesions: characterization with nonenhanced and dynamic contrast material- enhanced MR imaging, *Radiology*, **1994**, 190, 417 - 423.
- 75 Misselwitz B., Platzek J., Radüchel B., Oellinger JJ, Weinmann H-J. Gadofluorine 8: initial experience with a new contrast medium for interstitial MR lymphography. *MAGMA*, **1999**, 8, 1352 - 8661.
- 76 Silva A .C., Lee J. H., Aoki I., Koretsky A. P., Manganese-enhanced magnetic resonance imaging (MEMRI): methodological and practical considerations. *NMR Biomed.*, **2004**, 17, 532 - 543.
- 77 Watanabe T., Tammer R., Boretius S., Frahm J., Michaelis T., Chromium( VI) as a novel MRI contrast agent for cerebral white matter-preliminary results in mouse brain in vivo, *Magn. Reson. Med.*, **2006**, 56, 1 - 6.
- 78 Poduslo J. F., Wengenack T. M., Curran G. L., Wisniewski T., Sigurdsson E.M., Macura S. I., Borowski B. J., Jack C. R., Molecular targeting of Alzheimer's amyloid plaques for contrast-enhanced magnetic resonance imaging. *Neurobiol. Dis.*, **2002**, 11, 315 - 329.
- 79 Wadghiri Y. Z., Sigurdsson E. M., Sadowski M., Elliott J. I., Li Y. S., Scholtzova H., Tang C. Y., Aguinaldo G., Pappolla M., Duff K., Wisniewski T., Turnbull D. H., Detection of Alzheimer's amyloid in transgenic mice using magnetic resonance microimaging, *Magn. Reson. Med.*, **2003**, 50, 293 - 302.
- 80 Rubin D. L., Falk K. L., Sperling M. J., Ross M., Saini S., Rothman B., Shellock F., Zerhouni E., Stark D., Outwater E. K., Schmiedl U., Kirby L. C., Chezmar J., Coates T., Chang M., Silverman J. M., Rofsky N., Burnett K., Engel J., Young S. W., A multicenter clinical trial of Gadolite Oral Suspension as a contrast agent for MRI. *J. Magn. Reson. Imag.*, **1997**, 7, 865 - 872.

- 
- 81 Lonnemark M., Hemmingsson A., Carlsten J., Ericsson A., Holtz E., Klaveness J., Superparamagnetic particles as an MRI contrast agent for the gastrointestinal tract, *Acta Radiol.*, **1988**, 29, 599 - 602.
- 82 Gillies R. J., Raghunand N., Karczmar G. S., Bhujwala Z. M., MRI of the tumor microenvironment. *J. Magn. Reson. Imaging*, **2002**, 16, 430 - 450.
- 83 Chesler M., Regulation and modulation of pH in the brain. *Physiol Rev.*, **2003**, 83, 1183 – 1221.
- 84 Kalman F. K., Woods M., Caravan P., Jurek P., Spiller M, Tircso G., Kiraly R., Brücher E., Sherry A. D., Potentiometric and relaxometric properties of a gadolinium-based MRI contrast agent for sensing tissue pH. *Inorg. Chem.*, **2007**; 46, 5260 - 5270.
- 85 Mikawa M, Miwa N, Brautigam M, Akaike T., Maruyama A., A pH-sensitive contrast agent for functional magnetic resonance imaging (MRI), *Chem Lett.*, **1998**, 7, 693 – 694
- 86 Aime S., Crich S. G., Botta M., Giovenzana G., Palmisano G., Sisti M., A macromolecular Gd(III) complex as pH-responsive relaxometric probe for MRI applications, *Chem Commun.*, **1999**, 1577 - 1578.
- 87 Lowe M. P., Parker D., Reany O., Aime S., Botta M., Castellano G., Gianolio E., Pagliarini R., pH-dependent modulation of relaxivity and luminescence in macrocyclic gadolinium and europium complexes based on reversible intramolecular sulfonamide ligation. *J. Am. Chem. Soc.*, **2001**, 123, 7601 - 7609.
- 88 Hovland R., Glogard C., Aasen A. J., Klaveness J., Gadolinium DO3A derivatives mimicking phospholipids; preparation and in vitro evaluation as pH responsive MRI contrast agents. *J. Chem. Soc. Perkin Trans 2*, **2001**, 6, 929 - 933.
- 89 Toth E., Bolskar R. D., Borel A., González G., Helm L., Merbach A. E., Sitharaman B., Wilson L. J., Water-soluble gadofullerenes: toward high-relaxivity, pH-responsive MRI contrast agents. *J. Am. Chem. Soc.* **2005**, 127, 799 - 805.
- 90 Zhang S., Wu K., Sherry A. D., A novel pH-sensitive MRI contrast agent, *Angew Chem Int Ed Engl.*, **1999**, 38, 3192 - 3194.
- 91 Raghunand N., Howison C., Sherry A. D., Zhang S., Gillies R. J., Renal and systemic pH imaging by contrast-enhanced MRI. *Magn Reson Med.*, **2003**, 49, 249 - 257.
- 92 Garcia-Martin, M. L.; Martinez, G. V.; Raghunand, N.; Sherry, A. D.; Zhang, S. R.; Gillies, R. J., High resolution pH(e) imaging of rat glioma using pH-dependent relaxivity. *Magnetic Resonance in Medicine* **2006**, 55 (2), 309-315.
- 93 Ali, M. M.; Woods, M.; Caravan, P.; Opina, A. C. L.; Spiller, M.; Fettingner, J. C.; Sherry, A. D., Synthesis and relaxometric studies of a dendrimer-based pH-responsive MRI contrast agent. *Chemistry-a European Journal* **2008**, 14 (24), 7250-7258.
- 94 Aime, S.; Botta, M.; Fasano, M.; Terreno, E.; Kinches, P.; Calabi, L.; Paleari, L., A new ytterbium chelate as contrast agent in chemical shift imaging and temperature sensitive probe for MR spectroscopy. *Magnetic Resonance in Medicine* **1996**, 35 (5), 648-651.

- 95 Zuo, C. S.; Mahmood, A.; Sherry, A. D., TmDOTA(-): A sensitive probe for MR thermometry in vivo. *Journal of Magnetic Resonance* **2001**, *151* (1), 101-106.
- 96 Fosshem, S. L.; Il'yasov, K. A.; Hennig, J.; Bjornerud, A., Thermosensitive paramagnetic liposomes for temperature control during MR imaging-guided hyperthermia: In vitro feasibility studies. *Acad Radiol* **2000**, *7* (12), 1107-1115.
- 97 Louie, A. Y.; Huber, M. M.; Ahrens, E. T.; Rothbacher, U.; Moats, R.; Jacobs, R. E.; Fraser, S. E.; Meade, T. J., In vivo visualization of gene expression using magnetic resonance imaging. *Nature Biotechnology* **2000**, *18* (3), 321-325.
- Louie, A. Y.; Huber, M. M.; Ahrens, E. T.; Rothbacher, U.; Moats, R.; Jacobs, R. E.; Fraser, S. E.; Meade, T. J., In vivo visualization of gene expression using magnetic resonance imaging. *Nature Biotechnology* **2000**, *18* (3), 321-325.
- 98 Moats, R. A.; Fraser, S. E.; Meade, T. J., A "smart" magnetic resonance imaging agent that reports on specific enzymatic activity. *Angewandte Chemie-International Edition in English* **1997**, *36* (7), 726-728.
- 99 Nivorozhkin A. L., Kolodziej A. F., Caravan P., Greenfield M. T., Lauffer R. B., McMurry T. J., Enzyme-activated Gd(III) magnetic resonance imaging contrast agents with a prominent receptor-induced magnetization enhancement. *Angew Chem Int Ed Engl*, **2001**, *40*, 2903 – 2906.
- 100 Lauffer RB, McMurry TJ, Dunham SO, et al. Epix Medical Inc. Bioactivated diagnostic imaging contrast agents., *Patent publication number WO9736619*. 10 9, **1997**.
- 101 Anelli, P. L.; Bertini, I.; Fragai, M.; Lattuada, L.; Luchinat, C.; Parigi, G., Sulfonamide-functionalized gadolinium DTPA complexes as possible contrast agents for MRI: A relaxometric investigation. *European Journal of Inorganic Chemistry* **2000**, (4), 625-630.
- 102 Shiftan L, Israely T, Cohen M, Frydman V., Dafni H., Stern R., Neeman M., Magnetic resonance imaging visualization of hyaluronidase in ovarian carcinoma. *Cancer Res.*, **2005**, *65*, 10316 – 10323
- 103 Chen, J. W.; Pham, W.; Weissleder, R.; Bogdanov, A., Human myeloperoxidase: A potential target for molecular MR imaging in atherosclerosis. *Magnetic Resonance in Medicine* **2004**, *52* (5), 1021-1028.
- 104 Duimstra, J. A.; Femia, F. J.; Meade, T. J., A gadolinium chelate for detection of beta-glucuronidase: A self-immolative approach. *Journal of the American Chemical Society* **2005**, *127* (37), 12847-12855.
- 105 Matsumoto, H.; Inoue, N.; Takaoka, H.; Hata, K.; Shinke, T.; Yoshikawa, R.; Masai, H.; Watanabe, S.; Ozawa, T.; Yokoyama, M., Depletion of antioxidants is associated with no-reflow phenomenon in acute myocardial infarction. *Clinical Cardiology* **2004**, *27* (8), 466-470.

- 
- 106 Aime, S.; Botta, M.; Gianolio, E.; Terreno, E., A p(O-2)-responsive MRI contrast agent based on the redox switch of manganese(II/III) - Porphyrin complexes. *Angewandte Chemie-International Edition* **2000**, 39 (4), 747-750.
- 107 Raghunand, N.; Jagadish, B.; Trouard, T. P.; Galons, J. P.; Gillies, R. J.; Mash, E. A., Redox-sensitive contrast agents for MRI based on reversible binding of thiols to serum albumin. *Magnetic Resonance in Medicine* **2006**, 55 (6), 1272-1280.
- 108 Atanasijevic T, Shusteff M, Fam P, Jasanoff A., Calcium-sensitive MRI contrast agents based on superparamagnetic iron oxide nanoparticles and calmodulin, *Proc Natl Acad Sci U S A*, **2006**, 103, 14707 - 14712.
- 109 Li, W. H.; Fraser, S. E.; Meade, T. J., A calcium-sensitive magnetic resonance imaging contrast agent. *Journal of the American Chemical Society* **1999**, 121 (6), 1413-1414.
- 110 Hanaoka, K.; Kikuchi, K.; Urano, Y.; Narazaki, M.; Yokawa, T.; Sakamoto, S.; Yamaguchi, K.; Nagano, T., Design and synthesis of a novel magnetic resonance imaging contrast agent for selective sensing of zinc ion. *Chemistry & Biology* **2002**, 9 (9), 1027-1032.
- 111 Aime, S.; Botta, M.; Fasano, M.; Terreno, E., Paramagnetic Gd(III)-Fe(III) heterobimetallic complexes of DTPA-bis-salicylamide. *Spectrochimica Acta Part a-Molecular and Biomolecular Spectroscopy* **1993**, 49 (9), 1315-1322.
- 112 Parac-Vogt, T. N.; Elst, L. V.; Kimpe, K.; Laurent, S.; Burtea, C.; Chen, F.; Van Deun, R.; Ni, Y.; Muller, R. N.; Binnemans, K., Pharmacokinetic and in vivo evaluation of a self-assembled gadolinium(III)-iron(II) contrast agent with high relaxivity. *Contrast Media & Molecular Imaging* **2006**, 1 (6), 267-278.
- 113 Glogard, C.; Stensrud, G.; Aime, S., Novel radical-responsive MRI contrast agent based on paramagnetic liposomes. *Magnetic Resonance in Chemistry* **2003**, 41 (8), 585-588.
- 114 Ward, K. M.; Aletras, A. H.; Balaban, R. S., A new class of contrast agents for MRI based on proton chemical exchange dependent saturation transfer (CEST). *Journal of Magnetic Resonance* **2000**, 143 (1), 79-87.
- 115 Zhou, J. Y.; Wilson, D. A.; Sun, P. Z.; Klaus, J. A.; van Zijl, P. C. M., Quantitative description of proton exchange processes between water and endogenous and exogenous agents for WEX, CEST, and APT experiments. *Magnetic Resonance in Medicine* **2004**, 51 (5), 945-952.
- 116 Guivel-Scharen, V.; Sinnwell, T.; Wolff, S. D.; Balaban, R. S., Detection of proton chemical exchange between metabolites and water in biological tissues. *Journal of Magnetic Resonance* **1998**, 133 (1), 36-45.
- 117 Zhang, S. R.; Winter, P.; Wu, K. C.; Sherry, A. D., A novel europium(III)-based MRI contrast agent. *Journal of the American Chemical Society* **2001**, 123 (7), 1517-1518.
- 118 Zhang, S. R.; Merritt, M.; Woessner, D. E.; Lenkinski, R. E.; Sherry, A. D., PARACEST agents: Modulating MRI contrast via water proton exchange. *Accounts of Chemical Research* **2003**, 36 (10), 783-790.

- 119 Aime, S.; Delli Castelli, D.; Terreno, E., Novel pH-reporter MRI contrast agents. *Angewandte Chemie-International Edition* **2002**, *41* (22), 4334-4336.
- 120 Aime, S.; Barge, A.; Castelli, D. D.; Fedeli, F.; Mortillaro, A.; Nielsen, F. U.; Terreno, E., Paramagnetic lanthanide(III) complexes as pH-sensitive chemical exchange saturation transfer (CEST) contrast agents for MRI applications. *Magnetic Resonance in Medicine* **2002**, *47* (4), 639-648.
- 121 Zhang, S. R.; Michaudet, L.; Burgess, S.; Sherry, A. D., The amide protons of an ytterbium(III) dota tetraamide complex act as efficient antennae for transfer of magnetization to bulk water. *Angewandte Chemie-International Edition* **2002**, *41* (11), 1919-1921.
- 122 Aime S., Carrera C., Castelli D. D., Crich S. G., Terreno E., Tunable imaging of cells labeled with MRI-PARACEST agents. *Angew. Chem. Int. Edn Engl.*, **2005**; *44*, 1813 - 1815.
- 123 Aime, S.; Barge, A.; Castelli, D. D.; Fedeli, F.; Mortillaro, A.; Nielsen, F. U.; Terreno, E., Paramagnetic lanthanide(III) complexes as pH-sensitive chemical exchange saturation transfer (CEST) contrast agents for MRI applications. *Magnetic Resonance in Medicine* **2002**, *47* (4), 639-648.
- 124 Terreno, E.; Castelli, D. D.; Cravotto, G.; Milone, L.; Aime, S., Ln(III)-DOTAMGIY complexes: A versatile series to assess the determinants of the efficacy of paramagnetic chemical exchange saturation transfer agents for magnetic resonance imaging applications. *Investigative Radiology* **2004**, *39* (4), 235-243.
- 125 Goffeney, N.; Bulte, J. W. M.; Duyn, J.; Bryant, L. H.; van Zijl, P. C. M., Sensitive NMR detection of cationic-polymer-based gene delivery systems using saturation transfer via proton exchange. *Journal of the American Chemical Society* **2001**, *123* (35), 8628-8629.
- 126 Snoussi, K.; Bulte, J. W. M.; Gueron, M.; van Zijl, P. C. M., Sensitive CEST agents based on nucleic acid imino proton exchange: Detection of poly(rU) and of a dendrimer-poly(rU) model for nucleic acid delivery and pharmacology. *Magnetic Resonance in Medicine* **2003**, *49* (6), 998-1005.
- 127 Aime, S.; Castelli, D. D.; Terreno, E., Highly sensitive MRI chemical exchange saturation transfer agents using liposomes. *Angewandte Chemie-International Edition* **2005**, *44* (34), 5513-5515.
- 128 Winter, P. M.; Cai, K.; Chen, J.; Adair, C. R.; Kiefer, G. E.; Athey, P. S.; Gaffney, P. J.; Buff, C. E.; Robertson, J. D.; Caruthers, S. D.; Wickline, S. A.; Lanza, G. M., Targeted PARACEST nanoparticle contrast agent for the detection of fibrin. *Magnetic Resonance in Medicine* **2006**, *56* (6), 1384-1388.
- 129 Bowers, C. R.; Weitekamp, D. P., Para-Hydrogen and synthesis allow dramatically enhanced nuclear alignment. *Journal of the American Chemical Society* **1987**, *109* (18), 5541-5542.
- 130 Abragam A., *The Principles of Nuclear Magnetism*. Clarendon Press: Oxford, **1961**.

- 
- 131 Johansson, E.; Olsson, L. E.; Mansson, S.; Petersson, J. S.; Golman, K.; Stahlberg, F.; Wirestam, R., Perfusion assessment with bolus differentiation: A technique applicable to hyperpolarized tracers. *Magnetic Resonance in Medicine* **2004**, *52* (5), 1043-1051.
- 132 Magnusson, P.; Johansson, E.; Mansson, S.; Petersson, J. S.; Chai, C.-M.; Hansson, G.; Axelsson, O.; Golman, K., Passive catheter tracking during interventional MRI using hyperpolarized C-13. *Magnetic Resonance in Medicine* **2007**, *57* (6), 1140-1147.
- 133 Mansson, S.; Johansson, E.; Magnusson, P.; Chai, C. M.; Hansson, G.; Petersson, J. S.; Stahlberg, F.; Golman, K., C-13 imaging - a new diagnostic platform. *European Radiology* **2006**, *16* (1), 57-67.

# 3.

## *Fluorescence Imaging Background Concepts*

---

3.1. Optical Imaging	80
3.2. Luminescence	82
3.3. Tissue Optical Properties	91
3.4. Optical Imaging Technology	93
3.5. Optical Contrast Agents	95
3.6. References	102

### 3.1. OPTICAL IMAGING

Unlike any other imaging modality, optical imaging derives from the fact that it is possible to combine conventional display of tissue volumes using direct-optical, transillumination or tomographic techniques, with the capability of gaining information on molecular properties and function due to the high instrumental sensitivity for optical signals. Taking into account the various principles of optical imaging methods but not disregarding the limitation of penetration depth and spatial resolution in thick tissues, a number of potential applications are envisioned for clinical diagnostics. Over the past few years optical imaging techniques have joined the available methods for the assessment of tissue anatomy, physiology, metabolic and molecular function. This technology is attracting a lot of interest due to the fact that fluorescent dyes can be detected at low concentrations and non-ionizing, harmless radiation can be applied repeatedly to the patient. This technology has the additional advantage that it is less expensive (compared to other imaging techniques), small in size and, therefore, easily at hand to solve clinical problems. Table 3.1 summarizes the range of applications of optical imaging. The two leading imaging technologies are optical coherence tomography (OCT) and diffusion imaging.

Within this perspective the design of contrast agents for optical in vivo imaging of diseased tissues has gained a remarkable vitality.<sup>1,2</sup> Light is one of the most convenient vectors for transmitting signals that can easily reach regions of a complex molecular structure that are not accessible to other molecular messengers. When appropriate wavelengths are used, penetration depth may be substantial and light can reach regions of complex molecular structure which are not accessible to other molecular probes.

Sophisticated contrast agents have been synthesized and characterized for their capability to monitor disease-specific anatomic, physiological and molecular parameters through their optical signals.

**Table 3.1.** Major application areas of optical imaging.

<i>In vivo</i> optical imaging	<i>In vitro</i> diagnostics
<b>Non invasive clinical imaging</b>	
<ul style="list-style-type: none"> <li>• Tissue imaging</li> <li>• Microvascular</li> <li>• Ophthalmology</li> <li>• Dermatology</li> <li>• Brain</li> <li>• Breast</li> </ul>	
<b>Preclinical imaging</b>	
<ul style="list-style-type: none"> <li>• Pharmacokinetic</li> <li>• Drug-efficacy testing</li> </ul>	<ul style="list-style-type: none"> <li>• Genomics</li> <li>• Proteomics</li> <li>• Microarray readers</li> </ul>
<b>Patient monitoring</b>	
<ul style="list-style-type: none"> <li>• Biosensor implants</li> <li>• Pulse oximetry</li> </ul>	<ul style="list-style-type: none"> <li>• Biosensors</li> <li>• Pathogen detection</li> <li>• Point-of-care diagnostics</li> </ul>
<b>Intraoperative</b>	
<ul style="list-style-type: none"> <li>• Optical imaging</li> <li>• Cancer-cell detection</li> </ul>	

Semiconductor quantum dots (QDs) (e.g. CdSe nanocrystals with 2-10 nm diameter) and their bioconjugates are potential candidates as they are highly luminescent, tunable in the entire visible range and display a superior photostability compared to organic luminophores. This type of nanoparticles (NP) have been exploited for both *in vitro* analyses and *in vivo* imaging. Although there has been some reports regarding QDs with near-infrared (NIR) emission and with low toxicity. Therefore, their introduction into the biological and medical media has been still slow.<sup>3,4,5</sup> Alternately trivalent lanthanide ions,  $\text{Ln}^{3+}$ , present another option to organic luminescent stains in view of their singular properties. They enable easy spectral and time discrimination of their emission bands which span both the visible and NIR ranges.

The very first staining of biological cells with lanthanides dates back to 1969 by Scaff *et al.*<sup>6</sup> Bacterial smears (*Escherichia coli* cell walls) were treated with aqueous ethanolic solutions of europium chelate of 4, 4, 4-trifluoro-1-(2-thienyl)-

1,3-butanedione (thenoyltrifluoroacetate, TTA) and bright red spots appeared under mercury lamp illumination. Only in the mid-1970s that further attention was accorded to luminescent lanthanide bioprobes when Finnish researchers in Turku proposed  $\text{Eu}^{3+}$ ,  $\text{Sm}^{3+}$ ,  $\text{Tb}^{3+}$ , and  $\text{Dy}^{3+}$  polyaminocarboxylates and  $\beta$ -diketonates as luminescent sensors in time-resolved luminescent (TRL) immunoassays.<sup>7,8</sup> This technological push projected broader interest and subsequent developments. Examples of these developments can be found in homogeneous TRL assays,<sup>9</sup> optimization of bioconjugation methods for lanthanide luminescent chelates<sup>10</sup> and time-resolved luminescence microscopy (TRLM)<sup>11</sup> that resulted in applications of lanthanide luminescent bioprobes (LLBs)<sup>12,13</sup> in many fields of biology, biotechnology and medicine, including tissue<sup>14,15</sup> and cell imaging,<sup>16,17</sup> analyte sensing<sup>18</sup> and monitoring drug delivery.<sup>19</sup>

In order to design optical contrast agents it is necessary to first understand the concept of luminescence, the optical properties of tissues as well as comprehend the existing technology.

### 3.2. LUMINESCENCE

The term “Luminescence” was defined in 1888, by the German physicist Eilhardt Wiedemann, as the light emission characteristics not conditioned by an increase in temperature.<sup>20</sup> Within this thesis IUPAC rules<sup>21</sup> regarding molecular luminescence spectroscopy will be used, where the term “fluorescence” is used for processes which occur without change in spin. These are typically  $S_1 \rightarrow S_0$  (singlet to singlet ground state) or  ${}^2F_{5/2} \rightarrow {}^2F_{7/2}$  ( $\text{Yb}^{3+}$ ) transitions and “phosphorescence” for transitions implying a change in spin, most commonly  $T_1 \rightarrow S_0$  (triplet to singlet ground state) or  ${}^5D_0 \rightarrow {}^7F_J$  ( $\text{Eu}^{3+}$ ) transitions. The energy type used in the excitation of a luminescent material can be used to classify luminescent processes, as photoluminescence, when the excitation is by electromagnetic radiation; cathodoluminescence, when a beam of electrons is used; electroluminescence, when excitation is effected by an electric voltage; triboluminescence, when mechanical energy is the source of excitation; and chemiluminescence, when energy of a chemical reaction is employed.<sup>22</sup>

Not all materials exhibit the luminescence phenomenon even though their molecules can be excited to a higher state. This is due to the existence of a non-radiative pathway in

the return to the ground state (GS). This transition from a vibration energy level of an excited state to a vibration energy level of the GS is called internal conversion. The population of an excited state and the energy difference between the GS and excited states are among the important factors that affect the luminescence of a material. Figure 3.1 illustrates some of the typical processes involved in luminescence. The emission quantum yield indicates the efficiency of the luminescent material and will be defined in the next section.<sup>23</sup>

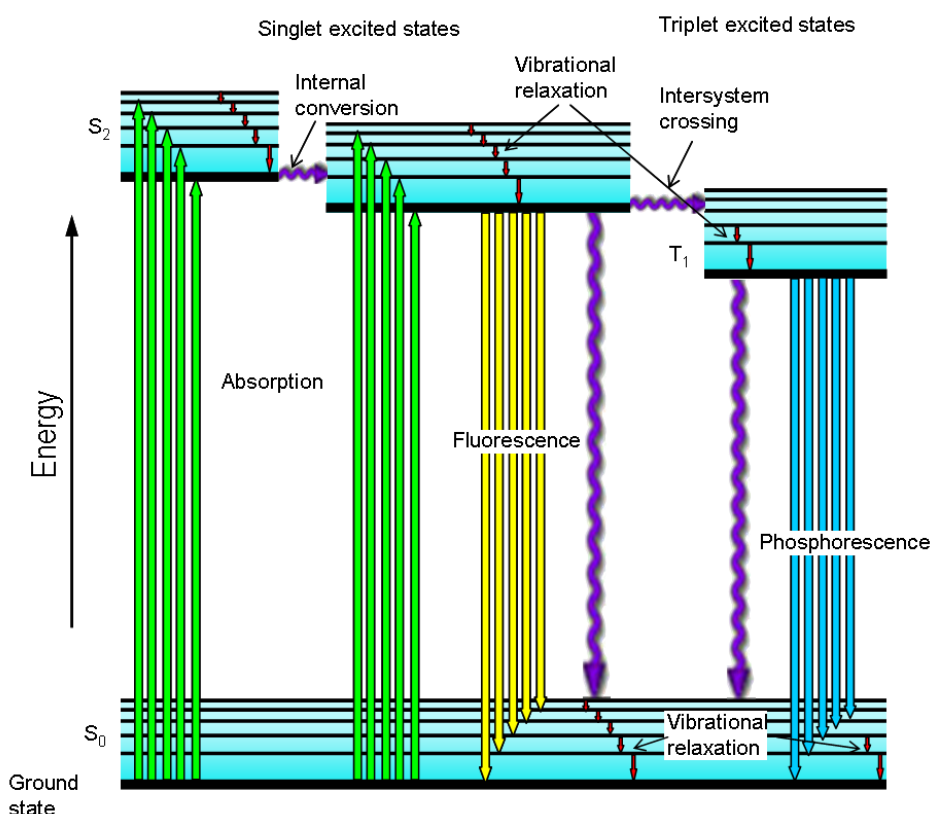


**Figure 3.1.** Partial energy-level diagram for a photoluminescent system.<sup>24</sup>

## LANTHANIDE LUMINESCENCE

The complex optical properties of the trivalent lanthanide ions, Ln<sup>3+</sup>, derives from special features of the electronic [Xe] 4f<sup>N</sup> configuration (N=0-14). The third ionization state is characterized (with the exception of lutetium, cerium and gadolinium) by the

removal of two electrons from the 6s orbital and one from the 4f orbital. Lanthanides (Ce–Lu) are unique among the elements (with the exception of the actinides) in markedly resembling each other in their chemical properties, particularly regarding oxidation states, due to their electronic configuration.<sup>25,26</sup>

These configurations generate a large variety of energy levels. Figure 3.2 displays partial energy diagrams for the lanthanide aquo ions.<sup>21</sup>  $\text{Eu}^{3+}$ ,  $\text{Gd}^{3+}$ , and  $\text{Tb}^{3+}$  are the best ions with respect to the energy gap requirement (as larger is that energy gap higher is the probability of radiative transitions) as they present a larger band gaps when compared to other trivalent lanthanides with  $\Delta E = 12\,300$  ( ${}^5D_0 \rightarrow {}^7F_6$ ),  $32\,200$  ( ${}^6P_{7/2} \rightarrow {}^8S_{7/2}$ ) and  $14\,800$  ( ${}^5D_4 \rightarrow {}^7F_0$ ),  $\text{cm}^{-1}$ , respectively.  $\text{Gd}^{3+}$  emits in the UV and it is not very useful as a luminescent probe since its luminescence interferes with either the emission or absorption processes in the organic part of the complex molecules.<sup>23</sup> The Russel-Saunders spin-orbit coupling scheme\* is normally used to characterize these energy levels, that is based on three quantum numbers,  $S$ ,  $L$  and  $J$ . It should be noted that this scheme does not characterize completely the energy levels, nevertheless, it is the commonly used.<sup>27</sup> The 4f electrons are not the outermost ones and they are “shielded” from external fields by the two electronic orbitals  $5s^2$  and  $5p^6$  with larger radial extension. Thus 4f electrons are only weakly perturbed by surrounding ligands charges resulting in special spectroscopic properties with parity-forbidden  $4f - 4f$  absorptions that have characteristic narrow-line emission (high purity). The emission occurs mostly in the visible and near-infrared (NIR) ranges and with very low molar absorption coefficients,  $\varepsilon$  (or absorption cross-sections,  $\sigma_{\text{ABS}}$ ). These are typically  $< 10 \text{ mol}^{-1} \text{ cm}^{-1}$  ( or  $\sigma_{\text{ABS}} < 4 \times 10^{-20} \text{ cm}^2$ ) when compared with

---

\* In this notation the orbital angular momenta of the individual electrons add up to form a resultant orbital angular momentum  $L$ . Within the same strategy the individual spin angular momenta are presumed to couple to produce a resultant spin angular momentum  $S$ . Finally  $L$  and  $S$  combine scattering events and form the total angular momentum  $J$ . In Russel-Saunders coupling scheme, the terms  $J$  and  $S$  define one of the  $(2S + 1)(2L + 1)$  terms (or multiplets) of the configuration, generic represented by  $({}^{2S+1})L_J$ , where  $(2S + 1)$  indicates the spin multiplicity.

$$J = \begin{cases} |S + L|, \dots, S - L \Leftarrow S > L \\ L + S, \dots, L - S \Leftarrow S \leq L \end{cases} \quad (3.1)$$

the molar absorption coefficient for  $3d - 3d$  transitions values that are 10 times higher, or for ligand-to-metal charge-transfer (LMCT) transitions that are 100 times higher.<sup>28</sup>

These transitions are formally parity-forbidden, the lifetimes of the excited states are long, which allows the use of time-resolved detection, a definitive asset for bioassays,<sup>29-34</sup> and luminescence microscopy.<sup>11,35,36</sup>

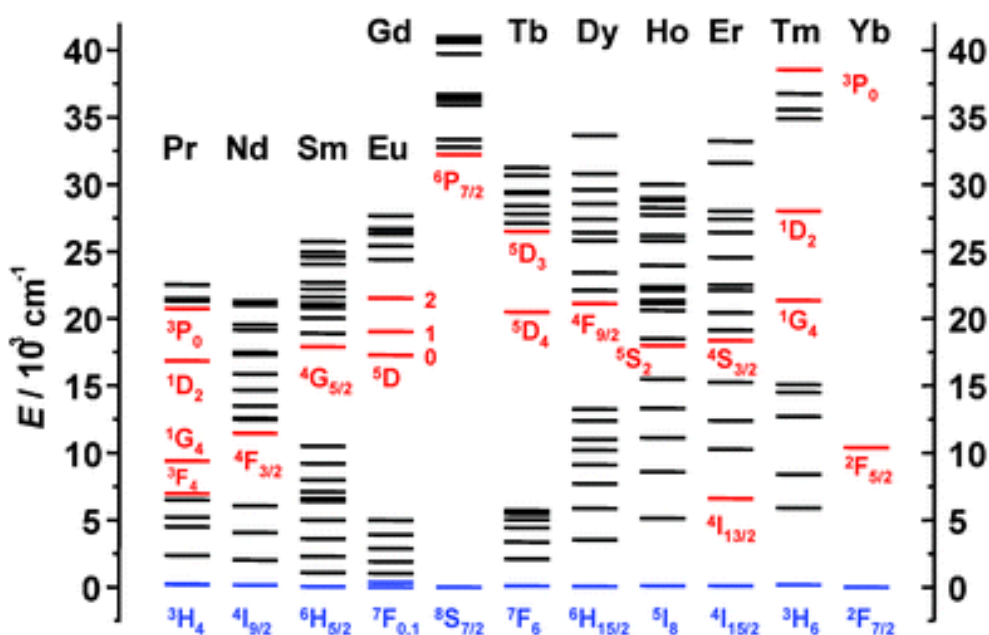


**Figure 3.2.** Partial energy diagrams for the lanthanide aquo ions. The main luminescent levels are drawn in red, while the fundamental level is indicated in blue.<sup>23</sup>

The direct  $\text{Ln}^{3+}$  photoexcitation is not very efficient as already mentioned. The design of lanthanide complexes, in which the ligands incorporate organic chromophores strongly bonded to the  $4f$  metal center, improves significantly the  $\text{Ln}^{3+}$  luminescence intensity. Weissman demonstrated in 1942 that the excitation of lanthanide complexes into the ligand states result in metal-centered luminescence. Part of the energy absorbed by the organic receptor(s) is transferred onto  $\text{Ln}^{3+}$  excited states and sharp emission bands originating from the metal ion are detected after rapid internal conversion to the emitting level. These chromophores typically present effective absorption cross-sections  $10^4$ – $10^5$

times higher and over a much broader spectral range than the  $\text{Ln}^{3+}$  corresponding ones. The phenomenon is termed sensitization of the metal-centered luminescence (also referred to as “antenna effect”) and is quite complex.<sup>37</sup>

When the  $\text{Ln}^{3+}$  ions are introduced into a host, the ion experiences an inhomogeneous electrostatic field, the so-called crystal field, which is produced by the  $\text{Ln}^{3+}$  ligands. In addition to the splitting of the energy of the  $4f$  orbital by spin-orbit coupling, individual  $J$  levels of a lanthanide ion are split further by the crystal field into a maximum of  $2J+1$  components, depending on the local symmetry of the  $\text{Ln}^{3+}$  ion, making the lanthanide emissions extremely sensitive to their environments. Figure 3.3 displays a schematic representation and order of magnitude of the effects of the intra-atomic and ligand field interactions acting on the  $4f^N$  configuration, in particular of the  $\text{Eu}^{3+}$  ion.

The  $4f-4f$  transitions have essentially electric-dipole (ED) and magnetic dipole (MD) character. ED transitions require a change of parity of the electron wavefunction and, then, they should be strictly forbidden within the  $4f$  configuration (due to the Laporte selection rule). Contrarily, MD transitions between those levels are permitted. For  $\text{Ln}^{3+}$  ions localised in crystalline sites without inversion symmetry, however, a mixing of opposite-parity states into the  $4f^N$  levels occur resulting in a relaxation of the Laporte selection rule and then in the observation of intra- $4f$  forced ED transitions.

Important parameters such as radiative lifetime values, emission quantum efficiency and quantum yield should be determined in order to adequately characterize an optical material. The concepts referred in this thesis are further described in *Carlos L.D et al.*<sup>28</sup> The radiative lifetime ( $\tau_{RAD}$ ) for a given  $f^N \psi' J'$  excited state is obtained as the reciprocal of the total transition radiative probability  $A_T$ , which is the sum of all possible radiative decay rates from the state  $J'$  towards lower levels  $J$ . The  $\tau_{RAD}$  is given by:<sup>28</sup>

$$\tau_{RAD} = \frac{1}{A_T} = \frac{1}{\sum_J A_{J'J}} \quad (3.2)$$

where  $A_{J'J}$ , the radiative transition probability, or Einstein’s spontaneous emission rate.

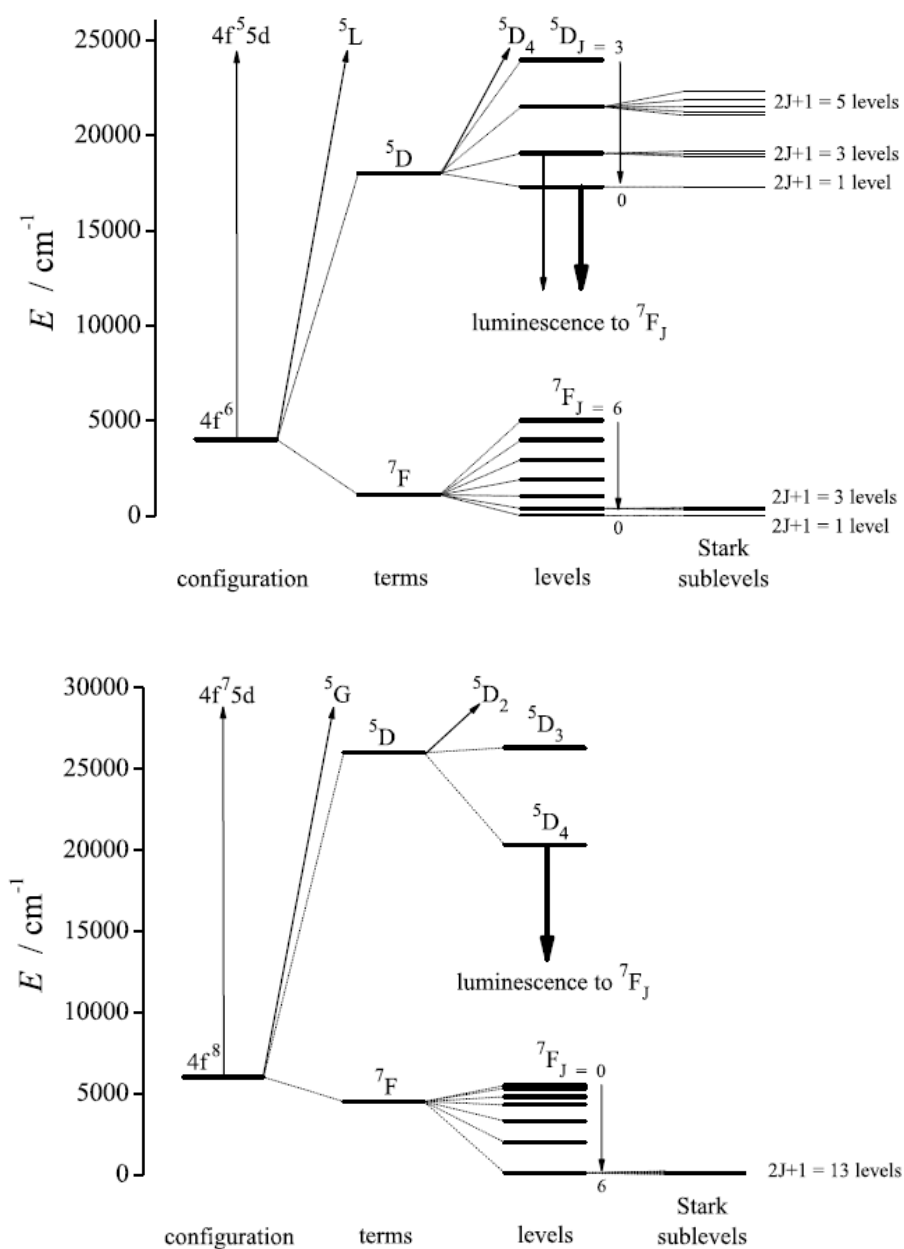


**Figure 3.3.** Schematic representation and order of magnitude of the effect of intra-atomic and ligand field interactions acting on the  $4f^N$  configuration of the  $\text{Eu}^{3+}$  (Top) and  $\text{Tb}^{3+}$  ions (Bottom).<sup>38</sup>

The emission quantum efficiency of a given excited level  $J'$  (also referred by some authors as intrinsic quantum yield<sup>39</sup>) is given by the ratio between the radiative decay rate and the total decay rate. This expression also includes all other processes contributing to the depopulation of level  $J'$ , such as nonradiative decay paths and energy-transfer processes.<sup>28</sup>

The emission quantum efficiency ( $\eta$ ) is calculated by:

$$\eta = \frac{\tau_{EXP}}{\tau_{RAD}} = \frac{A_{RAD}}{A_{RAD} + A_{NRAD}} \quad (3.3)$$

where the radiative lifetime described above and the experimental lifetime ( $\tau_{EXP} = \tau_{RAD} + \tau_{NRAD}$ ) are given by the reciprocal of the total decay rate.<sup>28</sup>

The emission quantum yield ( $\phi$ ) is an experimentally evaluated quantity given by the ratio of the number of photons emitted and the absorbed photons and can be described by:

$$\phi = \frac{\text{number of emitted photons}}{\text{number of absorbed photons}} \quad (3.4)$$

Typically, the emission quantum yield includes the absorption efficiency, the intersystem crossing efficiency, the donor–Ln<sup>3+</sup> energy-transfer efficiency, the intra-Ln<sup>3+</sup> nonradiative decay paths efficiency, , and the  $J'$ -level emission quantum efficiency  $\eta$ . According to equation 3.4 we can denote that  $\eta \geq \phi$ . If all the energy absorbed by the ligand excited states are transferred to the Ln<sup>3+</sup> excited levels.<sup>28</sup>

In the particular case of the Eu<sup>3+</sup> ions the intra-4*f* transitions generally occur between the  ${}^5D_0 \rightarrow {}^7F_J$  ( $J = 0 - 6$ ) levels. These transitions are essentially of the induced ED type, with the exception of the  ${}^5D_0 \rightarrow {}^7F_1$  transition that is a 100% MD transition. Attending to the pure MD character of the  ${}^5D_0 \rightarrow {}^7F_1$  transition it is possible to determine intensity parameters from the emission spectrum. Since this transition does not depend on the local ligand field seen by Eu<sup>3+</sup> it can become a reference for the entire spectrum. The  ${}^5D_0 \rightarrow {}^7F_1$  spontaneous decay rate,  $A_{01}$ , is given by  $A_{01} = A'_{01} n^3$ , where  $A'_{01} = 14.65 s^{-1}$  in

vacuum.<sup>40</sup> Within these parameters it is possible to express the intensity of the  ${}^5D_0 \rightarrow {}^7F_{0-6}$  transitions,  $I_{0J}$ , in terms of the area of their emission curves,  $S_{0J}$ :<sup>28</sup>

$$I_{0J} = hc\bar{\nu}A_{0J}N({}^5D_0) \equiv S_{0J} \quad (3.5)$$

where  $N({}^5D_0)$  is the population of the  ${}^5D_0$  emitting level; it is possible to express the total radiative decay rate as:<sup>28</sup>

$$A_T = \sum_{J=0}^6 A_{0J} = \frac{A_{0J}hc\nu_{01}}{S_{01}} \times \sum_{J=0}^6 \frac{S_{0J}}{hc\nu_{0J}} \quad (3.6)$$

It should be noted that the radiative contribution can be calculated from the relative intensities of the  ${}^5D_0 \rightarrow {}^7F_{0-4}$  transitions, as the branching ratio for the  ${}^5D_0 \rightarrow {}^7F_{5,6}$  transitions should be neglected due to their poor relative intensity. As already mentioned above, the emission quantum efficiency is defined by the ratio between experimental and radiative lifetimes. The intensity parameters  $\Omega_\lambda$  will be given by:<sup>28</sup>

$$\Omega_\lambda = \frac{3h}{64\pi^4 e^2 \bar{\nu}^3} \frac{9}{n(n^2 + 2)^2} \frac{1}{\left| \langle {}^5D_0 \| U^{(\lambda)} \| {}^7F_J \rangle \right|^2} A_{0J} \quad (3.7)$$

with  $\lambda = J = 2, 4, 6$ . Values for the squared reduced matrix elements are 0.0032 and 0.0023 for  $\lambda = J = 2$  and  $\lambda = J = 4$ , respectively.<sup>28,41</sup> As previously mentioned, the  ${}^5D_0 \rightarrow {}^7F_6$  transition has very low intensity making it very difficult for the determination of the rank 6 parameter.

The sensitivity of the  $4f$  transitions can be used to obtain further information about the metal ions local environment in addition to providing information on the light-emission properties of the  $\text{Ln}^{3+}$ -containing materials. In the case of the  $\text{Eu}^{3+}$  ion this important feature is even more prominent, since  $\text{Eu}^{3+}$  is a powerful local ion probe due to its peculiar spectroscopic characteristics. These characteristics include:<sup>28</sup>

- A large energy difference (gap) between the  ${}^5D_0$  first excited state and the high-energy  ${}^7F_6$  level of the fundamental septet (ca.  $12300\text{cm}^{-1}$ ). Given that for smaller gaps the desactivation through nonradiative process (e.g., O–H vibrations) is more likely to happen;
- A non-degenerated first excited state that allows a simpler Stark-effect analysis, with the subsequent correspondence between the observed J-splitting degeneracy and the  $\text{Eu}^{3+}$  local-site symmetry;
- The presence of the ligand-field-independent  ${}^5D_0 \rightarrow {}^7F_1$  magnetic-dipole transition, as discussed above;
- The presence of a single  ${}^5D_0 \rightarrow {}^7F_0$  line permitted for  $C_s, C_{1,2,3,4,6},$  and  $C_{2v,4v,6v}$  point symmetry groups with a predominantly electric-dipole nature, explained by *J*-mixing effects.<sup>42,43,44</sup> The energy of this non-degenerated transition can be directly related to the covalency of the chemical bonds of the first coordination shell in  $\text{Eu}^{3+}$  (the so called *nephelauxetic effect*);<sup>45</sup>
- The observation of vibronic lines in a relatively large spectral region of the  ${}^5D_0 \rightarrow {}^7F_2$  excitation transition ( $24400\text{--}21550\text{ cm}^{-1}$ ) allows the identification of vibration modes related to the  $\text{Ln}^{3+}$  local environment up to ca.  $3000\text{ cm}^{-1}$ ;
- The presence of ligand-to-metal charge-transfer (LMCT) in the UV-vis region of the excitation spectra assigned to particular ligand groups.

Important information about the metal-ion local coordination can be extracted from three distinctive parameters: *i*) the changes in the number of Stark components of each intra- $4f$  manifold and the variations of their relative intensity, *ii*) differences observed in the energy of particular lines, and *iii*) the analysis of the excited-state decay curves. Examples of the information extracted from these distinctive parameters are the existence of more than one  $\text{Eu}^{3+}$  local symmetry group, the number of coordinated water molecules, the magnitude of the ligand field, and the importance of the covalency of the  $\text{Eu}^{3+}$ -ligands bonds.<sup>28</sup>

The large values usually found for the full width at half maximum (fwhm) of the non-degenerated  ${}^5D_0 \rightarrow {}^7F_0$  line typically range from ca.  $20$  to  $30\text{ cm}^{-1}$ .<sup>46</sup> They indicate that the matrix where the  $\text{Eu}^{3+}$  ions are accommodated has a large distribution of similar local

sites. In the case where the  $\text{Eu}^{3+}$  local symmetry group does not present an inversion centre, the Laporte's rule is relaxed due to odd parity terms in the ligand field Hamiltonian,<sup>38</sup> and the emission spectrum will be dominated by the  ${}^5D_0 \rightarrow {}^7F_2$  transition. For  $\text{Eu}^{3+}$ -containing materials the number of water molecules ( $n_w$ ) in the first coordination shell may be obtained by the difference between the decay time values measured in  $\text{H}_2\text{O}$  and  $\text{D}_2\text{O}$  as:<sup>28</sup>

$$n_w = 1.11 \left[ \frac{1}{\tau_{\text{H}_2\text{O}}} - \frac{1}{\tau_{\text{D}_2\text{O}}} - 0.31 \right] \quad (3.8)$$

where  $\tau_{\text{H}_2\text{O}}$  and  $\tau_{\text{D}_2\text{O}}$  are the decay times in milliseconds in water and in  $\text{D}_2\text{O}$ , respectively, taken in this latter case as the purely radiative decay. As mentioned above, the purely radiative decay may also be calculated through the experimental emission spectrum and therefore  $\tau_{\text{RAD}}$  can be used in Equation 3.8 substituting  $\tau_{\text{D}_2\text{O}}$ ; while the value obtained experimentally for the decay  $\tau_{\text{EXP}}$  is used to substitute  $\tau_{\text{H}_2\text{O}}$ . In conclusion  $n_w$  can be calculated for many different  $\text{Eu}^{3+}$ -containing material within different medias.

### 3.3. TISSUE OPTICAL PROPERTIES

The optical properties of tissues are characterized by the use of light within the ultraviolet (UV) and the near-infrared (NIR) spectral region. The interaction of photons with tissue is based on three processes: *i*) absorption of light, *ii*) scattering of light and *iii*) emission of fluorescence. Tissue optical properties can be characterized by using these parameters separately.<sup>47</sup> As the penetration depth of light in living tissue strongly depends on the wavelength used,<sup>48</sup> the correct wavelength range should be chosen (since the amount of absorption in tissue is a function of the wavelength). Normally, the extent of scattering in tissue decreases with increasing wavelength. For wavelengths below 600 nm, absorption dominates scattering resulting in a small penetration depth of hundredths of micrometers up to a few millimetres, so that only superficial assessment of tissues is possible in this spectral region.

When direct visual inspection or characterization is used through microscopic techniques high spatial resolution images of tissue structures is obtained. Some examples are the examination of tissue surfaces using optical fibres incorporated into endoscopes or laparoscopes, as well as of ocular diseases through ophthalmoscopes and the direct assessment of skin diseases or tissues during surgical procedures.<sup>43</sup>

Light absorption in tissue originates from oxy- and deoxyhemoglobin, other porphyrins, melanin and structures involved in cellular metabolism (such as NADH and flavins) as well as from several structural tissue components (such as collagen), elastin and lipo-pigments. Most of these compounds exhibit characteristic fluorescence spectra (tissue autofluorescence) throughout the visible (VIS) spectral region up to approximately 700 nm.<sup>49,50</sup> Fluorescence presented by these fluorescent markers provides additional information on tissue structure and pathophysiological states.<sup>49,51</sup> This tissue autofluorescence phenomenon has already been thoroughly exploited to extract spectral patterns which indicate diseased tissue areas, e.g. in lymph node characterization;<sup>52</sup> endoscopy of the gastrointestinal tract<sup>50,53,54</sup> or cardiovascular diagnosis.<sup>55</sup>

In order to image a large tissue volume light within the spectral range (700–900 nm) is necessary as the tissue absorption coefficient is relatively low (resulting in penetration depths up to a few centimetres (figure 3.3)).<sup>56</sup> It is also possible to identify inhomogeneities as they exhibit a difference in absorption or fluorescence when compared to bulk tissue.

Due to the scattering process photons do not follow straight paths when propagating through tissue and mathematical models of photon transport are needed to calculate the optical properties of tissue.<sup>43</sup> This process limits the spatial resolution of the obtained image, where morphological and structural tissue parameters are not accessible. Tissue absorption is mainly determined by oxyhaemoglobin, deoxyhaemoglobin and water, which exhibit a well defined absorption minimum in the NIR spectral region (figure 3.3) and provide information that can be utilized to quantitatively calculate important physiological parameters, such as blood concentration (total haemoglobin) and oxygenation (ratio oxy/deoxy haemoglobin).<sup>57</sup> The absorption data, together with tissue-dependent scattering properties, can be fitted by mathematical models to reconstruct the most probable photon propagation throughout the tissue in order to generate a spatial map of tissue optical properties for a given illumination and detection geometry. This method has predominantly

been applied in the detection of breast tumours and imaging brain functions. Photon migration and diffuse light imaging are comprehensively described in reference.<sup>58</sup>

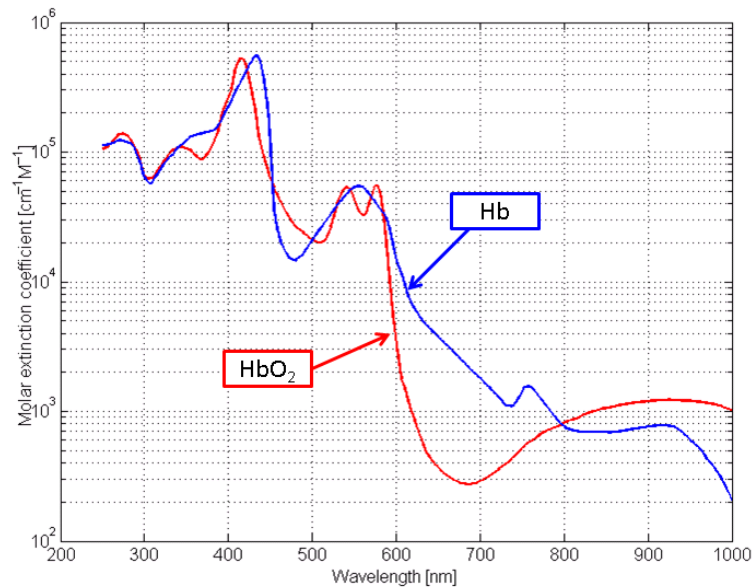


**Figure 3.3.** Absorption coefficients of oxyhemoglobin and deoxyhemoglobin as a function of wavelength. The near-infrared window of tissue is defined as the spectral region between approximately 700-900 nm, where the absorption coefficients are at minimal levels.<sup>59</sup>

### 3.4. OPTICAL IMAGING TECHNOLOGY

Over the past decade different types of optical imaging techniques have been developed for biomedical applications. These include various microscopy methods such as confocal microscopy, two-photon microscopy and coherent anti-Stokes Raman scattering (CARS) microscopy for *in vitro* and *ex vivo* applications as well as several methods for *in vivo* applications such as bioluminescence imaging, fluorescence imaging, diffused optical tomography and optical coherence tomography.<sup>43</sup> Several of these techniques can be used in combination, either simultaneously or sequentially, to provide complementary information from the same cells, tissues, organs or animals.<sup>60,61</sup>

Both bioluminescence and fluorescence imaging techniques have found wide applications for *in vivo* tumor optical imaging in mouse models, providing a non-invasive method with high resolution and a convenient real-time, high frequency visualization and

measurement of tumor biomarkers. The detection of disease progression and therapeutic response in the same animals is also possible. This minimizes the subject-to-subject variability and reduces the animal number required by a traditional method.<sup>43</sup> Most importantly, these *in vivo* studies can bridge the gap between *in vitro* (cell/tissue level) and *in vivo* (the whole animal) studies, while facilitating preclinical and further translational studies.<sup>61</sup>

Bioluminescence imaging (BLI) is typically based on the ATP- and O<sub>2</sub>-dependent enzymatic conversion of exogenous luciferin to oxyluciferin by luciferase within living cells. This reaction can produce photons with a broad yellow emission spectrum with a peak around 560 nm, detectable with a highly sensitive charge-coupled device (CCD) camera at 10-12 min after intraperitoneal injection of luciferin. The bioluminescence phenomena can last over 60 min in mice, providing multiple images of disease progression and therapeutic response based on the changes in the number of cells with luciferase expression or transcriptional activity. BLI has allowed quantitative measurements of tumor loadings, treatment response, immune cell trafficking and detection of gene transfer. It is also possible to obtain spatio-temporal information of whole biological systems *in vivo* within a short time frame that may accelerate the development of experimental therapeutic strategies.<sup>61,62,63</sup>

On the other hand, fluorescence imaging has an entirely different methodology that consists of exciting certain fluorophores in a living system by using external light and detecting fluorescence emission with a sensitive CCD camera.

There are several types of fluorophores: *i*) endogenous molecules (such as collagen or hemoglobin), *ii*) exogenous fluorescent molecules such as green fluorescent protein (GFP) or *iii*) small synthetic optical contrast agents. When compared to *in vitro* fluorescence microscope, *in vivo* fluorescence imaging is a complex process affected by many factors.<sup>43</sup> One of the major limitations of *in vivo* fluorescence imaging is light attenuation and scattering due to adjacent living tissues. As previously mentioned light in the near infrared (NIR) range (650-900 nm) can improve the light penetration.<sup>61,62,64</sup> It can also minimize the autofluorescence of some endogenous absorbers such as hemoglobin, water and lipids. In a full-body mouse illumination experiment, photon counts in the NIR range (670 nm) are about four orders of magnitude higher when compared to those in the green light range (530 nm) under similar conditions. Hence NIR fluorescence imaging has proved to be an effective solution in improving the imaging depth along with sensitivity and specificity. As a result NIR-fluorophores are important for successful *in vivo* optical imaging and future clinical applications.

### 3.5. OPTICAL CONTRAST AGENTS

As mentioned in the previous chapter, the general definition of Contrast Agents (CAs) is a chemical substance introduced to the anatomical or functional region being imaged in order to increase the differences between different tissues, or between normal and abnormal tissue.

Optical contrast agents are frequently used to stain portions of biological samples in order to obtain a greater understanding of the molecular, cellular and physiological changes at hand. Two important classes of these agents are the colorimetric and fluorescent markers. Colorimetric contrast agents modify the light absorption resulting in a contrast of observed colour; while fluorescent agents also modify light absorption, but subsequently re-emit a portion of the absorbed light at higher wavelengths (lower energy).<sup>43</sup> This phenomenon is leveraged to achieve greater sensitivity with the use of fluorescent markers. Through non illumination of the sample with light at the emission wavelengths of the fluorophore(s) present an enhanced signal to noise ratio will be achieved. In recent years, the attractiveness of fluorescent microscopy in biological sciences has grown; however, many challenges are still to be overcome in the application of fluorescent markers in biological systems. For instance, organic dyes are prone to rapid photobleaching limiting their application to long-term bioimaging investigation.<sup>65,66</sup> Many other dyes also have relatively broad emission spectra complicating their integration into multicolor imaging applications. In bioimaging, additional artifacts such as high light scattering via tissue interfaces, autofluorescence, and absorption by hemoglobin (Hb) in a mid-visible wavelength range are observed. The application of NIR range (650 to 900 nm) contrast agents can overcome many of these issues and is preferred for bio-imaging thick tissues. The development of NIR imaging agents such as NIR quantum dots (QDs) and dyes (e.g. cyanine dyes) have recently attracted significant attention.<sup>67,68</sup> In the case of optical imaging CA, they are normally molecules or nanoparticles bearing one or more fluorophores. Typical optical imaging CAs are injected intravascularly or intraperitoneally and allowed to accumulate at the target site over several hours to days. Fluorophores can be endogenous molecules (such as collagen or hemoglobin), exogenous fluorescent molecules such as green fluorescent protein (GFP) or small synthetic optical CAs.

Within the last decades multifunctional contrast agents have emerged substantially with the attempt to obtain the benefits of multiple imaging modalities with the use of a

single contrast agent.<sup>69,70</sup> One example can be found in the fluorescent and MRI active probes that allow for simultaneous detection by MRI and fluorescence microscopy by combining the advantages of 3D anatomical resolution at cellular level from MRI with the high sensitivity offered by fluorescence microscopy in a single particle.

### **Organic dyes**

Organic dyes, such as rhodamine and fluoresceins are the earliest and most classical luminescent materials employed in optical agents. Nevertheless, these dyes have some problematic limitations that are critical to the quality of optical imaging. Broad emission bands (which can pose a problem in multiplexing and sensitivity), short luminescence lifetimes *ca.*  $10^{-9}$  s, a small Stokes shift (difficulty in separating the excitation and emission signals), poor photochemical stability and susceptibility to photobleaching (photochemical destruction of the fluorophore) on the <sup>71,72</sup> are the basic drawbacks of these type of agents. Several attempts have been made in order to create new fluorescent dyes that are more resistant to photobleaching and insensitive to pH changes. The problem of short lifetimes and Stokes shift has still not been satisfactorily overcome. Despite these setbacks organic dyes continue to be very popular due to their low cost, high availability and practicality.<sup>72</sup>

### **Quantum dots**

Quantum dots (QDs) are crystalline semiconductors typically less than 10 nm in diameter and are considered to be another promising luminescent tag for optical imaging. They are reported to be several thousand times more stable against photobleaching, much brighter and have a spectral width reduced by up to one-third from conventional organic dyes.<sup>73,74</sup>

One of the special features of QDs is its emission wavelengths variation that is strongly size dependent: They can emit different colours spanning the entire visible/NIR region within the same material by merely changing the size of the particles. This is a consequence of the so called quantum confinement effect: a confinement of the hole and electron wave functions in the nanocrystals when the size of the particles are reduced

beyond the bulk-exciton Bohr radius, and consequently, an increase in the semiconductor band gap.<sup>72-78</sup> A combination of the broad absorption bands of QDs, narrow emission bands and their size dependent emissions offer the possibility of using them to tag biomolecules in ultrasensitive biological detection and in bioapplications such as gene-expression studies, high-throughput screening and medical diagnostics based on optical-coding technology.<sup>75</sup> Generally QDs have longer lifetimes (20- 50 ns) than that of organic dyes by one order of magnitude and so QDs are highly regarded as a new generation materials capable of bringing immense benefits to medical diagnosis.<sup>76,79</sup>

On the other hand, there are a few limitations that QDs have to overcome in order to be the ideal candidates for optical tags. An example is the danger of releasing toxic elements into biological systems, especially in *in vivo* analyses. The most optically efficient QDs are engineered with one or more toxic element such as cadmium and selenium.<sup>80</sup> CdSe QDs have luminescence properties from near UV to NIR regions with size-tunable absorption, this broad absorption band provide two advantages: *i)* freedom to select any excitation wavelength below the band gap energy and *ii)* minimize background by increasing Stokes shift. Another reported limitation of QDs is their tendency to suffer from optical blinking emission (continued on-off emission), a situation that is detrimental to real time imaging<sup>72,81-84</sup>

As already mentioned QDs are more resistant to photobleaching than organic dyes, however some studies have reported various degrees of QDs fluorescence quenching under irradiation in ambient environment, where some of the authors<sup>85,86</sup> conclusively pointed out photo-oxidation of the nanocrystals as the main/primary cause. In order to overcome photo-oxidation limitation researchers attempted to coat the QDs with a protective layer (shell) forming a core-shell type QD, where the inner core would be a semiconductor material, while the shell would be another semiconductor but with a wider band gap<sup>87</sup>. Unfortunately this attempt did not reach expectations. Within the same perspective emerged the coating with thiols<sup>88,89,90</sup>, polymers<sup>91,92,93</sup> or silica<sup>94,95</sup> serving not only as protective layers but as platforms for possible bioconjugations introducing multimodal perspective to QD.

In conclusion, invaluable effort is being invested by many researchers with uncompromised intentions to resolve the toxicity of high-quality QDs and develop non-toxic QDs in order to offer all the advantages of QDs to biomedical imaging and therapeutic interventions.

## Lanthanide Chelates (and time resolved fluorescence)

Considerable interest has been allotted to the application of kinetically stable lanthanide complexes as probes for biological imaging and assaying.<sup>96,97</sup> While efforts have been concentrated their on the development of gadolinium agents (as MRI contrast agents),<sup>35,98</sup> luminescent trivalent lanthanide ions such as terbium (Tb), europium (Eu), ytterbium (Yb) and neodymium (Nd) also have much to offer.<sup>99,100</sup> The large Stokes shifts and long-lived emission commonly associated with sensitised emission from these ions ensures the usage of time-gated spectroscopy to separate such long-lived signals from the short-lived signals that arise from scattered light and biological fluorescence.<sup>101</sup> As a result considerable interest has been given the use of luminescent lanthanides in bioassays and more recently the possibility of using time-resolved spectroscopy and microscopy.<sup>103-105</sup>

Lanthanide complexes can be tailor-made to exhibit different luminescent lifetimes by the exclusion of solvent molecules from the inner hydration sphere of the lanthanide ion. Therefore such complexes can be used in microscopy applications to gain more detailed information. Lanthanide complexes can be distinguished by their characteristic wavelengths of emission (due to the metal centre), very sharp emission bands (typically with a full width at half maximum of less than 10 nm) and their luminescent lifetimes (ca.  $10^{-3}$  s), which are controlled by their coordination environment.<sup>71</sup>

Time-resolved fluorescence (TRF), which is more or less an exclusive preserve of lanthanides compounds, has become by far the most effective way of eliminating background interferences in order to enhance sensitivity.<sup>102-105</sup> The introduction of a time delay ( $\sim 1$  or  $100 \mu\text{s}$ ), prior to detection of the emitted light eliminates interference from light scattering and auto-fluorescence enhancing greatly the signal to noise ratio (detection limits are conservatively in the  $10^{-12} - 10^{-15}$  M range) and hence the reliability of detection and monitoring.<sup>102</sup> The principle of TRF is illustrated in figure 3.4 and involves sequentially an excitation of the system, cessation of the excitation allowing enough decay time (during which the typical fluorescence from dyes and QDs would have decayed) for background interferences to have disappeared and measuring the luminescence of the lanthanide.

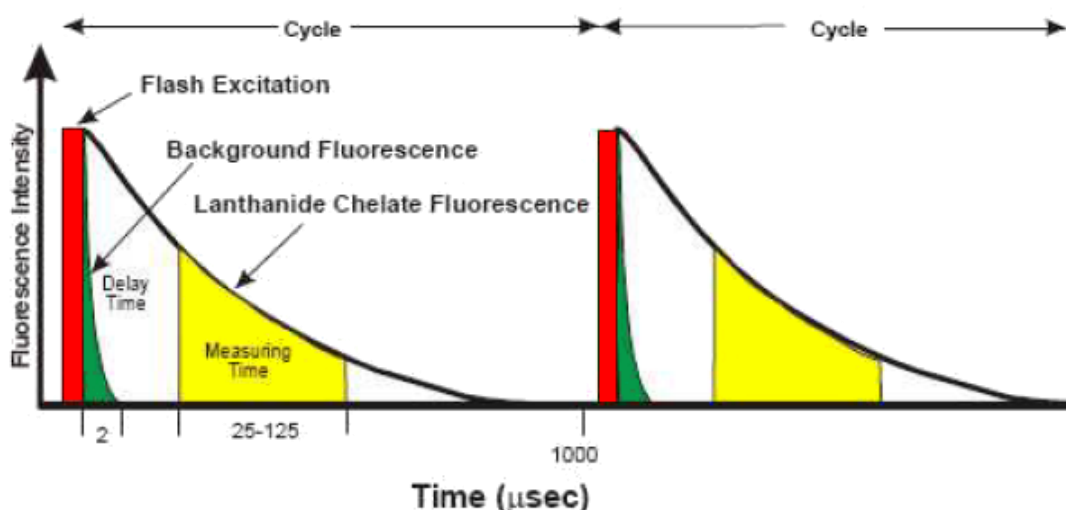


**Figure 3.4.** Principle of TRF. The excitation is removed, followed by a sufficient time delay, and later measurement of lanthanide fluorescence and the cycle can continue thereafter with new excitation.<sup>106</sup>

An important point in the design of an efficient lanthanide-based probe is to protect the lanthanide cation from solvent molecules. Particular attention should be paid in protecting the cation from water as the lanthanide emission is quenched by the presence of water molecules in the first coordination sphere of the lanthanide (non-radiative deactivation through O-H vibrators). NIR emitting lanthanide ions commonly have a lower quantum yield than those other lanthanide ions emitting in the visible range, since their non-radiative transitions have higher probability with regards to the lanthanide ions emitting in the visible range. Nevertheless, as previously mentioned, they are more suitable for biological applications as they can be excited at lower energy and NIR photons can go deeper into tissue.

Several research groups have devoted great effort to designing organic ligands, a great variety of which are now described in the literature and reviewed by Bünzli.<sup>37</sup> In general, small variations in a ligand structure can lead to remarkable changes in the photophysical properties. Several types of lanthanide carboxylates have been reported.<sup>107</sup>

## Lanthanide doped nanoparticles

Lanthanide doped NPs have emerged as a fast-growing platform in cell imaging due to the generation of low background noise for their NIR emission. To date the lanthanide oxide phosphor system has been the widely studied. Meiser et al. reported the synthesis of monodisperse fluorescent  $\text{LaPO}_4$  NPs<sup>108,109,110</sup> These NPs, approximately 7 nm in size, have fluorescence that originates from their bulk properties - transitions between  $d$  and  $f$  electron states and their local symmetry - and is independent of their size. These NPs were biofunctionalized via biotin-avidin chemistry with good photostability and fluorescent properties.<sup>111</sup>

Setua et al. produced highly monodispersed  $\text{Eu}^{3+}$  and  $\text{Gd}^{3+}$  doped  $\text{Y}_2\text{O}_3$  nanocrystals and presented bi-modal imaging applications of both paramagnetism that enabled magnetic resonance imaging and bright red-fluorescence. This aided the optical imaging of cancer cells, targeted specifically to their molecular receptors.<sup>112</sup>

Lanthanide up-converting NPs (UCNPs) are rare-earth doped ceramic-type materials such as oxides, oxysulfides, fluorides or oxyfluorides which convert infra-red light into the visible spectrum. They are usually synthesized as nanospheres and were introduced as probes for bioassays in the 1990s. Most of these UCNPs contain  $\text{Er}^{3+}$  ions as two-color (green, 540 nm; red, 654 nm) emitters and  $\text{Yb}^{3+}$  ions as sensitizers, but other  $\text{Ln}^{3+}$  pairs have also been proposed (e.g.,  $\text{Tm}^{3+}/\text{Ho}^{3+}/\text{Yb}^{3+}/\text{Tm}^{3+}$ ). These type of NPs present several advantages over classical bioprobes, including high sensitivity, multiplexing ability if several different  $\text{Ln}^{3+}$  ions are co-doped, low sensitivity to photobleaching and cheap laser diode excitation, in addition to deep penetration of the excitation NIR light. Initially, they were used in luminescent immunoassays. Presently their applications have been extended to luminescence imaging of cancerous cells.<sup>113</sup> Novel imaging systems based on UCNPs have been designed<sup>114</sup> and improved sensitivity of down to single molecule detection within cells is foreseen.<sup>115,116,117</sup>

Lanthanide up-converting NPs (UCNPs) have been developed as a new generation of luminescent labels due to their superb optical features, long lifetimes and excellent photostability. Among various kinds of UCNPs,  $\text{NaYF}_4$  is the most well-known system that has been employed in both cellular and in vivo animal imaging.<sup>118,119,120</sup>

Since the growth of this field is rapidly developing it is foreseen that lanthanide doped NPs will find their way into even more elaborate biotechnological applications in the coming future due to their relatively simple nanocomposition, deep penetration depth of

NIR and other advantageous physical features. Due to the potentially high toxicity of lanthanides, more detailed investigations will probably be required to evaluate their biochemical and physiological behaviours before lanthanide doped NPs are eventually approved for biomedical applications.

### 3.6. REFERENCES

---

- 1 Bornhop D.J., Contag C.H., Licha K., Murphy C.J., Advances in Contrast Agents, Reporters, and Detection *Biomed Optics* **2001**, 6, 106 – 110.
- 2 Weissleder R., A Clearer Vision for *in vivo* Imaging *Nature Biotechnol* **2001** 19, 316 – 317.
- 3 Martinez Maestro, L.; Martin Rodriguez, E.; Vetrone, F.; Naccache, R.; Loro Ramirez, H.; Jaque, D.; Capobianco, J. A.; Garcia Sole, J., Nanoparticles for highly efficient multiphoton fluorescence bioimaging. *Optics Express* **2010**, 18 (23), 23544-23553.
- 4 Wang, F.; Banerjee, D.; Liu, Y.; Chen, X.; Liu, X., Upconversion nanoparticles in biological labeling, imaging, and therapy. *Analyst* **2010**, 135 (8), 1839-1854.
- 5 Park, Y. I.; Kim, J. H.; Lee, K. T.; Jeon, K.-S.; Bin Na, H.; Yu, J. H.; Kim, H. M.; Lee, N.; Choi, S. H.; Baik, S.-I.; Kim, H.; Park, S. P.; Park, B.-J.; Kim, Y. W.; Lee, S. H.; Yoon, S.-Y.; Song, I. C.; Moon, W. K.; Suh, Y. D.; Hyeon, T., Nonblinking and Nonbleaching Upconverting Nanoparticles as an Optical Imaging Nanoprobe and T1 Magnetic Resonance Imaging Contrast Agent. *Advanced Materials* **2009**, 21 (44), 4467-4471.
- 6 Scaff W.L., Dyer D. L., Mori, K., Fluorescent Europium Chelate Stain *J. Bacteriol.* **1969**, 98, 246-248.
- 7 Soini E., Hemmilä I., Fluoroimmunoassay: Present Status and Key Problems *Clin. Chem.* **1979**, 25, 353 - 261.
- 8 Hemmilä, I.; Ståhlberg, T.; Mottram, P. *Bioanalytical Applications of Labelling Technologies*, 2nd ed.; Wallac Oy: Turku, Finland, **1995**.
- 9 Bazin H., Trinquet E., Mathis G., Time-resolved Amplification of Cryptate Emission: A Versatile Technology to Trace Biomolecular Interactions *Rev. Mol. Biotechnol.* **2002**, 82, 233 - 250.
- 10 Hovinen J., Guy P.M. Bioconjugation with Stable Luminescent Lanthanide(III) Chelates Comprising Pyridine Subunits *Bioconjugate Chem.* **2009**, 20, 404 - 421.
- 11 Connally R.E., Piper J.A. Time-gated Luminescence Microscopy *Ann. N. Y. Acad. Sci.* **2008**, 1130, 106- 116.
- 12 Moore E.G., Samuel A.P.S., Raymond K.N. From Antenna to Assay: Lessons Learned in Lanthanide Luminescence. *Acc. Chem. Res.* **2009**, 42, 542 - 552.
- 13 Bünzli J.-C.G., Lanthanide Luminescent Bioprobes (LLBs) *Chem. Lett.* **2009**, 38, 104 - 109.
- 14 Song B., Vandevyver C.D.B, Deiters E., Chauvin A.-S., Hemmilä I., Bünzli J.-C.G. A Versatile Method for Quantification of DNA and PCR Products Based on Time-resolved EuIII Luminescence. *Analyst.* **2008** 133,1749 - 1756.
- 15 Hess B.A., Kedzioriski A., Smentek L., Bornhop D.J. Role of the Antenna in Tissue Selective Probes Built of Lanthanide-Organic Chelates. *J. Phys. Chem. A* **2008**, 112, 2397 - 2407.

- 16 Montgomery C.P., Murray B.S., New E.J., Pal R., Parker, D. Cell-penetrating Metal Complex Optical Probes: Targeted and Responsive Systems Based on Lanthanide Luminescence *Acc. Chem. Res.* **2009**, 42, 925 - 937.
- 17 Bünzli J.-C.G., Chauvin A.-S., Vandevyver C.D.B., Song B., Comby S. Lanthanide Bimetallic Helicates for in Vitro Imaging and Sensing *Ann. N. Y. Acad. Sci.* **2008**, 1130, 97-105.
- 18 Dos Santos C.M.G., Harte A.J., Quinn, S.J., Gunnlaugsson T. Recent Developments in the Field of Supramolecular Lanthanide Luminescent Sensors and Self-assemblies *Coord. Chem. Rev.* **2008**, 252, 2512.
- 19 Fan Y., Yang P., Huang S., Jiang J., Lian H., Lin J. Luminescent and Mesoporous Europium-Doped Bioactive Glasses (MBG) as a Drug Carrier *J. Phys. Chem. C* **2009**, 113, 7826 - 7830632.
- 20 Harvey E.N., A History of Luminescence. From the Earliest Times Until 1900, American Philosophical Society, Philadelphia, **1957**.
- 21 Melhuish W.H., Nomenclature, Symbols, Units and their Usage in Spectrochemical Analysis VI: MOLECULAR LUMINESCENCE SPECTROSCOPY *Pure Appl. Chem.*, **1984**, 56, 231 - 245.
- 22 Blasse G., Grabmaier B.C., Luminescent Materials, Springer, Verlag Berlin Heidelberg, **1994**.
- 23 Bünzli J.-C.G., Piguet C. Taking Advantage of Luminescent Lanthanide Ions *Chem. Soc. Rev.* **2005**, 34, 1048 – 1077.
- 24 Skoog D.A., Holler F.J., Crouch S.R. Principles of Instrumental Analysis, 6th ed.; Thomson Brooks/Cole: Canada, pp 154, **2007**.
- 25 Kaltsoyannis N., Scott P., The f Elements, Oxford Chemistry Primers, ed. J. Evans, Oxford Science Publications, Oxford, **1999**.
- 26 Cotton S., Lanthanides and Actinides, McMillan Physical Science Series, McMillan Education, London, **1991**.
- 27 Hübner S., Optical Spectra of Transparent Rare Earth, Academic Press, New York **1978**.
- 28 Carlos L.D., Ferreira R.A.S., Zea Bermudez V., Ribeiro S.J.L. Lanthanide-Containing Light-Emitting Organic-Inorganic Hybrids: A Bet on the Future *Adv. Mater.* **2009**, 21, 509 – 534
- 29 Nishioka T., Fukui K., Matsumoto K. In Handbook on the Physics and Chemistry of Rare Earths; Gschneidner K.A., Bünzli J.-C.G., Pecharsky V.K., Eds.; Elsevier Science BV: Amsterdam, Vol. 37, Chapter 234, p 171 **2007**.
- 30 Yuan, J.; Wang, G. Lanthanide-based luminescence probes and time-resolved luminescence bioassays *Trends Anal. Chem.* **2006**, 25, 490 – 500.
- 31 T. Jüstel, H. Nikol, C. Ronda, New Developments in the Field of Luminescent Materials for Lighting and Displays *Angew. Chem. Int. Ed.* **1998**, 37, 3084 - 3103.

- 32 Werts M.H.V. Making sense of lanthanide luminescence *Sci. Prog.* **2005**, 88, 101 - 131.
- 33 Hasegawa Y., Wada Y., Yanagida S., Strategies for the Design of Luminescent Lanthanide(III) Complexes and their Photonic Applications, *J. Photochem. Photobiol. C* **2004**, 5, 183 – 202.
- 34 Hemmilä I., Laitala V. Progress in Lanthanides as Luminescent Probes. *J. Fluoresc.* **2005**, 15, 529 - 542.
- 35 Parker D., Dickins R. S., Puschmann H., Crossland C., Howard J.A.K. Being Excited by Lanthanide Coordination Complexes: Aqua Species, Chirality, Excited-State Chemistry, and Exchange Dynamics *Chem. Rev.* **2002**, 102, 1977 - 2010.
- 36 Mulder W.J.M., Griffioen A.W., Strijkers G.J., Cormode D.P., Nicolay K., Fayad Z.A. Magnetic and Fluorescent Nanoparticles for Multimodality imaging *Nanomedicine* **2007**, 2, 307 - 324.
- 37 Bünzli J.-C.G. Lanthanide Luminescence for Biomedical Analyses and Imaging *Chem. Rev.* **2010**, 110, 2729 - 2755.
- 38 Malta O.L., Carlos L.D. Intensities of 4f-4f Transitions in Glass Materials *Quim. Nova* **2003**, 26, 889 - 895.
- 39 S. Comby, J.-C. G. Bünzli, in Handbook on the Physics and Chemistry of Rare Earths (Eds: K. A. Gschneidner, Jr, J.-C. G. Bünzli, V. K. Pecharsky), *Elsevier, New York, U.S.A.*, pp. 217 – 254, **2007**.
- 40 Werts M.H.V., Jukes R.T.F., Verhoeven J.W. The emission spectrum and the radiative lifetime of  $\text{Eu}^{3+}$  in luminescent lanthanide complexes *Phys. Chem. Chem. Phys.* **2002**, 4, 1542 - 1548.
- 41 Lima P.P., Ferreira R.A.S., Freire R.O., Paz F.A.A., Fu L.S., Alves S., Carlos L.D., Malta O.L. Spectroscopic Study of a UV-Photostable Organic–Inorganic Hybrids Incorporating an  $\text{Eu}^{3+}$   $\beta$ -Diketonate Complex *ChemPhysChem* **2006**, 7, 735 - 746.
- 42 Porcher P., Caro P. Influence of J-mixing on the Phenomenological Interpretation of the Europium Ion Spectroscopic Properties *J. Lumin.* **1980**, 21, 207 - 216.
- 43 Malta O.L., Azevedo W.M., Gouveia E.A., Desa G.F. On the  $^5\text{D}_0 \rightarrow ^7\text{F}_0$  Transition of the  $\text{Eu}^{3+}$  Ion in the  $\{(\text{C}_4\text{H}_9)_4\text{N}\}_3\text{Y}(\text{NCS})_6$  Host *J. Lumin.* **1982**, 26, 337 - 343.
- 44 Carlos L.D., A. Videira L.L. Emission Spectra and Local Symmetry of the  $\text{Eu}^{3+}$  Ion in Polymer Electrolytes *Phys. Rev.* **1994**, 49, 11721 - 11728.
- 45 Carlos L.D., Malta O.L., Albuquerque R.Q. A Covalent Fraction Model for Lanthanide Compounds *Chem. Phys. Lett.* **2005**, 416, 238 - 242.
- 46 Carlos L.D., Ferreira R.A.S., Zea Bermudez V., Molina C., Bueno L.A., Ribeiro S.J.L. White Light Emission of  $\text{Eu}^{3+}$ -Based Hybrid Xerogels *Phys. Rev. B* **1999**, 60, 10042 - 10053.
- 47 Licha, K., Topics in Current Chemistry - Contrast Agents for Optical Imaging. *Springer-Verlag Berlin Heidelberg* **2002**, 222.

- 48 Wan S., Parrish A.J., Anderson R.R., Madden M. Transmittance of Nanionizing Radiation in Human Tissues *Photochem Photobiol* **1981**, 34, 679 – 681.
- 49 Andersson-Engels S., Wilson B.C. *In vivo* Fluorescence in Clinical Oncology: Fundamental and Practical Issues *Cell Pharmacol* **1992**, 3, 48 – 61.
- 50 Wagnieres G.A., Star W.M., Wilson B.C. *In Vivo* Fluorescence Spectroscopy and Imaging for Oncological Applications *Photochem Photobiol* **1998**, 68, 603 – 632.
- 51 Andersson-Engels S.K., linteberg C., Svanberg K., Svanberg S. *In vivo* Fluorescence Imaging for Tissue Diagnostics *Phys Med Biol* **1997**, 42, 815 – 824.
- 52 Moesta K.T., Ebert B., Handke T., Nolte D., Nowak C., Haensch W.E., Pandey R.K., Dougherty T.J., Rinneberg H., Schlag P.M. Protoporphyrin IX occurs naturally in colorectal cancers and their metastases *Cancer Res.* **2001**, 61, 991 – 999.
- 53 Stepp H., Sroka R., Baumgartner R. Fluorescence Endoscopy of Gastrointestinal Diseases: Basic Principles, Techniques, and Clinical Experience *Endoscopy* **1998**, 30,379 – 386.
- 54 Svanberg K., Wang I., Colleen S., Idvall I., Ingvar C., Rydell R., Jocham D., Diddens H., Bown S., Gregory G., Montan S., Andersson-Engels S., Svanverg S. Clinical Multi-colour Fluorescence Imaging of Malignant Tumours: Initial Experience *Acta Radiol* **1998**, 39, 2 – 9.
- 55 Maarek J-M.I., Marcu L., Fishbein M.C., Grundfest W.S. Time-resolved Fluorescence of Human Aortic Wall: Use for Improved Identification of Atherosclerotic Lesions *Lasers Surg. Med.* **2000**, 27, 241 – 254.
- 56 Grosenick D., Wabnitz H., Rinneberg H.H., Moesta K.T., Schlag P.M. Development of a Time-domain Optical Mammograph and First *in vivo* Applications *Appl. Opt.* **1999**, 38, 2927 – 2943.
- 57 Sevick E.M., Chance B., Leigh J., Nioka S., Maris M. Quantitation of Time- and Frequency-resolved Optical Spectra for the Determination of Tissue Oxygenation *Anal. Biochem.* **1991**, 195, 330 – 351.
- 58 De Haller E.B. Time-resolved Transillumination and Optical Tomography *J. Biomed. Optics* **1996**, 1,7 – 17.
- 59 <http://omlc.ogi.edu/spectra/hemoglobin>
- 60 Moriyama E.H., Zheng G., Wilson B.C. Optical Molecular Imaging: From Single Cell to Patient *Clin Pharmacol Ther.* **2008**, 84, 267 – 271.
- 61 Yunpeng Y., Xiaoyuan C. Integrin Targeting for Tumor Optical Imaging *Theranostics* **2011**, 1, 102 – 126.
- 62 Contag C.H., Ross B.D. It's Not Just About Anatomy: *In vivo* Bioluminescence Imaging as an Eyepiece into Biology *J. Magn. Reson. Imaging* **2002**, 16, 378 – 387.
- 63 Shah K., Weissleder R. Molecular Optical Imaging: Applications Leading to the Development of Present Day Therapeutics. *NeuroRx.* **2005**, 2, 215 – 225.

- 64 Tung C.H. Fluorescent Peptide Probes for *in vivo* Diagnostic Imaging. *Biopolymers* **2004**, 76, 391 – 403.
- 65 Chan W.C., Maxwell D.J., Gao X., Bailey R.E, Han M., Nie S. Luminescent Quantum Dots for Multiplexed Biological Detection and Imaging. *Curr. Opin Biotechnol* **2002**, 13, 40 – 46.
- 66 Bruchez M., Moronne M., Gin P., Weiss S., Alivisatos A.P. Semiconductor Nanocrystals as Fluorescent Biological Labels *Science* **1998**, 281, 2013 – 2016.
- 67 Licha K., Riefke B., Ntziachristos V., Becker A., Chance B., Semmler W. Hydrophilic Cyanine Dyes as Contrast Agents for Near-infrared Tumor imaging: Synthesis, Photophysical Properties and Spectroscopic *in vivo* Characterization *Photochem Photobiol* **2000**, 72, 392 – 398.
- 68 Pham W., Lai W.F., Weissleder R., Tung C.H. High Efficiency Synthesis of a Bioconjugatable Near-infrared Fluorochrome *Bioconjug Chem.* **2003**, 14, 1048 – 1105.
- 69 Huber M.M., Staubli A.B., Kustedjo K., Gray M.H.B., Shih J., Fraser S.E., Jacobs R.E., Meade T.J. Fluorescently Detectable Magnetic Resonance Imaging Agents *Bioconjug Chem* **1998**, 9, 242 – 249.
- 70 Santra S., Bagwe R.P., Dutta D., Stanley J.T., Walter G.A., Tan W., Moudgil B.M., Mericle R.A. Synthesis and Characterization of Fluorescent, Radio-opaque, and Paramagnetic Silica Nanoparticles for Multimodal Bioimaging Applications *Adv. Mater.* **2005**, 17, 2165 – 2169.
- 71 Pandya S., Yu J., Parker D. Engineering emissive europium and terbium complexes for molecular imaging and sensing *Dalton. Trans.* **2006**, 2757 - 2766.
- 72 Wang F., Tan W.B., Zhang Y., Fan X., Wang M. Luminescent nanomaterials for biological labelling *Nanotechnology* **2006**, 17, R1 – R13.
- 73 Rhyner M.N., Smith A. M., Gao X., Mao H., Yang L., Nie S Quantum Dots and Multifunctional Nanoparticles: New Contrast Agents for Tumor Imaging *Nanomedicine* **2006**, 1, 209 - 217.
- 74 Tan W., Wang K., He X., Zhao X.J., Drake T., Wang L., Bagwe, R.P. Bionanotechnology Based on Silica Nanoparticles *Med. Res. Rev.*, **2004**, 24, 621 – 638.
- 75 Tan W. B., Zhang Y. Multifunctional Quantum-Dot-Based Magnetic Chitosan Nanobeads *Adv. Mat.* **2005**, 17, 2375 – 2380.
- 76 Biju V., Itoh T., Ishikawa M. Delivering Quantum Dots to Cells: Bioconjugated Quantum Dots for Targeted and Nonspecific Extracellular and Intracellular Imaging *Chem. Soc. Rev.* **2010**, 39, 3031 – 3056.
- 77 Trindade T., Pickett N.L., O'Brien P. Nanocrystalline Semiconductors: Synthesis, Properties, and Perspectives *Chem. Mater.* **2001**, 13, 3843 - 3858.

- 78 Sapra S., Sarma D.D., Sanvito S., Hill N.A. Influence of Quantum Confinement on the Electronic and Magnetic Properties of (Ga,Mn)As Diluted Magnetic Semiconductor *Nano Lett.* **2002**, 2, 605 - 608.
- 79 Smith A. M., Dave S., Nie S., True, L., Gao, X. Multicolor quantum dots for molecular diagnostics of cancer *Expert Rev. Mol. Diagn.*, **2006**, 6 , 231 - 244.
- 80 Mericle R.A., Moudgil B.M., Tan W., Cao Z., Dutta D., Bertolino C., Liesenfeld B., Santra S. Fluorescence Lifetime Measurements to Determine the Core-shell Nanostructure of FITC Doped Silica Nanoparticles: An Optical Approach to Evaluate Nanoparticle Photostability *J. Lumin.*, **2006**, 117, 75 – 82.
- 81 Soukka T., Kuningas K., Rantanen T., Haaslahti V., Lovgren T. Photochemical characterization of up-converting inorganic lanthanide phosphors as potential labels. *J. Fluoresc.* **2005**, 15, 513 - 528.
- 82 Yuan C.T., Yu P., Ko H.C., Huang J., Tang J. Antibunching Single-Photon Emission and Blinking Suppression of CdSe/ZnS Quantum Dots *ACS Nano* **2009**, 3, 3051 – 3056.
- 83 Matsumoto Y., Kanemoto R., Itoh T., Nakanishi S., Ishikawa M., Biju V. Photoluminescence Quenching and Intensity Fluctuations of CdSe-ZnS Quantum Dots on an Ag Nanoparticle Film *J. Phys. Chem. C* **2008**, 112, 1345 – 1350.
- 84 Mansur H. S. Quantum Dots and Nanocomposites *WIREs Nanomedicine and Nanobiotechnology* **2010**, 2, 113 – 129.
- 85 Roy A., Singha A. Quantitative Analysis of Thermal Stability of CdSe/CdS Core-shell Nanocrystals Under Infrared Radiation *J. Mater. Res.* **2006**, 21, 1385 - 1389.
- 86 Wang, P. N., Xu L., Yang W.L., Wang C.C., Guo J., Chen J.-Y, Ma J. Photostability of thiol-capped CdTe quantum dots in living cells: the effect of photo-oxidation *Nanotechnology* **2006**, 17, 2083 - 2089.
- 87 Reiss P., Protiere M., Li L. Core/Shell Semiconductor Nanocrystals *Small* **2009**, 5, 154 – 168.
- 88 Medintz I. L., Uyeda H. T., Goldman E. R., Mattoussi H. Quantum Dot Bioconjugates for Imaging, Labelling and Sensing *Nat. Mater.* **2005**, 4, 435 – 446.
- 89 Medintz I. L., Clapp A. R., Mattoussi H., Goldman E. R., Fisher B., Mauro J. M. Self-assembled Nanoscale Biosensors Based on Quantum Dot FRET Donors *Nat. Mater.* **2003**, 2, 630 – 638.
- 90 Rosenthal S. J., McBride J., Pennycook S. J, Feldman L.C. Synthesis, Surface Studies, Composition and Structural Characterization of CdSe, Core/Shell, and Biologically Active Nanocrystals. *Surf. Sci. Rep.* **2007**, 62, 111 – 157.
- 91 Gao X.H., Cui Y.Y., Levenson R.M., Chung L.W.K., Nie S.M. *In vivo* Cancer Targeting and Imaging with Semiconductor Quantum Dots *Nat. Biotechnol.* **2004**, 22, 969 – 976.

- 92 Pellegrino T., Manna L., Kudera S., Liedl T., Koktysh D., Rogach A. L., Keller S., Rädler J., Natile G., Parak W. J. Hydrophobic Nanocrystals Coated with an Amphiphilic Polymer Shell: A General Route to Water Soluble Nanocrystals *Nano Lett.*, **2004**, 4, 703 – 707.
- 93 Biju V., Kanemoto R., Matsumoto Y., Ishii S., Nakanishi S., Itoh T., Baba Y., Ishikawa M. Photo Induced Photoluminescence Variations of CdSe Quantum Dots in Polymer Solutions *J. Phys. Chem. C* **2007**, 111, 7924 – 7932.
- 94 Nann T., Mulvaney P. Single Quantum Dots in Spherical Silica Particles *Angew. Chem., Int. Ed.* **2004**, 43, 5393 – 5396.
- 95 Selvan S. T., Tan T. T., Ying J. Y. Robust, Non-Cytotoxic, Silica-Coated CdSe Quantum Dots with Efficient Photoluminescence *Adv. Mater.* **2005**, 17, 1620 – 1625.
- 96 Toth E., Helm L., Merbach A. E. in *Comprehensive Coordination Chemistry II*, ed. M. D. Ward, Elsevier, Oxford, UK, pp. 841–882, **2004**.
- 97 Faulkner S., Matthews J.L. in *Comprehensive Coordination Chemistry II*, ed. M. D. Ward, Elsevier, Oxford, pp. 913–944, UK, **2004**.
- 98 Caravan P., Ellison J. J., McMurry T., Lauffer R. B. Gadolinium(III) Chelates as MRI Contrast Agents: Structure, Dynamics, and Applications *Chem. Rev.* **1999**, 99, 2293 – 2352.
- 99 Selvin, P.R. Principles and Biophysical Applications of Lanthanide-based Probes *Annu. Rev. Biophys. Biomol. Struct.* **2002**, 31, 275 - 302.
- 100 Klink S. I., Keizer H. Van Veggel F.C.J.M. Organo-d-Metal Complexes as New Class of Photosensitizers for Near-Infrared Lanthanide Emission, *Angew. Chem., Int. Ed.*, **2000**, 39, 4319 – 4321.
- 101 Alpha B., Lehn J.M., Mathis G. Energy Transfer Luminescence of Europium(III) and Terbium(III) Cryptates of Macrobicyclic Polypyridine Ligands *Angew. Chem., Int. Ed. Engl.*, **1987**, 26, 266 - 167.
- 102 Beeby A., Botchway S. W., Clarkson I. M., Faulkner S., Parker A. W., Parker D., Williams J. A. G. Luminescence Imaging Microscopy and Lifetime Mapping Using Kinetically Stable Lanthanide(III) Complexes *J. Photochem. Photobiol. B: Biol.* **2000**, 57, 83 – 89.
- 103 Charbonnière L. J., Ziessel R., Montalti M., Prodi L., Zaccheroni N., Boehme C. Wipff G. Luminescent Lanthanide Complexes of a Bis-bipyridine-phosphine-oxide Ligand as Tools for Anion Detection *J. Am. Chem. Soc.*, **2002**, 124, 7779 – 7788.
- 104 Charbonnière L. J., Weibel N., Estournes C., Leuvrey C., Ziessel R. Spatial and Temporal Discrimination of Silica Particles Functionalised with Luminescent Lanthanide Markers Using Time-resolved Luminescence Microscopy *New J. Chem.* **2004**, 28, 777 – 781.
- 105 Weibel N., Charbonniere L.J., Guardigli M., Roda A., Ziessel R. Engineering of Highly Luminescent Lanthanide Tags Suitable for Protein Labeling and Time-Resolved Luminescence Imaging *J. Am. Chem. Soc.*, **2004**, 126, 4888 – 4896.

- 106 <http://www.biotekstruments.ru/ru/resources/articles/time-resolved-fluorescent-compounds.html>
- 107 Parker D., Williams J.A.G. Responsive Luminescent Lanthanide Complexes. In Sigel A, Sigel H, editors. Metal Ions in Biological Systems, Vol. 40. The Lanthanides and their Interactions with Biosystems. *New York, NY: Marcel Dekker; 2003.*
- 108 Meyssamy H., Riwozki K., Kornowski A., Naused S., Haase M., Wet-Chemical Synthesis of Doped Colloidal Nanomaterials: Particles and Fibers of LaPO<sub>4</sub>:Eu, LaPO<sub>4</sub>:Ce and LaPO<sub>4</sub>:Ce,Tb *Adv. Mater.* **1999**, 11, 840 - 844.
- 109 Riwozki K., Meyssamy H., Kornowski A., Haase M. Liquid-Phase Synthesis of Doped Nanomaterials: Colloids of Luminescing LaPO<sub>4</sub>:Eu, CePO<sub>4</sub>:Tb 5 nm-Particles with Narrow Particle Size Distribution *J. Phys. Chem. B* 2000, 104, 2824 - 2828.
- 110 Riwozki K., Meyssamy H., Schnablegger H., Kornowski A., Haase M. Liquid-Phase Synthesis of Doped Nanomaterials: Colloids and Redispersible Powders of Strongly Luminescing LaPO<sub>4</sub>:Ce, Tb Nanocrystals *Angew. Chem.* **2001**, 40, 573.
- 111 Meiser F., Cortez C., Caruso F. Biofunctionalization of Fluorescent Rare-Earth-doped Lanthanum Phosphate Colloidal Nanoparticles *Angewandte Chemie* **2004**, 116, 6080 – 6083.
- 112 Setua S., Menon D., Asok A., Nair S., Koyakutty M. Folate Receptor Targeted, Rare-earth Oxide Nanocrystals for Bi-modal Fluorescence and Magnetic Imaging of Cancer Cells *Biomaterials* **2010**, 31, 714 – 729.
- 113 Wang M., Mi C., Zhang Y., Liu J., Li F., Mao C., Xu S. NIR-Responsive Silica-Coated NaYbF<sub>4</sub>:Er/Tm/Ho Upconversion Fluorescent Nanoparticles with Tunable Emission Colors and Their Applications in Immunolabeling and Fluorescent Imaging of Cancer Cells *J. Phys. Chem. C* **2009**, 113, 19021 - 19027.
- 114 Soga, K. Development of NIR fluorescence bioimaging system through polyscale technology *Bunseki Kagaku* **2009**, 58, 461 - 471.
- 115 Jiang, S.; Zhang, Y.; Lim, K. M.; Sim, E. K. W.; Ye, L., NIR-to-visible upconversion nanoparticles for fluorescent labeling and targeted delivery of siRNA. *Nanotechnology* **2009**, 20 (15).
- 116 Zhou, J.; Sun, Y.; Du, X.; Xiong, L.; Hu, H.; Li, F., Dual-modality in vivo imaging using rare-earth nanocrystals with near-infrared to near-infrared (NIR-to-NIR) upconversion luminescence and magnetic resonance properties. *Biomaterials* **2010**, 31 (12), 3287-3295.
- 117 Wang, M.; Mi, C.-C.; Wang, W.-X.; Liu, C.-H.; Wu, Y.-F.; Xu, Z.-R.; Mao, C.-B.; Xu, S.-K., Immunolabeling and NIR-Excited Fluorescent Imaging of HeLa Cells by Using NaYF<sub>4</sub>:Yb,Er Upconversion Nanoparticles. *Acs Nano* **2009**, 3 (6), 1580-1586.
- 118 Li Z., Zhang Y., Jiang S. Multicolor Core/shell-structured Upconversion Fluorescent Nanoparticles *Adv. Mat.* **2008**, 20, 4765 – 4769.

- 119 Park Y. I., Kim J. H., Kim J. H. Nonblinking and Nonbleaching Upconverting Nanoparticles as an Optical Imaging Nanoprobe and T<sub>1</sub> Magnetic resonance Imaging Contrast Agent *Adv. Mat.* **2009**, 21, 4467 – 4471.
- 120 Xiong L.-Q., Chen Z.-G., Yu M.-X., Li F.-Y., Liu C., Huang C.-H. Synthesis, Characterization, and *in vivo* Targeted Imaging of Amine-functionalized Rare-earth Upconverting Nanophosphors *Biomaterials* **2009**, 30, 5592 – 5600.

# 4.

## *Lanthanide-Chelate Grafted Silica Nanoparticles as Bimodal-Imaging Contrast Agents*

---

4.1. Introduction	113
4.2. Experimental Procedures	116
4.3. Results and Discussion	121
4.3.1 Characterization of Nanoparticles	121
4.3.2 Photoluminescence Properties	131
4.3.3 Relaxivity Properties	151
4.3.4 Cell Imaging	159
4.4. Conclusions	161
4.5. References	163

Chapter published as original article:

*Pinho S.L.C., Faneca H., Geraldes C.F.G.C., Delville M-H. Carlos L.D., Rocha J. Lanthanide-DTPA Grafted Silica Nanoparticles as Bimodal-Imaging Contrast Agents*

Publication in *Biomaterials* (2011), doi:10.1016/j.biomaterials.2011.09.086

*Pinho S.L.C., Faneca H., Geraldes C.F.G.C., Delville M-H. Carlos L.D., Rocha J Silica Nanoparticles for Bimodal MRI-Optical Imaging via Grafting of Gd<sup>3+</sup> and Eu<sup>3+</sup>/Tb<sup>3+</sup> Complexes*

Submitted to the *European Journal of Inorganic Chemistry*

#### 4.1. INTRODUCTION

Currently, clinical diagnostics and biomedical research employ an array of powerful *in vivo* imaging techniques, including confocal and Two-Photon Microscopy, Magnetic Resonance Imaging (MRI),<sup>1</sup> X-Ray Computed Tomography (CT),<sup>2</sup> Positron Emission Tomography (PET),<sup>3,4</sup> Single Photon Emission Computed Tomography (SPECT),<sup>5,6</sup> and Ultrasound.<sup>7</sup> Each of these techniques possesses unique strengths and weaknesses (spatial and temporal resolution and sensitivity limits), thus providing complementary information. Certain fused-modality instruments, such as PET/CT, have already appeared in the clinic.<sup>6</sup>

MRI has an excellent spatial resolution but suffers from low sensitivity, often requiring the administration of millimolar concentrations of commercial Gd<sup>3+</sup>-based contrast agents (CAs), in order to increase the intrinsic image contrast for an efficient detection of pathologies.<sup>8-12</sup> Radioactive tracers and optical imaging probes are orders of magnitude more sensitive and may be detected at much lower concentrations (picomolar or micromolar for PET or optical agents, respectively) but the corresponding imaging modalities have low spatial resolution.<sup>13,14</sup>

There has been an increasing interest in the development of multimodal imaging agents, integrating in a single molecular entity the requirements of MRI and a second imaging modality. Bimodal MRI and optical imaging probes combine the spatial resolution and unlimited tissue penetration of MRI with the sensitivity of optical imaging. The efficiency of this combined imaging technique has been demonstrated in studies

with animals. Modo *et al.* used a gadolinium-rhodamine-dextran agent to confirm by fluorescence microscopy that tracking of transplanted stem cells in ischemia-damaged rat hippocampus was possible by MRI.<sup>15</sup> Recently, several examples of bimodal agents have been synthesised and evaluated, including Gd<sup>3+</sup> complexes connected to organic dyes,<sup>16-18</sup> complexes of Gd<sup>3+</sup> and other visible<sup>19-24</sup> or near infrared (NIR)<sup>25,26</sup> emitting Ln<sup>3+</sup> ions, or various kinds of nanoparticle (NP) based systems.<sup>17-34</sup>

Lanthanide ions are particularly well suited for the design of bimodal MRI and optical agents.<sup>35</sup> Their unique electronic configuration affords exceptional magnetic and optical properties and similar chemical behaviour. Therefore, the replacement of one lanthanide by another, results in compounds with different physical properties but no major chemical differences. The advantage of using Gd<sup>3+</sup> complexes as MRI contrast agents has been largely demonstrated.<sup>8</sup> The Gd<sup>3+</sup> ion possesses seven unpaired electrons (highest spin density) and a symmetrical <sup>8</sup>S ground state, resulting in a slow electronic relaxation rate, and these are excellent features for reducing the longitudinal ( $T_1$ ) and transverse ( $T_2$ ) proton relaxation times of tissue water, thus enhancing image contrast. For example, [Gd(DTPA)(H<sub>2</sub>O)]<sup>2-</sup> has been approved for radiologic practice and medicine in 1988.<sup>36</sup>

All Ln<sup>3+</sup> ions, exception for La<sup>3+</sup> and Lu<sup>3+</sup>, are photoluminescent, some more efficient than others. Eu<sup>3+</sup> and Tb<sup>3+</sup> are the most commonly ions used because they emit in the visible spectrum (in the red and green regions, respectively) and have long luminescence lifetimes, in the millisecond range).<sup>14,37,38</sup> There are several advantages in using lanthanide complexes as luminescent probes versus organic dyes: *i*) resistance to photobleaching; *ii*) long-lived excited states, allowing the short-lived (ns range) biological background fluorescence to disperse before the lanthanide emission occurs; *iii*) absence of reabsorption; and *iv*) sharp emission bands (wavelengths are characteristic of the lanthanide).<sup>25</sup> Despite these positive features of lanthanides, reports on the use of Ln<sup>3+</sup> complexes in the design of combined MRI and optical probes are scarce.<sup>19-23</sup> The luminescence properties of the lanthanides ions may be enhanced by intramolecular energy transfer from moieties attached to the central ion, the so-called “antenna effect”. It is well known that the introduction of an aromatic ligand induces a considerable antenna effect, therefore enhancing the luminescence properties of the lanthanide ions.

Our approach is to combine the potential of the lanthanide complexes with the properties of NPs since these have the ability to *i*) carry large payloads of active

magnetic centres, therefore lowering the required concentrations, *ii*) be target-specific by labelling desired cells through phagocytic pathways, and *iii*) be grafted by molecules specific to cell surface markers. Many alternative designs of efficient nanosized carriers for MRI probes have been proposed.<sup>39,40</sup> Mesoporous silica nanoparticles (MSNs) have been shown to be very useful platforms for efficient relaxometric contrast agents because of their ability to carry a large payload of Gd<sup>3+</sup> chelates with high water accessibility and, thus, they have been used as multimodal probes after incorporation of a fluorescent dye into the silica carrier.<sup>41-46</sup> Core-shell hybrid nanoporous silica NPs containing a luminescent [Ru(bpy)<sub>3</sub>]Cl<sub>2</sub> core (bpy = 2,2'-bipyridine) and a paramagnetic monolayer coating of a silylated Gd(III) complex has also been studied.<sup>30,47,48</sup>

As a proof of concept, here report on the derivatization of nanoporous silica NPs with aminopropyltriethoxysilane (APS), followed by reaction with diethylenetriamine pentaacetic acid (DTPA) and complexation of Ln<sup>3+</sup> ions, forming the DTPA monoamide system SiO<sub>2</sub>@APS/DTPA:Ln (Ln = Eu<sup>3+</sup>, Tb<sup>3+</sup> and Gd<sup>3+</sup>). The thermodynamic stability constant of the Gd<sup>3+</sup>-DTPA complex is quite high, with a log K value of 22.46, which is very similar to the values for the Eu<sup>3+</sup> and Tb<sup>3+</sup> complexes.<sup>49</sup> It has been previously shown that, although the thermodynamic stability constants for Gd-DTPA monoamides decrease by log K ~2.6 relative to the Gd-DTPA ones, their blood pH conditional constants differ from Gd-DTPA only by log K ~1.2.<sup>50</sup> SiO<sub>2</sub>@APS/DTPA:Ln nanoparticles are not toxic<sup>51</sup> and similar materials accumulate mostly in the liver and spleen whereas the lung, kidney, and heart accounted for an accumulation of less than 5%.<sup>52</sup> The luminescence and water proton nuclear relaxation properties of these NPs both, in aqueous suspensions, and internalized in RAW 264.7 cells (mouse macrophage cell line), are studied in order to evaluate their usefulness as bimodal agents for MRI and optical imaging.

We also report the synthesis and grafting of nanoporous silica NPs with APS and a Ln<sup>3+</sup> complex with a ligand possessing an aromatic ring, which acts as an antenna for sensitizing Ln<sup>3+</sup>, thus improving light emission. Silica NPs are, thus, modified with 2,2',2'',2''' - [(pyridine-2,6-diyl)bis(methylenenitrilo)] tetrakis (acetic acid) (PMN), via a reaction with APS grafted on the NPs. Ln<sup>3+</sup> are complexed by PMN, forming the system SiO<sub>2</sub>@APS/PMN:Ln (Ln = Eu, Tb and Gd). The water proton nuclear relaxation and luminescence properties of such derivatized NPs in aqueous suspensions and internalized in RAW 264.7 cells (mouse macrophage cell line) cells are studied, in

order to assess their efficacy as Ln<sup>3+</sup>-based bimodal agents for MRI and optical imaging.

## 4.2. EXPERIMENTAL PROCEDURES

### ***Materials and purification methods***

EuCl<sub>3</sub> (99.99%), TbCl<sub>3</sub> (99.99%), GdCl<sub>3</sub> (99.99%), Tetraethoxysilane (TEOS) (98%), 3-aminopropyltrimethoxysilane (APS) (97%), diethylenetriamine pentaacetic bis-anhydride (DTPAA) (99.99%), 2,6-bis(bromomethyl) pyridine (98%), di(tert-butyl) iminobis(acetate) (98%), dry Na<sub>2</sub>CO<sub>3</sub> (99.5%), dry acetonitrile (MeCN) (99.8%), trifluoroacetic acid (CF<sub>3</sub>COOH) (99%) and diethyl ether (Et<sub>2</sub>O) (99.7%); N-hydroxysuccinimide (NHS) (98%), (1-Ethyl-3-[3-dimethyl aminopropyl]carbodiimide Hydrochloride (EDC) (99%) and Phosphate buffered saline (PBS) were purchased from Aldrich. Absolute ethanol (J.T. Baker) and ammonium hydroxide solution (5N) (Fluka) were used as received. All other reagents were of analytical grade. Water was deionized (resistivity larger than 18 MQ).

### ***Preparation of silica nanoparticles suspension***

The method used was derived from the so-called Stöber<sup>48,53</sup> process, widely used for the synthesis of silica beads with diameters from a few tens to a few hundreds of nanometers<sup>54</sup> and based on the hydrolysis/condensation of tetraethoxysilane (TEOS) catalyzed by ammonia in alcoholic media. Briefly, a solution of 250 mL of absolute ethanol and 17 mL ammonia was heated at 50 °C and 0.035 mol TEOS was added allowing reflux overnight. The average particle size, determined by transmission electron microscopy was 67 ± 6 nm.

### ***Preparation of the grafted amino-nanoparticles***

To the silica NPs suspension 4.5 mmol of APS (0.8 mL) were added and stirred for 3 h. The suspension was then left under reflux overnight. The nanoparticles were

then washed and purified by centrifugation three times with ethanol and then water to remove unreacted APS.

### ***Preparation of the DTPA-grafted amino-nanoparticles***

The amino-modified NPs suspension was centrifuged and the supernatant discarded, the wet NPs were slowly diluted in 20 mL of an ethanol-acetic acid solution 50/50 v/v % and 1 g of diethylene triaminepentaacetic bis-anhydride (DTPAA) was then slowly added to the solution (20/1 DTPAA/-NH<sub>2</sub>) at room temperature. The system was heated up and left to reflux overnight. The particles were filtered off and purified three times by centrifugation-redispersion in acetone-water 50/50 v/v % and finally three times in water.

### ***Preparation of the Ln<sup>3+</sup>- DTPA chelate-grafted amino-nanoparticles***

The DTPA-grafted NPs were redispersed in 20 mL of water. At room temperature, 0.3 mmol of LnCl<sub>3</sub> (0.11g for GdCl<sub>3</sub>) were slowly added to the colloidal suspension. This amount corresponds approximately to the quantity of molecules grafted onto the particles in the 20 mL of solution, assuming a coverage rate of 6 μmol/m<sup>2</sup>. After 24 h, the excess of unreacted Ln(III) was removed by centrifugation-redispersion three times in water.

### ***Preparation of the 2,2',2'',2'''-[(Pyridine-2,6-diyl)bis methylene nitrilo] tetrakis(acetic acid) compound (PMN)***

First the tetra(tert-butyl)2,2',2'',2'''-[(Pyridine-2,6-diyl)bis(methyleneni trilo)] tetrakis (acetate) compound (1) was synthesized. A mixture of 2,6-bis(bromomethyl)pyridine (318 mg, 1.20 mmol, solid), di(tert-butyl) iminobis(acetate) (588 mg, 2.40 mmol, solid), dry Na<sub>2</sub>CO<sub>3</sub> (630 mg, 6.0 mmol, solid) and dry MeCN (30 ml) was refluxed overnight under argon. Filtration (obtaining a yellow solution) and evaporation gave pure compound (yellow gel) (412 mg, 72%). <sup>1</sup>H-NMR (CDCl<sub>3</sub>) δ (ppm): 1.44 (s, 36 H); 3.47

(s, 8 H); 4.00 (s, 4 H); 7.48 (d, J = 7.5, 2 H); 7.63 (T, J = 7.5, 1 H). A solution of compound (1) (412 mg, 0.86 mmol) in CF<sub>3</sub>COOH (10 ml) was stirred for 2 h at RT. After evaporation, the mixture was triturated with Et<sub>2</sub>O and filtered to give pure compound (dark yellow gel) (288 mg, 92%). <sup>1</sup>H-NMR (DMSO) δ (ppm): 3.62 (s, 8 H); 4.24 (s, 4 H); 7.75 (d, J = 7.5, 2 H); 8.23 (t, J = 7.5, 1 H).

### ***Preparation of the PMN-grafted amino-nanoparticles***

The amino-modified NPs suspension was centrifuged and the supernatant discarded, the wet NPs were slowly diluted in 10 mL of PBS. While 0.5 g of PMN (1.35 x 10<sup>-3</sup> mol) were added to 15 mL of PBS, a yellow solution was formed. A solution of EDC was also prepared by adding 258.9 mg (1.35 x 10<sup>-3</sup> mol) in 4 mL of PBS. To the PMN solution 15.54 mg of NHS (1.35 x 10<sup>-4</sup> mol) was added and stirred at room temperature. Sequentially the EDC and NPs solutions were added, respectively. The system was left to react overnight. The particles were filtered off and purified three times by centrifugation-redispersion in water.

### ***Preparation of the Ln<sup>3+</sup>-PMN chelate-grafted amino-nano-particles***

The PMN-grafted NPs were redispersed in 20 mL of water. At room temperature, 33.3 μmol of LnCl<sub>3</sub> (8.78 mg for GdCl<sub>3</sub>) were slowly added to the colloidal suspension. This amount corresponds approximately to the quantity of molecules grafted onto the particles in the 10 mL of solution, assuming a coverage rate of 6 μmol/m<sup>2</sup>. After 24 h, the excess of unreacted Ln(III) was removed by centrifugation-redispersion three times in water.

### ***Cell culture and in vivo imaging***

RAW 264.7 cells (mouse macrophage cell line) were maintained at 37 °C, under 5% CO<sub>2</sub>, in Dulbecco's modified Eagle's medium-high glucose (DMEM-HG) (Sigma) supplemented with 10% (v/v) heat-inactivated fetal bovine serum (FBS) (Sigma), penicillin (100 U/mL) and streptomycin (100 μg/mL), and sodium bicarbonate (1.6 g/L). Cells were incubated with the respective NPs (2.5 x 10<sup>15</sup> Part/L for both types of NPs SAD:Ln and SAPMN:Ln ) at 37 °C, under 5% CO<sub>2</sub>, for 1 hour. After this incubation, cells were washed with PBS, fixed with 4% paraformaldehyde, for 15 min at room

temperature, and rinsed again with PBS. Then, cells were detached from the culture flasks by scraping, the cell suspensions were prepared in PBS and the cell pellets were obtained by centrifugation at 180g during 5 min.  $T_1$ -weighted MRI images of the cellular pellets were acquired on a 3.0 T Siemens TimTrio scanner, using a spin-echo sequence (TE = 12 ms, TR = 3000 ms, FOV= 100x 100, slice thickness = 3.00 mm, matrix = 128 x 256 at room temperature for SAD:Ln NPs and TE = 50 ms, TR = 3000 ms, FOV= 100x 100, slice thickness = 3.00 mm, matrix = 128 x 256 at room temperature for SAPMN:Ln NPs). The optical images were obtained by submitting the cellular pellets to a 450 W Xe arc lamp, as the excitation source and photographs were taken with a Canon 550D with EF-S 18-55mm.

### ***Particles Characterization***

TEM was performed at room temperature on a JEOL JEM-2000 FX transmission electron microscope using an accelerating voltage of 200 kV. Drops of diluted dispersions of nanoparticles were air-dried on carbon films deposited on 200-mesh copper grids. The excess liquid was blotted with filter paper. Diffuse Reflectance Infrared Fourier-Transform (DRIFT) spectra were recorded on a Bruker IFS Equinox 55FTIR spectrometer (signal averaging 64 scans at a resolution of  $4\text{ cm}^{-1}$  in KBr pellets containing *ca.* 2 mass % of material). The zeta potential of the nanoparticles was measured using a Zetasizer 3000HSA setup (Malvern Instruments) equipped with a He-Ne laser (50 mW, 532 nm). The zeta potential measurement based on laser Doppler interferometry was used to measure the electrophoretic mobility of nanoparticles. Measurements were performed for 20 s using a standard capillary electrophoresis cell. The dielectric constant was set to 80.4 and the Smoluchowsky constant  $f(\kappa a)$  was 1.5. The silica, europium, terbium, and gadolinium contents were measured by inductively coupled plasma / optical emission spectrometry ICP/OES (ES720, Varian) equipped with a crossflow nebulizer. Solutions for each element with a concentration of 1 g/L were used to prepare the standard solutions (SCP Science to Paris) and were used as internal standard to evaluate the instrumental drift.

The  $^{29}\text{Si}$  magic-angle spinning (MAS) nuclear magnetic resonance (NMR),  $^{29}\text{Si}$  cross-polarization (CP) MAS NMR and  $^{13}\text{C}$  CP/MAS NMR spectra were recorded on a Bruker Avance III 400 (9.4 T) spectrometer at 79.49 and 100.62 MHz, respectively.  $^{29}\text{Si}$  MAS NMR spectra were recorded with 2  $\mu\text{s}$  (tip angle *ca.*  $30^\circ$ ) rf pulses, a recycle delay of 60 s and 5.0 kHz spinning rate.  $^{13}\text{C}$  CP/MAS NMR spectra were recorded with 4  $\mu\text{s}$

$^1\text{H}$  90° pulses, 2 ms contact time, a recycle delay of 4 s and at a spinning rate of 8 kHz.  $^1\text{H}$  NMR spectra were recorded on a Bruker Avance-300 spectrometer at 300.13 MHz, using  $\text{CDCl}_3$  as the solvent. Chemical shifts are quoted in ppm from tetramethylsilane (TMS) and coupling constants  $J$  in Hz. Multiplicities are described with abbreviations as follow: s (singlet), d (doublet), t (triplet), q (quadruplet), m (multiplet). Spectra are described as  $\delta$  (multiplicity, number of protons, assignment, coupling constant).

$^1\text{H}$  longitudinal and transverse relaxation times ( $T_1$  and  $T_2$  respectively) of aqueous suspensions of nanoparticles were measured at 20 MHz on a Bruker Minispec mq20 relaxometer and at 499.83 MHz ( $B_0 = 11.7$  T) on a Varian Unity 500 NMR spectrometer, at 25 and 37 °C.  $T_1$  values were measured using the inversion recovery pulse sequence, while  $T_2$  values were measured using a Carr-Purcell-Meiboom-Gill (CPMG) pulse sequence. The time interval between two consecutive refocusing pulses ( $\tau_{CP}$ ) in the train of 180° pulses applied was 1.6 ms. The values of  $T_2^*$ , the transverse relaxation time in the presence local field inhomogeneities, were obtained from the water spectral line widths. All the experimental values were corrected for the diamagnetic contributions using aqueous suspensions of their respective NPs carrier  $\text{SiO}_2@$ APS/DTPA (SAD) and  $\text{SiO}_2@$ APS/PMN (SA/PMN) under the same conditions. The  $T_2$  values were also measured as a function of the  $\tau_{CP}$  parameter in a CPMG pulse sequence, for aqueous suspensions of the various NPs ( $\tau_{CP} = 0.05, 0.2, 0.4, 0.8, 1.6, 2, 3$ ).

The photoluminescence spectra were recorded between 14 K and room temperature with a modular double grating excitation spectrofluorimeter with a TRIAX 320 emission monochromator (Fluorolog-3, Jobin Yvon-Spex) coupled to a R928 Hamamatsu photomultiplier, using the front face acquisition mode. The excitation source was a 450 W Xe arc lamp. The emission spectra were corrected for detection and optical spectral response of the spectrofluorimeter and the excitation spectra were weighed for the spectral distribution of the lamp intensity using a photodiode reference detector. The lifetime measurements were acquired with the setup described for the luminescence spectra using a pulsed Xe-Hg lamp (6  $\mu\text{s}$  pulse at half width and 20–30  $\mu\text{s}$  tail). The absolute emission quantum yields were measured at room temperature using a Quantum Yield Measurement System C9920-02 from Hamamatsu with a 150 W Xenon lamp coupled to a monochromator for wavelength discrimination, an integrating sphere as sample chamber and a multi channel analyzer for signal detection.

## 4.3. RESULTS AND DISCUSSION

### 4.3.1. Characterization of Nanoparticles

Aqueous suspensions of silica NPs were synthesized by basic polymerization of silane monomers under Stöber conditions,<sup>48</sup> using an alcohol-water-ammonia medium and tetraethoxysilane (TEOS) as the silane precursor. TEM (Figure 4.1) reveals spherical, essentially monodispersed, particles with an average size of  $67 \pm 6$  nm (100 particles measured).

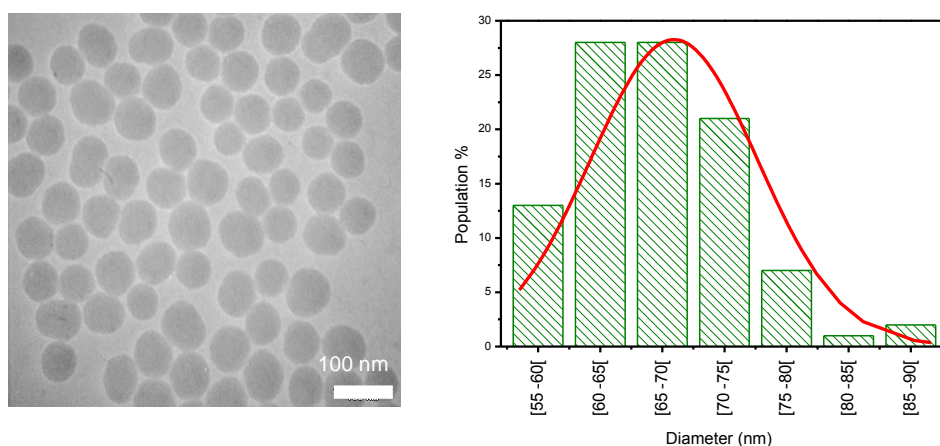


**Figure 4.1.** a) TEM images of the silica NPs; b) histogram depicting the experimental size distribution of the NPs and the corresponding calculated normal cumulative distribution for the specified mean and standard deviation.

These NPs were successively functionalized with APS, DTPA or PMN) and a lanthanide salt (Ln=Eu, Tb or Gd). The zeta potential titrations as a function of pH confirm the shift of the stability ranges of the NPs and the isoelectric points (IEPs) with the different modification steps (Figure 4.2).

After APS coating the suspension exhibited an IEP of *ca.*10 characteristic of the presence of free amino groups on the NPs surface.<sup>55-57</sup> Once the peptidic coupling (carboxyl groups from the DTPA or PMN with the free amino groups of the APS) was achieved, another clear shift of the IEP towards lower pH (IEP of *ca.* 6 for DTPA and *ca.* 5.5 for PMN) was observed. Upon coordination of the DTPA or PMN with  $\text{Eu}^{3+}$ ,  $\text{Tb}^{3+}$ ,  $\text{Gd}^{3+}$  (ions with similar association constants),<sup>58,59</sup> there was no major change of the IEP, which does not depend on the lanthanide chemical nature.<sup>55-59</sup>

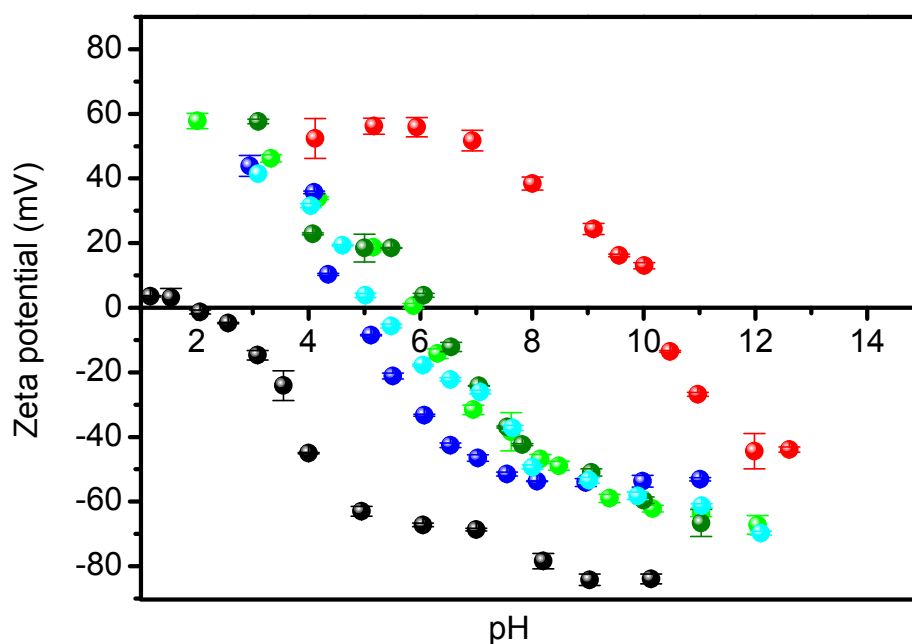


**Figure 4.2.** Zeta potential titrations as a function of pH for SiO<sub>2</sub> (S, ●), SiO<sub>2</sub>@APS (●), SiO<sub>2</sub>@APS/DTPA (●), SiO<sub>2</sub>@APS/PMN (●), SiO<sub>2</sub>@APS/DTPA:Ln (●) and SiO<sub>2</sub>@APS/PMN:Ln (●)

The amount of Ln<sup>3+</sup> ions present in the NPs strongly depends on the amount of DTPA (or PMN) grafted. Therefore, the same single set of DTPA or PMN grafted NPs was used throughout the study, presenting a ratio of *ca.* 10<sup>4</sup> ions per NP. As an example, Table 4.1 and Table 4.2 summarize the ICP data obtained on each sample for the quantification of Gd, Eu, Tb and Si.

**Table 4.1.** Elemental composition of samples SiO<sub>2</sub>@APS/DTPA:Ln (SAD:Ln) ascertained by ICP

	[Gd] (M)	[Eu] (M)	[Tb] (M)	[Si] (M)	[Gd] (Ions/NP)	[Eu] (Ions/NP)	[Tb] (Ions/NP)
SAD:Eu,Gd	1.50 × 10 <sup>-3</sup>	1.48 × 10 <sup>-3</sup>		0.820	9.59 × 10 <sup>3</sup>	9.46 × 10 <sup>3</sup>	
SAD:Tb,Gd	2.66 × 10 <sup>-3</sup>		3.15 × 10 <sup>-3</sup>	1.840	5.73 × 10 <sup>3</sup>		6.78 × 10 <sup>3</sup>
SAD:Eu,Tb		1.41 × 10 <sup>-3</sup>	1.24 × 10 <sup>-3</sup>	0.790		7.07 × 10 <sup>3</sup>	6.22 × 10 <sup>3</sup>

**Table 4.2.** Elemental composition of samples SiO<sub>2</sub>@APS/PMN:Ln (SAPMN:Ln) ascertained by ICP

	[Gd] (M)	[Eu] (M)	[Tb] (M)	[Si] (M)	[Gd] (Ions/NP)	[Eu] (Ions/NP)	[Tb] (Ions/NP)
SA/PMN:Eu		2.85 × 10 <sup>-3</sup>		0.162		7.0 × 10 <sup>4</sup>	
SA/PMN:Tb			3.37 × 10 <sup>-3</sup>	0.171			7.8 × 10 <sup>4</sup>
SA/PMN:Gd	3.33 × 10 <sup>-3</sup>			0.160	8.2 × 10 <sup>4</sup>		
SAP/MN:Eu,Gd	1.55 × 10 <sup>-3</sup>	1.62 × 10 <sup>-3</sup>		0.173	3.6 × 10 <sup>4</sup>	3.7 × 10 <sup>4</sup>	
SAP/MN:Tb,Gd	1.71 × 10 <sup>-3</sup>		1.57 × 10 <sup>-3</sup>	0.156	4.3 × 10 <sup>4</sup>		4.0 × 10 <sup>4</sup>
SAP/MN:Eu,Tb		1.71 × 10 <sup>-3</sup>	1.47 × 10 <sup>-3</sup>	0.157		4.3 × 10 <sup>4</sup>	3.7 × 10 <sup>4</sup>

DRIFT spectroscopy was also used to probe the effectiveness of the chemical modification for the SAD:Ln NPs<sup>48,51</sup> (Figure 4.3). The absorption bands in the DRIFT spectrum of the SiO<sub>2</sub>@APS samples (Figure 4.3) are assigned to APS and bare silica, evidencing the efficient APS-silanization of the silica NPs. The modification of the shape of the band at 3500 cm<sup>-1</sup> is due to the N-H vibrations. The 2983 cm<sup>-1</sup> and 2908 cm<sup>-1</sup> bands, assigned to the asymmetric and symmetric stretching vibrations of CH<sub>2</sub> groups of the grafted alkyl chain, confirm the anchoring of the amino propyl groups, as well as the presence of the 1631 cm<sup>-1</sup> and 1486 cm<sup>-1</sup> (the free and hydrogen bonding NH<sub>2</sub>, respectively), 800 cm<sup>-1</sup> (N-H bending mode), and 1448 cm<sup>-1</sup> (SiCH<sub>2</sub>) bands.

The following step was the chemical attachment of DTPA to the aminated NPs by the formation of an amide linkage between the primary amine group and one of the five carbonyl groups of DTPA. The occurrence of this chemical grafting was confirmed by the DRIFT spectrum with the formation of four absorption bands: one band characteristic of the secondary amide C=O stretch at 1685 cm<sup>-1</sup>, two due to asymmetrically coupled vibration (1631 cm<sup>-1</sup>) and symmetrically coupled stretching (1396 cm<sup>-1</sup>) of the two C-O bonds of the carboxylate anion, and the fourth band is characteristic of the C-N vibration stretch at 937 cm<sup>-1</sup> (Figure 4.3).

Evidence for the chelation of Ln<sup>3+</sup> (Ln= Gd, Eu, Tb) is also forthcoming from DRIFT spectroscopy.<sup>49</sup> Band assignments of the asymmetric and symmetric stretching vibrations of CH<sub>2</sub> groups of the grafted alkyl chain (2977 cm<sup>-1</sup>, 2935 cm<sup>-1</sup> and 2900 cm<sup>-1</sup>

<sup>1</sup>) and the 1415 cm<sup>-1</sup> (hydrogen bonding NH<sub>2</sub>), 804 cm<sup>-1</sup> (N-H bending mode), and 1448 cm<sup>-1</sup> (SiCH<sub>2</sub>) were identified. The complexation of the Ln<sup>3+</sup> induced a slight bathochromic shift of the two CO absorption bands, from 1631 to 1579 cm<sup>-1</sup> and 1396 to 1415 cm<sup>-1</sup> respectively, and the secondary amide (C=O) 1680 to 1685 cm<sup>-1</sup>. Finally, the C-N vibrational stretch remained unchanged at 937 cm<sup>-1</sup>.

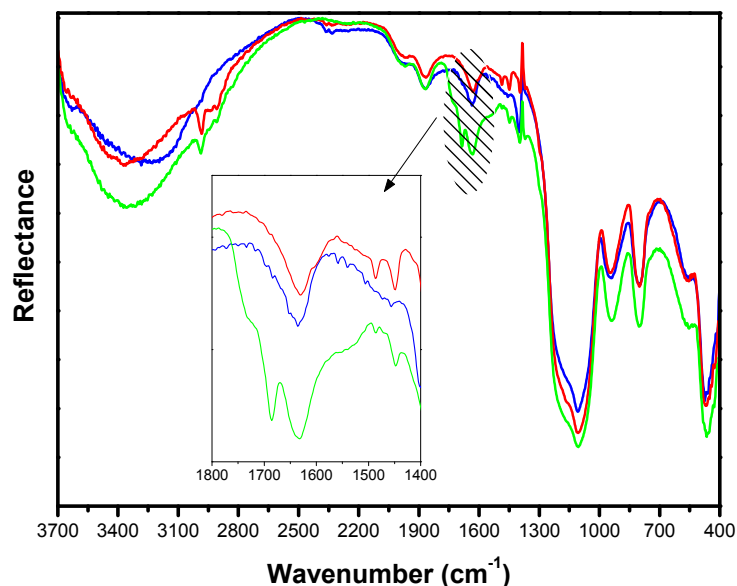


**Figure 4.3.** Diffuse Reflectance IR Fourier-Transform spectra (DRIFT) of (a) silica NPs (blue line), SiO<sub>2</sub>@APS (red line) and SiO<sub>2</sub>@APS/DTPA (green line). The inset depicts a selected region of the spectra.

Regarding SiO<sub>2</sub>@APS/PMN:Ln, DRIFT spectroscopy provided evidence for the grafting of APS to the SiO<sub>2</sub> surface<sup>60</sup> but no confirmation for the reaction between APS and PMN. Information on the latter was, however, forthcoming from solid-state NMR.

The <sup>13</sup>C CP/MAS NMR spectra of the SiO<sub>2</sub>, SiO<sub>2</sub>@APS and SiO<sub>2</sub>@APS/DTPA NPs are shown in Figure 4.4 (see also Table 4.3). The spectrum of the SiO<sub>2</sub> NPs reveals the presence of small amounts of ethanol (peaks at *ca.* 19 and 58 ppm). The spectrum of SiO<sub>2</sub>@APS displays three broad resonances, due to the Si-bonded propyl chains, at *ca.* 42 (C3), 22 (C2) and 9 ppm (C1).<sup>61</sup> Finally, the spectrum of SiO<sub>2</sub>@APS/DTPA contains the three APS peaks as well as broad resonances in the ranges 165-180 (carboxylate groups) and 50-65 ppm (remaining carbons) assigned to DTPA. Peaks from impurities are also present at *ca.* 25 ppm (acetic acid), 18 ppm (ethanol) and 30 ppm (acetone).

The  $^{29}\text{Si}$  CP/MAS and MAS NMR spectra of the derivatized NPs are shown in Figure 4.4B and C, respectively. The former exhibit resonances at *ca.* -92, -101 and -111 ppm, ascribed to  $\text{Q}^n(4-n)(\text{OH})$  local environments ( $^{29}\text{Si}$  linked to  $n$   $^{29}\text{Si}$  atoms via bridging O), respectively  $\text{Q}^2(2\text{OH})$  (such as geminal silanols),  $\text{Q}^3(\text{OH})$  (single silanols) and  $\text{Q}^4$  (siloxane).<sup>62</sup> The faint and broad resonance observed at *ca.* -66 ppm is ascribed to the organosiloxane ( $\text{T}^3$ ) atoms  $\text{R}'\text{Si}(\text{OSi})_3$ ,<sup>51</sup> providing evidence for the chemical bonding of APS to the surface of the silica NPs. The presence of  $\text{T}^2$  environments cannot be disregarded because the peak centred at -66 ppm is asymmetric, and may contain an unresolved resonance at *ca.* -60 ppm.<sup>63</sup> We note that several different  $\text{T}^3$  sites are possible in the aminosilane layer, as discussed, for example, in Albert et al.,<sup>63</sup> (Scheme 4.1 is, thus, just illustrative). Further evidence for such coupling is forthcoming from both the  $^{29}\text{Si}$  CP/MAS and MAS NMR spectra because the number of NPs surface hydroxyl groups decreases upon derivatization with APS: the population ratio  $(\text{Q}^2+\text{Q}^3)/\text{Q}^4$  (measured from the MAS NMR spectrum) decreases from 0.43 to 0.37.

Upon reaction of  $\text{SiO}_2@\text{APS}$  with DTPA, the number of silanol groups rises again:  $(\text{Q}^2+\text{Q}^3)/\text{Q}^4$  increases from 0.37 to 0.62. This is evidence for strong interactions between the amino group and silica surface silanols, when immobilized on silica gel via hydrogen-bonding interactions and formation of a five-membered cyclic intermediate. These results confirm previous reports, which provided evidence for a cyclic structure of the aminosilane layer based on models of five- or six- membered rings in which the nitrogen atoms interact with either the Si atom or one of the SiOH groups.<sup>64,65</sup> The existence of six-member ring models, containing either a  $\text{SiO}\cdots\text{NH}^+\text{H}(\text{R})$  or a  $\text{SiOH}\cdots\text{NH}(\text{R})$  bonding structure was also assumed using XPS results<sup>66,67</sup> and FTIR and Raman spectroscopy.<sup>68</sup>

The intensity of the  $\text{T}^3$  ( $+\text{T}^2$ ) CP/MAS peak decreases upon addition of DTPA (although this must be taken with caution because the CP/MAS spectra are not *a priori* quantitative). These results indicate that the reaction of  $\text{SiO}_2@\text{APS}$  with DTPA has the side effect of also modifying somewhat the  $\text{SiO}_2$  NPs surface.

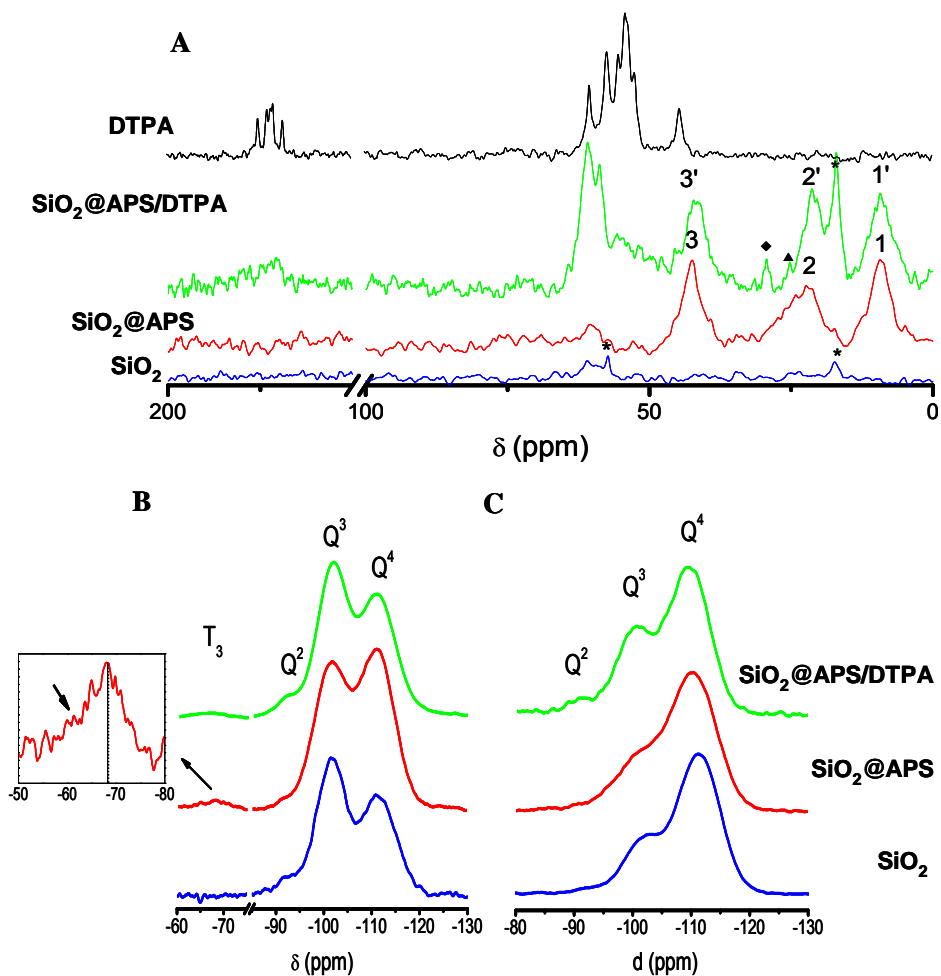
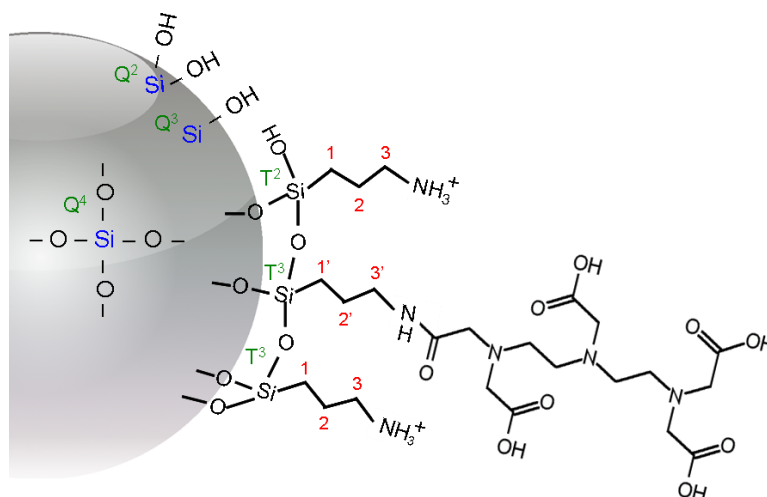


**Figure 4.4.**  $^{13}\text{C}$  CP/MAS NMR spectra of the  $\text{SiO}_2$  (blue),  $\text{SiO}_2$ @APS (red),  $\text{SiO}_2$ @APS/DTPA (green) and DTPA (black). (\* Ethanol,  $\blacktriangle$  Acetic acid and  $\blacklozenge$  Acetone) B)  $^{29}\text{Si}$  CP/MAS NMR spectra of the  $\text{SiO}_2$  (blue),  $\text{SiO}_2$ @APS (red) and  $\text{SiO}_2$ @APS/DTPA (green) C)  $^{29}\text{Si}$  MAS NMR spectra of the  $\text{SiO}_2$  (blue),  $\text{SiO}_2$ @APS (red) and  $\text{SiO}_2$ @APS/DTPA (green). The inset in B shows an expansion of the T region, exhibiting an asymmetric peak; the arrow depicts the region of a possible resonance from  $\text{T}^2$  environments.



**Scheme 4.1.** Representation of a SiO<sub>2</sub>-NPs functionalized with APS and coupled with DTPA.

**Table 4.3.** <sup>13</sup>C CP/MAS and <sup>29</sup>Si MAS NMR chemical shifts for SiO<sub>2</sub>, SiO<sub>2</sub>@APS and SiO<sub>2</sub>@APS/DTPA NPs and quantification of the <sup>29</sup>Si Q<sup>n</sup> resonances.

<sup>13</sup> C		<sup>29</sup> Si		SiO <sub>2</sub>	SiO <sub>2</sub> @APS	SiO <sub>2</sub> @APS/DTPA
Assignment	δ/ppm	Assignment	δ/ppm	δ/ppm	δ/ppm	δ/ppm
C 1	9	Q <sup>2</sup>	-92.7 (2.8%)	-92.8 (3.0%)	-91.0 (4.6%)	
C 1'	9	Q <sup>3</sup>	-102.1 (27.1%)	-100.9 (23.9%)	-100.3 (33.7%)	
C 2	23	Q <sup>4</sup>	-111.5 (70.1%)	-110.4 (73.1%)	-109.6 (61.7%)	
C 2'	22					
C 3	42					
C 3'	42					
DTPA	~170 – 180	T <sup>3</sup>		-65.4	-66.4	
DTPA	~58 – 62					
DTPA	~50					
DTPA	~55					

In the case of the SiO<sub>2</sub>@APS/PMN, the <sup>13</sup>C CP/MAS NMR spectra (Figure 4.5a) of SiO<sub>2</sub> and SiO<sub>2</sub>@APS/PMN exhibit two main peaks at 17.3 and 57.4-57.8 ppm, attributed to remains of ethanol solvent. The spectrum of SiO<sub>2</sub>@APS displays three broad resonances, given by the APS Si-bonded propyl chains, at ca. 42 (C3), 22 (C2) and 9 ppm (C1).<sup>60,61</sup> Although fainter, these resonances are also present in the spectrum of SiO<sub>2</sub>@APS/PMN, thus showing that the sample contains APS (albeit less). The <sup>29</sup>Si CP/MAS and MAS NMR spectra of the derivatized NPs are shown in Figures 4.5b and 4.5c, respectively. The former exhibit resonances at ca. - 92, - 101 and - 111 ppm, ascribed to Q<sup>n</sup>(4-n)(OH) local environments (<sup>29</sup>Si linked to n <sup>29</sup>Si atoms via bridging O), respectively Q<sup>2</sup>(2OH) (such as geminal silanols), Q<sup>3</sup>(OH) (single silanols) and Q<sup>4</sup> (siloxane).<sup>62</sup>

The faint resonance observed at ca. -67 ppm in the <sup>29</sup>Si CP/MAS and MAS NMR spectra of SiO<sub>2</sub>@APS and SiO<sub>2</sub>@APS/PMN is ascribed to the organosiloxane (T<sup>3</sup>) atoms R'Si(OSi)<sub>3</sub>,<sup>51</sup> providing evidence for the chemical bonding of APS to the surface of the silica NPs. Since the peak centred at - 67 ppm is asymmetric and may contain an unresolved resonance at ca. - 61 ppm therefore a T<sup>2</sup> environments cannot be disregarded.<sup>63</sup> As already proposed,<sup>60</sup> both the <sup>29</sup>Si CP/MAS and MAS NMR spectra: when the number of NPs surface hydroxyl groups decreases upon derivatization with APS, the population ratio (Q<sup>2</sup> + Q<sup>3</sup>)/Q<sup>4</sup> (measured from the MAS NMR spectrum) decreases from 0.43 to 0.37 (Table 4.3).

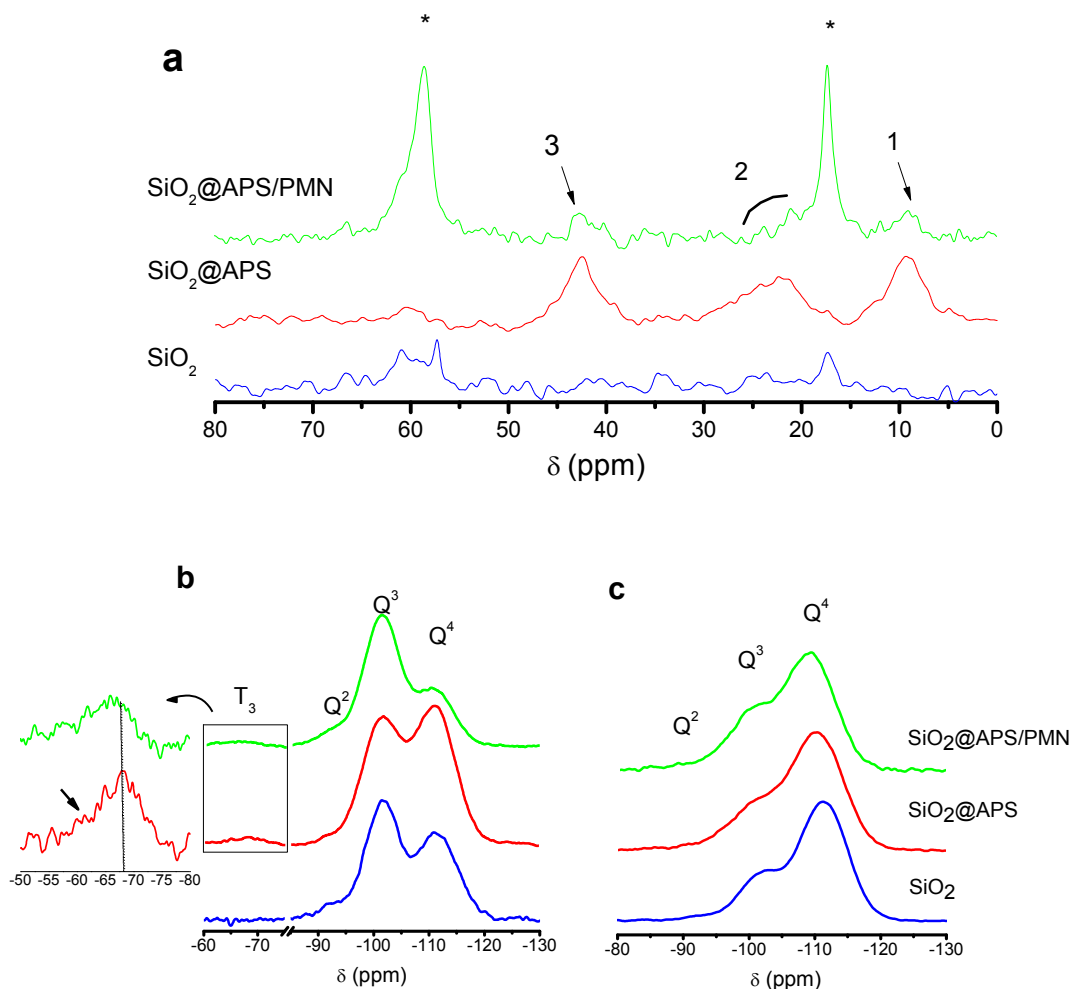
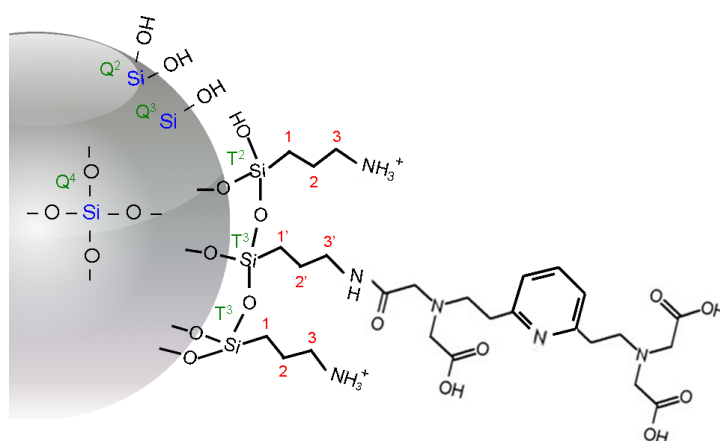


**Figure 4.5.** (a)  $^{13}\text{C}$  CP/MAS NMR spectra of the  $\text{SiO}_2$  (blue),  $\text{SiO}_2@$ APS (red) and  $\text{SiO}_2@$ APS/PMN (green). (\* Ethanol) (b)  $^{29}\text{Si}$  CP/MAS and (c)  $^{29}\text{Si}$  MAS NMR spectra of  $\text{SiO}_2$  (blue),  $\text{SiO}_2@$ APS (red) and  $\text{SiO}_2@$ APS/PMN (green). The inset in (b) expansion of the T region, exhibiting an asymmetric peak; the arrow depicts the region of a possible resonance from  $\text{T}^2$  environments.

**Table 4.3.**  $^{13}\text{C}$  CP/MAS and  $^{29}\text{Si}$  MAS NMR chemical shifts for  $\text{SiO}_2$ ,  $\text{SiO}_2@\text{APS}$  and  $\text{SiO}_2@\text{APS}/\text{PMN}$  NPs and quantification of the  $^{29}\text{Si}$   $Q^n$  resonances.

$^{29}\text{Si}$	$\text{SiO}_2$	$\text{SiO}_2@\text{APS}$	$\text{SiO}_2@\text{APS}/\text{DTPA}$
Assignment	$\delta/\text{ppm}$	$\delta/\text{ppm}$	$\delta/\text{ppm}$
$Q^2$	-92.7 (2.8%)	-92.8 (3.0%)	-92.3 (3.5%)
$Q^3$	-102.1 (27.1%)	-100.9 (23.9%)	-100.4 (30.2%)
$Q^4$	-111.5 (70.1%)	-110.4 (73.1%)	-109.3 (66.3%)
$T^3$		-65.4	-66.4

Upon coupling of PMN to  $\text{SiO}_2@\text{APS}$ , the number of silanol groups increases again:  $(Q^2 + Q^3)/Q^4$  from 0.37 to 0.51. This suggests that some APS is removed from the NPs surface, in accordance with the observation that the  $T^3$   $^{29}\text{Si}$  CP/MAS peak decreases concomitantly. It may also indicate strong interactions between the amino groups and silica surface silanols. As already mentioned possible hydrogen-bonding interactions and formation of a five-membered cyclic intermediate may occur when the amino groups are immobilized on the silica gel.



**Scheme 4.2.** Representation of a  $\text{SiO}_2$ -NPs functionalized with APS and coupled with PMN.

### 4.3.2. Photoluminescence Properties

#### **SiO<sub>2</sub>@APS/DTPA:Ln NPs**

The emission (steady-state and time-resolved) and excitation properties of the solids and samples in suspension were investigated. Figure 4.6 a displays the 300 K emission spectra of SiO<sub>2</sub>@APS/DTPA:Eu in the solid state excited at three different wavelengths. No energy shifts are observed for any transition when the wavelength is varied, indicating a single local environment for the Eu<sup>3+</sup> ions. This conclusion is also valid for suspensions of NPs, for which the only differences relative to the solid-state spectrum are the relative intensities of the intra-4f Stark components (Figure 4.7). The spectra comprise a series of sharp lines, assigned to the Eu<sup>3+</sup> <sup>5</sup>D<sub>0</sub>→<sup>7</sup>F<sub>0-4</sub> transitions, and a strong broad band between 380 and 560 nm, ascribed to the emission of the SiO<sub>2</sub>@APS/DTPA host. Figure 4.8 shows the emission spectra (300 K) of SiO<sub>2</sub>@APS/DTPA recorded with different excitation wavelengths. The spectra consist of two strong Gaussian-shape broad bands, at 280 - 320 nm and 320 - 600 nm, whose maximum shifts to the red as the excitation wavelength increases. The excitation spectra were monitored along with the hybrid host's emission (inset of Figure 4.8). They consist of two broad bands, between 240 and 300 nm and between 300 and 430 nm whose maximum shifts to the red<sup>69-72</sup>

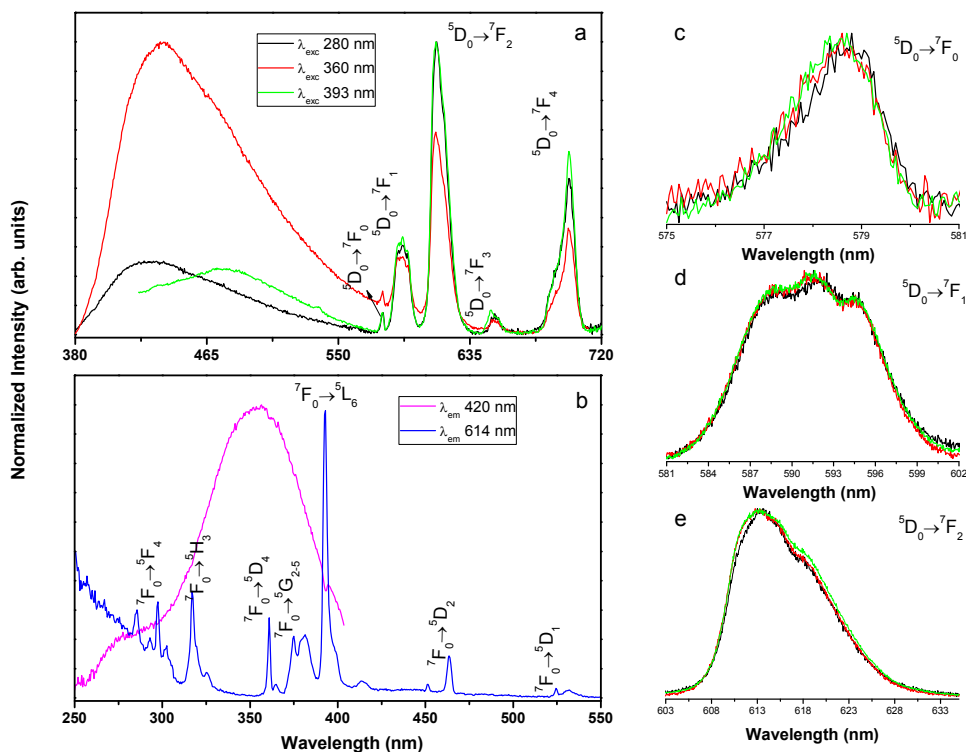


**Figure 4.6.** (a) Emission spectra (300 K) of SiO<sub>2</sub>@APS/DTPA:Eu (solid state) excited at 280 (black), 360 (red) and 393 nm (green); (b) Excitation spectra (300 K) of SiO<sub>2</sub>@APS/DTPA:Eu (solid state) monitored at 420 (magenta) and 614 nm (blue); (c) (d), and (e) show a magnification of the  $^5D_0 \rightarrow ^7F_{0-2}$  transitions.

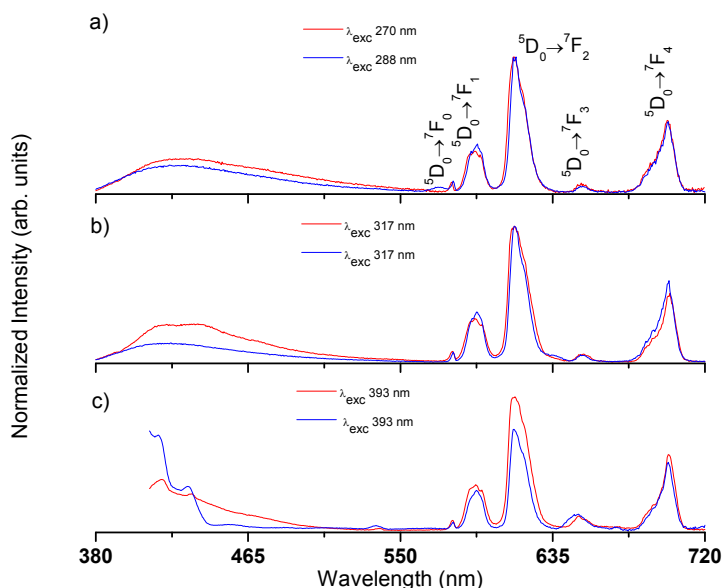


**Figure 4.7.** Emission spectra (300 K) of the SiO<sub>2</sub>@APS/DTPA:Eu in water solution (blue), solid state at 300K (red) excited at different wavelengths.

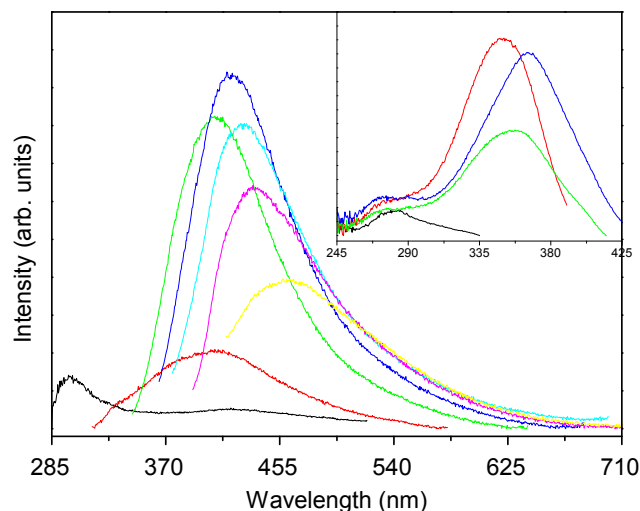


**Figure 4.8.** Emission spectra (300 K) of the SiO<sub>2</sub>@APS/DTPA excited at 270 (black), 300 (red), 330 (green), 350 (blue), 360 (cyan), 375 (magenta) and 400 nm (yellow). The inset shows the excitation spectra (300 K) monitored at 350 (black), 405 (red), 430 (green) and 450 nm (blue).

To shed more light onto the origin of this broad band, Figure 4.9 compares the emission spectra of the host in SiO<sub>2</sub>, SiO<sub>2</sub>@APS, SiO<sub>2</sub>@APS/DTPA and SiO<sub>2</sub>@APS/DTPA:Eu. In accord with previous results,<sup>68</sup> the Gaussian-shape broad band shifts to the blue with the addition of APS, from 440 (SiO<sub>2</sub>) to 430 nm (SiO<sub>2</sub>@APS, SiO<sub>2</sub>@APS/DTPA and SiO<sub>2</sub>@APS/DTPA:Eu). The full-width-at-half-maximum (fwhm) decreases from 133.8 (SiO<sub>2</sub>) to 109.0 (SiO<sub>2</sub>@APS), 99.7 (SiO<sub>2</sub>@APS/DTPA) and 84.8 nm (SiO<sub>2</sub>@APS/DTPA:Eu). The SiO<sub>2</sub> and the SiO<sub>2</sub>@APS emission spectra are in agreement with spectra reported for analogous materials and are ascribed to oxygen defects in the silica skeleton.<sup>69,70</sup> It should be noted that no calcination was used, whereas previous works report luminescence properties only after calcination.<sup>69,70</sup>

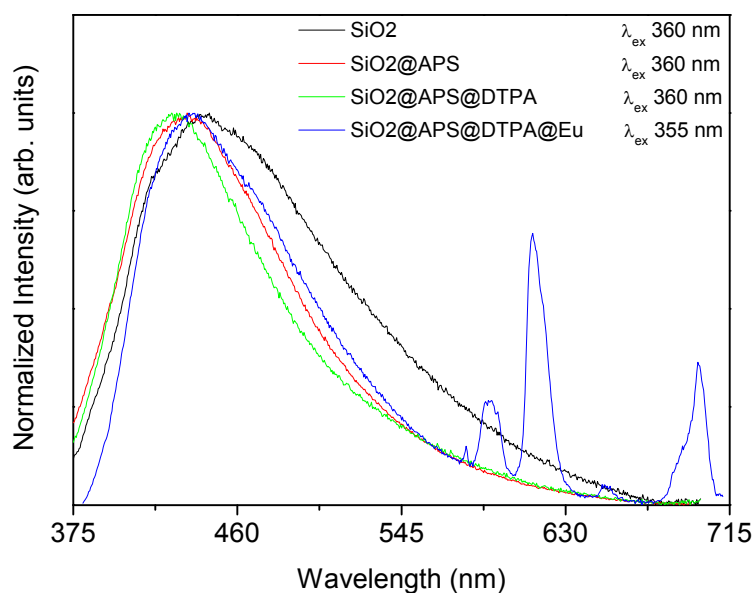


**Figure 4.9.** Emission spectra (300 K) of the SiO<sub>2</sub> (black), SiO<sub>2</sub>@APS (red), SiO<sub>2</sub>@APS/DTPA (green) and SiO<sub>2</sub>@APS/DTPA:Eu (blue) excited at 360 nm.

The SiO<sub>2</sub>@APS/DTPA:Eu emission spectra exhibit a series of sharp lines ascribed to the Eu<sup>3+</sup>  $^5D_0 \rightarrow ^7F_{0-4}$  intra-4f<sup>6</sup> transitions upon 280 and 360 nm excitation (host excited states, Figures 4.6 and 4.10) providing clear evidence for the energy transfer from the host to the Eu<sup>3+</sup> ion. The comparison between the emission spectra of DTPA:Eu and SiO<sub>2</sub>@APS/DTPA:Eu, displayed in Figure 4.11 (in particular the energy and fwhm of the  $^5D_0 \rightarrow ^7F_0$  line and the energy and relative intensities of the  $^7F_{1-4}$  Stark components), indicates an effective interaction between the Eu<sup>3+</sup> ions and the SiO<sub>2</sub>@APS/DTPA host, completely different from that observed for the DTPA:Eu complex.

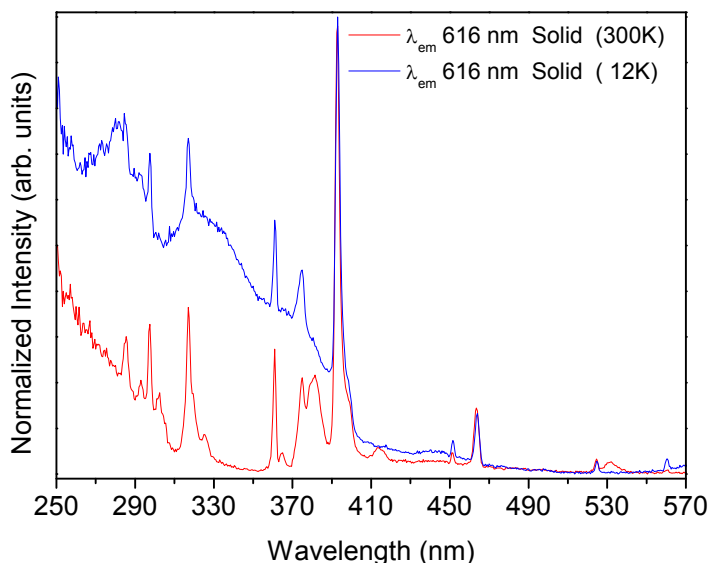


**Figure 4.10.** Excitation spectra of the SiO<sub>2</sub>@APS/DTPA:Eu monitored at 616 nm at different temperatures 300K (red) and 12K (blue).

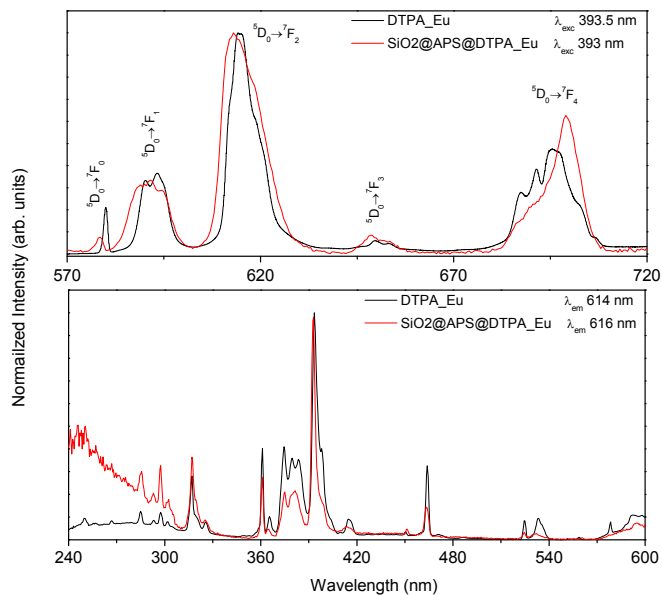


**Figure 4.11. Top:** Emission spectra (300 K) of the DTPA:Eu (black) and SiO<sub>2</sub>@APS/DTPA:Eu (red) excited at 393.5 nm and 393 nm, respectively; **Bottom:** Excitation spectra (300 K) of the DTPA:Eu (black) and SiO<sub>2</sub>@APS/DTPA:Eu (red) monitored at 614 nm and 616 nm, respectively.

The excitation spectra (300 K) of the same  $\text{SiO}_2\text{@APS/DTPA:Eu}$  system monitored at 420 nm (magenta) and 614 nm (blue), (Figure 4.6b), show two strong broad bands at 275 and 340 nm overlapping with a series of sharp lines ascribed to the  $\text{Eu}^{3+}$  intra-  $4f^6$  transitions between the  ${}^7F_0$  and the  ${}^5L_6$ ,  ${}^5D_{4,2,1}$ ,  ${}^5F_4$ ,  ${}^5H_3$ ,  ${}^5G_{2-5}$  levels. Lowering the temperature from 300 to 14 K, the relative intensity of the hybrid host bands increases and a new band appears at 330 nm (Figure 4.10). This temperature dependence supports the assignment of this new excitation band to a ligand-to-metal charge transfer (LMCT) transition, resulting from the interaction between the host and the  $\text{Eu}^{3+}$  ions.<sup>73</sup>

In order to get further insight into the  $\text{Eu}^{3+}$  local coordination, the  $4f^6$  emission lines were recorded at high resolution (Figure 4.6c-e). The detection of a single  ${}^5D_0 \rightarrow {}^7F_0$  line ( $17289.0 \pm 1.5 \text{ cm}^{-1}$ ) and the J-degeneracy splitting of the  ${}^7F_{1,2}$  levels into three Stark components, observed over the entire range of excitation wavelengths used, indicate that the  $\text{Eu}^{3+}$  cations reside in a single low-symmetry site. The larger intensity of the electric-dipole  ${}^5D_0 \rightarrow {}^7F_2$  transition, relative to the intensity of the magnetic-dipole  ${}^5D_0 \rightarrow {}^7F_1$  transition, indicates the absence of an inversion centre for the  $\text{Eu}^{3+}$  site.

The calculated value of the  ${}^5D_0 \rightarrow {}^7F_0$  fwhm,  $\sim 59 \text{ cm}^{-1}$ , is much larger than the values ( $20\text{-}30 \text{ cm}^{-1}$ )<sup>74</sup> reported for other organic-inorganic hybrids, suggesting for the  $\text{Eu}^{3+}$  ions a large distribution of similar local sites. The room-temperature  ${}^5D_0$  emission decay curve, monitored within the  ${}^5D_0 \rightarrow {}^7F_2$  transition at 614 nm and excited at 393 nm, is well fitted by a single exponential function, yielding a  ${}^5D_0$  lifetime of  $0.35 \pm 0.02 \text{ ms}$  (Figure 4.12). The slight deviation from a mono-exponential of the decay curve is in agreement with the aforementioned large distribution of the  $\text{Eu}^{3+}$  ions in similar local sites. Therefore, a decrease in the lifetime relative to the non-grafted monomeric complex  $[\text{Eu}(\text{DTPA})]^{2-}$  (structure already well characterized and studied<sup>75</sup>) is observed due to changes in the local environment of the  $\text{Eu}^{3+}$  ion.

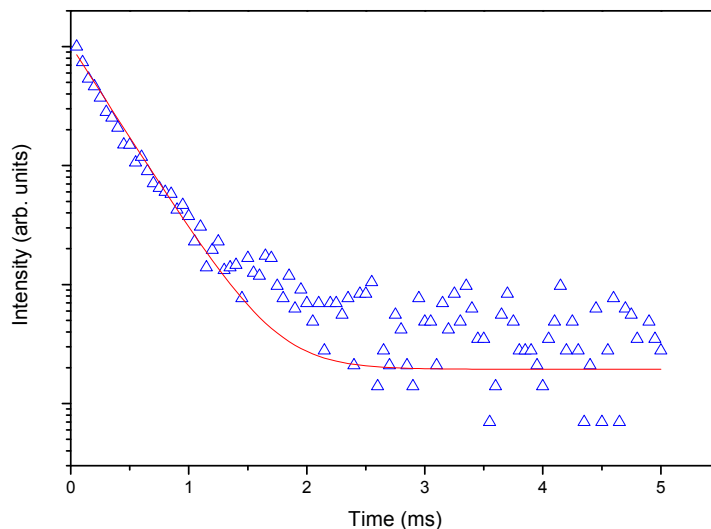


**Figure 4.12.** Emission decay curve of  $\text{Eu}^{3+}$  excited states ( ${}^5\text{D}_0$ ) from the sample  $\text{SiO}_2@\text{APS}/\text{DTPA}:\text{Eu}$ , which were monitored at 614 nm and excited 393 nm (blue), at 300 K in the solid state.

The experimental  $\Omega_2$  and  $\Omega_4$  intensity parameters were determined from the emission spectra shown in Figure 4.6 using the  ${}^5\text{D}_0 \rightarrow {}^7\text{F}_2$  and  ${}^5\text{D}_0 \rightarrow {}^7\text{F}_4$  electronic transitions, respectively, and expressing the emission intensity (I) in terms of the surface (S) under the emission curve as equation 3.5.

The branching ratio for the  ${}^5\text{D}_0 \rightarrow {}^7\text{F}_{5,6}$  transitions must be neglected as they are not observed experimentally and their influence on the depopulation of the  ${}^5\text{D}_0$  excited state may be ignored, and the  $\Omega_6$  parameter is not determined. The  ${}^5\text{D}_0 \rightarrow {}^7\text{F}_1$  transition does not depend on the local ligand field and may be used as a reference for the whole spectrum. An effective refractive index of 1.5 was used leading to  $A_{01} \approx 50 \text{ s}^{-1}$ .<sup>76</sup> The radiative emission rate is given by as equation 3.6:<sup>74,77,78,79</sup>

The  ${}^5\text{D}_0$  radiative ( $A_r$ ) and non-radiative ( $A_{nr}$ ) transition probabilities were determined for sample  $\text{SiO}_2@\text{APS}/\text{DTPA}:\text{Eu}$  and are  $0.3116 \text{ ms}^{-1}$  and  $3.0217 \text{ ms}^{-1}$ , respectively. The quantum efficiency ( $\eta$ ) [ $\eta = A_r / (A_r + A_{nr})$ ] was estimated based on the emission spectrum and the  ${}^5\text{D}_0$  lifetime ( $\tau^{-1} = A_r + A_{nr}$ ) as  $\eta = 0.09$ . This small value is essentially due to the high  $A_{nr}$  value. The emission absolute quantum yield ( $\phi$ ) was measured and found less than 0.01. The Judd-Ofelt intensity parameters ( $\Omega_{2,4}$ ) were  $1.10 \times 10^{-20} \text{ cm}^2$  and  $1.02 \times 10^{-20} \text{ cm}^2$ , respectively.

The photoluminescence characterization of the  $\text{SiO}_2@\text{APS/DTPA:Tb}$  sample was also carried out and gave similar results (Figures 4.13, 4.14, 4.15, and 4.16). Figure 4.13a displays the emission spectra at 300 K of the  $\text{SiO}_2@\text{APS/DTPA:Tb}$  in the solid state excited at 285 nm (black) and 377 nm (red). The spectra consist of a large broad band between 380 and 520 nm, ascribed to the emission of the  $\text{SiO}_2@\text{APS/DTPA}$  host, as for the Europium system, and of a series of straight lines assigned to the  $\text{Tb}^{3+}$   $^5\text{D}_4 \rightarrow ^7\text{F}_{6-0}$  intra-4f<sup>8</sup> transitions. No energy shifts are observed for any transition when the wavelength is varied, indicating that the  $\text{Tb}^{3+}$  ion is in a single local environment. This conclusion is also valid in solution at 300 K, where the only difference detected relatively to the spectrum recorded in the solid state is in the relative intensities of the intra-4f Stark components (see Figure 4.14).

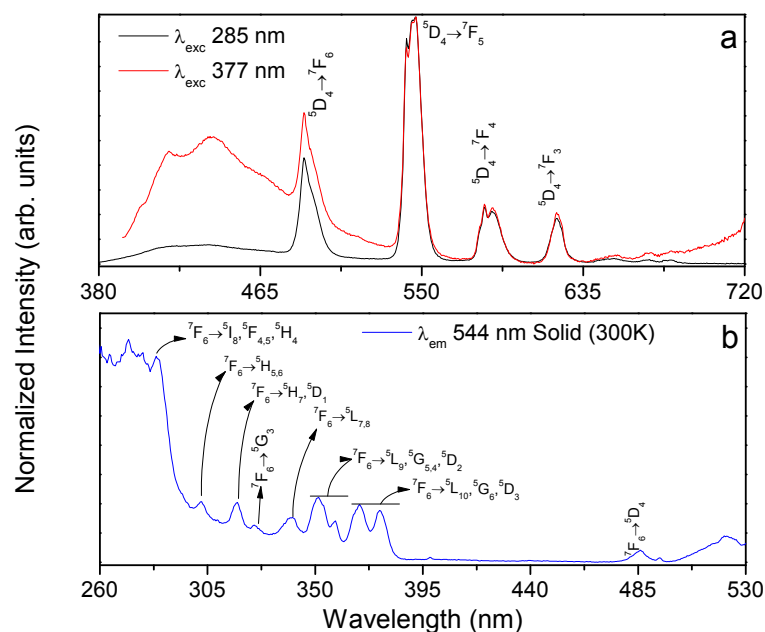


**Figure 4.13. (a)** Emission spectra (300 K) of the  $\text{SiO}_2@\text{APS/DTPA:Tb}$  (solid state) excited at 285 nm (black) and 377 nm (red); **(b)** Excitation spectra (300 K) of the  $\text{SiO}_2@\text{APS/DTPA:Tb}$  (solid state) monitored at 544 nm (blue).

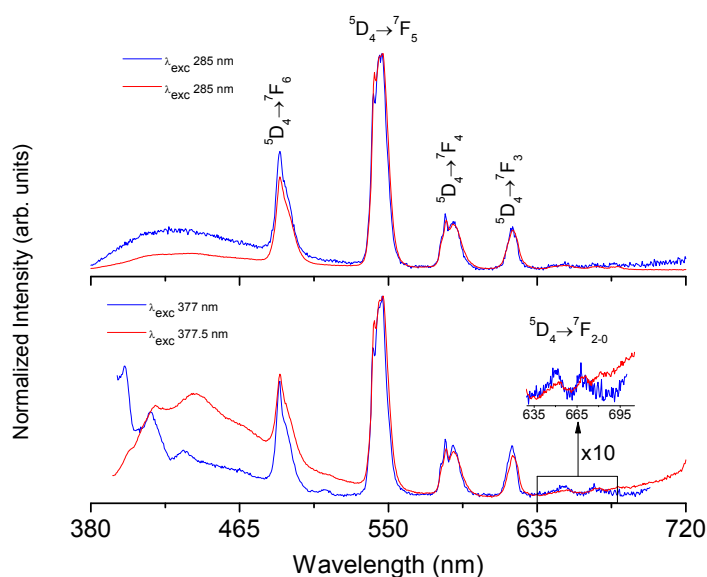


**Figure 4.14.** Emission spectra (300 K) of the  $\text{SiO}_2@\text{APS}@\text{DTPA}@\text{Tb}$  in the liquid (blue) and solid state at 300K (red): (a) excited at 285 nm; (b) excited at  $\sim 377$  nm.

The excitation spectra (300K) of the  $\text{SiO}_2@\text{APS}/\text{DTPA}:\text{Tb}$  monitored at 544 nm (blue), Figure 4.13b, show one large broad band peaking at 275 nm overlapping a series of straight lines ascribed to the  $\text{Tb}^{3+}$  intra-  $4f^8$  transitions between the  $^7F_6$  and the  $^5L_{10-7}$ ,  $^5G_{6-3}$ ,  $^5H_{7-4}$ ,  $^5D_{3-1}$ ,  $^5F_{5,4}$ ,  $^5I_8$ , levels. The broad band is ascribed to the convolution of the hybrid host excited states, as observed for the  $\text{SiO}_2@\text{APS}/\text{DTPA}:\text{Eu}$  NPs.

The comparison between the emission spectra of  $\text{DTPA}:\text{Tb}$  and  $\text{SiO}_2@\text{APS}/\text{DTPA}:\text{Tb}$ , displayed in Figure 4.15 (in particular the energy and fwhm of the  $^5D_4 \rightarrow ^7F_5$  line and the energy and relative intensities of the  $^7F_{6-3}$  Stark components), clearly points out to an effective interaction between  $\text{Tb}^{3+}$  ions and the  $\text{SiO}_2@\text{APS}/\text{DTPA}$  host, different from that discerned in the  $\text{DTPA}:\text{Tb}$  complex.

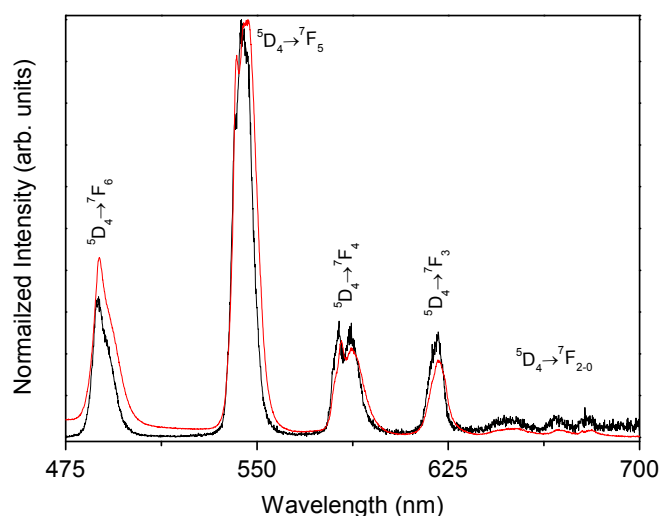


**Figure 4.15.** Emission spectra (300 K) of the DTPA:Tb (black) and SiO<sub>2</sub>@APS/DTPA:Tb (red) monitored at 544 nm.

The lifetime values of the Tb<sup>3+</sup> excited states (<sup>5</sup>D<sub>4</sub>) were monitored at 546 nm and excited at 377 nm, at 27 °C and solid state. The emission decay curves are well fitted by a single exponential function yielding  $\tau$  (<sup>5</sup>D<sub>4</sub>) = 1.87 ± 0.02 ms, indicating only one local coordination of the Tb<sup>3+</sup> cation (Figure 4.16).

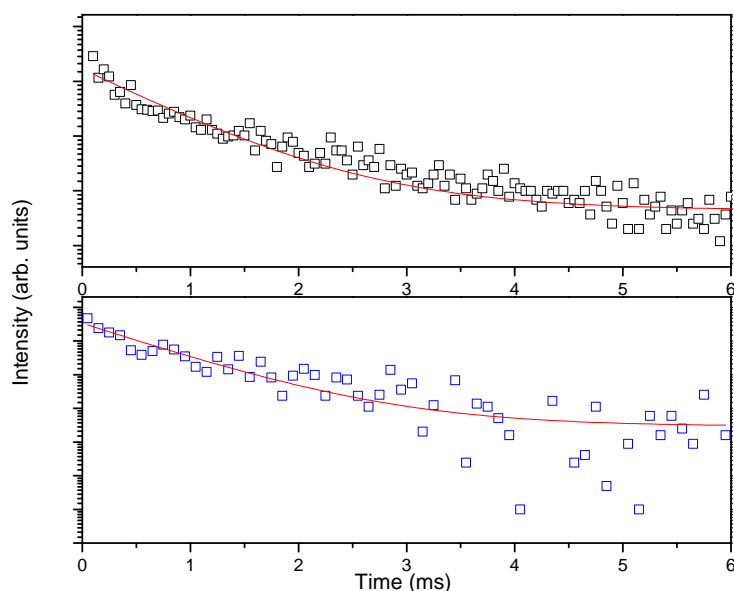


**Figure 4.16.** Emission decay curve of Tb<sup>3+</sup> excited states (<sup>5</sup>D<sub>4</sub>) from the sample SiO<sub>2</sub>@APS/DTPA:Tb, were monitored at 546 nm and excited at 272 nm (black) and at 377 nm (blue), at 300 K solid state.

For certain applications, it may be of interest to introduce two different lanthanide centres (Ln1, Ln2) optically-active in the visible range. For example, when the colours of the emission of Ln1 and the cell auto-fluorescence are similar, one may resort to the emission of Ln2. As a proof of concept,  $\text{SiO}_2\text{@APS/DTPA:EuTb}$  (1:1) NPs were prepared, and they display the red  $\text{Eu}^{3+}$  and green  $\text{Tb}^{3+}$  emission (Figure 4.17a). Bimodal, MRI and optical imaging, nanoparticles of  $\text{SiO}_2\text{@APS/DTPA:EuGd}$  (1:1) and  $\text{SiO}_2\text{@APS/DTPA:TbGd}$  (1:1) were prepared. Their emission spectra, depicted in Figure 4.17c,d clearly show that the  $\text{Eu}^{3+}$  and  $\text{Tb}^{3+}$  emission features described above are not influenced by the incorporation of  $\text{Gd}^{3+}$ .

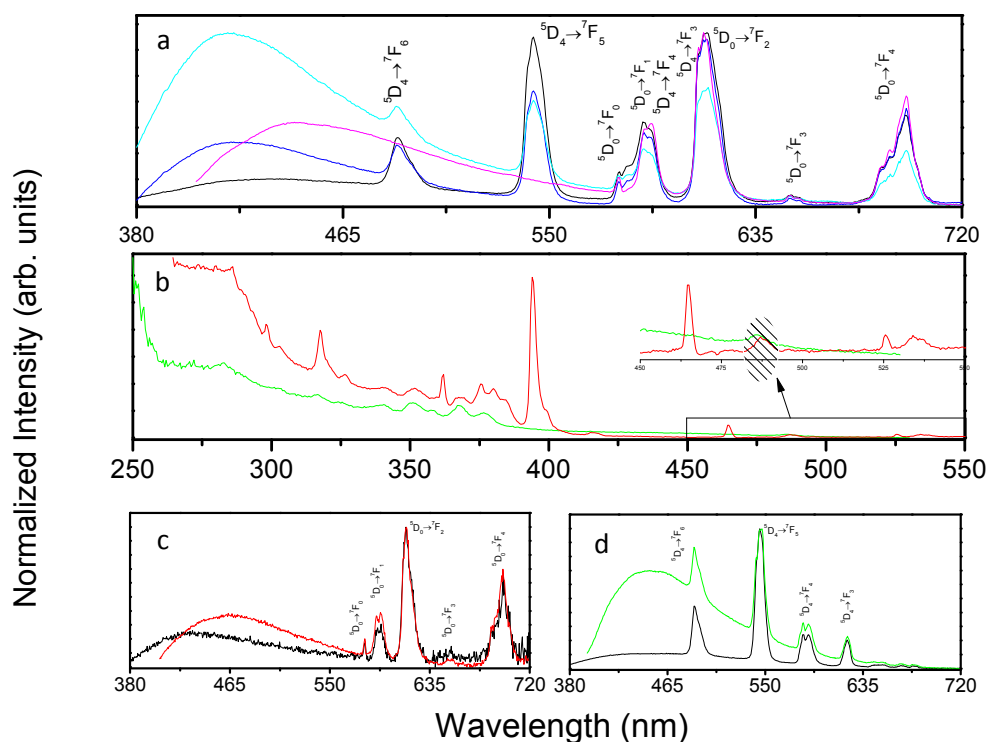
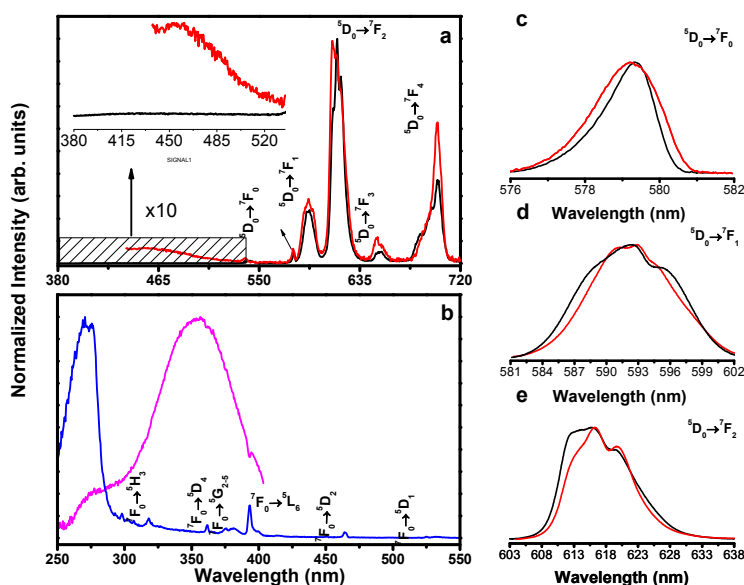


**Figure 4.17.** Room-temperature emission spectra of  $\text{SiO}_2\text{@APS/DTPA:EuTb}$  (1:1) in the solid state, excited at 284 (black), 317 (blue), 330 (cyan) and 393 nm (magenta). **(b)** Room-temperature excitation of  $\text{SiO}_2\text{@APS@DTPA@EuTb}$  (1:1) in the solid state, monitored at 543.5 (green) and 697.5 nm (red). **(c)** Room-temperature emission spectra of  $\text{SiO}_2\text{@APS/DTPA:EuGd}$  (1:1) in the solid state, excited at 290 (black), 394.5 nm (red), **(d)** Room-temperature emission spectra of  $\text{SiO}_2\text{@APS/DTPA:TbGd}$  (1:1) in the solid state, excited at 285 (black), 379 nm (green).

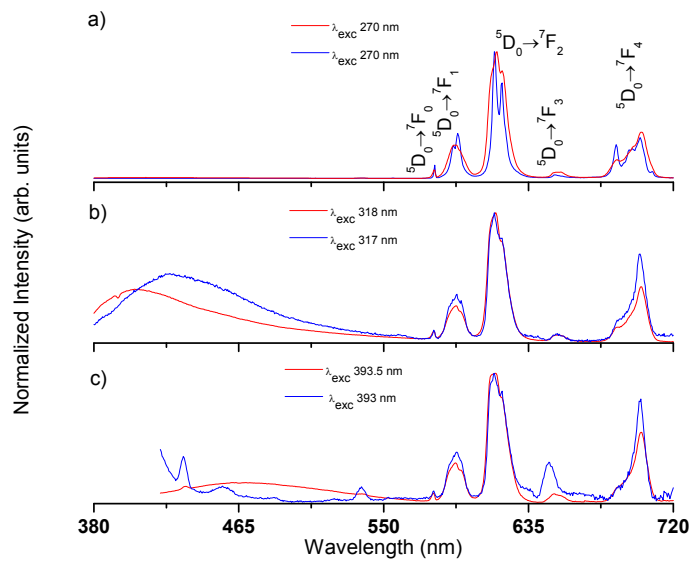
## SiO<sub>2</sub>@APS/PMN:Ln NPs

Figure 4.18a displays the 300 K emission spectra of SiO<sub>2</sub>@APS/PMN:Eu in the solid state excited at two different wavelengths, while Figure 4.19 compares the emission spectra measured at three different wavelengths in solid state and water suspension. The spectra comprise a series of sharp lines assigned to the Eu<sup>3+</sup> <sup>5</sup>D<sub>0</sub>→<sup>7</sup>F<sub>0-4</sub> transitions and a strong broad band centred at ca. 450 nm which, considering the emission spectra of SiO<sub>2</sub>, SiO<sub>2</sub>@APS and SiO<sub>2</sub>@APS/PMN (Figures 4.20 and 4.21), is attributed to oxygen defects in the silica host (and also to the NH<sub>2</sub> groups of the APS layer).<sup>70,73</sup> This broad band shifts to the blue with the addition of APS, from 440.0 (SiO<sub>2</sub>) to 430.0 nm (SiO<sub>2</sub>@APS, SiO<sub>2</sub>@APS/PMN), while the full-width-at-half-maximum (fwhm) decreases from 133.8 (SiO<sub>2</sub>) to 109.0 (SiO<sub>2</sub>@APS), 94.7 (SiO<sub>2</sub>@APS/PMN) and 82.6 nm (SiO<sub>2</sub>@APS/PMN:Eu).

The excitation spectra of SiO<sub>2</sub>@APS/PMN:Eu (300 K), Figure 3b, display two strong broad bands, peaking at 275.0 and 355.0 nm, overlapping with a series of Eu<sup>3+</sup> intra-4f<sup>6</sup> transitions between the <sup>7</sup>F<sub>0</sub> and the <sup>5</sup>L<sub>6</sub>, <sup>5</sup>D<sub>4,2,1</sub>, <sup>5</sup>F<sub>4</sub>, <sup>5</sup>H<sub>3</sub>, <sup>5</sup>G<sub>2-5</sub> levels. When the temperature is decreased from 300 to 12 K a new and very broad band in the range ca. 300-390 nm is observed (Figure 4.22).



**Figure 4.18.** Emission spectra (300 K) of SiO<sub>2</sub>@APS/PMN:Eu (solid state) excited at 270.5 (black) and 393.5 nm (red); b) Excitation spectra (300 K) of SiO<sub>2</sub>@APS/PMN:Eu (solid state) monitored at 420 (magenta) and 614 nm (blue); c) d), and e) show a magnification of the <sup>5</sup>D<sub>0</sub>→<sup>7</sup>F<sub>0-2</sub> transitions.



**Figure 4.19.** Emission spectra (300 K) of the  $\text{SiO}_2\text{@APS/PMN:Eu}$  in water solution (blue), solid state at 300K (red) excited at different wavelengths.

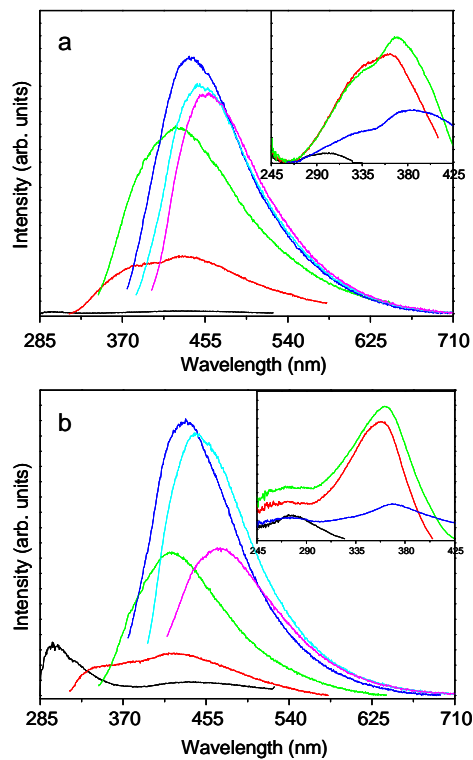


**Figure 4.20. (a)** Emission spectra (300 K) of the  $\text{SiO}_2\text{@APS/PMN}$  excited at 270.0 (black), 300.0 (red), 330.0 (green), 360.0 (blue), 370.0 (cyan) and 485.0 (magenta). The inset shows the excitation spectra (300 K) monitored at 340.0 (black), 425.0 (red), 440.0 (green) and 510.0 nm (blue); **(b)**

Emission spectra (300 K) of the  $\text{SiO}_2$ @APS excited at 270.0 (black), 300.0 (red), 330.0 (green), 360.0 (blue), 380.0 (cyan) and 400.0 (magenta). The inset shows the excitation spectra (300 K) monitored at 340.0 (black), 420.0 (red), 440.0 (green) and 520.0 nm (blue).

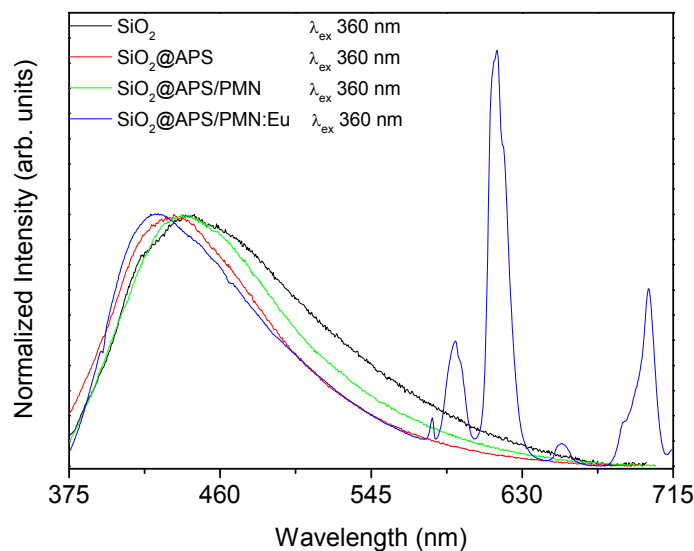


**Figure 4.21.** Emission spectra (300 K) of the  $\text{SiO}_2$  (black),  $\text{SiO}_2$ @APS (red),  $\text{SiO}_2$ @APS/PMN (green) and  $\text{SiO}_2$ @APS/PMN:Eu (blue) excited at 360.0 nm.

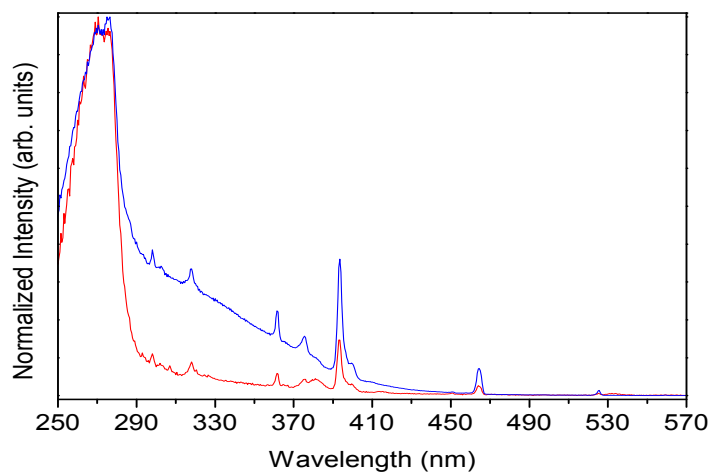


**Figure 4.22.** Excitation spectra of the  $\text{SiO}_2$ @APS/PMN:Eu monitored at 614 nm, 300 K (red) and 12 K (blue).

In order to get further insight into the  $\text{Eu}^{3+}$  local coordination, the  $4f^6$  emission lines were recorded at high resolution (Figure 4.18c-e). The spectra excited at 270.5 and 393.5 nm exhibit differences in the relative intensities and fwhm of the  ${}^5\text{D}_0 \rightarrow {}^7\text{F}_{0-2}$  transitions. The fwhm of the non-degenerated  ${}^5\text{D}_0 \rightarrow {}^7\text{F}_0$  line, in particular, is  $43.3 \pm 0.3 \text{ cm}^{-1}$ , at 270.5 nm, and  $53.5 \pm 0.5 \text{ cm}^{-1}$ , at 393.5 nm, which evidences the presence of (at least) two distinct  $\text{Eu}^{3+}$  local environments. A similar conclusion is reached for the NPs water suspensions (Figure 4.19).

The room-temperature  ${}^5\text{D}_0$  emission decay curve of solid  $\text{SiO}_2@\text{APS}/\text{PMN}:\text{Eu}$ , monitored within the  ${}^5\text{D}_0 \rightarrow {}^7\text{F}_2$  transition at 614.0 nm and excited at 270.0 nm, is well fitted by a bi-exponential function, yielding lifetimes  $\tau_1 = 0.242 \pm 0.071 \text{ ms}$  and  $\tau_2 = 0.927 \pm 0.023 \text{ ms}$  (Figure 4.23a), confirming the presence of two  $\text{Eu}^{3+}$  local environments. The  ${}^5\text{D}_0$  decay curve of the free  $[\text{Eu}(\text{PMN})]$  monomeric complex, recorded in the solid state excited at 275.0 nm (Figure 4.24), is well fitted by a mono-exponential function yielding a lifetime of  $0.292 \pm 0.062 \text{ ms}$  (in solution the reported lifetime is *ca.* 0.400 ms<sup>61-62</sup>).

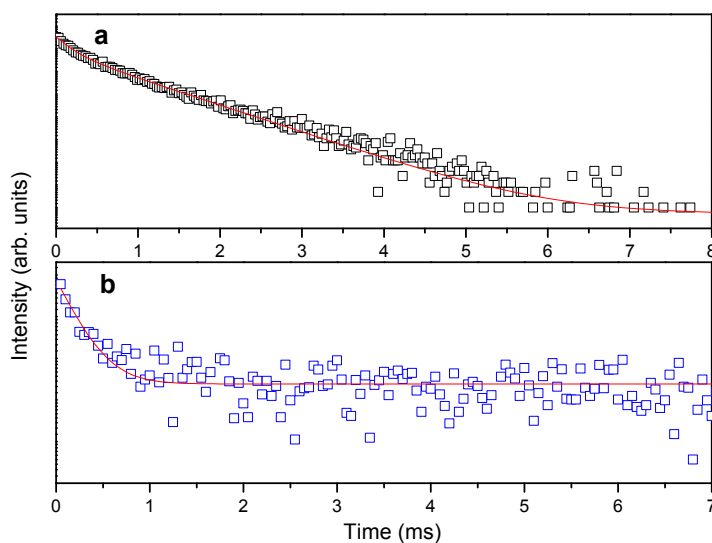


**Figure 4.23.** Emission decay curve of  $\text{Eu}^{3+}$  excited states ( ${}^5\text{D}_0$ ) from the sample  $\text{SiO}_2@\text{APS}/\text{PMN}:\text{Eu}$ , which were monitored at 614.0 nm and excited at a) 270.0 nm (black); b) 370.0 nm (blue), at 300 K in the solid state.

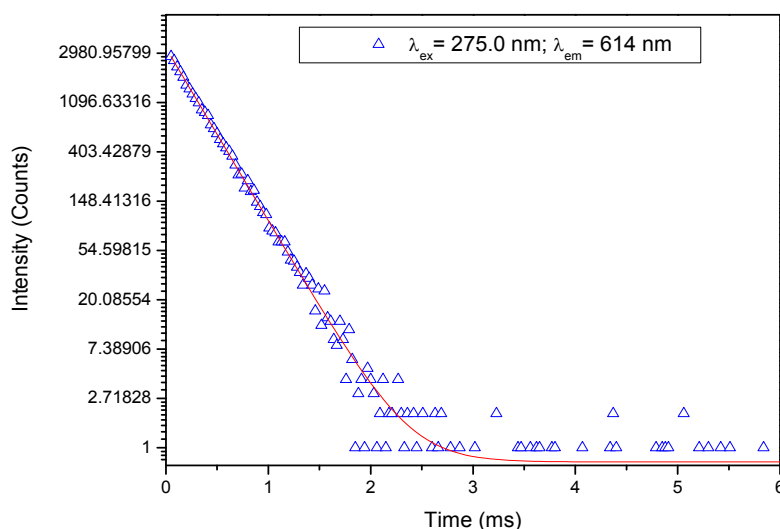


**Figure 4.24.**  $^5D_0$  emission decay curve of [Eu(PMN)], monitored at 614.0 nm and excited 275.0 nm (blue) at 300 K in the solid state.

Although the free [Eu(PMN)] complex and SiO<sub>2</sub>@APS/PMN:Eu exhibit similar lifetimes of, respectively, 0.29 and 0.24 ms ( $\tau_1$ ) there are indications that the latter is *not* attributed to the [Eu(PMN)] residue, rather to a Eu<sup>3+</sup> environment interacting strongly with the NPs surface, probably via silanol groups (which are far more abundant than the amino groups on the silica surface). The arguments are as follows. Figure 4.25 compares the emission and excitation spectra of the free [Eu(PMN)] complex and SiO<sub>2</sub>@APS/PMN:Eu NPs. The  $^5D_0 \rightarrow ^7F_0$  line of the latter can be fitted by two Gaussian bands, at ca. 578 and 580 nm (inset in Figure 4.25), in accord with the existence of two distinct Eu<sup>3+</sup> local environments. Whereas the low-energy-component (ca. 578 nm) is ascribed to a Eu<sup>3+</sup> site with a coordination shell similar to that of the free [Eu(PMN)] complex, the high-energy band (ca. 580 nm), not present in the complex, must correspond to a Eu<sup>3+</sup> coordination shell involving directly the SiO<sub>2</sub>@APS host. Therefore the excitation spectra monitored on both components provide information on the nature of the two distinct local sites. Figure 4.26 compares the excitation spectra of the SiO<sub>2</sub>@APS/PMN:Eu NPs, monitored at 578.0, 580.0 and 614.0 nm, and [Eu(PMN)] complex, monitored at 614.0 nm. While the spectra monitored at 580.0 nm and that of the free complex are similar (Figure 4.26), the spectrum monitored at 578.0 nm shows, in addition, a broad band ('pedestal') between 350.0 and 425.0. This band is, thus, assigned to the SiO<sub>2</sub>@APS host (Figure 4.18b and Figure 4.19). The  $^5D_0$  emission decay curve excited at 370.0 nm (Figure 4.25b) is well fitted by a mono-exponential

function yielding a lifetime of  $0.212 \pm 0.014$  ms<sup>66</sup> providing solid evidence for the previous assignment of the shorter lifetime to a Eu<sup>3+</sup> environment interacting strongly with the NPs surface, that corresponds to the low-energy component of the  $^5D_0 \rightarrow ^7F_0$  line at ca. 578.

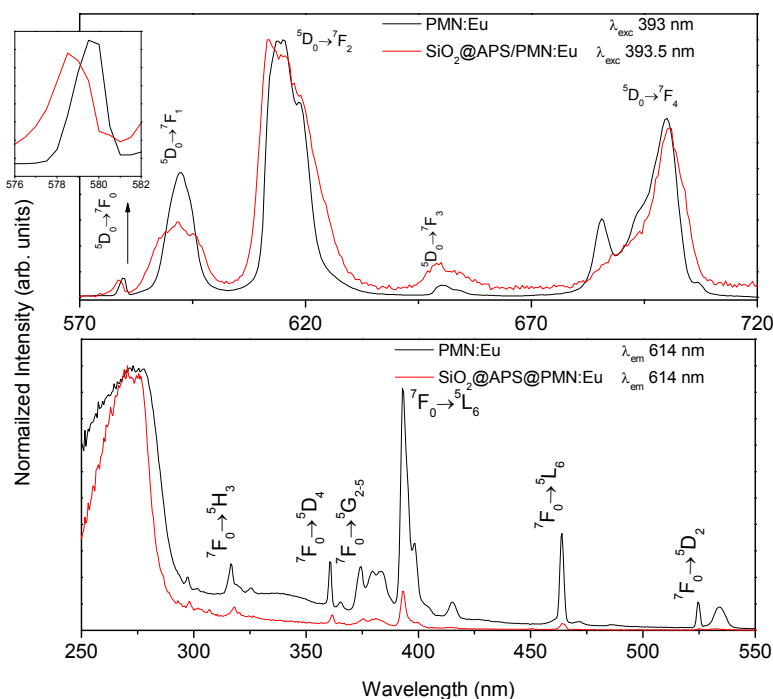


**Figure 4.25.** Top: Emission spectra (300 K) of [Eu(PMN)] (black) and SiO<sub>2</sub>@APS/PMN:Eu (red) excited at 393 nm and 393.5 nm, respectively; Bottom: Excitation spectra (300 K) of [Eu(PMN)] (black) and SiO<sub>2</sub>@APS/PMN:Eu (red) monitored at 614 nm.

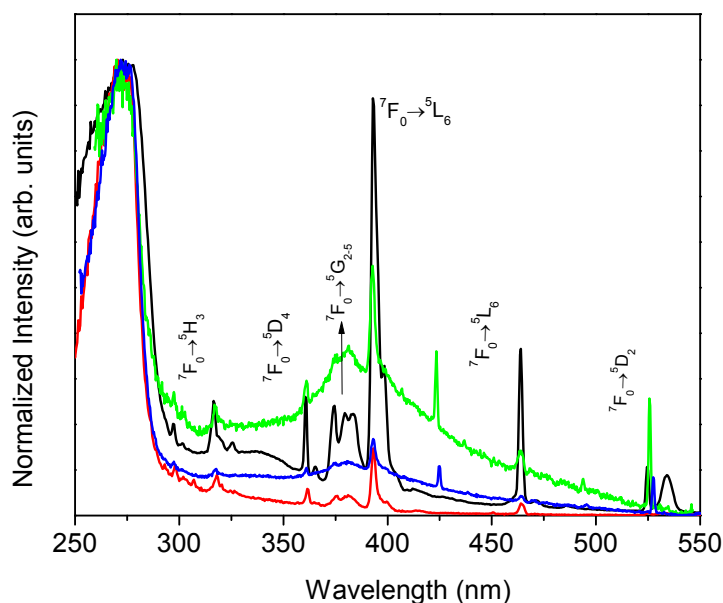


**Figure 4.26.** Excitation spectra (300 K) of [Eu(PMN)] (black, monitored at 614.0 nm) and SiO<sub>2</sub>@APS/PMN:Eu (monitored at 614.0, 578.0 and 580.0 nm, red, green and blue curves, respectively).

We assign the longer,  $\tau_2$ , lifetime to Eu<sup>3+</sup> coordinated to the PMN ligand and grafted via APS to the SiO<sub>2</sub> surface because the excitation spectra of the free [Eu(PMN)] complex and SiO<sub>2</sub>@APS/PMN:Eu are very similar (Figure 4.25 and Figure 4.26) in the region of the intra-4f lines, exhibiting also the same broad band at ca. 270 nm, assigned to the aromatic ring of PMN. The longer lifetime of SiO<sub>2</sub>@APS/PMN:Eu relatively to lifetime of the free [Eu(PMN)] complex may be due to differences in the Eu<sup>3+</sup> coordination spheres, in particular, brought about by the peptidic coupling of PMN to APS in the former.

The maximum emission absolute quantum yields of the free [Eu(PMN)] complex and SiO<sub>2</sub>@APS/PMN:Eu NPs (measured at 270.5 nm) were, respectively,  $0.04 \pm 0.01$  and  $0.05 \pm 0.01$ . Importantly, a much smaller value ( $0.01 \pm 0.01$ ) has been reported for a similar system but that did not contain an aromatic ‘antenna’, SiO<sub>2</sub>@APS@DTPA:Eu<sup>60</sup>

SiO<sub>2</sub>@APS/PMN:Tb NPs were also prepared and their emission spectra consist of (i) a broad band between 380.0 and 550.0 nm, ascribed to the emission of the SiO<sub>2</sub>@APS/PMN host as observed for the Eu-containing samples, and (ii) a series of sharp Tb<sup>3+</sup>  $^5D_4 \rightarrow ^7F_{6-0}$  intra-4f<sup>8</sup> lines (Figure 4.27).

As mentioned before, it is of interest to introduce two different optically-active lanthanide ions (Ln1, Ln2) emitting in the visible range. As a proof of concept,  $\text{SiO}_2\text{@APS/PMN:EuTb}$  (1:1) NPs were prepared, and they displayed the red,  $\text{Eu}^{3+}$ , and green,  $\text{Tb}^{3+}$ , emission (Figure 4.28).

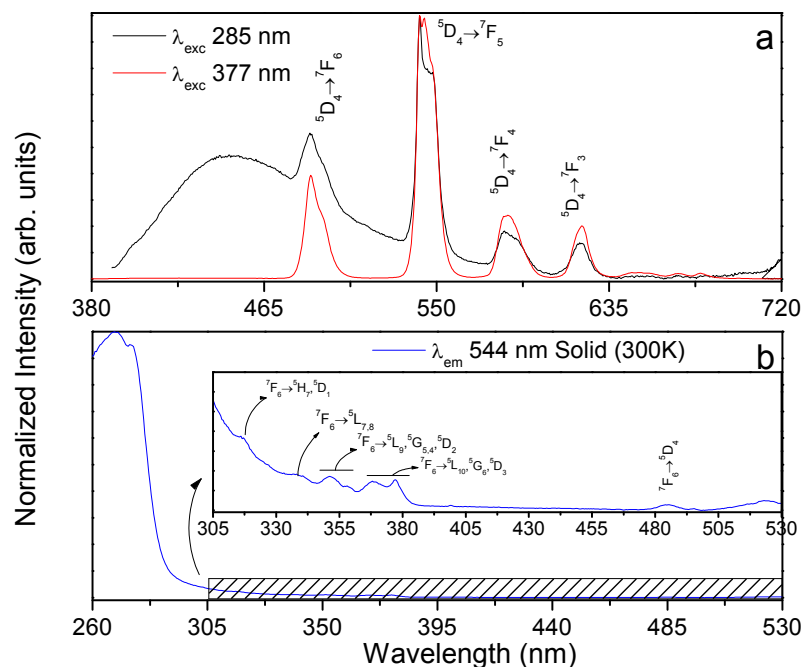


**Figure 4.27.** (a) Emission spectra (300 K) of the  $\text{SiO}_2\text{@APS/PMN:Tb}$  (solid state) excited at 280.0 nm (black) and 377.0 nm (red); (b) Excitation spectra (300 K) of the  $\text{SiO}_2\text{@APS/PMN:Tb}$  (solid state) monitored at 544.0 nm (blue).

The emission spectra of bimodal  $\text{SiO}_2\text{@APS/PMN:EuGd}$  (1:1) and  $\text{SiO}_2\text{@APS/PMN:TbGd}$  (1:1) NPs for MRI and optical imaging (Figure 4.29) are very similar to the spectra of the Gd-free samples (Figure 4.18a and Figure 4.28), thus showing that the  $\text{Eu}^{3+}$  and  $\text{Tb}^{3+}$  emission is not influenced by the presence of  $\text{Gd}^{3+}$ .

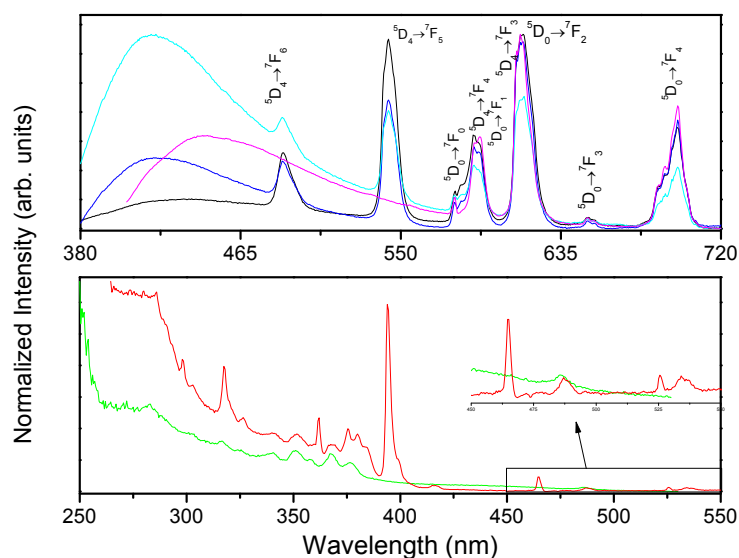


**Figure 4.28.** (a) Room-temperature emission spectra of  $\text{SiO}_2\text{@APS/PMN:EuTb}$  (1:1) in the solid state, excited at 284.0 (black), 317.0 (blue), 330.0 (cyan) and 393.0 nm (magenta). (b) Room-temperature excitation of  $\text{SiO}_2\text{@APS/PMN:EuTb}$  (1:1) in the solid state, monitored at 543.5 (green) and 697.5 nm (red).

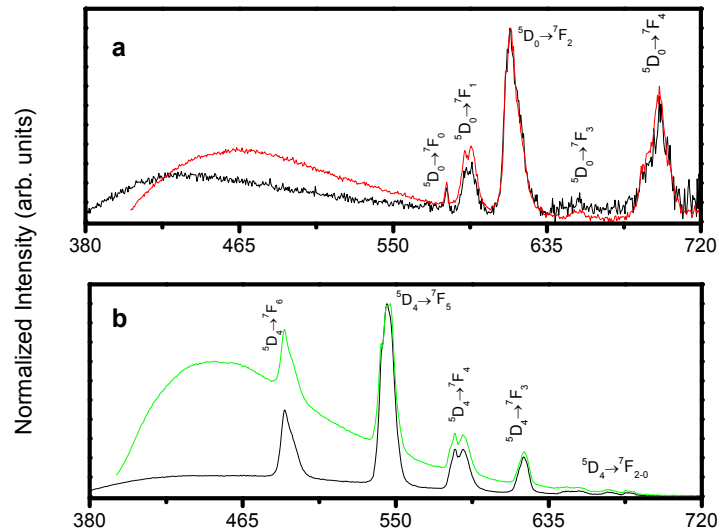


**Figure 4.29.** Room-temperature emission spectra of a)  $\text{SiO}_2\text{@APS/PMN:EuGd}$  (1:1), b)  $\text{SiO}_2\text{@APS/PMN:TbGd}$  (1:1) NPs, excited at, respectively, 290 nm (black), 394.5 nm (red), and 285 (black), 379 nm (green).

### 4.3.3. Relaxivity Properties

#### SiO<sub>2</sub>@APS/DTPA:Ln NPs

The SiO<sub>2</sub>@APS/DTPA:Ln (Ln= Gd, Eu:Gd (1:1), Tb:Gd (1:1) NPs suspensions remained stable throughout the NMR measurements, allowing the collection of consistent relaxation data. Table 4.4 shows the proton relaxivity values ( $r_{1p}$  and  $r_{2p}$ ), determined at two frequencies (20 MHz and 500 MHz) and two temperatures (25 °C and 37 °C) for the SiO<sub>2</sub>@APS/DTPA:Gd, SiO<sub>2</sub>@APS/DTPA:EuGd (1:1) and SiO<sub>2</sub>@APS/DTPA:TbGd (1:1) water suspensions. These relaxivities were calculated from the observed linear dependence of the  $R_i = 1/T_i, (i = 1,2)$  relaxation rates on the concentration of the Gd<sup>3+</sup> ions present in all samples, shown in Figure 4.30 to Figure 4.33. These values are constant over a large pH range, indicating that the paramagnetic NPs are stable and do not leach out Gd<sup>3+</sup>, Eu<sup>3+</sup> or Tb<sup>3+</sup> ions, even in highly basic conditions. The  $r_{ip} = (i = 1,2)$  values measured for the SiO<sub>2</sub>@APS/DTPA:Gd nanoparticles with 67 nm diameter are very similar to those reported for the monomeric [Gd(DTPA)]<sup>2-</sup> complex,<sup>8</sup> reflecting the virtually free rotational motion of the complex at the surface of the nanoparticles, which counteracts the effect of the slow global motion of the nanoparticle on the relaxivities. The  $r_{1p}$  values decrease with increasing frequency, as expected for the standard inner-sphere and outer-sphere dipolar mechanisms of proton relaxation. They are also almost constant with increasing temperature, reflecting that the  $T_1$  relaxation process is limited by slow-to-intermediate water exchange, characteristic of DTPA-amide systems.<sup>8,9</sup> These  $r_{1p}$  values are similar to those reported for nanoporous silica nanoparticles coated with covalently bound Gd-Si-DTPA<sup>30</sup> or Si-EDTA<sup>46</sup> derivatives, but smaller than when a Si-DTTA<sup>30</sup> derivative was used (H<sub>4</sub>DTTA = diethylenetriaminetetraacetic acid), mainly reflecting the different water accessibilities of the Gd<sup>3+</sup> ion in those systems. This water accessibility is much increased in mesoporous silica-based nanosystems covalently labelled with Gd-DTPA, Gd-DTTA or Gd-DOTA derivatives,<sup>40-45</sup> leading to  $r_{1p}$  values 5 to 10 times larger than for the corresponding monomeric complexes.

For the  $\text{SiO}_2@\text{APS}/\text{DTPA}:\text{GdEu}$  and  $\text{SiO}_2@\text{APS}/\text{DTPA}:\text{GdTb}$  NPs, where 50% of the DTPA-coordinated  $\text{Gd}^{3+}$  ions are replaced by  $\text{Eu}^{3+}$  or  $\text{Tb}^{3+}$ , the  $r_{1p}$  values (referred to one mM  $\text{Gd}^{3+}$ ) increase relative to the  $\text{SiO}_2@\text{APS}/\text{DTPA}:\text{Gd}$  NPs (Table 4.4), reflecting the dipolar relaxation effect of the extra ions at the particle surface. This increase is larger for the  $\text{Tb}^{3+}$  than for  $\text{Eu}^{3+}$  ions, as the former induces stronger  $T_1$  relaxation due to its slower electronic relaxation. The frequency and temperature dependence of  $r_{1p}$  for the mixed cation nanoparticles is the same as for the  $\text{Gd}^{3+}$  ones.

The  $r_{2p}$  values for the  $\text{SiO}_2@\text{APS}/\text{DTPA}:\text{Gd}$  NPs undergo a large increase when the measuring frequency increases (Table 4.4). Large  $r_{2p}$  values have also been observed for silica nanosystems covalently labelled with  $\text{Gd}^{3+}$  complexes, particularly at high frequencies.<sup>30,40-42,45-47</sup> This indicates that the  $T_2$ -relaxation process, besides the dipolar mechanism operating for  $T_1$ -relaxation, also has a strong outer-sphere contribution from field inhomogeneities created by the magnetized particles that the water protons experience (measured by the frequency shift at the particle surface,  $\Delta\omega$ ) as they diffuse nearby (with a diffusion correlation time  $\tau_D$ ), and which increase with the square of the external magnetic field strength.<sup>80</sup> The presence of this contribution is confirmed by the increase of  $r_{2p}$  values observed for the mixed  $\text{SiO}_2@\text{APS}/\text{DTPA}:\text{EuGd}$  NPs (Table 4.4). This magnetic susceptibility effect is particularly strong for  $r_{2p}$  values at 500 MHz, and can also be observed for the 20 MHz  $r_{2p}$  values of the mixed  $\text{SiO}_2@\text{APS}/\text{DTPA}:\text{TbGd}$  NPs. These effects of the nanoparticle-bound  $\text{Tb}^{3+}$  ions are stronger than those observed for the  $\text{Eu}^{3+}$  ions, in agreement with the larger magnetic moment of  $\text{Tb}^{3+}$ . However, their 500 MHz  $r_{2p}$  values decrease, rather than increase, when 50% of the  $\text{Gd}^{3+}$  ions are replaced by  $\text{Tb}^{3+}$  (Table 4.4). This may reflect a breakdown of the outer-sphere relaxation model for  $T_2$ -relaxation at high magnetic field due to the presence of the  $\text{Tb}^{3+}$  ions, when  $\tau_D \gg 1/\Delta\omega$ . In these conditions, the static dephasing regime (SDR) model describes the transverse relaxation and the value of  $r_2$  becomes dependent on the time interval between two consecutive refocusing pulses ( $\tau_{\text{CP}}$ ) in the train of  $180^\circ$  pulses applied in a Carr-Purcell-Meiboom-Gill (CPMG) pulse sequence.<sup>80,81</sup> In preliminary experiments, we have observed that  $r_2$  of suspensions of these particles indeed depends on  $\tau_{\text{CP}}$  (data not shown). A more complete study of the relaxation mechanisms of these mixed NPs is beyond the scope of the present study.

**Table 4.4.** Calculated  $^1\text{H}$  relaxivity values,  $r_{ip}$  ( $i = 1,2$ ), determined at 20 MHz and 500 MHz, at 25 °C and 37 °C for samples  $\text{SiO}_2@$ APS/DTPA:Gd,  $\text{SiO}_2@$ APS/DTPA:EuGd (1:1) and  $\text{SiO}_2@$ APS/DTPA:TbGd (1:1).

20 MHz	$r_{1p}$ ( $\text{s}^{-1}\text{mM}^{-1}$ )		$r_{2p}$ ( $\text{s}^{-1}\text{mM}^{-1}$ )	
	25°	37°	25°	37°
$\text{SiO}_2@$ APS/DTPA:Gd	$5.24 \pm 0.04$	$5.66 \pm 0.03$	$6.36 \pm 0.01$	$6.86 \pm 0.01$
$\text{SiO}_2@$ APS/DTPA:EuGd (1:1)	$8.08 \pm 0.03$	$8.39 \pm 0.02$	$10.09 \pm 0.003$	$10.26 \pm 0.007$
$\text{SiO}_2@$ APS/DTPA:TbGd (1:1)	$17.4 \pm 0.1$	$16.6 \pm 0.1$	$21.59 \pm 0.01$	$20.85 \pm 0.05$
500 MHz	$r_{1p}$ ( $\text{s}^{-1}\text{mM}^{-1}$ )		$r_{2p}$ ( $\text{s}^{-1}\text{mM}^{-1}$ )	
	25°	37°	25°	37°
$\text{SiO}_2@$ APS/DTPA:Gd	$2.08 \pm 0.04$	$1.93 \pm 0.03$	$26.6 \pm 0.4$	$34.8 \pm 0.6$
$\text{SiO}_2@$ APS/DTPA:EuGd (1:1)	$2.64 \pm 0.08$	$2.50 \pm 0.09$	$50 \pm 2$	$55 \pm 3$
$\text{SiO}_2@$ APS/DTPA:TbGd (1:1)	$13.1 \pm 0.6$	$9.5 \pm 0.7$	$22 \pm 1$	$22.2 \pm 0.6$

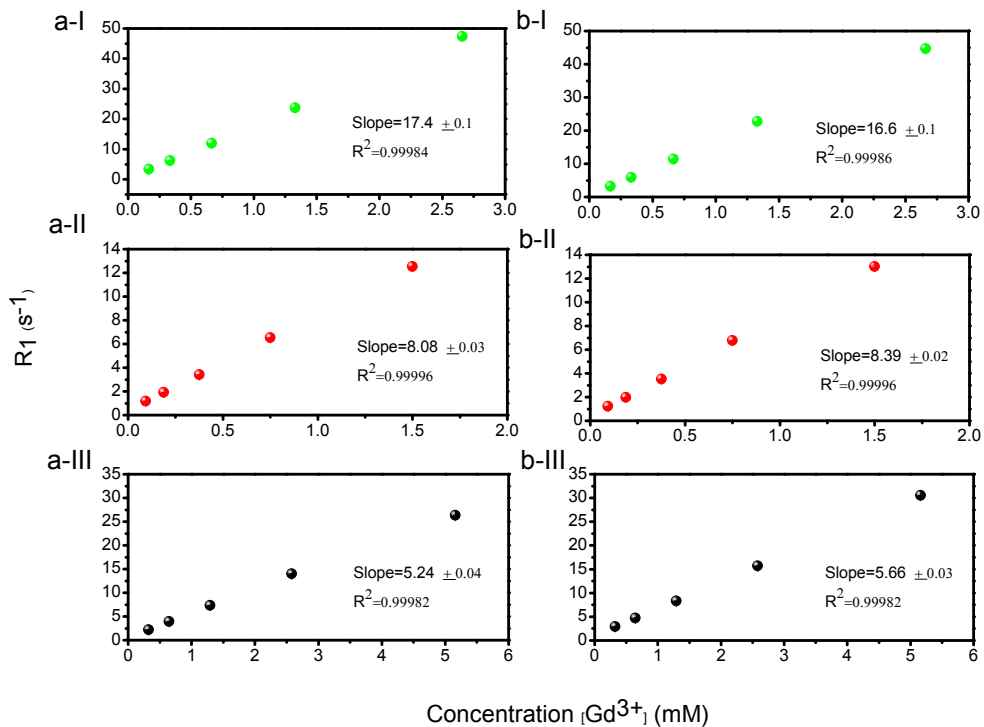


**Figure 4.30.**  $r_1$  values measured at 20 MHz; (a) 25°C and (b) 37°C and samples I-  $\text{SiO}_2@$ APS/DTPA:Gd; II-  $\text{SiO}_2@$ APS/DTPA:EuGd; (1:1) and III-  $\text{SiO}_2@$ APS/DTPA:TbGd (1:1).

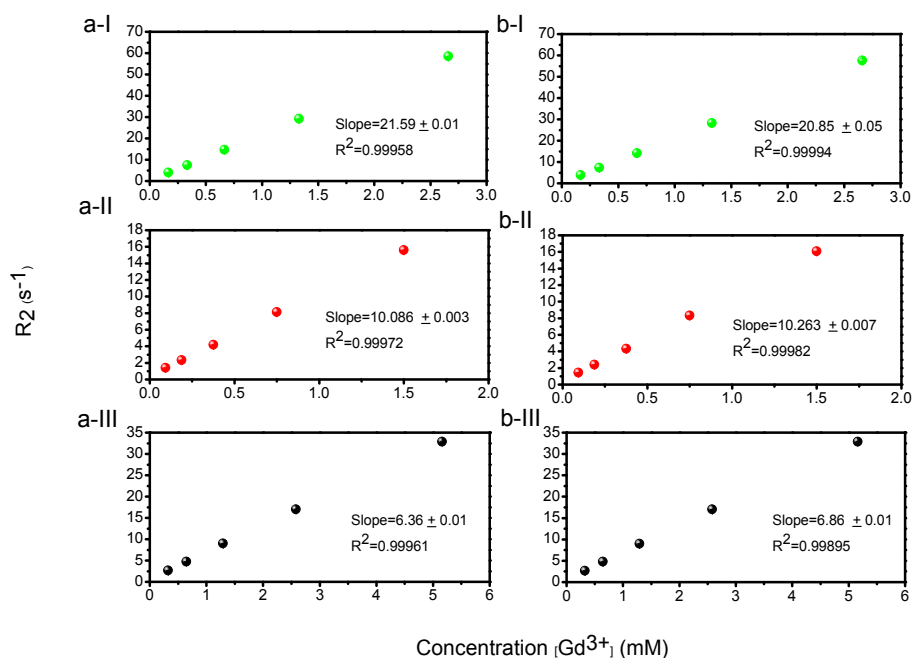


**Figure 4.31.**  $r_2$  values measured at 20 MHz; **(a)** 25°C and **(b)** 37°C and samples I- SiO<sub>2</sub>@APS/DTPA:Gd; **II-** SiO<sub>2</sub>@APS/DTPA:EuGd; (1:1) and **III-** SiO<sub>2</sub>@APS/DTPA:TbGd (1:1).

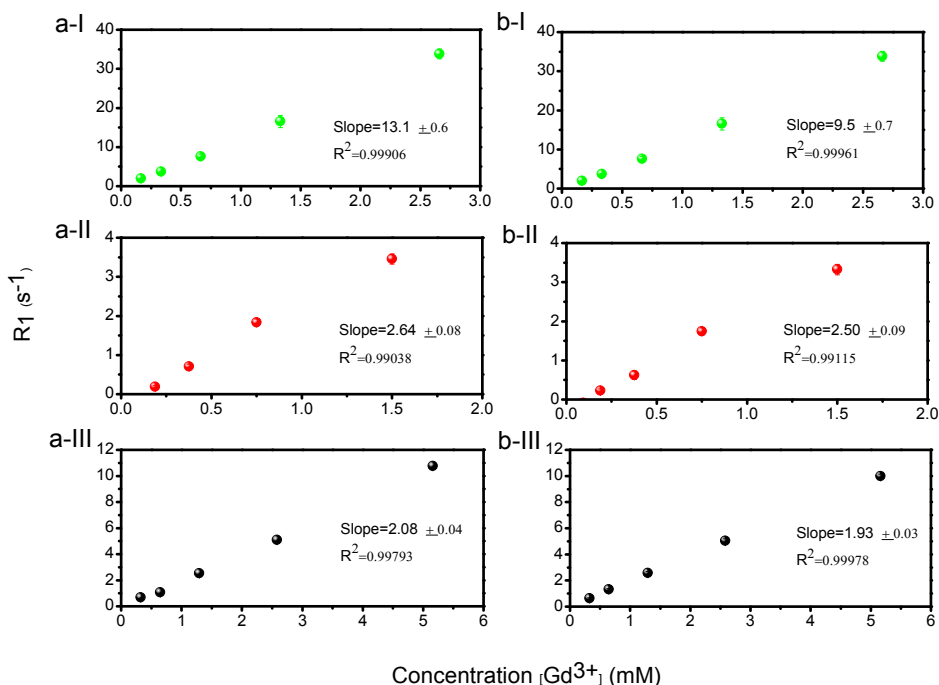


**Figure 4.32.**  $r_1$  values measured at 500 MHz; **(a)** 25°C and **(b)** 37°C and samples I- SiO<sub>2</sub>@APS/DTPA:Gd; **II-** SiO<sub>2</sub>@APS/DTPA:EuGd; (1:1) and **III-** SiO<sub>2</sub>@APS/DTPA:TbGd (1:1).

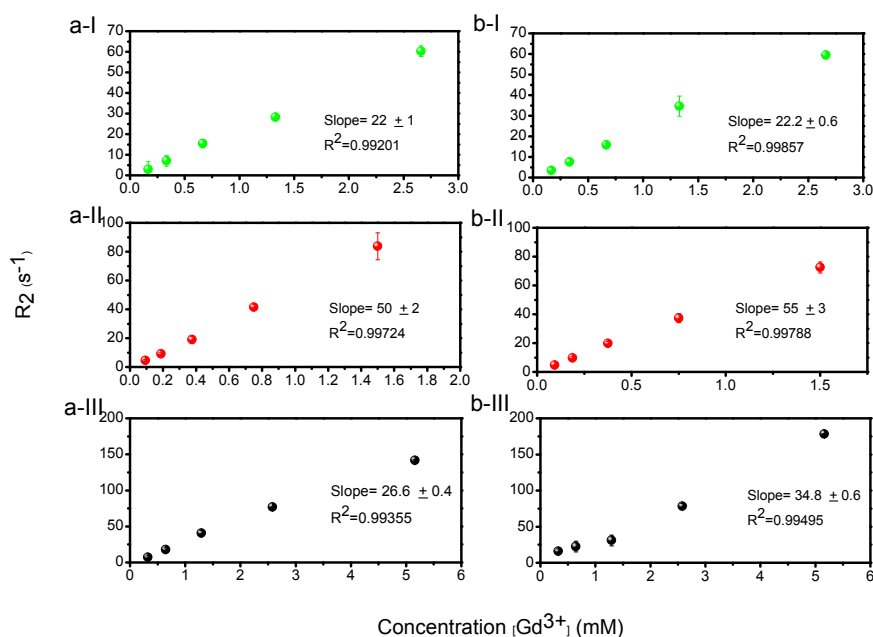


**Figure 4.33.**  $r_2$  values measured at 500 MHz; **(a)** 25°C and **(b)** 37°C and samples I- SiO<sub>2</sub>@APS/DTPA:Gd; II- SiO<sub>2</sub>@APS/DTPA:EuGd; (1:1) and III- SiO<sub>2</sub>@APS/DTPA:TbGd (1:1).

### SiO<sub>2</sub>@APS/PMN:Ln NPs

The SiO<sub>2</sub>@APS/PMN:Ln (Ln= Gd, Eu:Gd (1:1), Tb:Gd (1:1)) NPs suspensions were studied by NMR. Table 4.5 shows the proton relaxivity values ( $r_{1p}$  and  $r_{2p}$ ) determined at two frequencies (20 MHz and 500 MHz) and two temperatures (298 K and 310 K) for the SiO<sub>2</sub>@APS/PMN:Gd, SiO<sub>2</sub>@APS/PMN:EuGd (1:1) and SiO<sub>2</sub>@APS/PMN:TbGd (1:1) water suspensions. These relaxivities were calculated from the slopes of the observed linear dependence of the  $R_i = 1/T_i$ , ( $i = 1,2$ ) relaxation rates on the concentration of the Gd<sup>3+</sup> ions present in the samples, shown in figures 4.34 to 4.37. These values are constant over a large pH range, indicating that the paramagnetic NPs are stable and do not leach out the Ln<sup>3+</sup> ions, even in highly basic conditions. The  $r_i$  ( $i = 1,2$ ) values measured for the SiO<sub>2</sub>@APS/PMN:Gd nanoparticles with 67 nm diameter are very similar to those reported for the monomeric [Gd(DTPA)]<sup>2-</sup> complex<sup>8</sup> and our previous studies for SiO<sub>2</sub>@APS/DTPA:Gd NPs.<sup>60</sup>

In the cases of the mixed-metal  $\text{SiO}_2\text{@APS/PMN:GdEu}$  and  $\text{SiO}_2\text{@APS/PMN:GdTb}$  NPs, where 50% of the PMN-coordinated  $\text{Gd}^{3+}$  ions are replaced by  $\text{Eu}^{3+}$  or  $\text{Tb}^{3+}$ , the  $r_{1p}$  values (referred to one mM  $\text{Gd}^{3+}$ ) increase relative to the  $\text{SiO}_2\text{@APS/PMN:Gd}$  NPs (Table 4.5), and are in agreement with previous studies for  $\text{SiO}_2\text{@APS/DTPA:GdEu}$  and  $\text{SiO}_2\text{@APS/DTPA:GdTb}$  NPs.<sup>60</sup>

**Table 4.5.** Calculated  $^1\text{H}$  relaxivity values,  $r_{ip}$  ( $i = 1,2$ ), determined at 20 MHz and 500 MHz, at 25 °C and 37 °C for samples  $\text{SiO}_2\text{@APS/PMN:Gd}$ ,  $\text{SiO}_2\text{@APS/PMN:EuGd}$  (1:1) and  $\text{SiO}_2\text{@APS/PMN:TbGd}$  (1:1).

20 MHz	$r_{1p}$ ( $\text{s}^{-1}\text{mM}^{-1}$ )		$r_{2p}$ ( $\text{s}^{-1}\text{mM}^{-1}$ )	
	25°	37°	25°	37°
$\text{SiO}_2\text{@APS/PMN:Gd}$	$2.70 \pm 0.01$	$2.83 \pm 0.01$	$4.32 \pm 0.01$	$4.02 \pm 0.01$
$\text{SiO}_2\text{@APS/PMN:EuGd}$	$4.14 \pm 0.01$	$4.39 \pm 0.01$	$7.68 \pm 0.01$	$7.50 \pm 0.01$
$\text{SiO}_2\text{@APS/PMN:TbGd}$	$8.49 \pm 0.01$	$7.95 \pm 0.02$	$11.98 \pm 0.01$	$12.40 \pm 0.01$
500 MHz	$r_{1p}$ ( $\text{s}^{-1}\text{mM}^{-1}$ )		$r_{2p}$ ( $\text{s}^{-1}\text{mM}^{-1}$ )	
	25°	37°	25°	37°
$\text{SiO}_2\text{@APS/PMN:Gd}$	$1.05 \pm 0.03$	$1.10 \pm 0.02$	$80 \pm 1$	$56.4 \pm 0.8$
$\text{SiO}_2\text{@APS/PMN:EuGd}$	$2.13 \pm 0.05$	$1.91 \pm 0.06$	$227 \pm 4$	$174 \pm 2$
$\text{SiO}_2\text{@APS/PMN:TbGd}$	$2.26 \pm 0.04$	$2.13 \pm 0.05$	$89.9 \pm 0.8$	$79.4 \pm 0.9$

The  $r_{2p}$  values for the  $\text{SiO}_2\text{@APS/PMN:Gd}$  NPs increase sharply at high frequency (Table 4.5), as also observed for other silica nanosystems covalently labelled with  $\text{Gd}^{3+}$  complexes.<sup>42-44,46,5380-182</sup> This results from field inhomogeneities created by the magnetized particles (measured by the frequency shift at the particle surface,  $\Delta\omega$ ) that the water protons experience as they diffuse nearby (with a diffusion correlation time  $\tau_D$ ). This outer-sphere contribution to  $T_2$ -relaxation increases with the square of the external magnetic field strength.<sup>80</sup> This contribution also causes an increase of  $r_{2p}$  values for the mixed  $\text{SiO}_2\text{@APS/PMN:GdEu}$  NPs, in particular at 500

MHz, (Table 4.5). This effect is even stronger for the  $\text{Tb}^{3+}$ -containing NPs, due to its larger magnetic moment. The decrease of their 500 MHz  $r_{2p}$  values when 50% of the  $\text{Gd}^{3+}$  ions are replaced by  $\text{Tb}^{3+}$  (Table 4.5), may result from a breakdown of the outer-sphere relaxation model for  $T_2$ -relaxation at high magnetic fields due to the presence of the  $\text{Tb}^{3+}$  ions, when  $\tau_D \gg 1/\Delta\omega$ . In these conditions, the static dephasing regime (SDR) model describes the transverse relaxation and the value of  $r_2$  becomes dependent on the time interval between two consecutive refocusing pulses ( $\tau_{\text{CP}}$ ) in the train of  $180^\circ$  pulses applied in a Carr-Purcell-Meiboom-Gill (CPMG) pulse sequence.<sup>42</sup> In fact, preliminary experiments showed that the  $r_2$  of suspensions of these particles depend on  $\tau_{\text{CP}}$  (data not shown), as expected in those conditions.

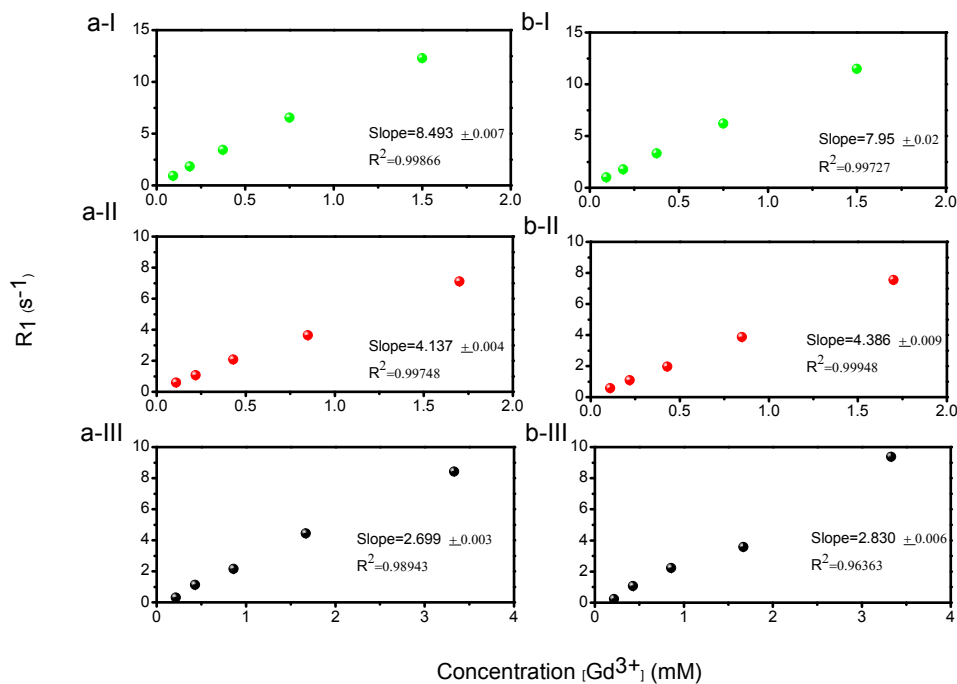


**Figure 4.34.**  $r_1$  values measured at 20 MHz; **(a)** 25°C and **(b)** 37°C and samples **I-**  $\text{SiO}_2\text{@APS/PMN:Gd}$ ; **II-**  $\text{SiO}_2\text{@APS/PMN:EuGd}$ ; (1:1) and **III-**  $\text{SiO}_2\text{@APS/PMN:TbGd}$  (1:1).

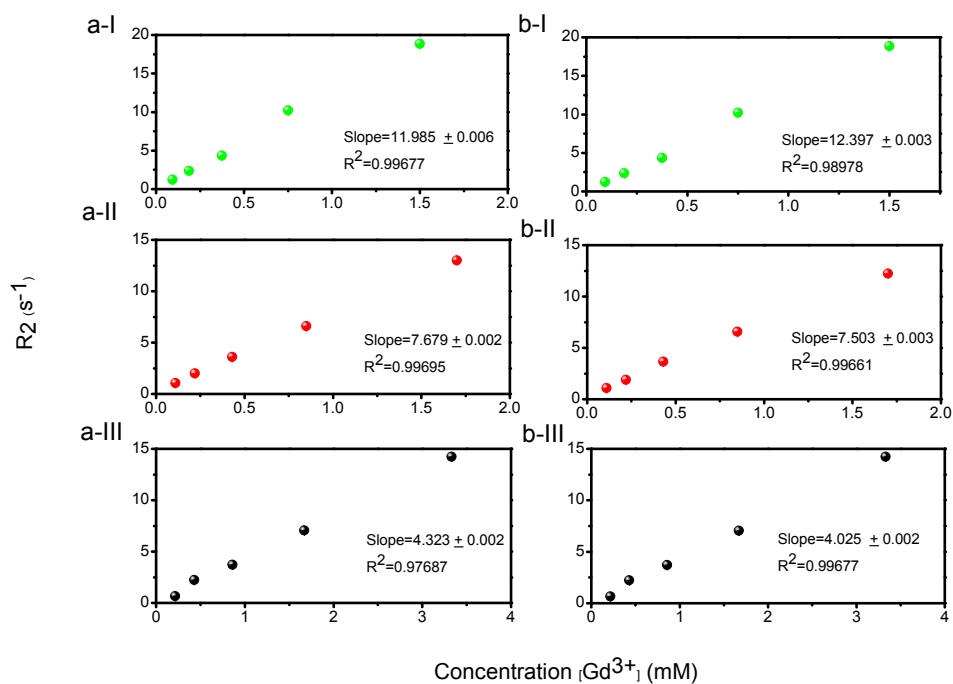


**Figure 4.35.**  $r_2$  values measured at 20 MHz; **(a)** 25°C and **(b)** 37°C and samples I- SiO<sub>2</sub>@APS/PMN:Gd; II- SiO<sub>2</sub>@APS/PMN:EuGd; (1:1) and III- SiO<sub>2</sub>@APS/PMN:TbGd (1:1).

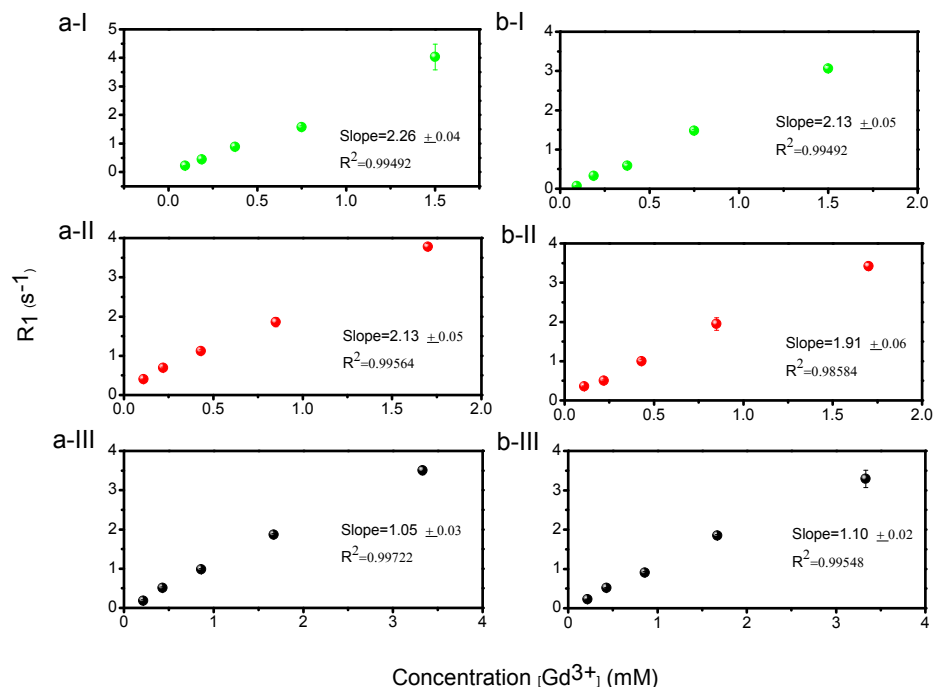


**Figure 4.36.**  $r_1$  values measured at 500 MHz; **(a)** 25°C and **(b)** 37°C and samples I- SiO<sub>2</sub>@APS/PMN:Gd; II- SiO<sub>2</sub>@APS/PMN:EuGd; (1:1) and III- SiO<sub>2</sub>@APS/PMN:TbGd (1:1).

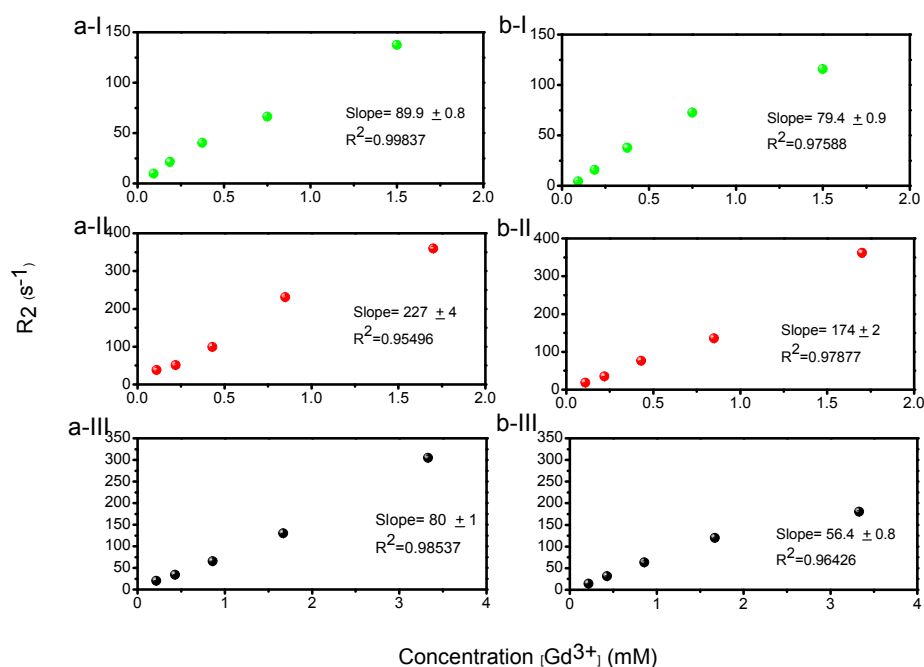


**Figure 4.37.**  $r_2$  values measured at 500 MHz; **(a)** 25°C and **(b)** 37°C and samples **I-**  $SiO_2@APS/PMN:Gd$ ; **II-**  $SiO_2@APS/PMN:EuGd$ ; (1:1) and **III-**  $SiO_2@APS/PMN:TbGd$  (1:1).

#### 4.3.4. Cell Imaging

Regarding the cellular uptake of the both NPs, the results obtained show that they are rapidly internalized by RAW 264.7 cells. In the case of the  $SiO_2@APS/DTPA:Ln$  study, the  $T_1$ -weighted MRI images of cellular pellets with cells incubated with and without NPs, are shown in Figure 4.38a. A clear increase in the intensity of the pellets (positive contrast), obtained with cells incubated with  $SiO_2@APS/DTPA:EuGd$  NPs (sample III), is observed relative to the pellets corresponding to unexposed cells (sample I), as opposed to the strong negative contrast caused by internalization of the  $T_2$ -shortening  $Fe_2O_3$  NPs (sample II). The optical features of the NPs internalized cells were also assessed at a wavelength of 393 nm. The results illustrated in Figure 4.38b demonstrate that the fluorescence of sample II is a combination of the autofluorescence of cells and the fluorescence exhibited by the  $SiO_2@APS/DTPA:EuGd$  NPs (violet is the combination of red and

blue). These observations confirm the potential of the NPs as optical imaging contrast agents.

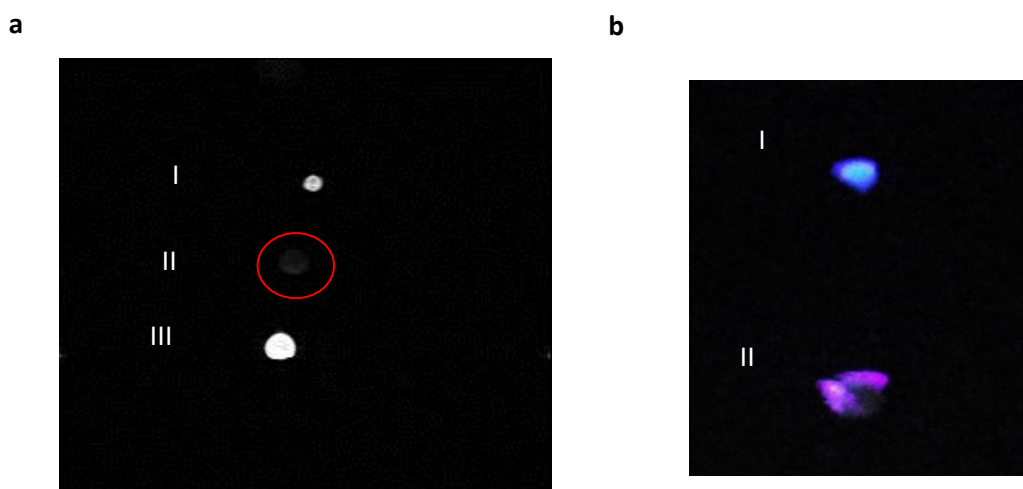


**Figure 4.38.** (a)  $T_1$ -weighted MRI image of cellular pellets corresponding to: I- no NP internalization (control); II-  $\gamma$ - $\text{Fe}_2\text{O}_3$  NPs ( $T_2$ ) NP cell internalization and III-  $\text{SiO}_2$ @APS/DTPA:EuGd NP cell internalization; (b) Photograph of cellular pellets, excited at 393 nm, corresponding to: I- no NP cell internalization (control) and II-  $\text{SiO}_2$ @APS/DTPA:EuGd NP cell incorporation.

In the case of the  $\text{SiO}_2$ @APS/PMN:Ln study, the  $T_1$ -weighted MRI images of cellular pellets with cells incubated with and without NPs, are shown in Figure 4.39a. A clear increase in the intensity of the pellets (positive contrast), obtained with cells incubated with  $\text{SiO}_2$ @APS/PMN:EuGd NPs (sample III), is observed relative to the pellets corresponding to unexposed cells (sample I), however the sample with cells incubated with  $\text{SiO}_2$ @APS/PMN:Gd NPs (sample II), however, displays a decrease in intensity of the pellets confirming the  $r_1$  values obtained above. The optical features of the NPs internalized cells were also assessed at a wavelength of 393 nm. The results illustrated in Figure 4.39c demonstrate that the fluorescence of sample II and III is a combination of the autofluorescence of cells (sample I) and the red fluorescence exhibited by the  $\text{Eu}^{3+}$  ion (in Figure 4.39b), (violet is the combination of red and blue). These observations confirm the potential of the NPs as optical imaging contrast agents.

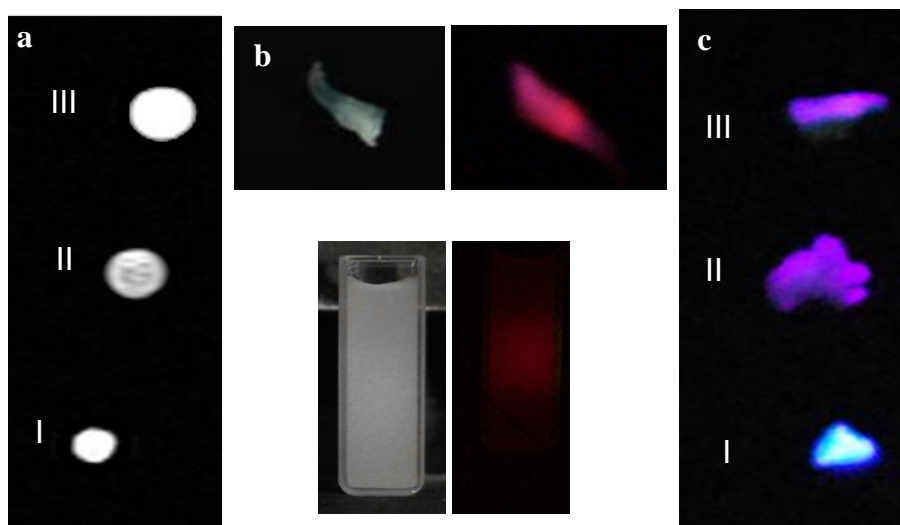


**Figure 4.39.** (a)  $T_1$ -weighted MRI image of cellular pellets: I- no NP internalization (control); II-  $\text{SiO}_2\text{@APS/PMN:Gd}$  cell internalized NPs; III-  $\text{SiO}_2\text{@APS/PMN:EuGd}$  cell internalized NPs; (b) Photograph of  $\text{SiO}_2\text{@APS/PMN:Eu}$  NPs in the solid state (top) and suspension (bottom), excited at 393 nm (right) and non-excited (left); (c) Photograph of cellular pellets, excited at 393 nm: I- no NPs cell internalization (control); II- $\text{SiO}_2\text{@APS/PMN:Eu}$  cell internalized NPs; III-  $\text{SiO}_2\text{@APS/PMN:EuGd}$  cell internalized NPs.

#### 4.4. CONCLUSIONS

Bimodal MRI - optical probes for bio-imaging, based on  $\text{SiO}_2$  nanoparticles derivatized with DTPA-Ln and PMN-Ln complexes ( $\text{SiO}_2\text{@APS/DTPA:Gd:Ln}$ ; and  $\text{SiO}_2\text{@APS/PMN:Gd:Ln}$ ; Ln=  $\text{Eu}^{3+}$ ,  $\text{Tb}^{3+}$ ) were developed. The incorporation of  $\text{Gd}^{3+}$  ions (the MRI probe) in the nanosystems does not change the emission properties of the  $\text{Eu}^{3+}$  and  $\text{Tb}^{3+}$  ions, while the relaxometric features are slightly better than the properties of the commercially-available  $[\text{Gd}(\text{DTPA})]^{2-}$  complex.

The grafting of pyridine-based aromatic ligands (efficient  $\text{Ln}^{3+}$  sensitizers) to the silica surface via APS, and their complexation with  $\text{Gd}^{3+}$ ,  $\text{Eu}^{3+}/\text{Tb}^{3+}$  ions affords relaxometry, and photoluminescent properties.

Both of these bimodal probes are rapidly and efficiently uptaken by RAW 264.7 cells (mouse macrophage cell line) and exhibit both,  $T_1$ -weighted MRI images of cellular pellets increased contrast and potential optical tracking by fluorescence. increased contrast and potential fluorescence tracking.

#### 4.5. REFERENCES

- 1 Townsend, D. W.; Beyer, T.; Blodgett, T. M., PET/CT scanners: A hardware approach to image fusion. *Seminars in Nuclear Medicine* **2003**, 33 (3), 193-204.
- 2 Momose, A.; Takeda, T.; Itai, Y.; Hirano, K., Phase-contrast X-ray computed tomography for observing biological soft tissues. *Nature Medicine* **1996**, 2 (4), 473-475.
- 3 Shokeen, M.; Anderson, C. J., Molecular Imaging of Cancer with Copper-64 Radiopharmaceuticals and Positron Emission Tomography (PET). *Accounts of Chemical Research* **2009**, 42 (7), 832-841.
- 4 Ametamey, S. M.; Honer, M.; Schubiger, P. A., Molecular imaging with PET. *Chemical Reviews* **2008**, 108 (5), 1501-1516.
- 5 Wadas, T. J.; Wong, E. H.; Weisman, G. R.; Anderson, C. J., Coordinating Radiometals of Copper, Gallium, Indium, Yttrium, and Zirconium for PET and SPECT Imaging of Disease. *Chemical Reviews* **2010**, 110 (5), 2858-2902.
- 6 Zhang, R.; Xiong, C.; Huang, M.; Zhou, M.; Huang, Q.; Wen, X.; Liang, D.; Li, C., Peptide-conjugated polymeric micellar nanoparticles for Dual SPECT and optical imaging of EphB4 receptors in prostate cancer xenografts. *Biomaterials* **2011**, 32 (25), 5872-5879.
- 7 Ntziachristos, V.; Razansky, D., Molecular Imaging by Means of Multispectral Optoacoustic Tomography (MSOT). *Chemical Reviews* **2010**, 110 (5), 2783-2794.
- 8 Caravan, P.; Ellison, J. J.; McMurry, T. J.; Lauffer, R. B., Gadolinium(III) chelates as MRI contrast agents: Structure, dynamics, and applications. *Chemical Reviews* **1999**, 99 (9), 2293-2352.
- 9 Bulte, J. W. M., The chemistry of contrast agents in medical magnetic resonance imaging. edited by A. E. Merbach and E. Toth. Wiley, Chichester, 2001, £135. *NMR in Biomedicine* **2004**, 17 (4), 210-210.
- 10 Terreno, E.; Castelli, D. D.; Viale, A.; Aime, S., Challenges for Molecular Magnetic Resonance Imaging. *Chemical Reviews* **2010**, 110 (5), 3019-3042.
- 11 Chen, K.-J.; Wolahan, S. M.; Wang, H.; Hsu, C.-H.; Chang, H.-W.; Durazo, A.; Hwang, L.-P.; Garcia, M. A.; Jiang, Z. K.; Wu, L.; Lin, Y.-Y.; Tseng, H.-R., A small MRI contrast agent library of gadolinium(III)-encapsulated supramolecular nanoparticles for improved relaxivity and sensitivity. *Biomaterials* **2011**, 32 (8), 2160-2165.
- 12 Raymond, K. N.; Pierre, V. C., Next generation, high relaxivity gadolinium MRI agents. *Bioconjugate Chemistry* **2005**, 16 (1), 3-8.
- 13 Jennings, L. E.; Long, N. J., 'Two is better than one'-probes for dual-modality molecular imaging. *Chemical Communications* **2009**, (24), 3511-3524.
- 14 Louie, A. Y., Multimodality Imaging Probes: Design and Challenges. *Chemical Reviews* **2010**, 110 (5), 3146-3195.

- 15 Modò, M.; Cash, D.; Mellodew, K.; Williams, S. C. R.; Fraser, S. E.; Meade, T. J.; Price, J.; Hodges, H., Tracking transplanted stem cell migration using bifunctional, contrast agent-enhanced, magnetic resonance imaging. *Neuroimage* **2002**, *17* (2), 803-811.
- 16 Mishra, A.; Pfeuffer, J.; Mishra, R.; Engelmann, J.; Mishra, A. K.; Ugurbil, K.; Logothetis, N. K., A new class of Gd-based DO3A-ethylamine-derived targeted contrast agents for MR and optical imaging. *Bioconjugate Chemistry* **2006**, *17* (3), 773-780.
- 17 Bernhard, C.; Goze, C.; Rousselin, Y.; Denat, F., First bodipy-DOTA derivatives as probes for bimodal imaging. *Chemical Communications* **2010**, *46* (43), 8267-8269.
- 18 Kotkova, Z.; Kotek, J.; Jirak, D.; Jendelova, P.; Herynek, V.; Berkova, Z.; Hermann, P.; Lukes, I., Cyclodextrin-Based Bimodal Fluorescence/MRI Contrast Agents: An Efficient Approach to Cellular Imaging. *Chemistry-a European Journal* **2010**, *16* (33), 10094-10102.
- 19 Lowe, M. P.; Parker, D.; Reany, O.; Aime, S.; Botta, M.; Castellano, G.; Gianolio, E.; Pagliarin, R., pH-dependent modulation of relaxivity and luminescence in macrocyclic gadolinium and europium complexes based on reversible intramolecular sulfonamide ligation. *Journal of the American Chemical Society* **2001**, *123* (31), 7601-7609.
- 20 Crich, S. G.; Biancone, L.; Cantaluppi, V.; Esposito, D. D. G.; Russo, S.; Camussi, G.; Aime, S., Improved route for the visualization of stem cells labeled with a Gd/Eu-chelate as dual (MRI and fluorescence) agent. *Magnetic Resonance in Medicine* **2004**, *51* (5), 938-944.
- 21 Nasso, I.; Galaup, C.; Havas, F.; Tisnes, P.; Picard, C.; Laurent, S.; Elst, L. V.; Muller, R. N., Bimodal system (luminophore and paramagnetic contrastophore) derived from Ln(III) complexes based on a bipyridine-containing macrocyclic ligand. *Inorganic Chemistry* **2005**, *44* (23), 8293-8305.
- 22 Nonat, A.; Gateau, C.; Fries, P. H.; Mazzanti, M., Lanthanide complexes of a picolinate ligand derived from 1,4,7-triazacyclononane with potential application in magnetic resonance imaging and time-resolved luminescence imaging. *Chemistry-a European Journal* **2006**, *12* (27), 7133-7150.
- 23 Picard, C.; Geum, N.; Nasso, I.; Mestre, B.; Tisnes, P.; Laurent, S.; Muller, R. N.; Vander Elst, L., A dual lanthanide probe suitable for optical (Tb<sup>3+</sup> luminescence) and magnetic resonance imaging (Gd<sup>3+</sup> relaxometry). *Bioorganic & Medicinal Chemistry Letters* **2006**, *16* (20), 5309-5312.
- 24 Laurent, S.; Elst, L. V.; Wautier, M.; Galaup, C.; Muller, R. N.; Picard, C., In vitro characterization of the Gd complex of 2,6-pyridinediylbis(methylene nitrilo) tetraacetic acid (PMN-tetraacetic acid) and of its Eu analogue, suitable bimodal contrast agents for MRI and optical imaging. *Bioorganic & Medicinal Chemistry Letters* **2007**, *17* (22), 6230-6233.

- 25 Pellegatti, L.; Zhang, J.; Drahos, B.; Villette, S.; Suzenet, F.; Guillaumet, G.; Petoud, S.; Toth, E., Pyridine-based lanthanide complexes: towards bimodal agents operating as near infrared luminescent and MRI reporters. *Chemical Communications* **2008**, (48), 6591-6593.
- 26 Tallec, G.; Imbert, D.; Fries, P. H.; Mazzanti, M., Highly stable and soluble bis-aqua Gd, Nd, Yb complexes as potential bimodal MRI/NIR imaging agents. *Dalton Transactions* **2010**, 39 (40), 9490-9492.
- 27 Tallec, G.; Imbert, D.; Fries, P. H.; Mazzanti, M., Highly stable and soluble bis-aqua Gd, Nd, Yb complexes as potential bimodal MRI/NIR imaging agents. *Dalton Transactions* **2010**, 39 (40), 9490-9492.
- 28 Mulder, W. J. M.; Koole, R.; Brandwijk, R. J.; Storm, G.; Chin, P. T. K.; Strijkers, G. J.; Donega, C. D.; Nicolay, K.; Griffioen, A. W., Quantum dots with a paramagnetic coating as a bimodal molecular imaging probe. *Nano Letters* **2006**, 6 (1), 1-6
- 29 Jin, T.; Yoshioka, Y.; Fujii, F.; Komai, Y.; Seki, J.; Seiyama, A., Gd(3+)-functionalized near-infrared quantum dots for in vivo dual modal (fluorescence/magnetic resonance) imaging. *Chemical Communications* **2008**, (44), 5764-5766
- 30 Rieter, W. J.; Kim, J. S.; Taylor, K. M. L.; An, H.; Lin, W.; Tarrant, T.; Lin, W., Hybrid silica nanoparticles for multimodal Imaging. *Angewandte Chemie-International Edition* **2007**, 46 (20), 3680-3682.
- 31 Hu, K.-W.; Jhang, F.-Y.; Su, C.-H.; Yeh, C.-S., Fabrication of Gd(2)O(CO(3))(2)center dot H(2)O/silica/gold hybrid particles as a bifunctional agent for MR imaging and photothermal destruction of cancer cells. *Journal of Materials Chemistry* **2009**, 19 (15), 2147-2153
- 32 van Tilborg, G. A. F.; Vucic, E.; Strijkers, G. J.; Cormode, D. P.; Mani, V.; Skajaa, T.; Reutelingsperger, C. P. M.; Fayad, Z. A.; Mulder, W. J. M.; Nicolay, K., Annexin A5-Functionalized Bimodal Nanoparticles for MRI and Fluorescence Imaging of Atherosclerotic Plaques. *Bioconjugate Chemistry* **2010**, 21 (10), 1794-1803.
- 33 Choo, E. S. G.; Tang, X.; Sheng, Y.; Shuter, B.; Xue, J., Controlled loading of superparamagnetic nanoparticles in fluorescent nanogels as effective T(2)-weighted MRI contrast agents. *Journal of Materials Chemistry* **2011**, 21 (7), 2310-2319.
- 34 Ke, J.-H.; Lin, J.-J.; Carey, J. R.; Chen, J.-S.; Chen, C.-Y.; Wang, L.-F., A specific tumor-targeting magnetofluorescent nanoprobe for dual-modality molecular imaging. *Biomaterials* **2010**, 31 (7), 1707-1715.
- 35 Bottrill, M.; Nicholas, L. K.; Long, N. J., Lanthanides in magnetic resonance imaging. *Chemical Society Reviews* **2006**, 35 (6), 557-571.
- 36 Runge, V. M.; Carollo, B. R.; Wolf, C. R.; Nelson, K. L.; Gelblum, D. Y., Gd DTPA: a review of clinical indications in central nervous system magnetic resonance imaging.

- Radiographics : a review publication of the Radiological Society of North America, Inc* **1989**, 9 (5), 929-58.
- 37 Sammes, P. G.; Yahioğlu, G., Modern bioassays using metal chelates as luminescent probes. *Natural Product Reports* **1996**, 13 (1), 1-28.
- 38 Bulte, J. W. M.; Modo, M. M., In Nanoparticles in biomedical imaging - emerging technologies and applications. *Springer, New York* **2008**.
- 39 Na, H. B.; Song, I. C.; Hyeon, T., Inorganic Nanoparticles for MRI Contrast Agents. *Advanced Materials* **2009**, 21 (21), 2133-2148.
- 40 Taylor, K. M. L.; Kim, J. S.; Rieter, W. J.; An, H.; Lin, W.; Lin, W., Mesoporous silica nanospheres as highly efficient MRI contrast agents. *Journal of the American Chemical Society* **2008**, 130 (7), 2154-2155.
- 41 Tsai, C.-P.; Hung, Y.; Chou, Y.-H.; Huang, D.-M.; Hsiao, J.-K.; Chang, C.; Chen, Y.-C.; Mou, C.-Y., High-contrast paramagnetic fluorescent mesoporous silica nanorods as a multifunctional cell-imaging probe. *Small* **2008**, 4 (2), 186-191.
- 42 Hsiao, J.-K.; Tsai, C.-P.; Chung, T.-H.; Hung, Y.; Yao, M.; Liu, H.-M.; Mou, C.-Y.; Yang, C.-S.; Chen, Y.-C.; Huang, D.-M., Mesoporous silica nanoparticles as a delivery system of gadolinium for effective human stem cell tracking. *Small* **2008**, 4 (9), 1445-1452.
- 43 Carniato, F.; Tei, L.; Cossi, M.; Marchese, L.; Botta, M., A Chemical Strategy for the Relaxivity Enhancement of Gd(III) Chelates Anchored on Mesoporous Silica Nanoparticles. *Chemistry-a European Journal* **2010**, 16 (35), 10727-10734.
- 44 Carniato, F.; Tei, L.; Dastru, W.; Marchese, L.; Botta, M., Relaxivity modulation in Gd-functionalised mesoporous silicas. *Chemical Communications* **2009**, (10), 1246-1248.
- 45 Steinbacher, J. L.; Lathrop, S. A.; Cheng, K.; Hillegass, J. M.; Butnor, K.; Kauppinen, R. A.; Mossman, B. T.; Landry, C. C., Gd-Labeled Microparticles in MRI: In vivo Imaging of Microparticles After Intraperitoneal Injection. *Small* **2010**, 6 (23), 2678-2682.
- 46 Santra, S.; Bagwe, R. P.; Dutta, D.; Stanley, J. T.; Walter, G. A.; Tan, W.; Moudgil, B. M.; Mericle, R. A., Synthesis and characterization of fluorescent, radio-opaque, and paramagnetic silica nanoparticles for multimodal bioimaging applications. *Advanced Materials* **2005**, 17 (18), 2165-2169.
- 47 Wu, C.; Hong, J.; Guo, X.; Huang, C.; Lai, J.; Zheng, J.; Chen, J.; Mu, X.; Zhao, Y., Fluorescent core-shell silica nanoparticles as tunable precursors: towards encoding and multifunctional nano-probes. *Chemical Communications* **2008**, (6), 750-752.
- 48 Stöber, W.; Fink, A.; Bohn, E., Controlled Growth of Monodisperse Silica Spheres in Micron Size Range. *Journal of Colloid and Interface Science* **1968**, 26 (1), 62-69.
- 49 Rizkalla, E. N.; Choppin, G. R.; Cacheris, W., Thermodynamics NMR, and Fluorescence Studies for the Complexation of Trivalent Lanthanides, Ca<sup>2+</sup>, Cu<sup>2+</sup>, and Zn<sup>2+</sup> by Diethylenetriaminepentaacetic Acid bis(methlamide). *Inorganic Chemistry* **1993**, 32 (5), 582-586.

- 50 Sherry, A. D.; Cacheris, W. P.; Kuan, K. T., Stability-constants for Gd<sup>3+</sup> Binding to model DTPA-conjugates and Proteins - Implications for their use as Magnetic Resonance Contrast Agents. *Magnetic Resonance in Medicine* **1988**, *8* (2), 180-190.
- 51 Voisin, P.; Ribot, E. J.; Miraux, S.; Bouzier-Sore, A.-K.; Lahitte, J.-F.; Bouchaud, V.; Mornet, S.; Thiaudiere, E.; Franconi, J.-M.; Raison, L.; Labrugere, C.; Delville, M.-H., Use of lanthanide-grafted inorganic nanoparticles as effective contrast agents for cellular uptake imaging. *Bioconjugate Chemistry* **2007**, *18* (4), 1053-1063.
- 52 Kumar, R.; Roy, I.; Ohulchanskyy, T. Y.; Vathy, L. A.; Bergey, E. J.; Sajjad, M.; Prasad, P. N., In Vivo Biodistribution and Clearance Studies Using Multimodal Organically Modified Silica Nanoparticles. *ACS Nano* **2010**, *4* (2), 699-708.
- 53 Lu, Y.; Yin, Y. D.; Mayers, B. T.; Xia, Y. N., Modifying the surface properties of superparamagnetic iron oxide nanoparticles through a sol-gel approach. *Nano Letters* **2002**, *2* (3), 183-186.
- 54 Nozawa, K.; Gailhanou, H.; Raison, L.; Panizza, P.; Ushiki, H.; Sellier, E.; Delville, J. P.; Delville, M. H., Smart control of monodisperse Sotber silica particles: Effect of reactant addition rate on growth process. *Langmuir* **2005**, *21* (4), 1516-1523.
- 55 Dehaan, J. W.; Vandenbogaert, H. M.; Ponjee, J. J.; Vandeven, L. J. M., Characterization of modified silica powders by fourier transform infrared spectroscopy and cross-polarization magic angle spinning NMR. *Journal of Colloid and Interface Science* **1986**, *110* (2), 591-600.
- 56 Sakthivel, A.; Hijazi, A. K.; Al Hmaideen, A. I.; Kuehn, F. E., Grafting of Cu(NCCH<sub>3</sub>)(6) B{C<sub>6</sub>H<sub>3</sub>(m-CF<sub>3</sub>)(2)}(4) (2) on the surface of aminosilane modified SBA-15. *Microporous and Mesoporous Materials* **2006**, *96* (1-3), 293-300.
- 57 Sakthivel, A.; Zhao, J.; Kuhn, F. E., Grafting of the eta(5)-CPMo(CO)(3) moiety on pure and surface modified SBA-15 molecular sieves. *Microporous and Mesoporous Materials* **2005**, *86* (1-3), 341-348.
- 58 Harder, R.; Chaberek, S., The Interaction of Rare Earth Ions with Diethylenetriaminepentaacetic Acid. *Journal of Inorganic & Nuclear Chemistry* **1959**, *11* (3), 197-209.
- 59 Lauffer, R. B., Paramagnetic Metal-complexes as Water Proton Relaxation Agents for NMR Imaging - Theory and Design. *Chemical Reviews* **1987**, *87* (5), 901-927.
- 60 S.L.C. Pinho, H. Faneca, C.F.G.C. Geraldés, M.H. Delville, L.D. Carlos, J.Rocha, *Biomaterials*, in press.
- 61 Nunes, S. C.; Bermudez, V. D. Z.; Cybinska, J.; Ferreira, R. A. S.; Legendziewicz, J.; Carlos, L. D.; Silva, M. M.; Smith, M. J.; Ostrovskii, D.; Rocha, J., Structure and photoluminescent features of di-amide cross-linked alkylene siloxane hybrids. *Journal of Materials Chemistry* **2005**, *15* (35-36), 3876-3886.

- 62 Schulz, H.; Pratsinis, S. E.; Ruegger, H.; Zimmermann, J.; Klapdohr, S.; Salz, U., Surface functionalization of radiopaque Ta<sub>2</sub>O<sub>5</sub>/SiO<sub>2</sub>. *Colloids and Surfaces a-Physicochemical and Engineering Aspects* **2008**, *315* (1-3), 79-88.
- 63 Albert, K.; Brindle, R.; Schmid, J.; Buszewski, B.; Bayer, E., CP/MAS NMR Investigations of Silica-Gel Surfaces Modified with Aminopropylsilane. *Chromatographia* **1994**, *38* (5-6), 283-290.
- 64 Plueddemann, E., Interfaces in polymer matrix composites In: Brautman LJ, Krock RH editors. Composite Materials. *Academic Press, New York* **1974**, *6*.
- 65 Boerio, F. J.; Schoenlein, L. H.; Greivenkamp, J. E., Adsorption of Gamma-Aminopropyltriethoxysilane onto Bulk Iron from Aqueous Solutions. *J Appl Polym Sci* **1978**, *22* (1), 203-213.
- 66 Anderson, H. R.; Fowkes, F. M.; Hielscher, F. H., Electron Donor-Acceptor Properties of Thin Polymer Films on Silicon 2. Tetrafluoroethylene Polymerized by RF Glow Discharge Techniques. *Journal of Polymer Science Part B-Polymer Physics* **1976**, *14* (5), 879-895.
- 67 Moses, P. R.; Wier, L. M.; Lennox, J. C.; Finklea, H. O.; Lenhard, J. R.; Murray, R. W., Chemically Modified Electrodes 9.X-Ray Photoelectron-Spectroscopy of Alkylamine-silanes Bound to Metal-oxide Electrodes. *Analytical Chemistry* **1978**, *50* (4), 576-585.
- 68 Ishida, H.; Chiang, C. H.; Koenig, J. L., The structure of aminofunctional silane coupling agents: 1.  $\gamma$ -aminopropyltriethoxysilane and its analogues. *Polymer* **1982**, *23* (2), 251-257.
- 69 Jakob, A. M.; Schmedake, T. A., A novel approach to monodisperse, luminescent silica spheres. *Chemistry of Materials* **2006**, *18* (14), 3173-3175.
- 70 Wang, L.; Estevez, M. C.; O'Donoghue, M.; Tan, W., Fluorophore-free luminescent organosilica nanoparticles. *Langmuir* **2008**, *24* (5), 1635-1639.
- 71 Nobre, S. S.; Lima, P. P.; Mafra, L.; Ferreira, R. A. S.; Freire, R. O.; Fu, L.; Pischel, U.; Bermudez, V. d. Z.; Malta, O. L.; Carlos, L. D., Energy transfer and emission quantum yields of organic-inorganic hybrids lacking metal activator centers. *Journal of Physical Chemistry C* **2007**, *111* (8), 3275-3284.
- 72 Bermudez, V. D.; Carlos, L. D.; Duarte, M. C.; Silva, M. M.; Silva, C. J. R.; Smith, M. J.; Assuncao, M.; Alcacer, L., A novel class of luminescent polymers obtained by the sol-gel approach. *Journal of Alloys and Compounds* **1998**, *275*, 21-26.
- 73 Ferreira, R. A. S.; Nobre, S. S.; Granadeiro, C. M.; Nogueira, H. I. S.; Carlos, L. D.; Malta, O. L., A theoretical interpretation of the abnormal D-5(0)  $\rightarrow$  F-7(4) intensity based on the Eu<sup>3+</sup> local coordination in the Na<sub>9</sub> EuW<sub>10</sub>O<sub>36</sub> center dot 14H<sub>2</sub>O polyoxometalate. *J Lumin* **2006**, *121* (2), 561-567.
- 74 Carlos, L. D.; Ferreira, R. A. S.; Bermudez, V. d. Z.; Ribeiro, S. J. L., Lanthanide-Containing Light-Emitting Organic-Inorganic Hybrids: A Bet on the Future. *Advanced Materials* **2009**, *21* (5), 509-534.

- 75 Bryden, C. C.; Reilley, C. N., Europium luminescence lifetimes and spectra for evaluation of 11 europium complexes as aqueous shift reagents for nuclear magnetic resonance spectrometry. *Analytical Chemistry* **1982**, *54* (4), 610-615.
- 76 Malta, O. L.; dos Santos, M. A. C.; Thompson, L. C.; Ito, N. K., Intensity parameters of 4f-4f transitions in the Eu(dipivaloylmethanate)(3) 1,10-phenanthroline complex. *J Lumin* **1996**, *69* (2), 77-84.
- 77 Carlos, L. D.; Messaddeq, Y.; Brito, H. F.; Ferreira, R. A. S.; Bermudez, V. D.; Ribeiro, S. J. L., Full-color phosphors from europium(III)-based organosilicates. *Advanced Materials* **2000**, *12* (8), 594-598.
- 78 Lima, P. P.; Ferreira, R. A. S.; Freire, R. O.; Paz, F. A. A.; Fu, L. S.; Alves, S.; Carlos, L. D.; Malta, O. L., Spectroscopic study of a UV-photostable organic-inorganic hybrids incorporating an Eu(3+) beta-diketonate complex. *Chemphyschem* **2006**, *7* (3), 735-746.
- 79 Carnall, W.; Crosswhite, H., In energy level structure and transition probabilities of the trivalent lanthanides in LaF<sub>3</sub>. *Argonne Natl Lab. Rept* **1977**.
- 80 Norek, M.; Peters, J. A., MRI contrast agents based on dysprosium or holmium. *Progress in Nuclear Magnetic Resonance Spectroscopy* **2011**, *59* (1), 64-82.
- 81 Gillis, P.; Moyny, F.; Brooks, R. A., On T-2-shortening by strongly magnetized spheres: A partial refocusing model. *Magnetic Resonance in Medicine* **2002**, *47* (2), 257-263
- 82 V.A. Runge, B.R. Carollo, C.R. Wolf, K.L. Nelson, *RadioGraphics* **1989**, *9*, 929-958.

# 5.

## *Core-Shell Nanoparticles for Bimodal-Imaging Contrast Agents*

---

5.1. Introduction	172
5.2. Experimental Procedures	174
5.3. Results and Discussions	178
5.3.1. Characterization of Nanoparticles	178
5.3.2. Relaxivity Properties	185
5.3.3. Cell Imaging	199
5.4. Conclusions	201
5.5. References	204

Chapter published as original article:

*Pinho S.L.C., Pereira G.A., Voisin P., Kassem J., Bouchaud V., Etienne L., Peters J.A., Carlos L.D., Mornet S., Geraldes C.F.G.C., Rocha J., Delville M-H.*

Fine tuning of the relaxometry of  $\gamma$ -Fe<sub>2</sub>O<sub>3</sub>@SiO<sub>2</sub> nanoparticles by tweaking the silica coating thickness.

ACSNano 4 (9) 5339 – 5349 (2010) DOI: 10.1021/nn101129r

*Pinho S.L.C., Laurent S., Rocha J., Roch A., Delville M-H., Carlos L.D., Elst L.V., Muller R.N., Geraldes F.G.C.* Relaxometric studies of  $\gamma$ -Fe<sub>2</sub>O<sub>3</sub>@SiO<sub>2</sub> core shell nanoparticles: when the coating matters.

Submitted J. Phys. Chem. C (2011)

## 5.1. INTRODUCTION

Nanoparticles (NPs) made of inorganic or organic materials exhibit many novel properties compared with the bulk materials.<sup>1</sup> Magnetic NPs have unique properties such as superparamagnetism, high coercivity, low Curie temperature, high magnetic susceptibility, etc.<sup>2</sup> Magnetic NPs are of great interest in a broad range of disciplines, from magnetic fluids to data storage, catalysis,<sup>3</sup> and bio-applications.<sup>4</sup> Examples of applications of NPs in the study of biology and biomedicine are magnetic bioseparation,<sup>5</sup> cell sorting,<sup>6,7</sup> detection of biological entities,<sup>8</sup> clinical diagnosis and therapy (such as MRI, magnetic resonance imaging),<sup>9-18</sup> MFH (magnetic fluid hyperthermia)<sup>19</sup> targeted drug delivery,<sup>20-23</sup> immunoassays,<sup>24</sup> and biomacromolecule purification.<sup>25</sup> Magnetic iron oxide NPs play an important role in these applications and they have been used in *in vitro* diagnosis for about 50 years.<sup>26</sup> In the last decade, numerous investigations have been carried out in the field of magnetic NPs,<sup>27</sup> especially on magnetite and maghemite due to their biocompatibility, FDA approval<sup>28</sup> and absence of toxicity.<sup>29-31</sup>

The control of the NPs size, shape, stability, and dispersibility in specific solvents is a technological challenge. Bio-applications, for example, require water-solubility and colloidal stability. However, most reported syntheses of high-quality NPs of metals,<sup>32,33</sup> semiconductors,<sup>34,35</sup> and metal oxides<sup>36-38</sup> involve non-aqueous solvents and coating with monolayers of hydrophobic surfactants. Several strategies to tackle these

challenges have been formulated,<sup>39</sup> such as i) polymer coating,<sup>40,41</sup> ii) exchanging the original hydrophobic stabilizer with dendrons,<sup>42,43</sup> thiols or even oligomeric phosphines<sup>44</sup> and iii) silica coatings.<sup>45-53</sup>

In order to expand the scope of the iron oxide NPs in biological applications, biomolecules have been employed as coatings, such as amino acids,<sup>54</sup> vitamins,<sup>55,56</sup> proteins,<sup>57</sup> antibodies,<sup>58,59</sup> polypeptides,<sup>60</sup> biotin, avidin<sup>61</sup> and saccharides.<sup>62</sup> However, silica coating remains one of the most popular and well-known techniques for NP surface modification, because the resulting cross-linked silica shell protects the core from the environment and the other way around. The silica coating also provides colloidal stability in biological solutions by avoiding inter-particle interactions and agglomeration. Furthermore, it can act as an anchor for the binding of biological vectors at the NPs surface.<sup>63</sup> Although there are several publications concerning silica coatings, only a few methods have been reported for the preparation of water-soluble silica-coated NPs with a high colloidal stability and with sizes below 20 nm.<sup>45,50,53</sup>

Particles with tunable size are important when considering biomedical applications. While small NPs exhibit reduced nonspecific interactions, minimal steric effects, and high clearance rates,<sup>64</sup> larger NPs are subjected to internalization by macrophages. The thickness of the silica shell has also a strong influence on the physical properties of the NPs, especially in terms of contrast agent efficacy for magnetic resonance imaging. We describe the synthesis of  $\gamma\text{-Fe}_2\text{O}_3\text{@SiO}_2$ , core-shell NPs with tuned shell thicknesses. These particles were characterized by Transmission Electron Microscopy (TEM), zeta potential determinations, Diffuse Reflectance Infrared Fourier-Transform and Nuclear Magnetic Resonance. The longitudinal ( $T_1$ ) and transversal ( $T_2$ ) relaxation times of aqueous suspensions of the prepared particles were measured, and their cytotoxicity was investigated. We show that the shell thickness of  $\gamma\text{-Fe}_2\text{O}_3\text{@SiO}_2$  NPs has a significant impact on their relaxivities. This silica layer exhibits two regions around the core, one, which is porous to water, and a second one, which is not.

## 5.2. EXPERIMENTAL PROCEDURES

### ***Materials and purification methods***

Iron (III) chloride hexahydrate (98%), iron (II) chloride tetrahydrate (99%), iron (III) nitrate nonahydrate (99%), tetraethoxysilane (TEOS) (98%), and citric acid (99.5%) were purchased from Aldrich. Absolute ethanol (J.T. Baker) and ammonia (Carlo Erba) were used as received. All other reagents were of analytical grade. All the experiments were performed in deionized Milli-Q water.

### ***Preparation of the maghemite ferrofluid suspension***

The aqueous maghemite suspension was synthesized by precipitation from iron chlorides.<sup>65,66</sup> Briefly, the Fe<sub>3</sub>O<sub>4</sub> precipitate (black dispersion of magnetite), obtained by alkalization of the FeCl<sub>2</sub> and FeCl<sub>3</sub> (Fe<sup>2+</sup>/Fe<sup>3+</sup> = 1/2) aqueous mixture, was successively oxidized with 2M HNO<sub>3</sub> and 0.33 M Fe(NO<sub>3</sub>)<sub>3</sub> · 9H<sub>2</sub>O solutions at 100 °C in order to obtain particles with a Fe<sup>2+</sup>/Fe<sup>3+</sup> ratio lower than 0.05. With this oxidation process, magnetite is converted into maghemite. The brown dispersion was peptized in a 2 M HNO<sub>3</sub> solution under vigorous stirring in order to create positive surface charges. The acidic precipitate was isolated by magnetic separation, washed with acetone and dispersed at pH ~ 2.5 in water with nitric acid. The iron concentration was determined by volumetric titration as well as by ICP measurements and the average particle size, as determined by transmission electron microscopy (TEM), was 10 ± 2 nm

### ***Preparation of the maghemite ferrofluid core-shell suspension***

The selected method was derived from the so-called Stöber process<sup>67</sup> widely used for the synthesis of silica beads with diameters from a few tens to a few hundreds of nanometers.<sup>68</sup> It is based on the hydrolysis/condensation of tetraethoxysilane (TEOS) catalyzed by ammonia in alcoholic media. The surface of γ-Fe<sub>2</sub>O<sub>3</sub> NPs was activated by acidic treatment: where 7.55 mL of γ-Fe<sub>2</sub>O<sub>3</sub> colloidal suspension (concentration 74.4 g/L) were dispersed in 40 mL of 0.01 M citric acid. They were

isolated by decantation on a magnet. The particles were dispersed in 12 mL of water and peptization was performed by adding 20  $\mu\text{L}$  of ammonia. Then, the alkaline sol of citrated-  $\gamma\text{-Fe}_2\text{O}_3$  NPs was poured in 1 L of ethanol-water-ammonia solution 75/23.5/1.5 v/v/v %, to obtained a 0.561 g/L concentration. The appropriate amounts of TEOS precursors were added to the dispersion under mild stirring to reach the targeted shell thickness. They were set to comply with the desired thickness of the silica shell according to equation 5.1 and added in multiple steps.

$$V_{TEOS} = N_{part} \left( \frac{\rho_{SiO_2} M_{TEOS}}{\rho_{TEOS} M_{SiO_2}} \right) \frac{4}{3} \pi \left[ (r + e_{shell})^3 - r^3 \right] \quad (5.1)$$

Where  $e_{shell}$  is the shell thickness (the difference  $\frac{4}{3} \pi \left[ (r + e_{shell})^3 - r^3 \right]$  then corresponding to the volume of the silica shell ( $V_{SiO_2}$ ),  $\rho_{SiO_2}$  is the density and  $M_{SiO_2}$  the molecular weight of  $\text{SiO}_2$ ;  $V_{TEOS}$ ,  $\rho_{TEOS}$ ,  $M_{TEOS}$  are the volume, density and molecular weight of TEOS;  $N_{part}$  is the number of  $\gamma\text{-Fe}_2\text{O}_3$  NPs. The very first amount of added TEOS (763  $\mu\text{L}$ ) corresponds to the smallest observable silica shell thickness (roughly 1 nm). Then, after 12h of the reaction, 200 mL of this solution were stocked for analysis and replaced by the same amount of reaction medium. For the following step, the resulting solution was added with the necessary amount of TEOS to increase the shell thickness, and left to react another 12h. 200 mL of this solution were also stocked for analysis and replaced by the same amount of reaction medium. This procedure was used to get thicker shell sizes (the number of particles in each volume being recalculated to estimate the right amount of TEOS). Under these conditions, no secondary nucleation was observed, which is in agreement with the results reported by Chen et al.<sup>69</sup> Two series of core shell NPs were synthesised and will be denoted series A and B. The difference between these two series was size of the NPs, in series B a better range of thinner coating was produced in order to better understand the influence of the silica shell.

### **Particle characterization**

TEM was performed at room temperature on a JEOL JEM-2000 FX transmission electron microscope using an accelerating voltage of 200 kV. Drops of diluted dispersions of core-shell were air-dried on carbon films deposited on 200-mesh copper grids. The excess liquid was blotted with filter paper. The Diffuse Reflectance Infrared Fourier-Transform (DRIFT) spectra were recorded on a Bruker IFS Equinox 55FTIR spectrometer (signal averaging 64 scans at a resolution of 4 cm<sup>-1</sup> in KBr pellets containing ca. 2 mass % of material). The zeta potential of the NPs was assessed using a Zetasizer 3000HSA setup (Malvern Instruments) equipped with a He-Ne laser (50 mW, 532 nm). The zeta potential measurement based on laser Doppler interferometry was used to measure the electrophoretic mobility of NPs. Measurements were performed for 20s using a standard capillary electrophoresis cell. The dielectric constant was set to 80.4 and the Smoluchowsky constant  $f(ka)$  was 1.5. The iron content has been measured by inductively coupled plasma / optical emission spectrometry ICP/OES (ES720, Varian) equipped with a crossflow nebulizer. A 1 g/L iron solution was used to prepare the standard solutions (SCP Science to Paris) and was used as internal standard to evaluate the instrumental drift.

Measurements of water proton longitudinal and transverse relaxation times ( $T_1$  and  $T_2$  respectively) of aqueous suspensions of the NPs were carried out at 20 MHz on a Bruker Minispec mq20 relaxometer and at 499.83 MHz ( $B_0 = 11.7$  T) on a Varian Unity 500 NMR spectrometer at 25 °C. The  $T_1$  relaxation times were measured using the inversion recovery pulse sequence, while the  $T_2$  relaxation times were measured using a Carr-Purcell-Meiboom-Gill (CPMG) pulse sequence and varying the time interval between two consecutive refocusing pulses ( $\sigma_{CP}$ ) in the train of 180° pulses applied. The values of  $T_2^*$ , the transverse relaxation time in the presence local field inhomogeneities, were obtained from the water spectral line widths. All the experimental values were corrected for the diamagnetic contribution using aqueous suspensions of hollow silica NPs, to obtain each paramagnetic contribution. These hollow shells were prepared by dilution of the core by addition of concentrated HCl.

The magnetization measurements were performed on a known amount of ferrofluid using a vibrating sample magnetometer VSM-NUVO (MOLSPIN, Newcastle

Upon Tyne, U.K.). Magnetometry of NPs allows the determination of the saturation magnetisation ( $M_{sat}$ ) and the radius of the superparamagnetic crystals ( $r$ ) by fitting the data with a Langevin function ( $L(x) = \coth(x) - \frac{1}{x}$  where  $x = \frac{\mu_{sat} B_0}{k_b T}$ ) with  $\mu_{sat}$  as the magnetic moment at saturation,  $B_0$  as the magnetic field,  $k_b$  as the Boltzmann constant and  $T$  as the temperature.

The NMRD profiles were recorded at 37 °C over a magnetic field range from 0.24 mT to 0.24 T on a field cycling Stellar relaxometer (Mede, Italy). Additional longitudinal ( $R_1$ ) and transverse ( $R_2$ ) relaxation rate measurements were performed at 0.47 and 1.41 T on Minispec mq20 and Minispec mq60 relaxometers, respectively (Bruker, Karlsruhe, Germany).

### **Toxicity tests**

Cytotoxicity of the  $\gamma\text{-Fe}_2\text{O}_3\text{@SiO}_2$  NPs was tested by counting the cells in a Malassez chamber and using the MTT assay to evaluate the cell viability after the NPs preparation process. The core-shell NPs FF, 1A, 2A, 5A and 7A had diameters ranging between 10 and 143 nm. Briefly, microglial cell lines were seeded at the rate of *ca.*  $16 \times 10^3$  cells/cm<sup>2</sup> in 35 mm diameter plates and allowed to attach for 24 h. The cells were then incubated for 0, 45 min, 24 h, 48 h, 72 h, 96 h, 120 h and 144 h in 1 mL of culture medium for control cells and supplemented with 60  $\mu\text{L}$  of different NPs (0.16 mM) for treated cells. MTT and counting assays were performed as duplicate for each condition and the data were averaged. After incubation, cells were scraped from the dishes, then stained with trypan blue and counted with a haemocytometer. The MTT assay is a colorimetric assay that measures the reduction of yellow 3-(4,5-dimethylthiazol-2-yl)-2,5-diphenyl tetrazolium bromide (MTT) by dehydrogenase mostly from mitochondria. The MTT enters the cells and passes into the mitochondria, where it is reduced to an insoluble, colored (dark purple) formazan product. After cell culturing in the presence of NPs, 260  $\mu\text{L}$  of the MTT solution in culture medium (0.5 mg/mL) was added into each well. The plate was then incubated at 37 °C in 5 % CO<sub>2</sub> for 45 min. The medium was removed and 1 mL of PBS solution was added, then cells were scraped and centrifuged at 1000 rpm for 5 min. The supernatant was removed and 1 mL of dimethyl sulfoxide (DMSO) was added to the pellets to dissolve the formazan crystals and then it was centrifuged again at 1000 rpm for 5 min. Supernatants were taken and their

absorbance was measured with a U-2800A (UV-VIS) spectrophotometer (Hitachi, Japan) at 570 nm. Since reduction of MTT can only occur in metabolically active cells, the level of activity is an estimation of the viability of the cells as compared to untreated cells. The cell viability (%) was calculated according to equation 5.2:

$$\text{Cell viability \%} = \text{OD}_{570}(\text{sample}) / \text{OD}_{570}(\text{control}) \times 100 \quad (5.2)$$

where  $\text{OD}_{570}(\text{sample})$  represents the optical density of the wells treated with various iron sizes, and  $\text{OD}_{570}(\text{control})$  represents that of the wells treated with medium culture.

## 5.3. RESULTS AND DISCUSSION

### 5.3.1. Characterization of Nanoparticles

The aqueous maghemite suspension was synthesized by basic precipitation from iron chlorides, followed by complete oxidation of the magnetite material. For the coating, a polymerization of silane monomers in the presence of the NPs under Stöber conditions<sup>67,70</sup> was performed. This procedure is widely used since it provides uniform silica coating with a controllable thickness. Stöber's conditions involve alcohol-water-ammonia as the medium and tetraethoxysilane (TEOS) as the silane monomer. A pre-activation of the surface of the NPs through acidic treatment was found to improve the silica coating, leading to a simple and highly reproducible method for producing monodispersed water-soluble stable colloidal NPs with silica shells whose thickness is tunable in the range 2-70 nm.

To tune the silica shell thickness, the required amount of TEOS was calculated from the initial and the desired final particle size,<sup>71,72</sup> taking into account the number of  $\gamma\text{-Fe}_2\text{O}_3$  NPs,  $N_{\text{part.}}$ , by means of equation 5.1.

The estimated and experimental thicknesses of the silica coatings are collected in Table 5.1, while Figure 5.1 displays the TEM images obtained at various stages of the NPs synthesis for series A and B.

TEM showed that spherical core-shell ( $\gamma$ -Fe<sub>2</sub>O<sub>3</sub>@SiO<sub>2</sub>) NPs with different shell sizes were obtained; as clearly evidenced by these images, all the  $\gamma$ -Fe<sub>2</sub>O<sub>3</sub> particles were surrounded by the silica layer. The scheme on the right of the lower row of the images defines the measured size or diameter (d) of the NPs, and their silica shell thickness (t). The average thickness of silica shells was determined from these images by measurements in four directions for each particle and at least 100 particles per  $\gamma$ -Fe<sub>2</sub>O<sub>3</sub>@SiO<sub>2</sub> sample, showing that the size dispersion of the particles is very small.

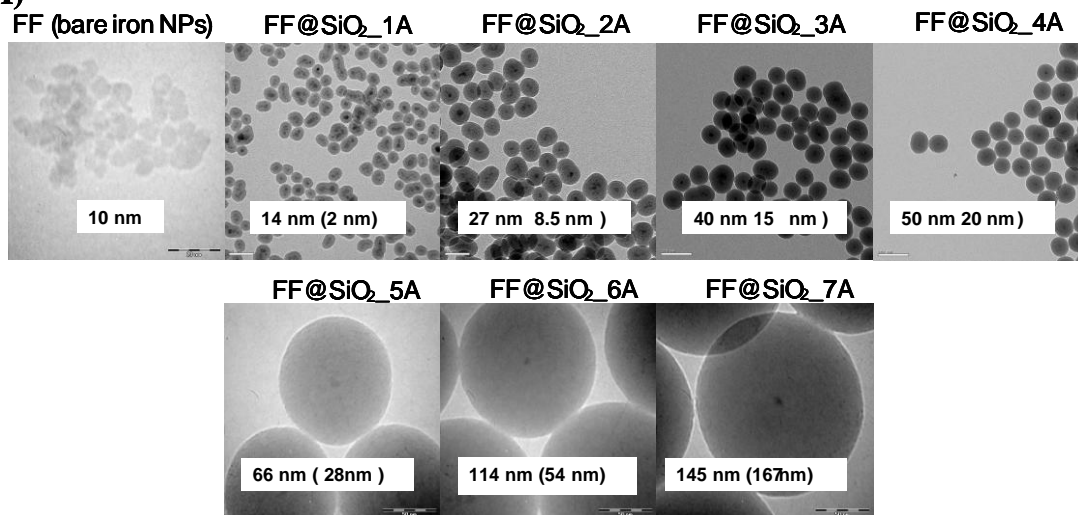
Figure 5.2 shows the relationship between the obtained shell thicknesses of the series A NPs and the expected ones through calculations. They are proportional to the amount of TEOS added during the preparation. Note the deviation from a slope of 1, which is significant of the errors taking place at each step as well as some aggregation of the maghemite particles, as can be detected by TEM.

The ratio of Fe/Si was determined for the series B NPs by ICP (Table 5.2). When the diameter of the NPs increases, the concentration of Fe with respect to Si decreases, as expected (Figure 5.3).

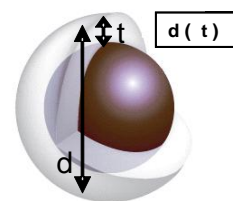
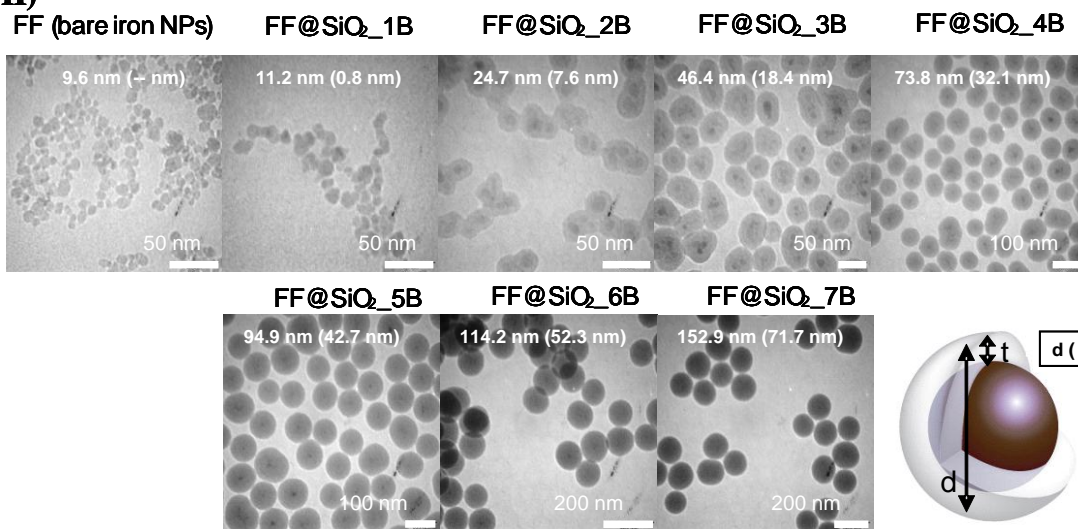
**Table 5.1.** Synthesis of maghemite core-shell ( $\gamma$ -Fe<sub>2</sub>O<sub>3</sub>@SiO<sub>2</sub>) NPs for series A: comparison between estimated and experimental values of shell thicknesses.

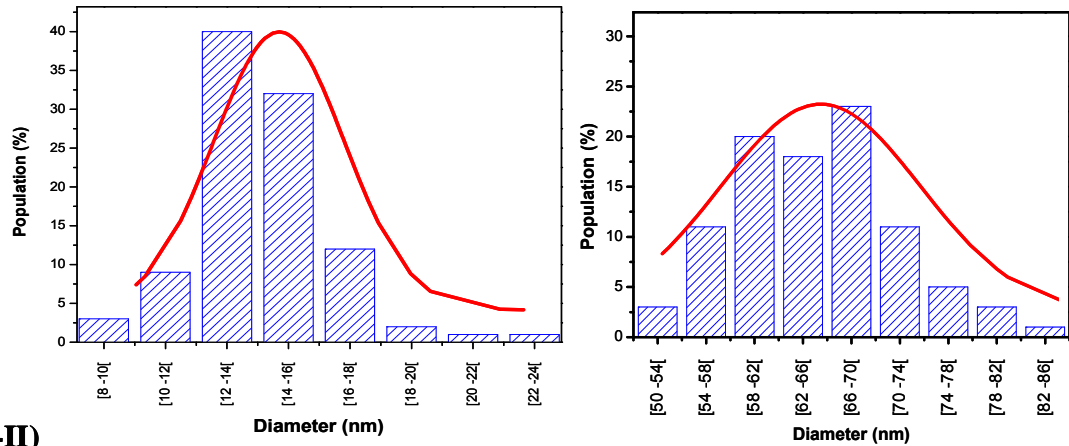
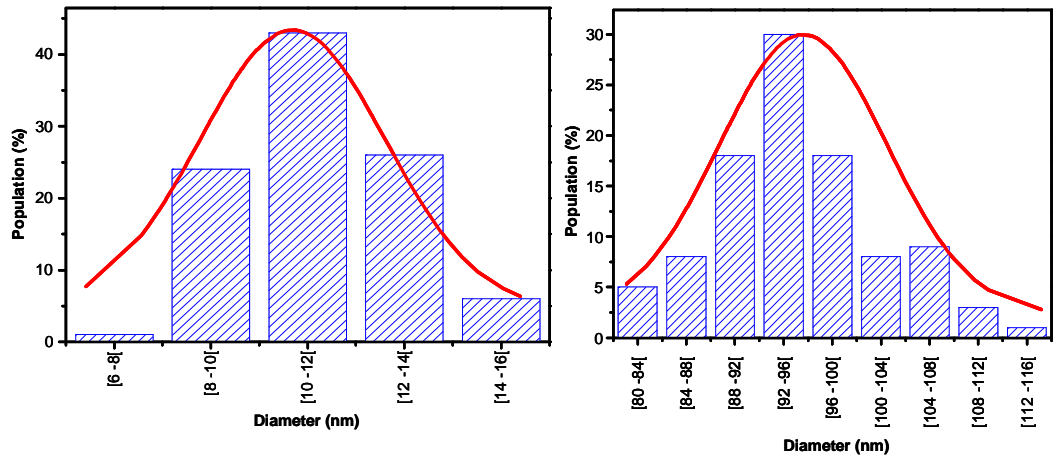
Sample	Estimated shell thickness (nm) <sup>a</sup>	Experimental shell thickness (nm)	Experimental diameter (nm)
FF@SiO <sub>2</sub> _1A	1 ± 1	2 ± 1	14 ± 2
FF@SiO <sub>2</sub> _2A	4 ± 1	8 ± 2	27 ± 5
FF@SiO <sub>2</sub> _3A	10 ± 1	15 ± 4	40 ± 8
FF@SiO <sub>2</sub> _4A	18 ± 2	20 ± 4	50 ± 7
FF@SiO <sub>2</sub> _5A	23 ± 3	28 ± 4	66 ± 8
FF@SiO <sub>2</sub> _6A	31 ± 3	52 ± 6	114 ± 14
FF@SiO <sub>2</sub> _7A	56 ± 6	67 ± 5	145 ± 10

**a-I)**



**a-II)**



**b-I)****b-II)**

**Figure 5.1. a)** TEM images showing the average size (diameter  $d$ ) of different maghemite core-shell ( $\gamma$ - $\text{Fe}_2\text{O}_3$ @ $\text{SiO}_2$ ) NPs and of their silica shell thickness ( $t$ ): **I)** for series A and **II)** for series B; **b)** histograms with experimental size distributions and corresponding calculated normal cumulative distributions for the specified mean and standard deviation: **I)** samples FF@ $\text{SiO}_2$ \_1A ( $\gamma$ - $\text{Fe}_2\text{O}_3$ @ $\text{SiO}_2$  14 nm) (left) and FF@ $\text{SiO}_2$ \_5A ( $\gamma$ - $\text{Fe}_2\text{O}_3$ @ $\text{SiO}_2$  66 nm) (right) **II)** samples FF@ $\text{SiO}_2$ \_1B ( $\gamma$ - $\text{Fe}_2\text{O}_3$ @ $\text{SiO}_2$  11.2 nm) (left) and FF@ $\text{SiO}_2$ \_5B ( $\gamma$ - $\text{Fe}_2\text{O}_3$ @ $\text{SiO}_2$  94.9 nm) (right) and corresponding calculated normal cumulative distributions for the specified mean and standard deviation

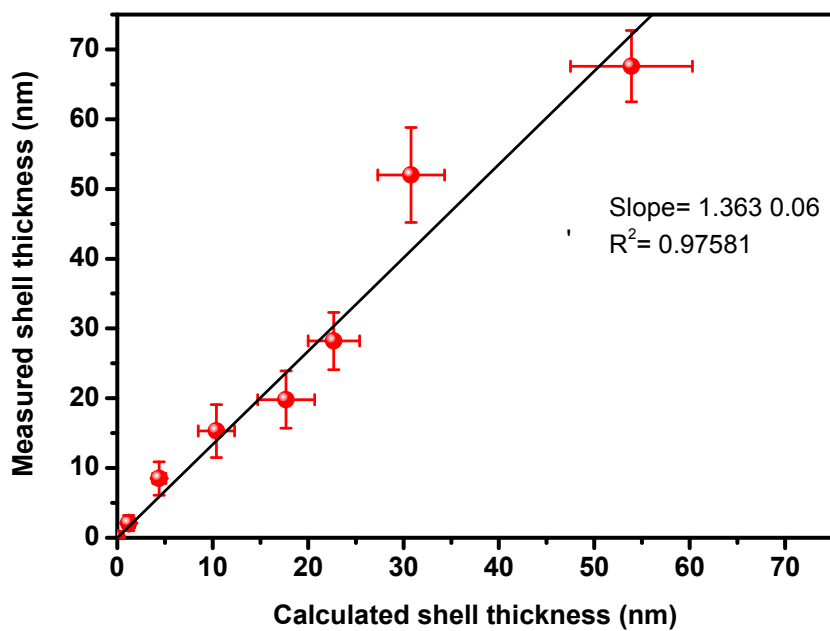


**Figure 5.2.** Correlation between the experimental thickness of the silica shell as determined by TEM and the thickness calculated with eq. 1.

**Table 5.2** Fe/Si ratio obtained by ICP and average diameter determined by TEM for different NPs for series B

Sample	Fe/Si	Diameter (nm)
FF		9.6 ± 1.3
FF@SiO <sub>2</sub> _1B	1.1230	11.2 ± 1.7
FF@SiO <sub>2</sub> _2B	0.2440	24.7 ± 3.2
FF@SiO <sub>2</sub> _3B	0.0563	46.4 ± 8.0
FF@SiO <sub>2</sub> _4B	0.0183	73.8 ± 8.1
FF@SiO <sub>2</sub> _5B	0.0075	94.9 ± 7.0
FF@SiO <sub>2</sub> _6B	0.0038	114.2 ± 12.7
FF@SiO <sub>2</sub> _7B	0.0017	152.9 ± 13.1

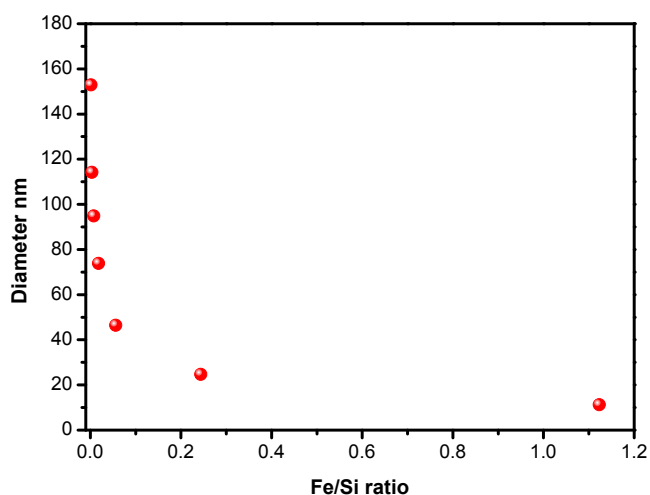


**Figure 5.3.** Dependence of the core-shell NPs (series B) diameter on the Fe/Si ratio.

Figure 5.4 shows the zeta potential titrations as a function of pH, and both the pH range of stability and the isoelectric points (IEP) of the two types of particles (2.3 for silica and 7.0 for  $\gamma$ -Fe<sub>2</sub>O<sub>3</sub>). Silica has long been used as a nonmagnetic coating material, in order to avoid aggregation or sedimentation of ferrofluid magnetic NPs because of its extraordinary stability over a wide range of polar and non-polar solvents.

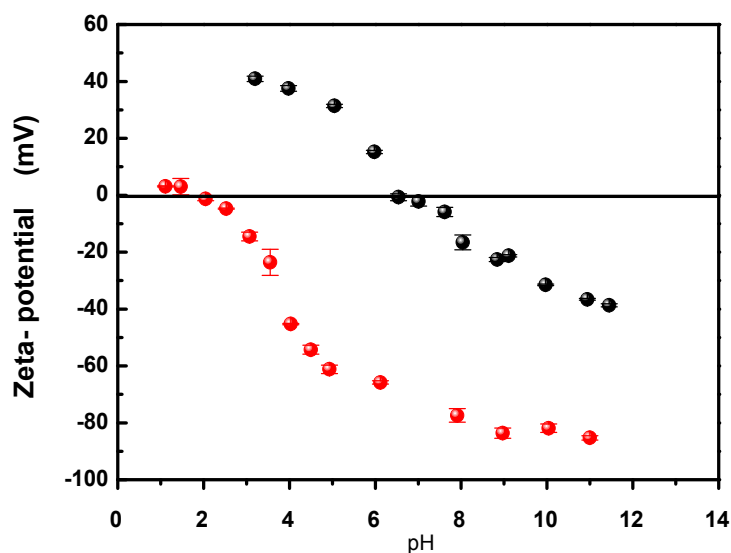


**Figure 5.4.** Zeta potential titrations as a function of pH of  $\gamma$ -Fe<sub>2</sub>O<sub>3</sub> (●) and  $\gamma$ -Fe<sub>2</sub>O<sub>3</sub>@SiO<sub>2</sub> (●) aqueous suspensions.

In particular, aqueous dispersions of silica are known to be stable over a large pH range (IEP at pH 2). The shift of the IEP towards lower pH values (from ~6.5-7 to ~2.5) upon coating (Figure 5.4) provides an additional confirmation that the coating was successful. The large negative zeta potential (- 80 mV) at physiological pH of the coated NPs suggests that the aqueous suspensions will be highly stable under *in vivo* conditions and will not flocculate at pH 7.

DRIFT spectroscopy was also used to probe the effectiveness of the chemical coating of silica on the maghemite NPs (FF) (Figure 5.5). Several absorption bands in the DRIFT spectrum of  $\gamma$ -Fe<sub>2</sub>O<sub>3</sub>@SiO<sub>2</sub> samples (Figure 5.5) are assigned to silica; and clearly show that this material covers the surface of the maghemite NPs. The bound Si-OH groups are characterized by the very broad IR absorption band in the 2800-3700 cm<sup>-1</sup> region whereas the so-called free Si-OH groups provide a narrow IR absorption band at 3630 cm<sup>-1</sup>. The stretching band at 1635 cm<sup>-1</sup> shows the presence of residual physisorbed water molecules, while the large bands centered at 1864 cm<sup>-1</sup>, 1108 cm<sup>-1</sup> and 796 cm<sup>-1</sup> are assigned to the Si-O and Si-O-Si stretching modes.

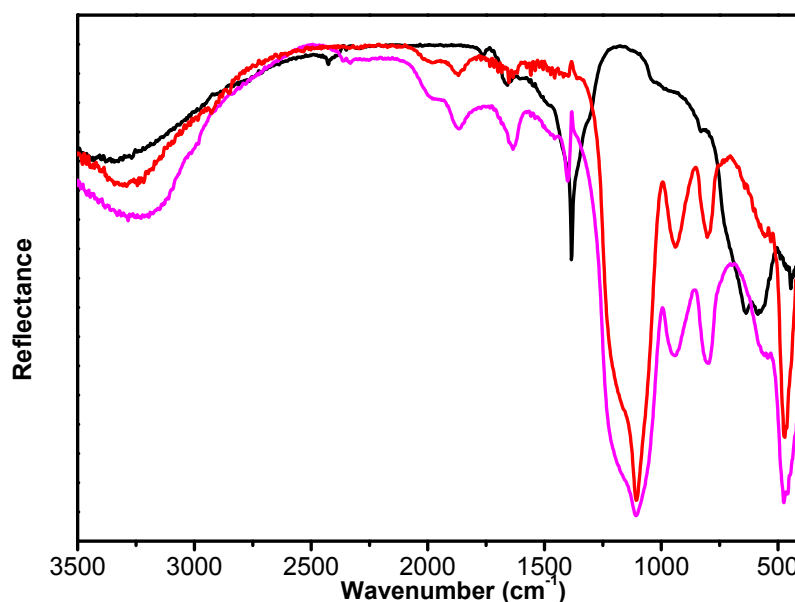


**Figure 5.4.** Diffuse Reflectance IR Fourier-Transform spectra (DRIFT) of maghemite NPs (black), silica NPs (pink) and  $\gamma$ -Fe<sub>2</sub>O<sub>3</sub>@SiO<sub>2</sub> (red)

### 5.3.2. Relaxivity Properties

In order to investigate the influence of the shell thickness of the silica coating on the MRI contrast agent (CA) efficiency of the  $\gamma\text{-Fe}_2\text{O}_3$  NPs, the  $r_i$  ( $i = 1,2$ ) relaxivities (defined as enhancement of  $R_i = 1/T_i$ ,  $i = 1,2$ , the relaxation rates per mM concentration of CA) of the different core-shell NPs were measured at two resonance frequencies (20 and 500 MHz) and two temperatures (25 and 37° C). Figure 5.5 shows typical values of the  $r_1$  and  $r_2$  relaxivities for the aqueous suspensions of  $\gamma\text{-Fe}_2\text{O}_3@SiO_2$  NPs (series A) as a function of the diameter  $d$  of the NPs with a 10.0 nm diameter  $\gamma\text{-Fe}_2\text{O}_3$  core and an increasing thickness of its silica layer, giving  $d$  values of 14 nm (sample 1A) to 145 nm (sample 7A) (Table 5.2).

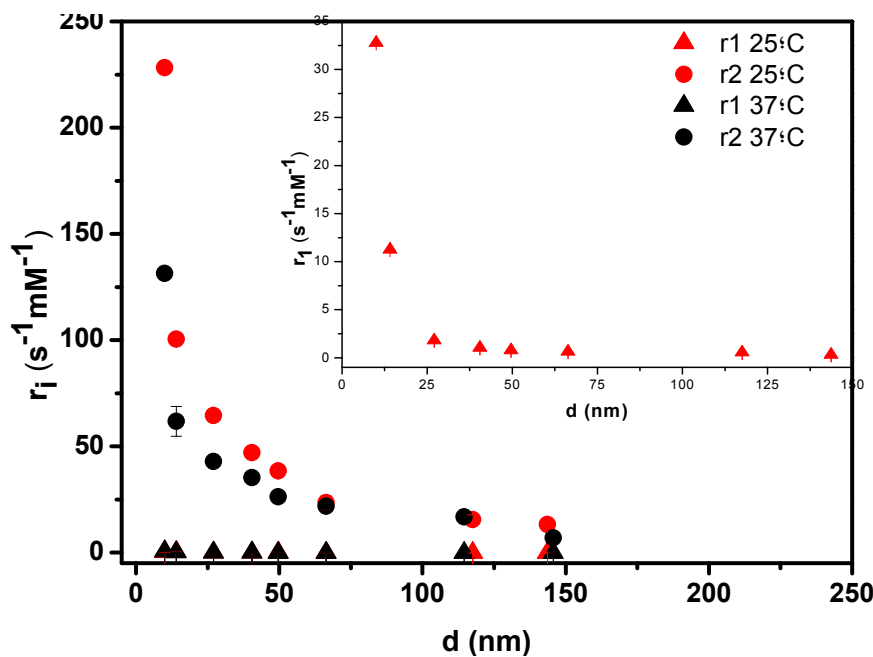


**Figure 5.5.** Dependence of water relaxivities of aqueous suspensions of the  $\gamma\text{-Fe}_2\text{O}_3@SiO_2$  NPs on their diameter, as a result of increased silica layer thickness: a) inset:  $r_1$  at 20 MHz (25 °C); b) main plot:  $r_i$  ( $i = 1, 2$ ) at 500 MHz (25 °C and 37 °C).  $r_2$  relaxivities were measured at  $\tau_{CP} = 1.6$  ms.

**Table 5.3.** Parameters obtained from analysis of  $r_2$  ( $\tau_{CP} = 1.6$  ms) and  $r_2^*$  values of aqueous suspensions of core-shell ( $\gamma\text{-Fe}_2\text{O}_3@SiO_2$ ) NPs at  $B_0 = 11.7$  T and 25 °C.

Sample	Diameter (nm) <sup>a</sup>	$r_2$ ( $s^{-1}mM^{-1}$ )	$r_2^*$ ( $s^{-1}mM^{-1}$ )	$2r_i$ (nm)	$2r_{dif}$ (nm)
FF	10 ± 2	228 ± 2	230 ± 1	13 ± 1	13 ± 1
FF@SiO <sub>2</sub> _1A	14 ± 2	100 ± 1	103 ± 1	29 ± 1	30 ± 1
FF@SiO <sub>2</sub> _2A	27 ± 5	64 ± 2	68 ± 1	44 ± 1	46 ± 2
FF@SiO <sub>2</sub> _3A	40 ± 8	47 ± 2	58 ± 1	52 ± 1	63 ± 3
FF@SiO <sub>2</sub> _4A	50 ± 7	38 ± 2	57 ± 1	53 ± 1	77 ± 5
FF@SiO <sub>2</sub> _5A	66 ± 8	23 ± 3	52 ± 1	58 ± 2	126 ± 18
FF@SiO <sub>2</sub> _6A	114 ± 14	15 ± 2	35 ± 1	86 ± 2	192 ± 30
FF@SiO <sub>2</sub> _7A	145 ± 10	13 ± 2	33 ± 1	90 ± 2	225 ± 33

The  $r_1$  values obtained at 20 MHz decrease with the increase of the silica shell thickness. This decrease is initially quite sharp, from  $32.0 s^{-1}mM^{-1}$  for NPs without silica coating ( $d = 10.0$  nm) to  $11.2 s^{-1}mM^{-1}$  for  $d = 14$  nm, while the  $r_1$  values become very small ( $< 2 s^{-1}mM^{-1}$ ) for  $d > 25$  nm (Figure 5.5, inset). At 500 MHz,  $r_1$  values are very small in all cases, even in the absence of silica shell (Figure 5.5).

For superparamagnetic NPs, the relaxivities  $r_i$  ( $i = 1, 2$ ) are dominated by the outer-sphere relaxation mechanism, which is due to the effect of local magnetic field gradients generated by the NPs on the water protons diffusing near their surface.<sup>73 74</sup> Taking into account the effect of water diffusion through the non-fluctuating magnetic field ( $B_0$ ) inhomogeneities created by the time-averaged value of the magnetic moment ( $\langle \mu_z \rangle$ ) of the NPs aligned onto  $B_0$ , and the effect of the fluctuation of the magnetic moment itself ( $\Delta \mu_z$ ), a theoretical model was developed, where the  $r_1$  and  $r_2$  relaxivities contain terms proportional to  $\langle \mu_z \rangle^2$ , which define the Curie relaxation<sup>75</sup> and dominate at high field, and fluctuating terms proportional to  $\Delta \mu_z^2$  (Néel relaxation) that dominate at low field.<sup>74,76</sup> This model accounts quite well for the magnetic field dependence of  $r_1$  for ultra small particles of iron oxide (USPIO) (diameters of 10-40 nm) at high fields ( $B_0 > 0.02$  T, corresponding to  $\sim 0.8$  MHz Larmor frequency), where Curie relaxation

dominates, but does not account for the small  $r_1$  dispersion observed at low field (below 1 MHz), which depends on the crystal anisotropy energy.<sup>77</sup> Above 1 MHz,  $r_1$  depends on the translational diffusion correlation time  $\tau_D$  and decreases with increase of the proton Larmor frequency  $\omega_1$ , with an inflection point defined by the condition  $\omega_1 \tau_D \sim 1$ .  $\tau_D = r_p^2/D$ , where  $D$  is the relative diffusion coefficient of the paramagnetic center and the water molecule and  $r_p$  is the radius of the particle, which determines their distance of closest approach.

The decrease of the  $r_1$  values at 20 MHz with the increase of the silica shell thickness reflects the decrease of the outer-sphere contribution of the core to  $r_1$  due to the increase of the distance of closest approach of the diffusing bulk water molecules to the superparamagnetic core of the particle. This induces an increase of the translational diffusion correlation time,  $\tau_D$ . At least a large part of the silica layer is expected to be impermeable to water. The relative diffusion coefficient  $D$  is expected to be nearly constant for all NPs. Being the sum of the diffusion constants of water ( $D_{H_2O}$ ) and of the NP ( $D_{NP}$ ), it is dominated by  $D_{H_2O}$  due to the large size of the NPs and the slow diffusion of water in the putative silica surface layer. The very small  $r_1$  values obtained at 500 MHz result from the expected field dependence of outer-sphere relaxation.

The effective transverse relaxation rates ( $R_2^*$ ) for the aqueous suspensions of the  $\gamma$ -Fe<sub>2</sub>O<sub>3</sub>@SiO<sub>2</sub> NPs were obtained from the spectral line widths of their proton water resonance. Values of  $R_{2p}^*$  (the paramagnetic contribution to  $R_2^*$ ) were calculated by subtraction of the diamagnetic contribution of aqueous suspensions of diamagnetic iron oxide-free silica NPs from each paramagnetic contribution, using the spectral line widths for the various samples. Finally, the corresponding relaxivities,  $r_2^*$ , were obtained (see Table 5.2). The line broadening effects reflect the dephasing of the water proton magnetic moments diffusing past the magnetic field gradients in the vicinity of the small superparamagnetic NPs, causing their  $T_2$ -shortening.

The transverse relaxation times are characterized by the correlation times  $\tau_D$ ,  $(\Delta\omega)^{-1}$ , and  $\tau_{CP}$ . The uncoated particles have a radius of 5 nm, from which it can be calculated that for these particles  $\tau_D$  is  $10^{-8}$  s. From simulations reported by Gillis et al.,<sup>78</sup> the transverse relaxivity may be predicted by the outer sphere theory (eq. 5.3),

where  $\Delta\omega$  is the difference in the Larmor frequency at the particle surface and the infinity and  $v$  is the volume fraction of the particles.

$$r_2 = r_2^* = \frac{4}{9} \Delta\omega^2 v \tau_D \quad (5.3)$$

Upon coating, both  $\tau_D$  and  $(\Delta\omega)^{-1}$  will decrease and we assume that the outer sphere regime remains valid.

The  $r_2$  values were measured as a function of the time interval between two consecutive  $180^\circ$  pulses ( $\tau_{CP}$ ) in a CPMG pulse sequence, for aqueous suspensions of the various NPs of increasing diameter. Figure 5.6 shows that the transverse relaxivities of these NPs are virtually independent of  $\tau_{CP}$  for all silica shell sizes. This observation is not surprising, since the  $\tau_D$  values of the systems measured are all much smaller than the applied  $\tau_{CP}$  values and, consequently the refocusing pulses are fully effective.

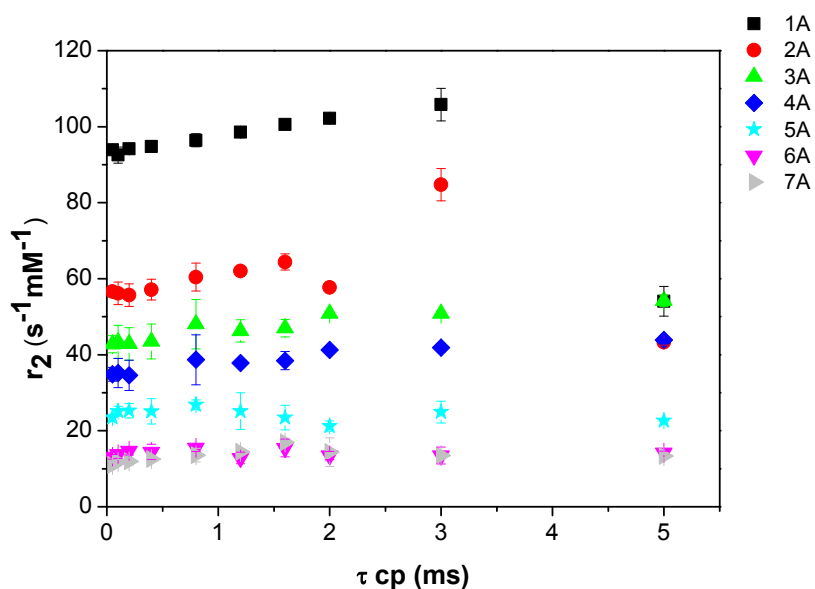


**Figure 5.6.** Dependence of  $r_2$  water proton relaxivities (500 MHz, 25 °C) of aqueous suspensions of the  $\gamma$ -Fe<sub>2</sub>O<sub>3</sub>@SiO<sub>2</sub> NPs (series A) on  $\tau_{cp}$  as a function of their diameter, as a result of increased silica layer thickness.

Figure 5.5 and Table 5.3 show that the  $r_2$  relaxivity (measured at  $\tau_{CP} = 1.6$  ms) sharply decreases when the thickness of the coating of the NPs increases. As discussed above for  $r_1$  effects, this results from the decrease of the outer-sphere contribution of the core to  $r_2$  due to the increase of the distance of closest approach of the diffusing bulk water molecules to the superparamagnetic core of the particle.

Data show that  $r_2 \cong r_2^*$  for the smallest particles ( $\gamma$ -Fe<sub>2</sub>O<sub>3</sub> NPs (core), 1A and 2A), but  $r_2 < r_2^*$  for particles with thicker coatings. It is possible that for the thicker coatings the silica layer is only impermeable to water up to a certain silica shell thickness. The diffusion of the water molecules in the permeable silica layer may be relatively slow. If in this layer the diffusion is so slow that the condition  $\tau_D \gg (\Delta\omega)^{-1}$  holds, the diffusion correlation time is not effective when refocusing pulses are applied and, consequently, the phase incoherence of the water protons is fully refocused in that part of the system, resulting in zero contribution to  $r_2$ . As far as  $r_2$  and  $r_2^*$  are concerned, it will be assumed that the particles consist of three spheres<sup>79</sup> with radii  $r_c$ ,  $r_i$ , and  $r_{diff}$  (Figure 5.7).

a)

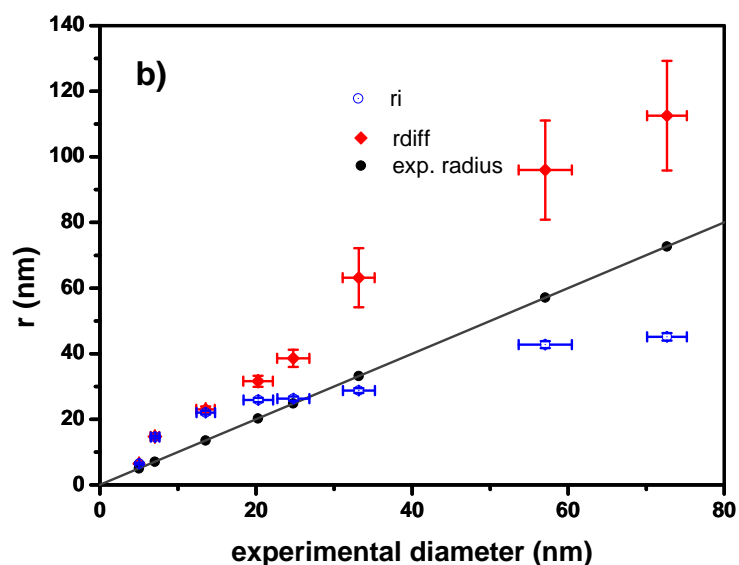
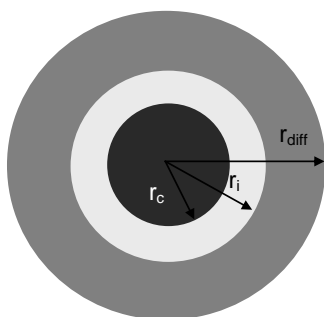


**Figure 5.7.** a) Schematic representation of a  $\gamma$ -Fe<sub>2</sub>O<sub>3</sub>@SiO<sub>2</sub> NP. Here,  $r_c$  is the radius of the core and  $r_i$  and  $r_{diff}$  are the radii of imaginary spheres, as defined in the text. b) Variation of the silica permeability to water molecules with the shell thickness.

Here,  $r_c$  is the radius of the core (5 nm),  $r_i$  is the radius of the sphere around the core, that seems to be impermeable to water, and  $r_{diff}$  is the radius of a sphere, in which any water molecule that is inside diffuses very slowly and does not contribute to  $r_2$ . Water molecules outside the latter sphere are assumed to contribute fully to  $r_2$ , whereas all water (including that inside the latter sphere) contributes to  $r_2^*$ .

Taking into account the distance dependence of  $\Delta\omega$ ,  $v$  and  $\tau_D$ , the following scaling may be applied:<sup>80 81</sup>

$$\Delta\omega_i = \Delta\omega_c \left( \frac{r_c}{r_i} \right)^3 \quad (5.4)$$

$$v_i = v_c \left( \frac{r_i}{r_c} \right)^3 \quad (5.5)$$

$$\tau_{D_i} = \tau_{D_c} \left( \frac{r_i}{r_c} \right)^2 \quad (5.6)$$

Combination of eqs (5.4-5.6) gives:

$$r_2^* = r_{2,c} \left( \frac{r_c}{r_i} \right) \quad (5.7)$$

Similarly, it can be derived that:

$$r_2 = r_{2,c} \left( \frac{r_c}{r_{diff}} \right) \quad (5.8)$$

Using the two latter equations and the experimental values of  $r_2$  and  $r_2^*$ , the values of  $r_i$  and  $r_{diff}$  were calculated for the various samples (see Table 5.2 and Figure 5.7b). These calculated  $r_{diff}$  values are in relatively fair agreement with the particle diameters obtained from the TEM measurements. The results also suggest that the water impermeable part of the silica coating tends to a maximum value of 40 nm, while the water permeable part increases with the coating thickness.

The core-shell NPs (series B) were studied by relaxometry and magnetometry. As expected for particles with the same magnetic core, the size and the saturation magnetization obtained by magnetometry remain almost constant (Table 5.4 and Figure 5.8).

**Table 5.4.** Magnetization values of the NPs (series B) obtained by magnetometry.

Sample	$r$ (nm) <sup>a</sup>	$M_{sat}$ (Am <sup>2</sup> /kg)
FF	5.5	62.1
FF@SiO <sub>2</sub> _1B	5.7	55.7
FF@SiO <sub>2</sub> _2B	5.5	58.4
FF@SiO <sub>2</sub> _3B	5.6	57.4
FF@SiO <sub>2</sub> _4B	5.6	56.2
FF@SiO <sub>2</sub> _5B	5.6	55.4
FF@SiO <sub>2</sub> _6B	5.6	55.9
FF@SiO <sub>2</sub> _7B	5.6	57.8

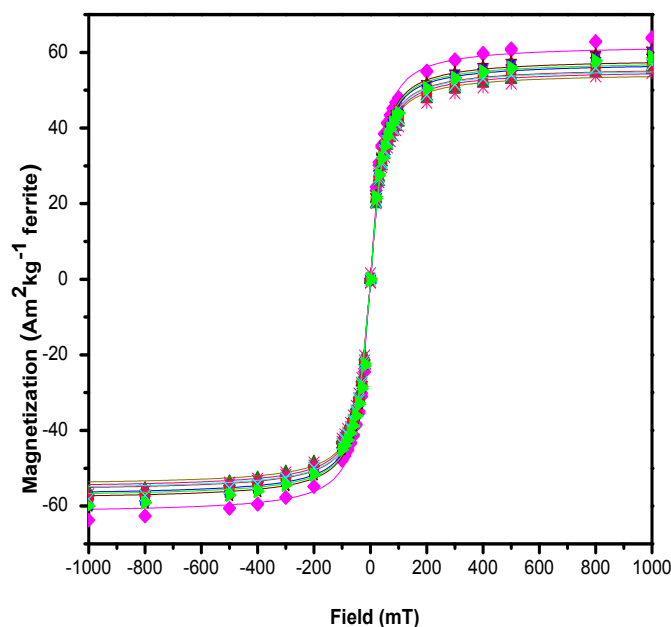


**Figure 5.8.** Magnetometry curves of the NPs:FF (magenta,  $\blacklozenge$ ); FF@SiO<sub>2</sub>\_1B; (olive,  $\blacktriangle$ ); FF@SiO<sub>2</sub>\_2B (wine,  $\blackstar$ ); FF@SiO<sub>2</sub>\_3B (blue,  $\blacksquare$ ); FF@SiO<sub>2</sub>\_4B (red,  $\bullet$ ); FF@SiO<sub>2</sub>\_5B (pink,  $\ast$ ); FF@SiO<sub>2</sub>\_6B (cyan,  $\times$ ) and FF@SiO<sub>2</sub>\_7B (green,  $\blacktriangleright$ ).

In order to investigate the influence of the shell thickness of the silica coating on the MRI contrast agent (CA) efficiency of the  $\gamma$ -Fe<sub>2</sub>O<sub>3</sub> NPs, the  $r_i$  ( $i = 1,2$ ) relaxivities (defined as enhancement of  $R_i = 1/T_i$ ,  $i = 1,2$ , the relaxation rates per mM concentration of CA) of the different core-shell NPs were measured at two resonance frequencies (20 and 60 MHz) and 37 °C (Table 5.5). Their relaxometric behavior shows a decrease of the relaxation rates on increasing the size of the NPs, in agreement with preliminary data.<sup>82</sup>

The <sup>1</sup>H NMRD profiles recorded at 37 °C confirm the decrease of  $r_1$  when the coating is thicker (Figure 5.9). All NMRD profiles (Figure 5.8) have been fitted using the phenomenological model developed by Roch et al.<sup>77</sup>

**Table 5.5:** Relaxivity values of the NPs aqueous solutions at 20 and 60 MHz (37 °C)

Sample	$r_1$ (20 MHz, s <sup>-1</sup> mM <sup>-1</sup> )	$r_2$ (20 MHz, s <sup>-1</sup> mM <sup>-1</sup> )	$r_1$ (60 MHz, s <sup>-1</sup> mM <sup>-1</sup> )	$r_2$ (60 MHz, s <sup>-1</sup> mM <sup>-1</sup> )
FF	35.17	129.25	15.96	130.28
FF@SiO <sub>2</sub> _1B	21.82	114.18	7.66	117.03
FF@SiO <sub>2</sub> _2B	8.14	96.16	2.05	102.08
FF@SiO <sub>2</sub> _3B	2.38	85.89	0.72	92.91
FF@SiO <sub>2</sub> _4B	0.84	50.25	0.40	55.02
FF@SiO <sub>2</sub> _5B	0.55	39.78	0.32	43.63
FF@SiO <sub>2</sub> _6B	0.57	40.57	0.34	43.06
FF@SiO <sub>2</sub> _7B	0.55	39.18	0.34	43.06

For each sample, the anisotropy energy is high enough to neglect the precession at the electronic frequency of the magnetization of the particle. This results in the absence of dispersion at low field in the NMRD curve. Accordingly, the fitting equation may be reduced to the “high anisotropy approximation”:

$$R_1 = 3 \cdot C \cdot \left\{ \left[ \frac{7 \cdot L(x)}{x} + 3 \left( 1 - L^2(x) - \frac{2 \cdot L(x)}{x} \right) \right] \cdot J^F(\omega_I, \tau_D, \tau_N) + 3 \cdot L^2(x) \cdot J^A(\omega_I, \tau_D) \right\} \quad (5.9)$$

where  $R_1$  is the water proton longitudinal relaxation rate. The constant  $C$  is equal to (in cgs units)  $C = \frac{32 \cdot \pi}{405000} \gamma_i^2 \cdot \mu_{sp}^2 \cdot \left( \frac{C_p}{d \cdot D} \right)$ , where  $\gamma_i$  is the gyromagnetic ratio of proton ( $2.67519 \cdot 10^4 \text{ rad} \cdot \text{G}^{-1} \cdot \text{s}^{-1}$ ),  $\mu_{sp}$  is the magnetic moment of the NP (e.m.u) s<sup>-1</sup>,  $C_p$  is the number of particles per liter,  $d$  is the diameter of the NP (cm),  $D$  is the solvent media self diffusion coefficient (cm<sup>2</sup>s<sup>-1</sup>) and  $L(x)$  is the Langevin function, with

$x = \frac{\mu_{sat} B_0}{k_b T}$ , where  $B_0$  is the magnetic field,  $k_b$  the Boltzmann constant and  $T$  the temperature.

The  $J^F(\omega, \tau_D, \tau_N)$  function is the Freed expression of the spectral density expressed as:<sup>83</sup>

$$J^F(\omega, \tau_D, \tau_N) = \text{Re} \left[ \frac{1 + \frac{(i \cdot \omega \tau_D + \tau_D / \tau_N)^{1/2}}{4}}{1 + (i \cdot \omega \tau_D + \tau_D / \tau_N)^{1/2} + \frac{4 \cdot (i \cdot \omega \tau_D + \tau_D / \tau_N)}{9} + \frac{(i \cdot \omega \tau_D + \tau_D / \tau_N)^{3/2}}{9}} \right] \quad (5.10)$$

where  $\omega_1$  is the proton Larmor angular frequency ( $\text{rad} \cdot \text{s}^{-1}$ ),  $\tau_N$  is the Néel relaxation rate ( $\text{s}^{-1}$ ) and  $\tau_D = \frac{d^2}{4D}$  is the translational correlation time ( $\text{s}^{-1}$ ).

The  $J^A(\omega, \tau_D)$  function is the Ayant expression of the spectral density expressed as:<sup>84</sup>

$$J^A(\omega, \tau_D) = \frac{1 + \frac{5(\omega \tau_D)^{1/2}}{8} + \frac{(\omega \tau_D)}{8}}{1 + (\omega \tau_D)^{1/2} + \frac{(\omega \tau_D)}{2} + \frac{(\omega \tau_D)^{3/2}}{6} + \frac{4(\omega \tau_D)^2}{81} + \frac{(\omega \tau_D)^{5/2}}{81} + \frac{(\omega \tau_D)^3}{648}} \quad (5.11)$$

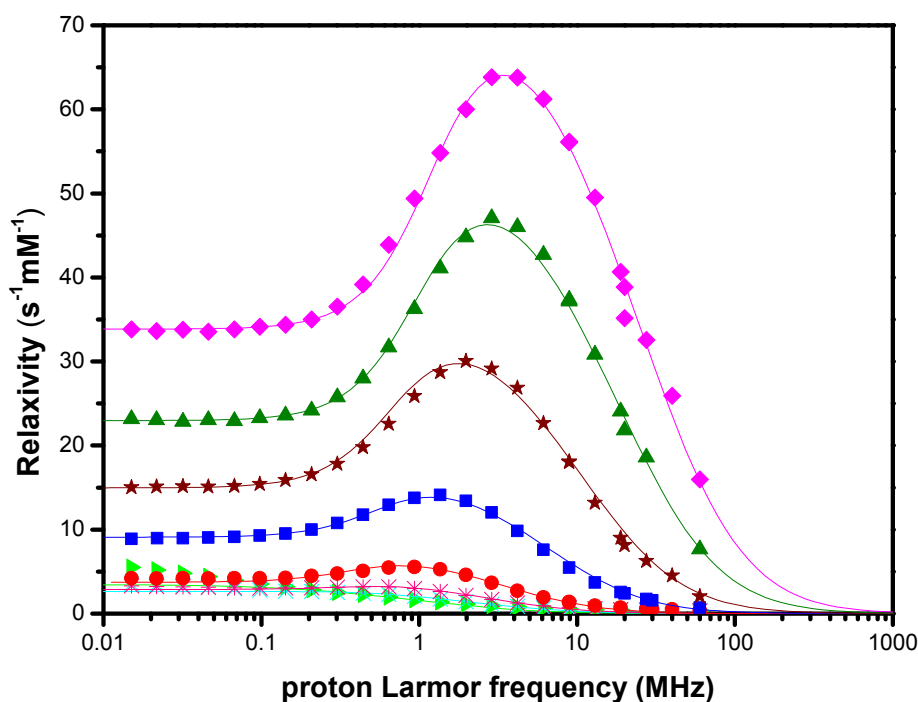


**Figure 5.9:**  $^1\text{H}$  NMRD profiles for the NPs aqueous solutions and their theoretical fittings. NPs: FF (magenta,  $\blacklozenge$ ); FF@SiO<sub>2</sub>\_1; (olive,  $\blacktriangle$ ); FF@SiO<sub>2</sub>\_2 (wine,  $\star$ ); FF@SiO<sub>2</sub>\_3 (blue,  $\blacksquare$ ); FF@SiO<sub>2</sub>\_4 (red,  $\bullet$ ); FF@SiO<sub>2</sub>\_5 (pink,  $\ast$ ); FF@SiO<sub>2</sub>\_6 (cyan,  $\times$ ) and FF@SiO<sub>2</sub>\_7 (green,  $\blacktriangleright$ ).

This equation provides a good fitting of the NMRD curves for NPs covered with the thinnest silica layers. However, when the coating becomes very thick, the diamagnetic contribution of the silica cannot be neglected in the fitting of the NMRD profile. This contribution must be added to that of the magnetic particles alone. As shown by Roose et al.,<sup>85</sup> the NMRD profile of such large diamagnetic particles is characterized by dispersion at very low fields.

For this reason the central region of the NMRD profiles of the particles covered with the thickest layers of silica (see samples FF@SiO<sub>2</sub>\_4B, FF@SiO<sub>2</sub>\_5B, FF@SiO<sub>2</sub>\_6B, FF@SiO<sub>2</sub>\_7B) are fitted “by eye” with the superparamagnetic relaxation (between 0.5 and 10MHz). A better fit could be obtained after subtraction of the diamagnetic contribution of the silica. The values of the parameters obtained by fitting the NMRD profiles are presented in Table 5.5 together with those obtained by TEM and magnetometry.

A good linear relationship is obtained between the NPs sizes measured by electron microscopy and those obtained by fitting the NMRD profiles (Figure 5.9 and Table 5.5). Importantly, the sizes obtained by NMRD for particles coated with a thick layer of silica are significantly lower than those measured by transmission electron microscopy, indicating that a significant part of the silica coating is permeable to water. Indeed, the effective distance of closest approach of the water protons to the superparamagnetic core, as determined by equation 1, is shorter than the NPs thickness as given by TEM, in agreement with what was proposed before for these systems.<sup>82</sup>

Interestingly, the magnetization  $M_{\text{sat}}$  expressed relatively to the global weight of the particles, and obtained from the relaxometric data decreases significantly for the larger particles (Table 5.5). A correlation can be drawn between the values of  $M_{\text{sat}}$  obtained by both magnetometry (which gives the value of the magnetization of the crystal itself) and relaxometry (which gives the value of the magnetization of “the” particle, i.e. the crystal plus the coating). Assuming a waterproof coating, such a correlation is achieved by multiplying the former one by the factor in eq. 5.12:

$$M_s^{\text{coat}} = M_s^{\text{bp}} \frac{4.90 \times d_{\text{bp}}^3}{4.90 \times d_{\text{bp}}^3 + 2.2 \times (d_{\text{coat}}^3 - d_{\text{bp}}^3)} \quad (5.12)$$

where  $M_s^{\text{coat}}$  is the average saturation magnetization per kilo of coated particle material,  $M_s^{\text{bp}}$  is the saturation magnetization of the bare maghemite particle,  $d_{\text{bp}}$  is the diameter of the bare particle,  $d_{\text{coat}}$  is the diameter of the coated particle, and 4.90 and 2.2 are, respectively, the specific mass of maghemite and silica. The  $M_{\text{sat}}$  values of Table 5.5 show that, by covering the magnetic crystal and “expelling” the water further and further away from it creates bigger and bigger particles of the same “magnetic content”, so behaving like larger but less magnetized particles. However, the fact that the magnetization dilution of the core-shell NPs measured by NMRD is significantly smaller than that predicted from eq.5.12 clearly indicates again that the silica shell is not waterproof, but is partly water permeable. This observation is of paramount importance in the context of the development of contrastophores for molecular imaging.

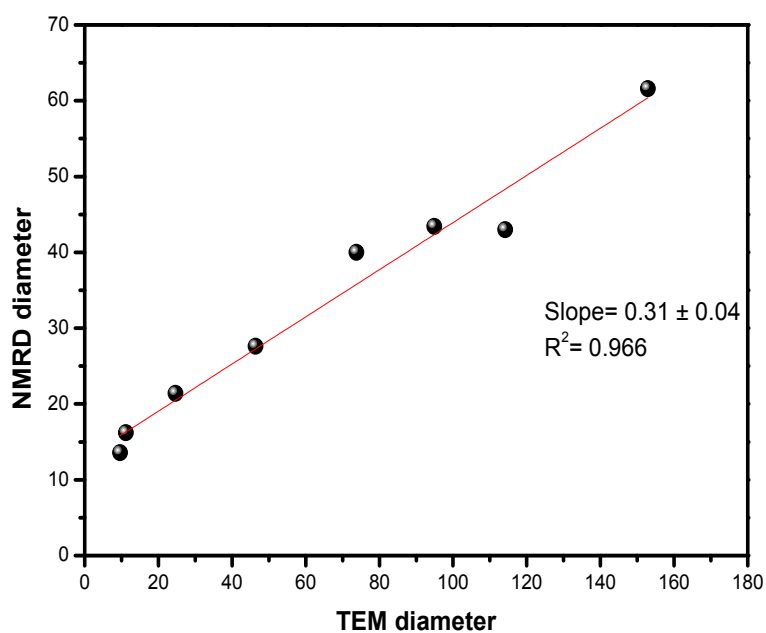


**Figure 5.19:** Comparison between the NPs diameter obtained by NMRD fitting and TEM.

**Table 5.5:** Parameters obtained for the NPs samples by different techniques.

Sample number	TEM diameter (nm)	Magnetic diameter (nm)	NMRD diameter (nm)	M <sub>sat</sub> Crystal Magnetometry (Am <sup>2</sup> /kg of iron oxide)	Measured M <sub>sat</sub> NMRD (Am <sup>2</sup> /kg of particle)	Calculated M <sub>sat</sub> NMRD (Am <sup>2</sup> /kg of particle) <sup>a</sup>	Calculated M <sub>sat</sub> TEM (Am <sup>2</sup> /kg of particle) <sup>b</sup>
FF	9.6	11.0	13.6	62.1	51.1	51.1	51.1
FF@SiO <sub>2</sub> _1B	11.2	11.4	16.2	55.7	47.9	39.0	40.4
FF@SiO <sub>2</sub> _2B	24.7	11.0	21.4	58.4	39.0	22.2	6.2
FF@SiO <sub>2</sub> _3B	46.4	11.2	27.6	57.4	23.9	11.9	1.00
FF@SiO <sub>2</sub> _4B	73.8	11.2	40.0	56.2	12.3	4.3	0.25
FF@SiO <sub>2</sub> _5B	94.9	11.2	43.4	55.4	8.2	3.4	0.12
FF@SiO <sub>2</sub> _6B	114.2	11.2	43.0	55.9	6.4	3.5	0.07
FF@SiO <sub>2</sub> _7B	152.9	11.2	61.6	57.8	5.1	1.2	0.03

<sup>a,b</sup> Calculated from equation [5.12] using <sup>a</sup>NMRD diameters and <sup>b</sup>TEM diameters.

The conditions under which the equations for outer sphere relaxation are valid still have to be discussed. This formalism is based on a small perturbation theory. By simulation, Gillis and al.<sup>78</sup> have shown that for magnetite particles without diamagnetic coating, the results of the outer sphere theory are valid when  $\tau_D$  is shorter than  $10^{-7}$ s. If the measurement is made at 37 °C ( $D = 3.10^{-9} \text{ m}^2\text{s}^{-1}$ ), the diameter should, thus, be smaller than 30 nm. In the same work, the authors also showed that the conditions of application of the outer sphere theory are fixed by the condition  $(\Delta\omega)_r \cdot \tau_D < 1$ , where  $(\Delta\omega)_r$  is the chemical shift between the proton in the equatorial plane of the particle and the bulk proton. For bare particles, the value of this product is 0.45. The variation of the value of  $(\Delta\omega)_r \cdot \tau_D$  with the thickness of the coating is related to the equatorial magnetic field of the particle which is given by:

$$B_{eq}^{coat} = B_{eq}^{bp} \frac{d_{bp}^3}{d_{coat}^3} \quad (5.13)$$

where  $B_{eq}^{coat}$  is the equatorial magnetic field of the coated particle and  $B_{eq}^{bp}$  is the equatorial magnetic field of the bare particle.

As  $(\Delta\omega)_r = \sqrt{\frac{4}{5}} \cdot \gamma \cdot B_{eq}$  ( $B_{eq}$  being the equatorial field of the crystal and  $\gamma$  the proton gyromagnetic ratio), the ratio between the product  $[(\Delta\omega)_r \cdot \tau_D]_{coat}$  of coated particle and the product  $[(\Delta\omega)_r \cdot \tau_D]_{bp}$  for bare particle is given by

$$\frac{[(\Delta\omega)_r \cdot \tau_D]_{coat}}{[(\Delta\omega)_r \cdot \tau_D]_{bp}} = \frac{d_{bp}}{d_{coat}} \quad (5.14)$$

Thus, although the overall size of the NPs increases, the conditions for application of the outer sphere theory become more and more favorable for thicker

coatings because the dependence on the diameter is cubic for ( $\Delta\omega$ ) and of power one for  $\tau_D$ .

### 5.3.3. Cytotoxicity

The cytotoxicity of the  $\gamma$ -Fe<sub>2</sub>O<sub>3</sub>@SiO<sub>2</sub> NPs (series A) was assessed after incubations with microglial cell lines for 3/4 h, 24 h, 48 h, 72 h, 96 h, 120 h, and 144 h. For each time point, cells were incubated or not with the NPs (0.16 mM). Then, the cells were separated in two sets, one used as control and the other one being submitted to the MTT assay. This test was performed to characterize the viability of the cells and evaluate the residual toxicity after the internalization of the NPs.<sup>86</sup> The cell viability tests (Figure 5.20), show that with and without NPs as well as for all NPs sizes except for [7A], cells can survive internalization and the cell growth process is maintained up to 144 h. Additionally, cells internalized with both  $\gamma$ -Fe<sub>2</sub>O<sub>3</sub> or  $\gamma$ -Fe<sub>2</sub>O<sub>3</sub>@SiO<sub>2</sub> particles exhibit the same lag phase of 48 h as the control ones.

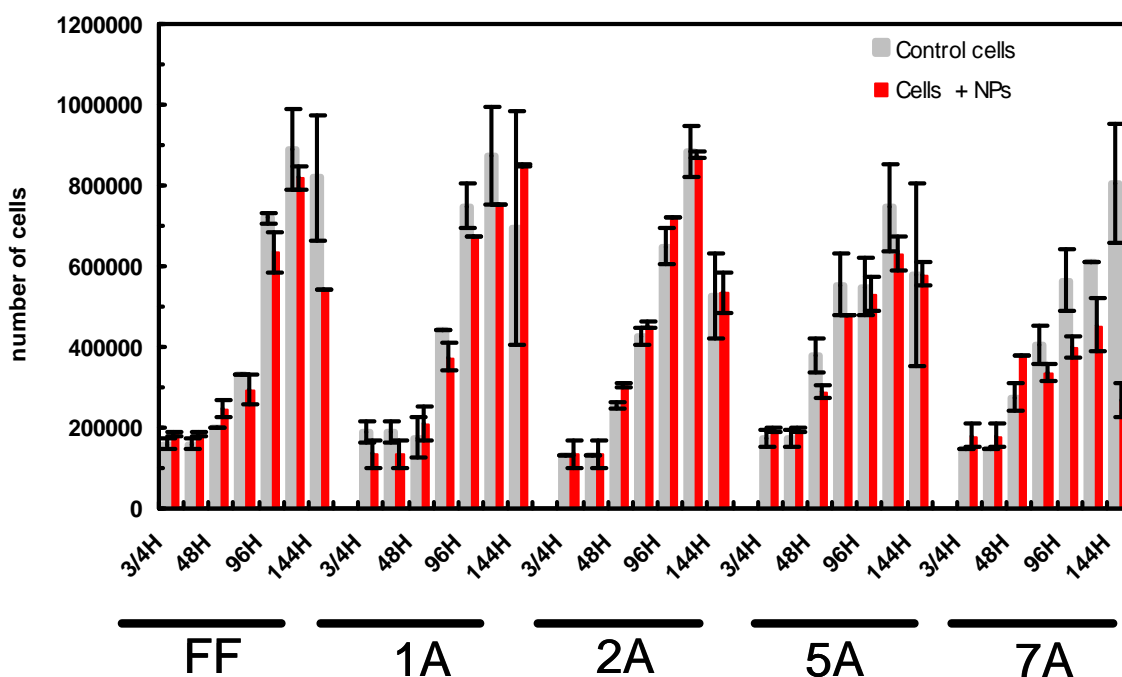


**Figure 5.20.** Cell viability after exposure to different core-shell NPs sizes incubated at different times.

The MTT test characteristic of the mitochondrial dehydrogenase activity was performed after NPs cell internalization. This metabolic test is illustrated in Figure 5.21 by the measurement of the 570 nm absorbance of incubated cells at different time course with different sizes of core-shell NPs.

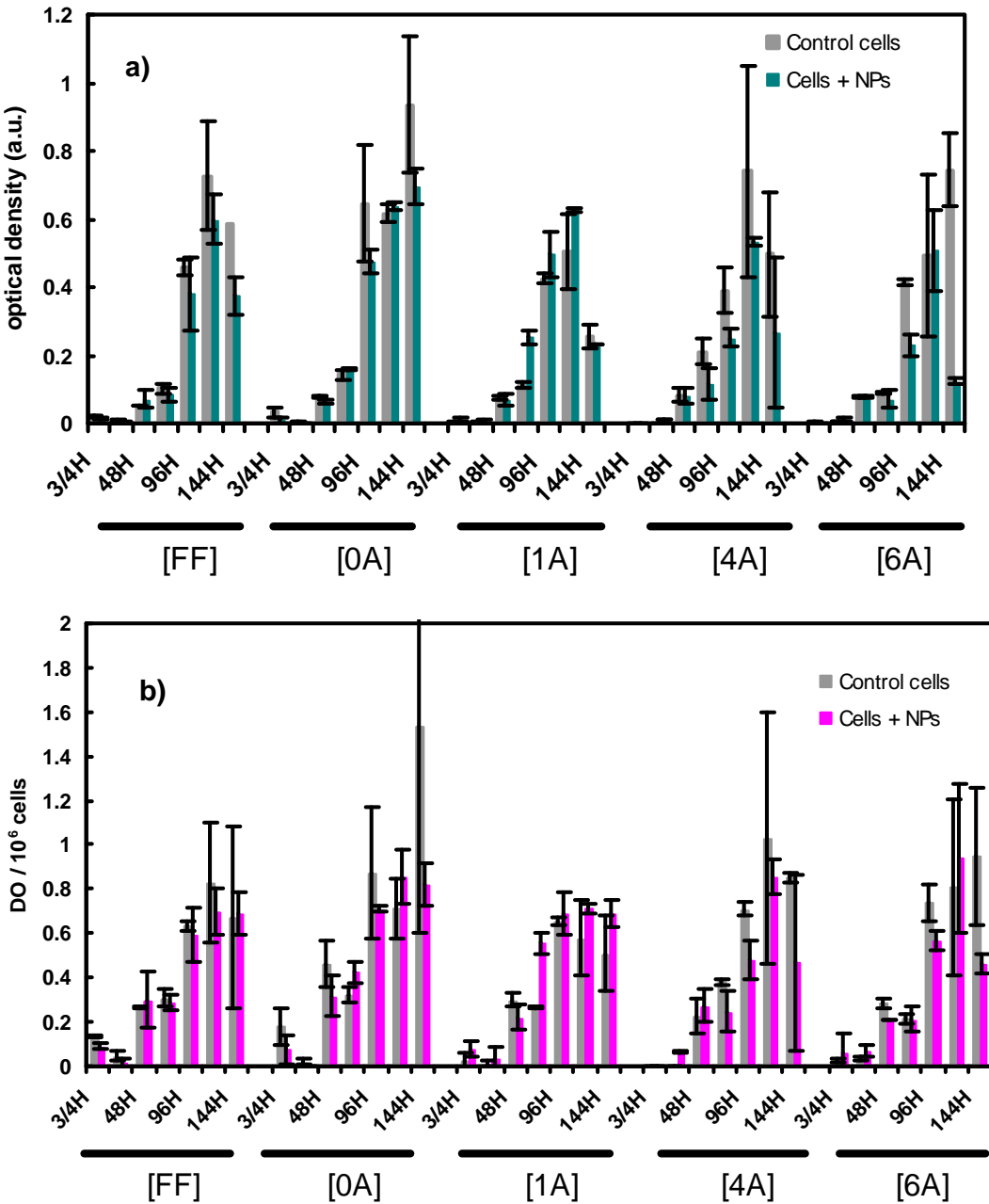


**Figure 5.21.** Variation of total activity, and b) activity per million of cells of mitochondrial dehydrogenase of microglial cells as given by the variation of the solubilized formazan optical density of the medium with incubation times for different sizes of NPs after incubation without (control cells) and with both coated and uncoated particles of different sizes (cells + NPs).

Both coated and uncoated particles induce an optical density of the cells, which varies with the incubation time with a maximum value for 120 h, following the same behaviour as that of the control cells. Like the cell growth in the preceding experiment, the dehydrogenase activity is not affected by NPs internalization in the cells from FF to 5A. In these experiments, the crude analysis of the dehydrogenase activity is relevant for the cell viability, but is not enough to give information about modifications of the cell phenotype. However, the dehydrogenase activity is drastically modified for the larger particles (e.g. 7A). Such NPs are known to be internalized and stored in lysosome-like vesicles. In case of NPs 7A, the consequences of their accumulation inside such cells able to phagocytise particles larger than 100 nm are still unknown. Their impact on the local changes in the overall redox potential due to the high load of iron in the vesicles is still an open question. We also normalized the activity per cell as a variation of the optical density per million cells as shown in Figure 5.21b. This allows all along the time of culture, the characterization of the cell growth on the dehydrogenase expression and the possible contribution of the NPs uptake during the growth time. The growth of control cells shows a basal level decreasing until 24 h that correlates with the lag phase of growth. Then the expression of the dehydrogenase per cell increases in two major steps, the first one between 48 h and 72 h, and the second one between 96 h and 144 h. After this period of time, the cells are nearly confluent. When the cells are incubated with NPs, the activity per cell is not significantly affected except for sample 7A after 144 h of exposure. Therefore, one can safely assume that in these conditions, the dehydrogenase expression does not appear to be sensitive to the vesicular load with these core-shell NPs.

## 5.4. CONCLUSIONS

The understanding of the relationship between the coating properties and the changes in relaxivity is vital for designing magnetic NP probes for MRI. This is important for medical applications, as a higher contrast typically leads to a higher sensitivity and reduces the amount of contrast agent required for imaging. Our choice of a silica coating was motivated by the increased stability of the resulting NP suspensions and the ensuing ease of conjugation of targeting molecules to the surface of the contrast agents for sensing and imaging. We have shown that in  $\gamma$ -Fe<sub>2</sub>O<sub>3</sub>@SiO<sub>2</sub> core-shell NPs, the coating thickness has a significant impact on their  $r_2$  and  $r_2^*$

relaxivities at medium and high fields and on  $r_1$  relaxivities at medium fields, as a result of decreased outer-sphere relaxation effects. Comparing the  $r_2$  and  $r_2^*$  values for the different sizes of particles we were able to divide the silica coating in two regions, one impermeable close to the  $\gamma$ -Fe<sub>2</sub>O<sub>3</sub> core and one permeable to water and at the interface with the bulk water. We have shown that by controlling this coating we are able to tune the size of these two regions. The impermeable one seems to increase up to a maximum value of 40 nm, while the permeable region goes on increasing with the coating thickness. The diffusion of the water molecules in the permeable silica region is relatively slow resulting in zero contribution to  $r_2$ . The effect of silica coating of increasing thickness on the  $r_2/r_1$  ratio is different from that reported for nanocrystalline superparamagnetic iron oxide NPs (MIONs) coated with a polyethylene glycol (PEG)-modified, phospholipid micelle coating with increasing molecular weights which increase the particle diameter, where this increase causes a  $r_2$  decrease and a  $r_1$  increase.<sup>79</sup>

The magnetometric curves  $\gamma$ -Fe<sub>2</sub>O<sub>3</sub>@SiO<sub>2</sub> have been fitted with a Langevin function and the NMRD profiles with the model developed by Roch *et al.* The latter provides a good fitting of the NMRD curves for the particles covered with the thinnest silica layers. However, with increasing coating thickness, the silica diamagnetic contribution cannot be neglected in the fitting of the NMRD profile and must be added to the contribution of the magnetic particles. A linear relationship between the NP sizes measured by TEM and by fitting the NMRD profiles is obtained, but the sizes obtained by NMRD are significantly lower than those measured by TEM. A correlation also exists between the values of  $M_{\text{sat}}$  obtained by magnetometry and relaxometry, whereby the  $M_{\text{sat}}$  value of the superparamagnetic core strongly decreases with the increasing thickness of the diamagnetic silica shell. However such a  $M_{\text{sat}}$  dilution as measured by NMRD is lower than expected for water-impermeable silica layers. Both results reflect the fact that a significant part of the silica coating is permeable to water, in agreement with what was proposed before for these systems.<sup>40</sup> The depth of this water-permeable layer is uncertain, as the exchange of the more deeply penetrating water molecules could become too slow to influence the measured relaxivity. This observation is of paramount importance in the context of the development of contrastophores for molecular imaging. The adequate silica shell thickness may, thus, be tuned to allow for both, a sufficiently high response as contrast agent, and an adequate grafting of targeted biomolecules.

Additionally, preliminary cytotoxicity studies confirmed that these contrast agents do not appear detrimental to microglial cells. However, as the naked NPs have the highest relaxivities, and the coating thickness does not play a role in their cytotoxicity, a preliminary conclusion is that overall optimal particles should have a minimal coating thickness to provide solution stability and a basis for surface conjugation without compromising their relaxivities.

Therefore, our results provide clues for the design of magnetic NP based contrast agents and their optimization for specific applications in medical diagnosis. This is up to now the only technique to provide clear evidence that a silica layer used as a coating in a core-shell system, exhibits regions that are porous to water and regions that are not. The knowledge of these systems may be extended to other systems and applications.

## 5.5. REFERENCES

- 1 LaConte, L.; Nitin, N.; Bao, G. Magnetic Nanoparticle Probes *Mater. Today* **2005**, 8, 32-38.
- 2 Prigogine, I.; Stuart, A. *Advance in Chemical Physics*; Darmann, J.L.; Fiorani, D.; Ronc E. Eds., , Wiley, New York, **1977**.
- 3 Stevens, P. D.; Fan, J.; Gardimalla, H. M. R.; Yen, M.; Gao, Y. Superparamagnetic Nanoparticle-Supported Catalysis of Suzuki Cross-Coupling Reactions *Org. Lett.* **2005**, 7, 2085-2088.
- 4 Mornet, S.; Vasseur, S.; Grasset, F.; Veverka, P.; Goglio, G.; Demourgues, A.; Portier, J.; Pollert E.; Duguet, E. Magnetic Nanoparticle Design for Medical Applications *Prog. Solid State Chem.* **2006**, 34, 237-247.
- 5 Sieben, S.; Bergemann, C.; Lübe, A.; Brockmann, B.; Rescheleit, D. Comparison of Different Particles and Methods for Magnetic Isolation of Circulating Tumor Cells *J. Magn. Magn. Mater.* **2001**, 225, 175-179.
- 6 Paul, A. L.; Chandra, G. R.; Terstappen, L. W. M. M. Optimization of Ferrofluids and Protocols for the Enrichment of Breast Tumor Cells in Blood *J. Magn. Magn. Mater.* **2001**, 225, 301-307.
- 7 Miller, M. M.; Prinz, G. A.; Cheng, S. F.; Bounnak, S. Detection of a Micron-Sized Magnetic Sphere Using a Ring-Shaped Anisotropic Magnetoresistance-Based Sensor: A Model for a Magnetoresistance-Based Biosensor *Appl. Phys. Lett.* **2002**, 81, 2211-2213.
- 8 Zhao, M.; Josephson, L.; Tang, Y.; Weissleder, R. Magnetic Sensors for Protease Assays *Angew. Chem. Int. Ed.* **2003**, 42, 1375-1378.
- 9 Okuhata, Y. Delivery of Diagnostic Agents for Magnetic Resonance Imaging *Adv. Drug Deliv. Rev.* **1999**, 37, 121-137.
- 10 Wunderbaldinger, P.; Josephson, L.; Weissleder R. Tat Peptide Directs Enhanced Clearance and Hepatic Permeability of Magnetic Nanoparticles *Bioconj. Chem.* **2002**, 13, 264-268.
- 11 Halavaara, J.; Tervahartiala, P.; Isoniemi, H.; Höckerstedt, K. Efficacy of Sequential Use of Superparamagnetic Iron Oxide and Gadolinium in Liver MR Imaging *Acta Radiol.* **2002**, 43, 180-185.
- 12 Bulte, J. W. Intracellular Endosomal Magnetic Labeling of Cells *Methods Mol. Med.* **2006**, 124, 419-439.
- 13 Modo, M.; Bulte, J. W. Cellular MR Imaging *Mol. Imaging* **2005**, 4, 143-164.

- 14 Burtea, C.; Laurent, S.; Roch, A.; Vander Elst, L.; Muller R. N., C-MALISA (Cellular Magnetic-Linked Immunosorbent Assay), a New Application of Cellular ELISA for MRI *J. Inorg. Biochem.*, **2005**, 99, 1135-1144.
- 15 Boutry, S.; Laurent, S.; Vander Elst, L.; Muller, R. N. Specific E-Selectin Targeting with a Superparamagnetic MRI Contrast Agent *Contrast Med. Mol. Imaging*, **2006**, 1, 15-22.
- 16 Babes, L., Denizot, B., Tanguy, G., Le Jeune, J. J., Jallet, P. J. Synthesis of Iron Oxide Nanoparticles Used as MRI Contrast Agents: A Parametric Study *Colloid Interface Sci.* **1999**, 212, 474-482.
- 17 Sonvico, F.; Dubernet, C.; Colombo, P.; Couvreur, P. Metallic Based Nanotechnology, Applications in Diagnosis and Therapeutics *Curr. Pharm. Des.* **2005**, 11, 2091-2105.
- 18 Corot, C.; Robert, P.; Idee, J. M.; Port, M. Recent Advances in Iron Oxide Nanocrystal Technology for Medical Imaging *Adv. Drug Delivery Rev.* **2006**, 58, 1471-1504.
- 19 Jordan, A.; Scholz, R.; Wust, P.; Schirra, H.; Schiestel, T.; Schmidt H., Felix R. Endocytosis of Dextran and Silane-Coated Magnetite Nanoparticles and the Effect of Intracellular Hyperthermia on Human Mammary Carcinoma Cells in Vitro *J. Magn. Magn. Mater.* **1999**, 194, 185-196.
- 20 Roullin, V. G.; Deverre, J.R.; Lemaire, L.; Hindré, F.; Julienne, M. C. V.; Vienet, R.; Benoit, J. P. Anti-Cancer Drug Diffusion Within Living Rat Brain Tissue: An Experimental Study Using [3H](6)-5-Fluorouracil-Loaded PLGA Microspheres *Eur. J. Pharm. Biopharm.* **2002**, 53, 293-299.
- 21 Lübbe, A. S.; Alexiou, C. C.; Bergemann, C. J. *Surg. Res.* 2001, 95, 200-206.
- 22 Jain, T. K.; Morales, M. A.; Sahoo, S. K.; Leslie-Pelecky, D. L.; Labhasetwar, V. Iron-Oxide Nanoparticles for Sustained Delivery of Anticancer Agents *Mol. Pharm.* **2005**, 2, 194-205.
- 23 Chourpa, L.; Douziech-Eyrolles, L.; Ngaboni-Okassa, L.; Fouquenot, J. F.; Cohen-Jonathan, S.; Souce, M.; Marchais, H.; Dubois, P. Molecular Composition of Iron Oxide Nanoparticles, Precursors for Magnetic Drug Targeting, as Characterized by Confocal Raman Microspectroscopy *Analyst* **2005**, 130, 1395-1403.
- 24 Mary, M. in: Hafeli, U.; Schutt, W.; Zborowski M. (Eds.), *Scientific and Clinical Applications of Magnetic Carriers*, Plenum Press, New York, 1997.
- 25 Elaissari, A.; Rodrigue, M.; Meunier, F.; Herve, C. J. *Magn. Magn. Mater.* 2001, 225, 127-133.
- 26 Gupta, A. K.; Gupta, M., Synthesis and surface engineering of iron oxide nanoparticles for biomedical applications. *Biomaterials* **2005**, 26 (18), 3995-4021.
- 27 Cornell, R. M.; Schwertmann, U. *The Iron Oxides: Structures, Properties, Reactions, Occurrences and Uses* (Wiley-VCH, Weinheim, 2003).
- 28 Josephson, L. Magnetic Nanoparticles for MR Imaging. in *BioMEMS and Biomedical Nanotechnology* Ferrari, M., Ed.; Springer: New York, **2006**; Vol. 1, p 227.

- 29 Sun, Y. K.; Ma, M.; Zhang, Y.; Gu, N. Synthesis and Characterization of Biocompatible Fe<sub>3</sub>O<sub>4</sub> Nanoparticles *Colloids Surf.* **2004**, 245, 15– 19.
- 30 Berry, C. C.; Curtis, A. S. G. Functionalisation of Magnetic Nanoparticles for Applications in Biomedicine *J. Phys. D. Appl. Phys.* **2003**, 36, R198– R206.
- 31 Chan, D. C. F.; Kirpotin, D. B.; Bunn, P. A., Jr. Synthesis and Evaluation of Colloidal Magnetic Iron Oxides for the Site-Specific Radio Frequency-Induced Hyperthermia of Cancer *J. Magn. Mater.* **1993**, 122, 374 – 378.
- 32 Jana, N. R.; Peng, X. Single-Phase and Gram-Scale Routes toward Nearly Monodisperse Au and Other Noble Metal Nanocrystals *J. Am. Chem. Soc.* **2003**, 125, 14280 – 14281.
- 33 Sun, S.; Murray, C. B.; Weller, D.; Folks, L.; Moser, A. A. Monodisperse FePt Nanoparticles and Ferromagnetic FePt Nanocrystal Superlattices *Science* **2000**, 287, 1989-1992.
- 34 Li, J. J.; Wang, Y. A.; Guo, W.; Keay, J. C.; Mishima, T. D.; Johnson, M. B.; Peng, X. Large-Scale Synthesis of Nearly Monodisperse CdSe/CdS Core/Shell Nanocrystals Using Air-Stable Reagents via Successive Ion Layer Adsorption and Reaction *J. Am. Chem. Soc.* **2003**, 125, 12567– 12575.
- 35 Murray, C. B.; Norris, D. J.; Bawendi, M. G. Synthesis and Characterization of Nearly Monodisperse CdE (E = S, Se, Te) Semiconductor Nanocrystallites *J. Am. Chem. Soc.* **1993**, 115, 8706 – 8715.
- 36 Sun, S.; Zeng, H. Monodisperse MFe<sub>2</sub>O<sub>4</sub> (M = Fe, Co, Mn) Nanoparticle *J. Am. Chem. Soc.* **2002**, 124, 8204-8205.
- 37 Jana, N. R.; Chen, Y.; Peng, X. Size- and Shape-Controlled Magnetic (Cr, Mn, Fe, Co, Ni) Oxide Nanocrystals via a Simple and General Approach *Chem. Mater.* **2004**, 16, 3931 – 3935.
- 38 Hyeon, T.; Lee, S. S.; Park, J.; Chung, Y.; Na, H. B. Synthesis of Highly Crystalline and Monodisperse Maghemite Nanocrystallites without a Size-Selection Process *J. Am. Chem. Soc.* **2001**, 123, 12798– 12801.
- 39 Wu, W.; He, Q.; Jiang, C. Magnetic Iron Oxide Nanoparticles: Synthesis and Surface Functionalization Strategies *Nanoscale Res. Lett.* **2008**, 3, 397– 415.
- 40 Gao, X.; Cui, Y.; Levenson, R. M.; Chung, L. W. K.; Nie, S. In Vivo Cancer Targeting and Imaging with Semiconductor Quantum Dots *Nat. Biotechnol.* **2004**, 22, 969– 976.
- 41 Pellegrino, T.; Manna, L.; Kudera, S.; Liedl, T.; Koktysh, D.; Rogach, A. L.; Keller, S.; Radler, J.; Natile, G.; Parak, W. Hydrophobic Nanocrystals Coated with an Amphiphilic Polymer Shell: A General Route to Water Soluble Nanocrystals *Nano Lett.* **2004**, 4, 703 - 707.

- 42 Guo, W.; Li, J. J.; Wang, Y. A.; Peng, X. Luminescent CdSe/CdS Core/Shell Nanocrystals in Dendron Boxes: Superior Chemical, Photochemical, and Thermal Stability *J. Am. Chem. Soc.* **2003**, 125, 3901-3909.
- 43 Kim, M.; Chen, Y.; Liu, Y.; Peng, X. Super-stable, High-quality Fe<sub>3</sub>O<sub>4</sub> Dendron-Nanocrystals Dispersible in Both Organic and Aqueous Solutions *Adv. Mater.* **2005**, 17, 1429 – 1436.
- 44 Kim, S. W.; Kim, S.; Tracy, J. B.; Jasanoff, A.; Bawendi, M. G. Phosphine Oxide Polymer for Water-Soluble Nanoparticles *J. Am. Chem. Soc.* **2005**, 127, 4556-4557.
- 45 Schroedter, A.; Weller, W. Ligand Design and Bioconjugation of Colloidal Gold Nanoparticles *Angew. Chem., Int. Ed.* **2002**, 41, 3218-3221.
- 46 Lee, D. C.; Mikulec, F. V.; Pelaez, J. M.; Koo, B.; Korgel, B. A. Synthesis and Magnetic Properties of Colloidal MnPt Nanocrystals *J. Phys. Chem. B* **2006**, 110, 11160- 11166.
- 47 Veisheh, O.; Sun, C.; Gunn, J.; Kohler, N.; Gabikian, P.; Lee, D.; Bhattarai, N.; Ellenbogen, R.; Sze, R.; Hallahan, A.; Olson, J. ; et al. An Optical and MRI Multifunctional Nanoprobe for Targeting Gliomas *Nano Lett.* **2005**, 5, 1003 – 1008.
- 48 Liu, X.; Xing, J.; Guan, Y.; Shan, G.; Liu, H. Synthesis of Amino-Silane Modified Superparamagnetic Silica Supports and Their Use for Protein Immobilization *Colloids Surf. A* **2004**, 238, 127– 131.
- 49 Yi, D. K.; Selvan, S. T.; Lee, S. S.; Papaefthymiou, G. C.; Kundaliya, D.; Ying, J. Y. Silica-Coated Nanocomposites of Magnetic Nanoparticles and Quantum Dots *J. Am. Chem. Soc.* **2005**, 127, 4990-4991.
- 50 Schroedter, A.; Weller, W.; Eritja, R.; Ford, W. E.; Wessels, J. M. Biofunctionalization of Silica-Coated CdTe and Gold Nanocrystals *Nano Lett.* **2002**, 2, 1363– 1367.
- 51 Bruchez, M.; Moronne, M.; Gin, P.; Weiss, S.; Alivisatos, A. P. Semiconductor Nanocrystals as Fluorescent Biological Labels *Science* **1998**, 281, 2013– 2016.
- 52 Gerion, D.; Pinaud, F.; Williams, S. C.; Parak, W. J.; Zanchet, D.; Weiss, S.; Alivisatos, A. P. Synthesis and Properties of Biocompatible Water-Soluble Silica-Coated CdSe/ZnS Semiconductor Quantum Dots *J. Phys. Chem. B* **2001**, 105, 8861-8871
- 53 Darbandi, M.; Thomann, R.; Nann, T. Single Quantum Dots in Silica Spheres by Microemulsion Synthesis *Chem. Mater.* **2005**, 17, 5720-5725.
- 54 Sousa, M. H.; Rubim, J. C.; Sobrinho, P. G.; Tourinho, F. A. Biocompatible Magnetic Fluid Precursors Based on Aspartic and Glutamic Acid Modified Maghemite Nanostructures *J. Magn. Magn. Mater.* **2001**, 225, 67– 72.
- 55 Mornet, S.; Vasseur, S.; Grasset, F.; Duguet, E. Magnetic Nanoparticles Design for Medical Diagnosis and Therapy *J. Mater. Chem.* **2004**, 14, 2161– 2175.
- 56 Xie, J.; Wang, C. H. Self-Assembled Biodegradable Nanoparticles Developed by Direct Dialysis for the Delivery of Paclitaxel *Pharm. Res.* **2005**, 22, 2079– 2090.

- 57 He, H.; Liu, H.; Zhou, K.; Wang, W.; Rong, P. Characteristics of Magnetic Fe<sub>3</sub>O<sub>4</sub> Nanoparticles Encapsulated with Human Serum Albumin *J. Cent. South Univ. Technol.* **2006**, 13, 6– 11.
- 58 Tiefenauer, L. X.; Kuhne, G.; Andres, R. Y. Antibody-Magnetite Nanoparticles: In Vitro Characterization of a Potential Tumor-Specific Contrast Agent for Magnetic Resonance Imaging *Bioconjugate Chem.* **1993**, 4, 347– 352.
- 59 Nam, J. M.; Stoeva, S. I.; Mirkin, C. A. Bio-Bar-Code-Based DNA Detection with PCR-like Sensitivity *J. Am. Chem. Soc.* **2004**, 126, 5932-5933.
- 60 Lewin, M.; Carlesso, N.; Tung, C.-H.; Tang, X.-W.; Cory, D.; Scadden, D. T.; Weissleder, R. Tat Peptide-Derivatized Magnetic Nanoparticles Allow In Vivo Tracking and Recovery of Progenitor Cells *Nat. Biotechnol.* **2000**, 18, 410 – 414.
- 61 Weizmann, Y.; Patolsky, F.; Lioubashevski, O.; Willner, I. Magneto-mechanical Detection of Nucleic Acids and Telomerase Activity in Cancer Cells *J. Am. Chem. Soc.* **2004**, 126, 1073– 1080.
- 62 Lartigue, L.; Oumzil, K.; Guari, Y.; Larionova, J.; Guérin, C.; Montero, J.-L.; Barragan-Montero, V.; Sangregorio, C.; Caneschi, A.; Innocenti, C.; Kalaivani, T.; Arosio, P.; Lascialfari, A. Water-Soluble Rhamnose-Coated Fe<sub>3</sub>O<sub>4</sub> Nanoparticles *Org. Lett.* **2009**, 11, 2992-2995.
- 63 Ashtari, P.; He, X. X.; Wang, K. M.; Gong, P., An efficient method for recovery of target ssDNA based on amino-modified silica-coated magnetic nanoparticles. *Talanta* **2005**, 67 (3), 548-554.
- 64 Allemann, E.; Gurny, R.; Doelker, E., Drug-loaded Nanoparticles - Preparation Methods and Drug Targeting Issues. *European Journal of Pharmaceutics and Biopharmaceutics* **1993**, 39 (5), 173-191.
- 65 Massart, R., Preparation of Aqueous Ferrofluids without using Surfactant - Behavior as a Function of the pH and the Counterions. *Comptes Rendus Hebdomadaires Des Seances De L Academie Des Sciences Serie C* **1980**, 291 (1), 1-3.
- 66 Mornet, S.; Gasset, F.; Portier, J.; Duguet, E. Maghemite@Silica Nanoparticles for Biological Applications *European Cells and Materials*, 2002, Vol. 3. Suppl. 2, 110-113.
- 67 Stöber, W.; Fink, A.; Bohn, E., Controlled Growth of Monodisperse Silica Spheres in Micron Size Range. *Journal of Colloid and Interface Science* **1968**, 26 (1), 62-69.
- 68 Nozawa, K.; Gailhanou, H.; Raison, L.; Panizza, P.; Ushiki, H.; Sellier, E.; Delville, J. P.; Delville, M. H., Smart control of monodisperse Sotber silica particles: Effect of reactant addition rate on growth process. *Langmuir* **2005**, 21 (4), 1516-1523.
- 69 Chen, S.-L.; Dong, P.; Yang, G.-H.; Yang, J.-J. Characteristic aspects of formation of new particles during the growth of monosize silica seeds *J. Colloid Interface Sci.*, **1996**, 180, 237-241.

- 70 Lu, Y.; Yin, Y. D.; Mayers, B. T.; Xia, Y. N., Modifying the surface properties of superparamagnetic iron oxide nanoparticles through a sol-gel approach. *Nano Letters* **2002**, *2* (3), 183-186.
- 71 Mornet, S.; Elissalde, C.; Hornebecq, V.; Bidault, O.; Duguet, E.; Brisson, A.; Maglione, M., Controlled growth of silica shell on Ba<sub>0.6</sub>Sr<sub>0.4</sub>TiO<sub>3</sub> nanoparticles used as precursors of ferroelectric composites. *Chemistry of Materials* **2005**, *17* (17), 4530-4536.
- 72 Gaudon, M.; Basly, B.; Fauque, Y.; Majimel, J.; Delville, M. H., Thermo-chromic Phase Transition on CuMo<sub>0.9</sub>W<sub>0.1</sub>O<sub>4</sub>@SiO<sub>2</sub> Core-Shell Particles. *Inorganic Chemistry* **2009**, *48* (5), 2136-2139.
- 73 Muller, R. N.; Roch, A.; Colet, J.-M.; Ouakssim, A.; Gillis, P. in: A. E. Merbach, É. Tóth (Eds.), *The Chemistry of Contrast Agents in Medical Magnetic Resonance Imaging*, Wiley, New York, Chapter 10, pp. 417-435 (2001).
- 74 Laurent, S.; Forge, D.; Port, M.; Roch, A.; Robic, C.; Elst, L. V.; Muller, R. N., Magnetic iron oxide nanoparticles: Synthesis, stabilization, vectorization, physicochemical characterizations, and biological applications. *Chemical Reviews* **2008**, *108* (6), 2064-2110.
- 75 Gueron, M., Nuclear relaxation in macromolecules by paramagnetic ions: a novel mechanism. *Journal of Magnetic Resonance* **1975**, *19* (1), 58-66.
- 76 Roch, A.; Muller, R.N. Longitudinal relaxation of water protons in colloidal suspensions of superparamagnetic crystals Proc. 11th Annu. Meet. Soc. Magn. Reson. Med. 1992, *11*, 1447.
- 77 Roch, A.; Muller, R. N.; Gillis, P., Theory of proton relaxation induced by superparamagnetic particles. *Journal of Chemical Physics* **1999**, *110* (11), 5403-5411.
- 78 Gillis, P.; Moïny, F.; Brooks, R. A., On T<sub>2</sub>-shortening by strongly magnetized spheres: A partial refocusing model. *Magnetic Resonance in Medicine* **2002**, *47* (2), 257-263.
- 79 LaConte, L.E.W.; Nitin, N.; Kurkiya, O.; Caruntu, D.; O'Connor, C. J.; Hu, X.; Bao, G. Coating thickness of magnetic iron oxide nanoparticles affects R<sub>2</sub> relaxivity *J. Magn. Res. Imaging* **2007**, *26*, 1634-1641.
- 80 Norek, M.; Pereira, G. A.; Geraldés, C. F. G. C.; Denkova, A.; Zhou, W.; Peters, J. A. NMR Transversal relaxivity of suspensions of lanthanide oxide nanoparticles *J. Phys. Chem. C* **2007**, *111*, 10240-10246.
- 81 Pereira, G. A.; Norek, M.; Peters, J. A.; Ananias, D.; Rocha, J.; Geraldés, C. F. G. C. NMR transversal relaxivity of aqueous suspensions of particles of Ln(3+)-based zeolite type materials *Dalton Trans*, **2008**, 2241-2247.
- 82 Pinho, S. L. C.; Pereira, G. A.; Voisin, P.; Kassem, J.; Bouchaud, V.; Etienne, L.; Peters, J. A.; Carlos, L. D.; Mornet, S.; Geraldés, C. F. G. C.; Rocha, J.; Delville, M.-H., Fine Tuning of the Relaxometry of gamma-Fe<sub>2</sub>O<sub>3</sub>@SiO<sub>2</sub> Nanoparticles by Tweaking the Silica Coating Thickness. *ACS Nano* **2010**, *4* (9), 5339-5349.

- 83 Freed, J. H., Dynamic effects of pair correlation functions on spin relaxation by translational diffusion in liquids. II. Finite jumps and independent T1 processes. *Journal of Chemical Physics* **1978**, *68* (9), 4034-4037.
- 84 Ayant, Y.; Belorizky, E.; Alizon, J.; Gallice, J., Calculation of spectral densities for relaxation resulting from random translational modulation of magnetic dipolar coupling in liquids. *Journal De Physique* **1975**, *36* (10), 991-1004.
- 85 Roose, P.; Vancraen, J.; Finsy, R.; Eisendrath, H., Field-Cycling Proton Nuclear Magnetic Relaxation-Dispersion Study of Aqueous Colloidal Silica Sols. *Journal of Magnetic Resonance, Series A* **1995**, *115* (1), 20-25.
- 86 Voisin, P.; Ribot, E. J.; Miraux, S.; Bouzier-Sore, A.-K.; Lahitte, J.-F.; Bouchaud, V.; Mornet, S.; Thiaudiere, E.; Franconi, J.-M.; Raison, L.; Labrugere, C.; Delville, M.-H., Use of lanthanide-grafted inorganic nanoparticles as effective contrast agents for cellular uptake imaging. *Bioconjugate Chemistry* **2007**, *18* (4), 1053-1063.

# **6.**

## *Final Conclusions and Future Work*

---

The objective of this thesis was to design and prepare bio-imaging probes, in particular exhibiting MRI and photoluminescence bimodality. Two different types of nanoparticles performing as  $T_1$  and  $T_2$  MRI contrast agents were synthesised and their physical and chemical properties characterised, namely texture, structure,  $^1\text{H}$  dynamics and relaxometry and photoluminescence properties. The combination of the properties of trivalent lanthanide complexes and nanoparticles offered an excellent solution for bimodal imaging. The following relevant observations and conclusions may prompt future studies on related systems.

- **$T_1$ -type contrast agents**

- Bimodal MRI-photoluminescence probes for bio-imaging consisting on  $\text{SiO}_2$  nanoparticles derivatized with DTPA- $\text{Ln}^{3+}$  and PMN- $\text{Ln}^{3+}$  complexes ( $\text{SiO}_2@$ APS/DTPA:Gd:Ln; and  $\text{SiO}_2@$ APS/PMN:Gd:Ln;  $\text{Ln}^{3+} = \text{Eu}^{3+}, \text{Tb}^{3+}$ ) were developed. These systems bear an active magnetic centre ( $\text{Gd}^{3+}$ ) and photoluminescent ions ( $\text{Eu}^{3+}$  or  $\text{Tb}^{3+}$ ) on the surface of silica nanoparticles.
- The number of  $\text{Ln}^{3+}$  ( $\text{Eu}^{3+}$ ,  $\text{Tb}^{3+}$  and  $\text{Gd}^{3+}$ ) ions on the surface the  $\text{SiO}_2@$ APS/DTPA nanoparticles (up to ca.  $10^4$  ions per nanoparticle) is determined by the amount of DTPA grafted. Because the  $\text{SiO}_2@$ APS/PMN nanoparticles exhibit a second type of local coordination for the  $\text{Ln}^{3+}$  ion it is difficult to quantify the amount of PMN complex grafted, although it is possible to estimate the amount of  $\text{Ln}^{3+}$  per nanoparticle (up to ca.  $10^5$  ions per nanoparticle).
- The tandem use of  $^{13}\text{C}$  and  $^{29}\text{Si}$  solid-state NMR and DRIFT spectroscopy was shown to be very powerful approach to study the modification of the surface of the nanoparticles. Upon APS derivatization the number of surface hydroxyl groups decreases and the  $^{29}\text{Si}$  ( $\text{Q}^2+\text{Q}^3$ )/ $\text{Q}^4$  population ratio is reduced from 0.43 to 0.37. For the  $\text{SiO}_2@$ APS/DTPA system, clear evidence of the covalent bonding between APS and DTPA is provided by the secondary amide C=O stretch at  $1685\text{ cm}^{-1}$ . Since the number of silanol groups increases (the ratio ( $\text{Q}^2+\text{Q}^3$ )/ $\text{Q}^4$  increases from 0.37 to 0.62) reaction of  $\text{SiO}_2@$ APS with DPTA has the side effect of modifying the surface of the  $\text{SiO}_2$  nanoparticles. Although the APS to PMN covalent

bonding could not be ascertained by DRIFT or NMR evidence for it was forthcoming from photoluminescence spectroscopy. As observed in the DTPA system, the reaction between APS and PMN modified the nanoparticles surface, increasing the number of silanol groups, with  $(Q^2+Q^3)/Q^4$  raising from 0.37 to 0.51.

- Complexation of DTPA and PMN to  $\text{Ln}^{3+}$  ions emitting in the visible region afforded long-life excited states, resistance to photo-bleaching, and sharp emission bands. The photoluminescence properties of the systems were not changed by the incorporation of  $\text{Gd}^{3+}$  ions. Evidence was obtained for the energy transfer from the DTPA/PMN ligand to  $\text{Ln}^{3+}$ . The grafting of PMN, a pyridine-based aromatic antenna ligand enhanced this energy transfer. While in the  $\text{SiO}_2@\text{APS}/\text{DTPA}:\text{Eu}$  system the  $\text{Eu}^{3+}$  ions reside in a single low-symmetry site, with a large local distribution, in the  $\text{SiO}_2@\text{APS}/\text{PMN}:\text{Eu}$  system there are two local  $\text{Eu}^{3+}$  environments. We conjectured that in one site the  $\text{Eu}^{3+}$  coordinates to the PMN chelate, while in a second site it interacts strongly with the NPs surface via the silanol groups, which are far more abundant than the amino groups on the silica surface.
- The incorporation of  $\text{Gd}^{3+}$  ions, the MRI probe, in the nanosystems does not change the emission properties of the  $\text{Eu}^{3+}$  and  $\text{Tb}^{3+}$  ions. The relaxometric features of these nanoparticles are slightly better than the properties of the commercially-available  $[\text{Gd}(\text{DTPA})]^{2-}$  complex.
- The bimodal probes are rapidly and efficiently uptaken by RAW 264.7 cells (mouse macrophage cell line) exhibiting the  $T_1$ -weighted MRI images of cellular pellets increased contrast and potential optical tracking by fluorescence.
- In future studies an alternative and more efficient procedure should be devised for grafting the PMN complex, ensuring that a single  $\text{Eu}^{3+}$  local environment is present.

- **$T_2$ -type contrast agents**

- Iron oxide nanoparticles coated with silica layers of different thickness were prepared. The stability of the resulting nanoparticles suspensions is

increased by this silica shell, which also allows the straightforward grafting of targeting molecules.

- ③ The thickness of this silica shell changed considerably the  $r_2$  and  $r_2^*$  relaxivities at medium and high  $B_0$  fields (0.47 T and 11.7 T), and the  $r_1$  relaxivity at medium  $B_0$  fields (0.47 T) as a result of decreased outer-sphere relaxation effects.
- ③ A model was proposed to explain the impact of the silica shell on the  $r_2$  and  $r_2^*$  relaxivities. This model partitions the silica coating in two regions, one impermeable to water and close to the  $\gamma\text{-Fe}_2\text{O}_3$  core, the other porous to water and at the interface with the bulk water.
- ③ The magnetometry curves of the  $\gamma\text{-Fe}_2\text{O}_3@\text{SiO}_2$  nanoparticles were fitted with a Langevin function and the NMRD profiles with the model of Roch *et al.* A good fit of the NMRD curves was obtained for particles covered with the thinnest silica layers. For particles with relatively thick silica layers it was necessary to introduce a contribution from the diamagnetic silica.
- ③ The cell viability and mitochondrial dehydrogenase expression given by the microglial cells were evaluated and confirmed that these contrast agents are not detrimental to the microglial cells.
- ③ The knowledge obtained with these systems may now be extended to other systems and applications. The results provide clues for the design of contrast agents based on superparamagnetic nanoparticles and their optimisation for specific medical diagnosis applications.
- ③ In future work this system should be extended to bimodal, by grafting a photoluminescence probe.



### Résumé :

Cette thèse décrit une stratégie de synthèse de nouvelles générations des nanoparticules (NPs) pour applications biomédicales, visant à une amélioration de leurs performances pour l'imagerie, le diagnostic thérapeutique. Ces NPs présentent plusieurs fonctionnalités leur permettant de réaliser des tâches multiples. Deux types de sondes bimodales ont été développés et étudiés afin d'évaluer leur potentiel comme agents (1) de contraste en IRM et (2) luminescents. Ces objets combinent les propriétés des complexes de lanthanide ( $\text{Ln}^{3+}$ ) et celles des NPs de silice ou de type cœur-écorce  $\text{Fe}_2\text{O}_3@\text{SiO}_2$  pour une imagerie bimodale. Ces NPs testées sur des cellules vivantes ont permis d'illustrer la preuve du concept aussi bien en IRM avec une augmentation d'intensité des images et un impact significatif sur les relaxivités  $r_1$ ,  $r_2$  et  $r_2^*$  qu'en photoluminescence. L'étude du système cœur-écorce a montré que l'influence du contrôle fin de l'écorce autour du noyau d'oxyde de fer a pu être modélisée.

### Mots clés :

Nanoparticules multifonctionnelles,	cœur-écorce/couronne,	$\text{Fe}_2\text{O}_3$ ,
Lanthanides,	agents de contraste IRM	agents de contraste optiques
relaxométrie,	RMND,	photoluminescence

---

Title: Multifunctional nanoparticles for MR and fluorescence imaging.

### Abstract:

This thesis describes a strategy of synthesis of new generations of nanoparticles (NPs) for biomedical applications, aiming at an improvement of their performances for the imaging, and the therapeutic diagnosis. These NPs present several functionalities enabling them to carry out multiple tasks. Two types of bimodal probes were developed and studied so as to evaluate their potential as contrast agents (1) in MRI and (2) and luminescence. These objects combine the properties of the lanthanide complexes ( $\text{Ln}^{3+}$ ) and those of NPs of silica or core/shell  $\text{Fe}_2\text{O}_3@\text{SiO}_2$  for a bimodal imaging. These NPs tested on living cells were able to illustrate the proof of the concept not only in MRI with an increase of intensity of the images and a significant impact on the relaxivities  $r_1$ ,  $r_2$  and  $r_2^*$  but also in photoluminescence. The study of the core/shell system showed that the influence of the fine control of the shell around the iron oxide core could be modeled.

### Keywords :

Multifunctional nanoparticles,	core-shell/corona,	$\text{Fe}_2\text{O}_3$ ,
Lanthanides,	MRI contrast agents	optical contrast agents
relaxometry,	RMND,	Photoluminescence